A GENERALIZED FLUIDIZED BED REACTOR MODEL ACROSS THE FLOW REGIMES

by

IBRAHIM A. ABBA

B.Eng., Ahmadu Bello University, Nigeria, 1991
M.Sc., University of Petroleum & Minerals, Saudi Arabia, 1995

A THESIS SUBMITTED IN PARTIAL FULFILMENT OF

THE REQUIREMENTS FOR THE DEGREE OF

DOCTOR OF PHILOSOPHY

in

THE FACULTY OF GRADUATE STUDIES

Department of Chemical and Biological Engineering

We accept this thesis as conforming
to the required standard

THE UNIVERSITY OF BRITISH COLUMBIA

July, 2001

In presenting this thesis in partial fulfilment of the requirements for an advanced degree at the University of British Columbia, I agree that the Library shall make it freely available for reference and study. I further agree that permission for extensive copying of this thesis for scholarly purposes may be granted by the head of my department or by his or her representatives. It is understood that copying or publication of this thesis for financial gain shall not be allowed without my written permission.

Department of _Chemical & Biological Engng._

The University of British Columbia
Vancouver, Canada

Date _Oct. 9, 2001_

DE-6 (2/88)

Abstract

A large number of industrial catalytic and non-catalytic processes employ fluidized beds, and newer and more challenging applications are emerging. Driven by the growth in applications and the challenges they bring, reliable reactor models for fluidized beds are vital for the design, scale-up and optimal operation of these processes. Traditionally, models are often developed with a particular process in mind based on consideration of the operating conditions and flow regime of fluidization, with the range of applicability limited to the cases tested. The complexity is compounded by the existence of distinctly different flow regimes. Considerable uncertainty exists in flow regime transition criteria, and most existing models predict discontinuities at the boundaries, contrary to experimental evidence. In addition, most practically important fluid bed reactors involve complex reactions, sometimes accompanied by significant volume change, with selectivity critical. However, there are few attempts to evaluate reactor model performance using commercial-scale data with selectivity as a criterion.

In this research, sponsored by the Mitsubishi Chemical Corporation in Japan, a new generic fluid bed reactor (GFBR) model is developed applicable across the flow regimes most commonly encountered in industrial scale fluid bed reactors: bubbling, turbulent and fast fluidization. The model interpolates between three regime-specific models – the generalized two-phase bubbling bed model, dispersed plug flow, and the generalized core-annulus model – by probabilistic averaging of hydrodynamic and dispersion variables based on the uncertainty in the flow regime transitions. Predictions of hydrodynamic variables across the three fluidization flow regimes are realistic, while conversion predictions are in good agreement with available experimental data. The probabilistic approach leads to improved predictions of reactor performance compared with any of the three separate models for individual flow regimes, while overcoming the difficulties in predicting the transition boundaries among these flow regimes and avoiding discontinuities at these boundaries.

Model predictions of selectivities, yields and conversions for two industrial-scale processes (oxidation of naphthalene to phthalic anhydride and oxy-chlorination of ethylene) are reasonable and compare favourably with available plant data. Ability of the model to aid in simulation experimentation over a wide range of conditions is

demonstrated. Model predictions are strongly influenced by the reaction kinetics, gas dispersion, superficial gas velocity and reactor temperature. Their accuracy strongly depends on utilizing reliable estimates of the model parameters. Accounting for the volume change due to reaction, caused by a change in the number of moles as well as variations in temperature and pressure along the reactor, improves the performance of the model relative to industrial data. Multiple flow regimes can exist in the same reactor due to changing volumetric flow. The probabilistic modeling approach is shown to effectively track such changes.

Application of the GFBR model to gas-solid reactions is demonstrated by coupling a single-particle model with the generic fluid bed reactor model. Predictions from the combined model for the zinc sulfide roasting process are reasonable. However, in order to fully realize the potential of the combined model, some extensions are required.

Gas mixing experiments were conducted using both steady state and step change tracer injection in a 4.4 m high and 0.286 m ID column to provide better understanding of the effects of dispersion in each phase, as well as interphase mass transfer, with increasing gas velocities. Data interpretation using a one-dimensional single-phase model and a generalized two-phase model confirmed the expected trends of increasing dispersion in both the low- and high-density phases as the superficial gas velocity is increased. Beyond the transition velocity, U_c, however, the dispersion coefficients decreased in some cases.

The GFBR model provides a means of predicting hydrodynamics states and quantities in reactors. For given particle properties, operating conditions and reactor geometry, it is possible to predict the flow regime(s) and key hydrodynamic and thermal properties. The model is a useful tool for the design and simulation of fluid bed processes. Further pursuit of the probabilistic modeling approach is well warranted.

Table of Contents

List of Tables

List of Figures

xii

Acknowledgements

Chapter 1

Introduction

Fluidized bed reactors constitute an integral part of the chemical process industries. Over the years, newer and more challenging applications have been sought, from biochemical and petrochemical to applications in microelectronics. As applications grow, so do the challenges and the need for gaining further insight. Reactor models for fluidized beds are therefore indispensable in the design, scale-up and optimal operation of chemical processes. Efforts are being made continually to develop new and efficient models and to refine existing ones. Fluidized bed reactor models range from those based on the simple "two-phase theory" of Toomey and Johnston (1952) to complex ones based entirely on solving continuity, momentum and energy equations using fast computers (e.g. Ding and Gidaspow, 1990).

Despite the voluminous literature in this area (e.g., see Geldart, 1986; Kunii and Levenspiel, 1991; Geldart and Rhodes, 1992; Grace et al., 1997), a number of reactor modeling issues remain to be addressed. Traditionally, reactor models have been constructed and applied to specific processes based on consideration of the operating conditions and regime of fluidization. However, although criteria for transition to different flow regimes have been the subject of many studies, they have not yet been established with certainty, as highlighted in a recent review (Bi et al., 2000). Hence, a number of questions arise as flow conditions in the fluidized bed change across the flow regime spectrum as shown in Fig. 1.1: For example, is the concept of bubbles applicable to flow regimes beyond bubbling? What is the degree of certainty that the bed operates within a prescribed flow regime for a given set of operating conditions and particle properties? What mathematical formulation best describes a particular flow regime, assuming certainty of being in that regime? How are the multiple flow regimes within the same bed addressed for systems accompanied by changing volumetric flow? How are the fluidization regimes best identified for different classes of particles?

To address these and other questions, a broad-based reactor model capable of reliably predicting changes within the bed over a wide range of operating conditions is

1

needed. Such a model should be applicable over the fluidization flow regimes of interest and provide a means of predicting the transition boundaries among these flow regimes, while giving improved predictions of particle and gas dynamics and of reactor performance. This is the goal of this project, sponsored by the Mitsubishi Chemical Corporation (MCC) in the interest of achieving better understanding of the behavior of gas-phase fluidized bed reactors. An improved model should provide more reliable scale-up (e.g., for the propane-based acrylonitrile process), rigorous simulation experimentation of existing processes for performance enhancement and exploration of alternatives for other processes (e.g., air-based to oxygen-based oxy-chlorination).

We begin with an overview of the pertinent hydrodynamics flow regimes and transition velocities to set the stage for the model development in Chapter 2. Second, fluidized bed reactor models constructed for the different flow regimes are briefly reviewed, from which key outstanding issues are identified. The specific objectives of this study are then outlined.

1.1 Hydrodynamic Flow Regimes and Transition Velocities

In gas fluidization, a suspension of fine solid particles behaves like a liquid due to upflow of a gas. If sufficient gas passes upward through the particles, the bed begins to fluidize. At low velocity, when the gas merely percolates through the interstices in the bed of stagnant particles, the bed is in a fixed state (Fig. 1.1a). As the velocity is increased, the bed undergoes transition from a fixed bed to an expanded bed in which the particles move apart and vibrate in restricted regions and where the particles are just suspended by the upflowing gas; the bed is then referred to as incipiently fluidized. At higher flows, bubbles coalesce and grow as they rise to the top of the bed. Because of large bubbles leaving the column in an irregular manner, the pressure drop across the bed fluctuates with high amplitude and frequency. Such a bed is called a bubbling fluidized bed as shown in Fig. 1.1b. The gas bubbles coalesce and grow as they rise and may eventually become big enough to fill the column cross-section. These large bubbles are called slugs, and the flow regime is called slugging (see Fig. 1.1c). At sufficiently high velocity, the upper surface of the bed disappears, and entrainment becomes appreciable. Rapid coalescence and splitting of bubbles are observed leading to turbulent motion of solid

clusters and voids of various sizes and shapes. The pressure drop across the bed fluctuates at high frequency with small amplitude. Such a bed is referred to as a turbulent fluidized bed and is shown schematically in Fig. 1.1d. Transition from turbulent to fast fluidization (Fig. 1.1e) occurs when the velocity is increased even further resulting in substantial entrainment. This usually necessitates the use of cyclones to recycle the entrained solids as indicated in Fig. 1.1e. Pneumatic conveying (dilute phase contacting) occurs when the feed rate of the solids is small enough and velocity of the gas high enough that solids are carried through the column as dispersed particles (Fig. 1.1f).
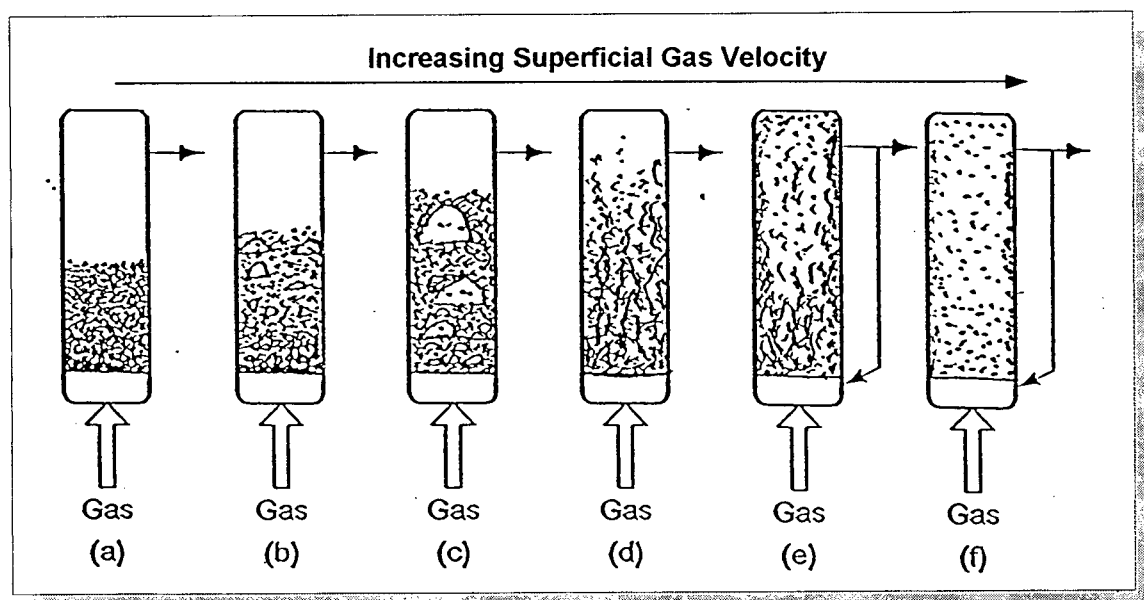
Figure 1.1. Flow patterns in gas-solids fluidized beds (adapted from Grace, 1986): (a) fixed bed; (b) bubbling bed; (c) slug flow; (d) turbulent fluidization; (e) fast fluidization; (f) pneumatic conveying.

Bi and Grace (1995a) proposed a flow regime diagram capturing all the regimes as shown in Fig. 1.2. The scope of this thesis is limited to the three principal fluidization flow regimes: bubbling, turbulent and fast fluidization, as they are by far the most widely applied by industry. There have been many attempts to establish criteria for regime transitions (see Yerushalmi and Cankurt, 1979; Bi and Grace, 1995a; Bi et al., 2000). The following mark the onset of the three regimes of interest in this work:

- Velocity at which bubbles first appear, minimum bubbling velocity, U_{mb} (Abrahamsen and Geldart, 1980).

- Velocity U_c at which the standard deviation of absolute pressure fluctuations reaches a maximum (Yerushalmi and Cankurt, 1979; Bi and Grace, 1995b), often used to demarcate the onset of the turbulent fluidization regime.

- Velocity U_{se} at which significant entrainment of particles occurs (Bi et al., 1995), thought to denote the onset of the fast fluidization flow regime.

Correlations for determining the U_c and U_{se} transition velocities are presented in Chapter 2, while that for U_{mb} is given in Appendix A. The uncertainty in these correlations is discussed in Chapter 2.

1.2 Fluidized Bed Reactor Models

Reactor models attempt to obviate the need for experiments by capturing the physicochemical state of the system through appropriate mathematical representations. Models can be categorized as either mechanistic or empirical. Mechanistic models incorporate continuity and energy balances, and are derived mainly on the basis of detailed understanding of the underlying mechanisms of the process in question. Empirical models are derived from specific observed behavior of the system with little or no attention to physical mechanisms. Our focus throughout this thesis is on the former.

1.2.1 Bubbling bed

The bubbling fluidization regime has been extensively studied. The two-phase theory of fluidization considers the fluid bed as a two-phase system consisting of a discontinuous phase made up of bubbles and a continuous phase made of a dense mixture of solid particles and gas, with mass transfer occurring between the two phases (Toomey
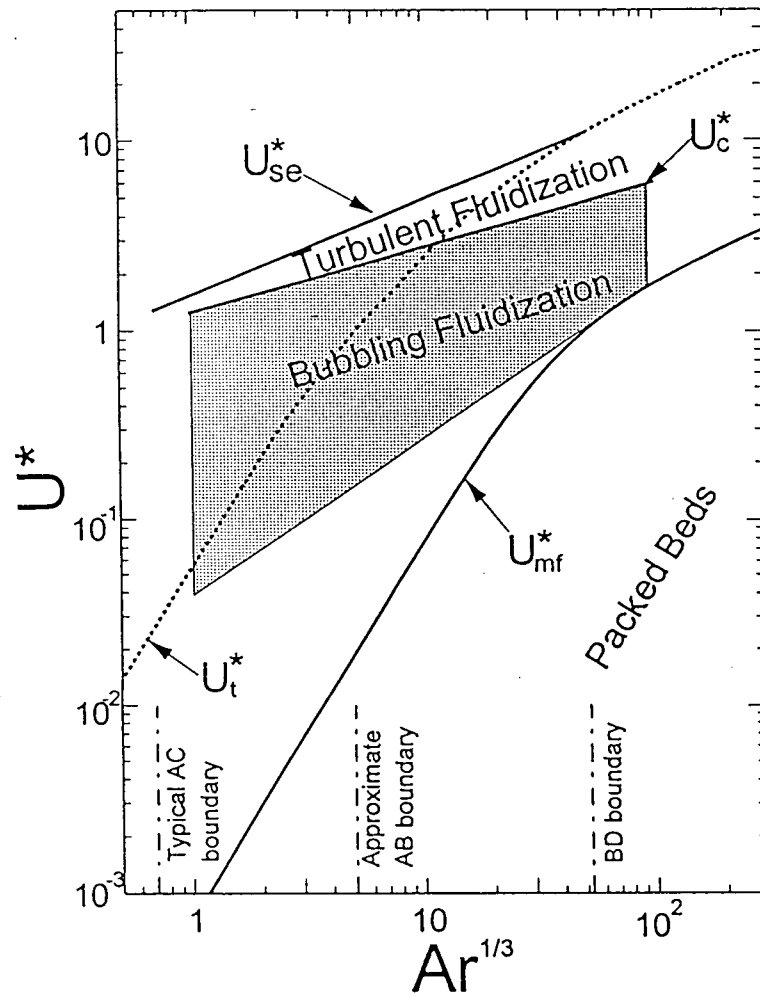
Figure 1.2. Flow regime map for gas-solids fluidization. Heavy lines indicate transition velocities, while shaded regions designate typical operating range of bubbling fluidized beds (Bi and Grace, 1995a).

and Johnston, 1952). Most bubbling bed models are based on this concept, while others (e.g., Kunii and Levenspiel, 1969) consider clouds around the bubbles as a third phase. These models can be classified into two-phase models and bubbling bed models. The bubbling bed models consider the dilute phase as consisting of well-defined bubbles whose diameters are key parameters, while two-phase models consider the dilute phase as a continuous system. They incorporate solid fractions, mixing parameters and interchange coefficients and can be used for modeling and scale-up purposes. Such models include the Grace (1984) two-phase model, the Kunii and Levenspiel (1969) three-phase model, the Kato and Wen (1969) bubble assemblage model and the Partridge and Rowe (1966) cloud model. A modified form of the Kato and Wen model was successful in simulating the partial oxidation of methane to synthesis gas in a bubbling fluidized bed (Mleczko et al., 1996; Wurzel and Mleczko, 1998). Because of the extensive literature on this subject, details of these models are not covered here. They have either been derived or comprehensively summarized by Grace (1971, 1984, 1986), Kunii and Levenspiel (1991) and more recently by Marmo et al. (1999).

1.2.2 Turbulent bed

Because of the advantages of the turbulent regime such as enhanced gas-solids contacting, reduced gas backmixing and favourable bed-to-surface heat transfer (e.g. see Massimilla, 1973; Avidan, 1997; Chaouki et al., 1999; Sotudeh-Gharebaagh et al., 1999; Bi et al., 2000), many commercial fluid bed processes operate in the turbulent fluidization regime. In addition, the bottom section of fast-fluidized beds is also often considered to operate in the turbulent fluidization flow regime. Relatively little has been reported on the reactor performance and modeling for turbulent bed reactors compared to the abundance of information on bubbling and fast-fluidized bed reactors. Turbulent fluidized bed reactor models have assumed single phase one-dimensional plug flow (van Swaaij, 1978; Fane & Wen, 1982), a continuous stirred tank reactor (e.g. Wen, 1984; Hashimoto et al., 1989), axially dispersed plug flow (Avidan, 1982; Wen, 1984; Edwards & Avidan, 1986; Li and Wu, 1991; Foka et al., 1994) or two-phase behaviour with interchange of gas between dilute and dense phases/regions (Krambeck et al., 1987; Foka et al., 1996; Ege et al., 1996; Venderbosch, 1998; Thompson et al., 1999).

For example, Foka et al. (1994) reported satisfactory prediction of conversion in a catalytic turbulent fluidized bed methane combustor with a single-phase axially dispersed plug flow model. They showed that the idealized limiting case of perfect mixing (CSTR) consistently under-predicted the conversion, while the plug flow model over-predicted it, consistent with experimental evidence on the behaviour of turbulent beds showing that there is appreciable backmixing of gas, intermediate between these two idealized cases. The two-phase model with axial dispersion has also been shown to give satisfactory prediction of methane conversion (Foka et al., 1996) and carbon monoxide conversion (Venderbosch, 1998) in the turbulent regime. Werther and Wein (1994) considered a combination of a bubbling bed model to represent the lower dense part of the reactor and a fast fluidization model for the freeboard. The core-annulus model and its variants have also been reported to have had some success in accounting for the solids hold-up and the radial variations in flow structure experimentally observed in turbulent fluidized beds (e.g. Abed, 1984; Ege et al., 1996; Kunii and Levenspiel, 1997).

Bi et al. (2000) summarized models developed for turbulent fluidized bed reactors, accounting for interchange of gas between low- and high-density phases, axial dispersion, gas convection and reaction.

1.2.3 Fast Fluidization

Yerushalmi et al. (1976) coined the term fast fluidization to indicate the flow regime between turbulent fluidization and pneumatic transport. Since then, circulating fluidized beds (CFBs), operating in the fast fluidization regime, have developed very quickly. Hundreds are now in operation for combustion and other chemical reactions. For example, CFB has been used for direct oxidation of butane to maleic anhydride (Contractor et al., 1994), pyrolysis (Berg, 1989) and combustion of fuels (Itoh et al., 1991).

Not surprisingly, many CFB reactor models have been proposed. Models can be broadly classified into single-region one-dimensional models and distinctly two-region models with and without allowance for hydrodynamic axial gradients. Some single-region models completely ignore radial and axial gradients, assuming plug flow of gas (e.g., Ouyang et al., 1995), while others allow for axial gradient (e.g., Arena et al., 1995).

Single region models have generally not been very successful as they do not give good description of actual behavior in CFB reactors. Two-region models are more realistic as there is ample evidence that there exist distinct dilute core and dense annular regions, especially for fully developed conditions (Ouyang et al., 1995; Schoenfelder et al., 1996). Models in this category include those that ignore axial hydrodynamic gradients (Brereton, et al., 1988, Kagawa et al., 1991) and those that consider axial gradients (Pugsley, et al., 1992, Puchyr et al., 1997; Kunii and Levenspiel, 2000).

In addition, a number of other so-called "two-fluid models" CFD have been established based on fundamental continuity, momentum and energy equations (Ding and Gidaspow, 1990; Sinclair, 1997). Although rapid advances are being made, computational limitations have limited the viability of the two-fluid models. However, given the recent advances in computing power, practical contributions are anticipated. Berruti et al. (1995) and Grace and Lim (1997) have given excellent reviews of the different categories of CFB models.

It is clear from the above that regardless of the model adopted for the bubbling, turbulent and fast-fluidized bed reactors, one must account appropriately for interchange of gas between the low and high-density structures, and dispersion due to chaotic motion. Generalized forms of the representative models (two-phase model (Grace, 1984), dispersed plug flow model (Edwards and Avidan, 1986) and core-annulus model (Brereton et al., 1988)) for the three flow regimes provide the framework for the generic model development in this work, presented in detail in Chapter 2. These regime-specific models are chosen because they are realistic and have had some success in describing the physical phenomena in the individual flow regimes. In addition, after the generalizations (explained in Chapter 2), they become fully compatible with each other so that a single model formulation for each of two phases can describe the phenomena across all three flow regimes.

1.3 Outstanding Issues

Models are often developed with a particular process in mind, and the range of applicability is then limited to the cases tested. The complexity is compounded by the existence of distinctly different flow regimes in fluidized beds that call for different

models, often requiring fundamentally different approaches and assumptions. Grace et al. (1999) outlined some limitations of existing models. The many models call into question the need for newer ones; however, a closer look reveals a number of critical issues that have yet to be addressed. For example:

(i) A practical model that adequately captures and describes the physicochemical fluid bed phenomena on a general scale applicable over multiple operating flow regimes is lacking. The closest attempt was by Grace (1986) who presented a framework for a general two-phase, one-dimensional model. In the analysis that followed, the general scheme was reduced to limiting cases through a series of assumptions.

(ii) In addition to the considerable uncertainty in the regime transition correlations and diagrams, the flow regime transitions are, in reality, diffuse rather than sharp as the transition criteria might suggest. As a result, predictions from most models result in discontinuities at the boundaries, whereas smooth transitions are observed in practice as the gas velocity is increased. Only recently has this aspect received attention (Thompson, et al., 1999; Grace et al., 1999).

(iii) A sound model should be capable of closely approximating the phenomena within the bed as well as be useful in providing guidelines for enhancing reactor performance, e.g. through optimization. Most practically important fluid bed reactors involve complex reactions where selectivity is critical. However, the number of such reactions handled and reported in performance analysis of models is normally small. It is, therefore, not surprising that there has been little comparison of models using selectivity as a criterion. There is a need to address this issue as most commercially important reactions follow complex paths with the desired product being an intermediate.

(iv) Models need to be validated using commercial-scale data. Most models are either never tested against large-scale data or, when this is done, compared only to the data for which the model was developed.

(v) A number of industrial gas phase reactions are accompanied by significant volume change due to reaction. The volume change can cause significant change in the bed hydrodynamics and reactor performance. Most existing models have been limited to single reactions with simple first order kinetics or single reactions with non-linear

kinetics; they have also been mostly limited to the bubbling flow regime of fluidization and to isothermal, isobaric conditions. No attempts have been reported to assess the impact of volume changes on the performance of a commercial-scale reactor. Efforts to address this issue are strongly warranted.

(vi) At present, no model in the open literature combines a single-particle model with a generalized fluid bed reactor model. Although complex, this task is important given the number of industrial fluidized bed processes involving gas-solid reactions.

1.4 Research Objectives

The purpose of this study is to address some of the issues outlined above. The principal objectives are to:

(a). Develop a generic fluidized bed reactor model applicable over the most commonly encountered fluidization regimes: bubbling, turbulent and fast fluidization, by capturing features of the limiting models and quantifying the uncertainty in regime boundaries.

(b). Overcome the difficulties in predicting the transition boundaries among these flow regimes and eliminate discontinuities at the boundaries, while giving improved predictions of particle and gas dynamics and of reactor performance.

(c). Conduct experimental investigation of gas mixing in bubbling-turbulent fluidized bed to provide better understanding of the effects of dispersion in each phase as well as interphase mass transfer, over a range of gas velocities spanning regime boundaries.

(d). Compare model predictions with experimental results and plant data for a number of pilot and commercial-scale systems with established reaction schemes, and compare various models using selectivity as the criterion.

(e). Establish a tool for making inferences about hydrodynamic quantities and states such as voidage, gas velocity, solids densities and flow regimes, and for aiding in design and scale-up; and also to offer means for reliable screening of options before committing major capital outlays to new projects or upgrading existing ones.

1.5 Thesis Layout

The remainder of the thesis is laid out in the following fashion.

Chapter 2 presents the complete development of the generic fluidized bed reactor (GFBR) model, a model which provides a seamless way of covering the complete range of gas velocities and flow conditions from minimum bubbling right up to fully fast fluidization conditions. It provides an overview of the different approaches to modeling across multiple operating regimes; in particular, it treats regime-specific and probabilistic approaches. The probabilistic approach adopted is then presented in detail. The numerical technique employed is also briefly explained. The chapter ends by describing how the generalized model is applied to specific cases in the subsequent chapters.

Chapter 3 presents gas-mixing experiments conducted using both steady state and step change tracer injection. Data are interpreted to determine the dispersion coefficients in both phases and the interphase mass transfer coefficient using a one-dimensional single-phase model and a generalized two-phase model.

In Chapter 4, the GFBR model is validated using experimental ozone decomposition data of Sun (1991), covering a wide range of superficial gas velocities and catalyst activities. The capability of the model in eliminating discontinuities at the boundaries, while giving improved predictions of particle and gas dynamics and of reactor performance is demonstrated. The regime-specific modeling approach is compared with the probabilistic approach.

Chapter 5 examines the application of the model to both catalytic and non-catalytic gas-solid industrial processes – oxy-chlorination of ethylene, oxidation of naphthalene to phthalic anhydride and zinc sulfide roasting – for which plant measurements are available, accompanied by sufficient details of reactor configuration and operating conditions. The model's ability to aid in "simulation experimentation" over a wide range of conditions is illustrated. For the non-catalytic process, a framework is presented for coupling the GFBR model with a single-particle gas-solid reaction model; the application of the combined model is demonstrated using zinc sulfide roasting as a case study.

In Chapter 6, the GFBR model is extended to variable-density gas-phase systems, accounting for changes in both temperature and pressure, as well as variations in total

molar flowrate along the reactor height. Multiple reactions with non-linear kinetics for the oxy-chlorination process treated in Chapter 5 are considered to assess the impact of volume change on the hydrodynamics and reactor performance. The influence of bulk transfer of gas between the low and high-density phases is also considered. This chapter effectively implements the full capability of the GFBR model as applied to catalytic gas-phase reactions.

The thesis concludes in Chapter 7 by summarizing key results and observations. Recommendations for further work are also outlined.

Chapter 2

Integrated Approach to FBR Modeling

2.1 Introduction

Until recently, each of the fluidization flow regimes described in Chapter 1 was treated quite separately with a distinct reactor model. An implicit assumption has been that the flow regime is known with certainty for given operating conditions and particle properties. This results in substantial discontinuities at the boundaries between the flow regimes, notwithstanding the fact that the transitions tend to be diffuse and gradual in nature, with a continuous variation in reactor performance as one passes from one flow regime to another (e.g. see Sun, 1991). Most catalytic fluid bed processes of commercial importance (e.g. acrylonitrile, phthalic anhydride, oxy-chlorination etc.) operate between the bubbling and turbulent or between the turbulent and fast fluidization flow regimes (Bolthrunis, 1989; Rhodes, 1996). The turbulent fluidized bed possesses aspects of both bubbling beds, where the mass transfer resistance between the bubble and dense phases affects conversion and selectivity, and fast-fluidized beds, where there is relatively rapid interchange between the dilute core and the dense annular region containing most of the particles. There is considerable uncertainty regarding flow regime transition correlations.

In earlier UBC/MCC work (Thompson et al., 1999; Grace et al., 1999), a "Generalized Bubbling Turbulent" (GBT) model was introduced based on the probabilistic averaging approach. This model provides a smooth transition between the bubbling and turbulent flow regimes and gives good agreement with available data for low and intermediate gas velocities. This approach is extended in this thesis so that the new model, which we call the Generic Fluidized Bed Reactor (GFBR) model provides a seamless way of covering the complete range of gas velocities and flow conditions from minimum bubbling right up to fully fast fluidization conditions. As noted in Chapter 1, the goals are to overcome the difficulties in predicting the transition boundaries among the three flow regimes and to eliminate discontinuities at the boundaries, while giving improved predictions of particle and gas dynamics and reactor performance.

2.2. Generic Descriptors: L- and H-phases

There are many ways in which the different phases and regions observed in fluidized beds have been described in the fluidization literature. The dense phase/region has been described as "dense, emulsion, more dense, annulus, clusters" etc. while the dilute phase/region has been variously referred to as "bubble, dilute, lean, void, core, less dense" etc. As a result of this array of confusing labels, it has not only been difficult to unify these descriptors into a coherent and standard form, but misleading descriptors have often been used in the literature (e.g. reference to the distorted and transitory voids in the turbulent flow regime as bubbles). Therefore, we introduce generic descriptors that realistically represent the different phases/regions encountered in all the fluidization flow regimes. As in Thompson et al. (1999), we use for the dilute phase/region the descriptor "low-density"(L) phase and for the dense phase/region the term "high-density" (H) phase. Thus, for the three flow regimes under consideration, the L-phase represents the bubble phase at low U, voids at intermediate U and core region at high U, while the H-phase represents dense/emulsion phase at low U, dense phase at intermediate U and annular region at high U.

2.3. Generic Fluid Bed Reactor (GFBR) Model

Our approach involves formulation of model equations that describe phenomena within each of the three flow regimes while providing smooth transitions between them without ever achieving complete certainty of being in any regime. This enables prediction of reactor performance variables for the three regimes through weighted averaging of the three regime-specific models themselves (not of their predictions). A schematic representation of the generalized model is shown in Fig. 2.1. The remainder of section 2.3 introduces formally the probabilistic approach and explains in detail all the steps involved in the probabilistic modeling approach.

But first, section 2.3.1 presents an overview of the different approaches to handling multiple models when operating across multiple regimes. Here, the pitfalls in the regime-specific approach within different contexts are highlighted. An attempt is made to distinguish the different approaches and to explain the basis for choosing the path taken.
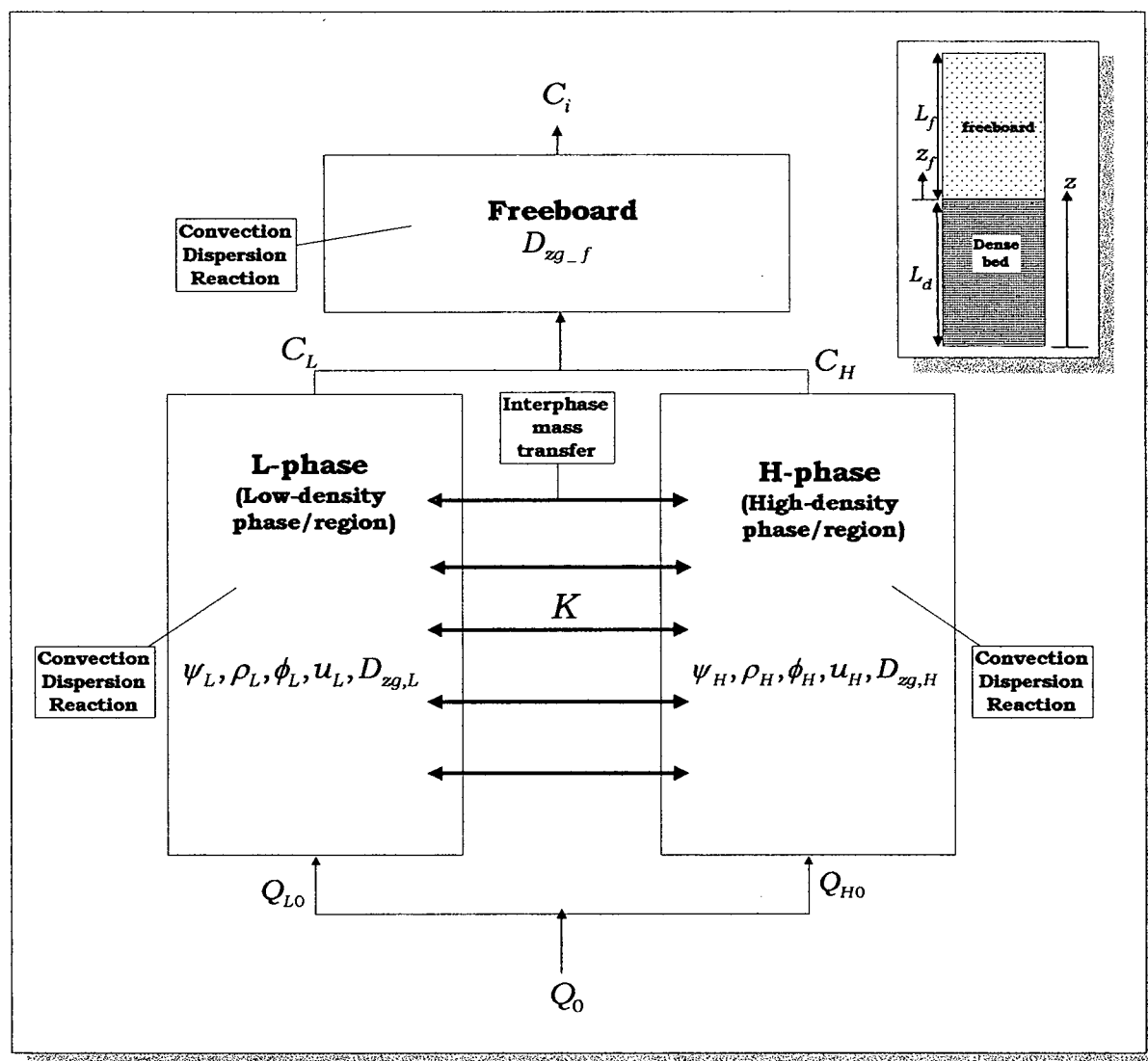
Figure 2.1. Schematic of generalized one-dimensional, two-phase/region model with freeboard (inset shows axial notations for the two regions)

2.3.1 Modeling across Operating Regimes

Figure 2.2 qualitatively presents two approaches (modular and synergistic) to managing multiple models. For illustration purpose, three candidate local models (1, 2 and 3) are applied across three operating flow regimes over a range of values of a hydrodynamic variable such as superficial gas velocity or gas hold-up. The distinguishing features of these approaches and their methodologies are described below.

2.3.1.1 Regime-Specific Approach

As illustrated in Fig. 2.2a, a broad-based fluid bed reactor model across the fluidization flow regimes can be developed via formulation of separate models, each unique and specific to a particular fluidization regime. In this way, the particular model employed during simulation depends on the fluidization conditions and regime determination criteria. We label this approach the "Regime-specific" approach. There are a number of drawbacks of this approach, namely: (i) Regime-specific models do not fully capture the physical phenomena in the bed, especially near the operating regime boundaries. (ii) There is an implicit assumption of complete certainty in determining the regime boundaries. (iii) The approach does not provide means of predicting hydrodynamic states and quantities. (iv) This approach results in discontinuities at regime boundaries. (v) The regime-specific models tend to ignore hydrodynamic regime changes within the same bed for given operating conditions (e.g. caused by a change in the molar flowrate or variation in cross-sectional area due to baffles).

Figure 2.3. outlines the steps involved in this approach. Although this approach is the traditional and easiest approach to modeling, because of the above inadequacies, it is not considered any further in this thesis, except in Chapter 4 where predictions from this approach are compared with predictions from the probabilistic approach and with experimental data.

2.3.1.2 Synergistic (Probabilistic) Approach

This approach is based on formulation of generalized model equations that can adequately describe phenomena within each flow regime. The approach does not assume complete certainty of being in any particular fluidization regime for any operating conditions; instead it interpolates between the various models. It creates synergy by
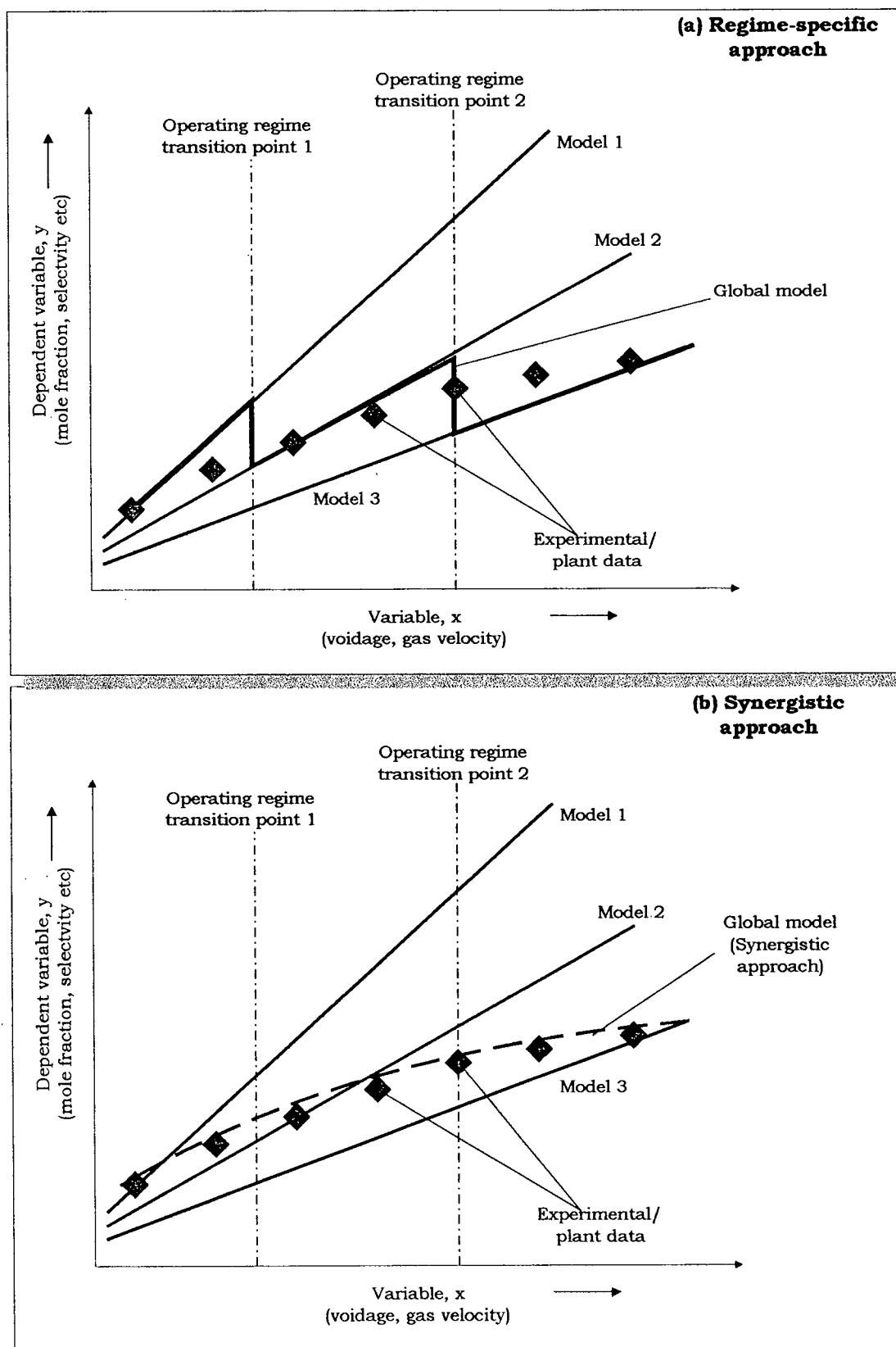
Figure 2.2. Illustration of the different approaches to managing multiple models
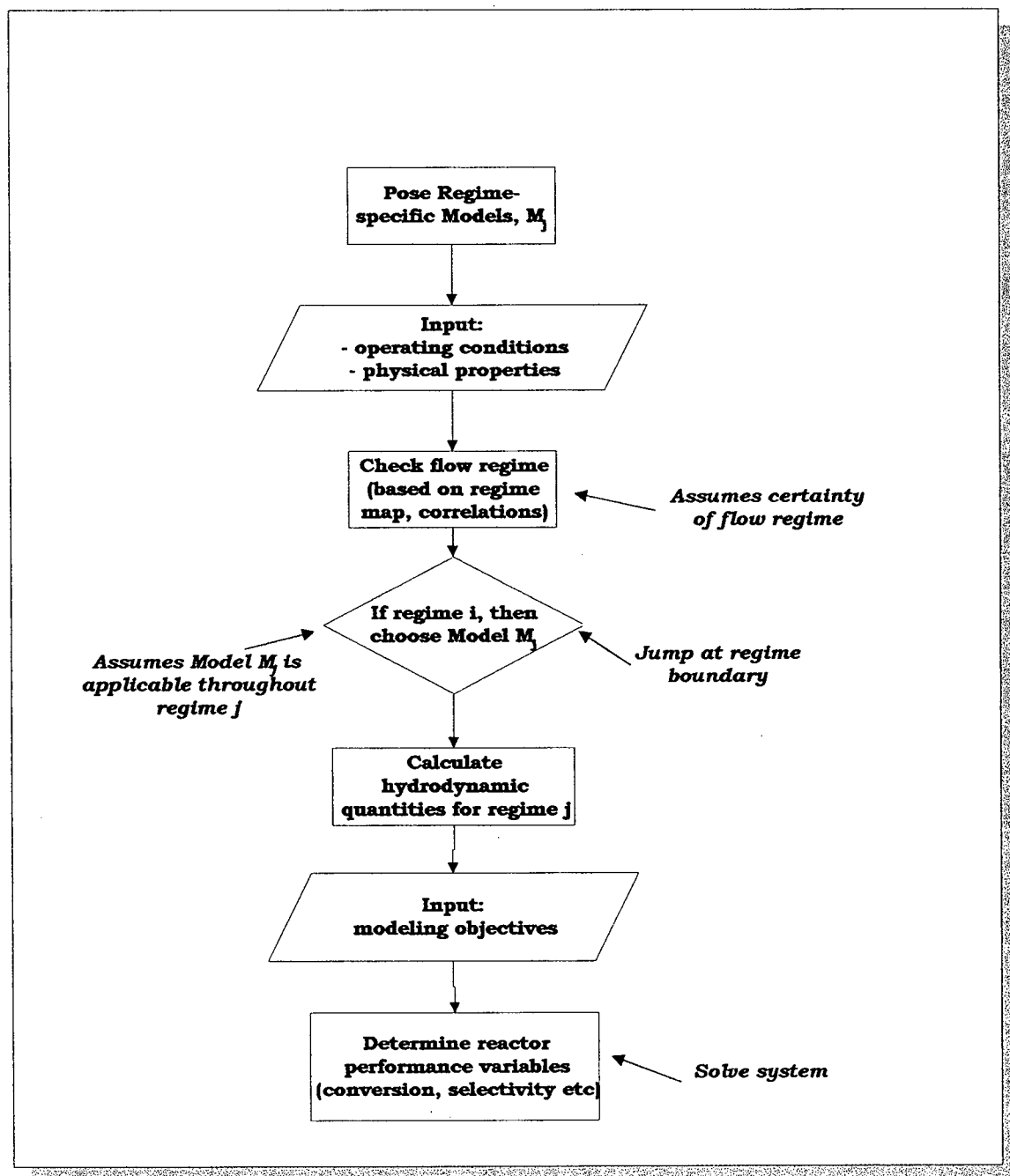
Figure 2.3. Illustration of modeling across flow regimes via regime-specific approach.

capturing salient features of the limiting models at any given operating point, and is labeled the "Probabilistic" approach. Probability theory dictates that, when dealing with multiple models, the net minimum risk prediction from the combination of all models at a given point in an operating regime, i.e., the point prediction with minimum variance in prediction errors, is their probabilistic average (see Lainiotis, 1971; Thompson, 1996; Murray-Smith and Johansen, 1997). The continuous prediction from the global model (shown as a broken line in Fig. 2.2b) results from interpolating between the three hypothetical models (models 1, 2 and 3) using the probabilities of the models being applicable as the weighting factors. There are two broadly possible approaches to combining the multiple regime-specific models probabilistically into a global one as outlined in Fig. 2.4.

(i) In the first case (approach a), this is achieved as follows: at each point along the variable path x, estimate the probability that each of the regime-specific models is applicable either by comparing available experimental / plant data with the model prediction or by quantifying the uncertainties in regime transitions along the variable path. The overall model prediction at that point is then simply the weighted average of the point predictions of the regime-specific models with the probability of the models being applicable at these points as weighting factors. Symbolically:

$$\hat{y}(x) = \sum_{j=1}^{N_{regime}} y_j(x) \times P(M_j|x,H)$$

where the global point prediction of the performance variable $\hat{y}$ (mole fraction, conversion etc) is the average of the point predictions from the individual models y_j weighted by the probability $P(M_j|x,H)$ that model M_j is applicable at that point given the state variable x, conditioned on the hypothesis H, where the hypothesis embodies information about the assumptions inherent in the model structure, correlations etc. The limitation of this approach is that, because kinetics are typically non-linear, the global point prediction at a given point may not fall between those predicted by the individual models and thus, it cannot be assured that all model equations are satisfied at all points.

(ii) In the second approach (approach b), one interpolates at a finer level, i.e. by continuously averaging the parameters of the local models and using them in a
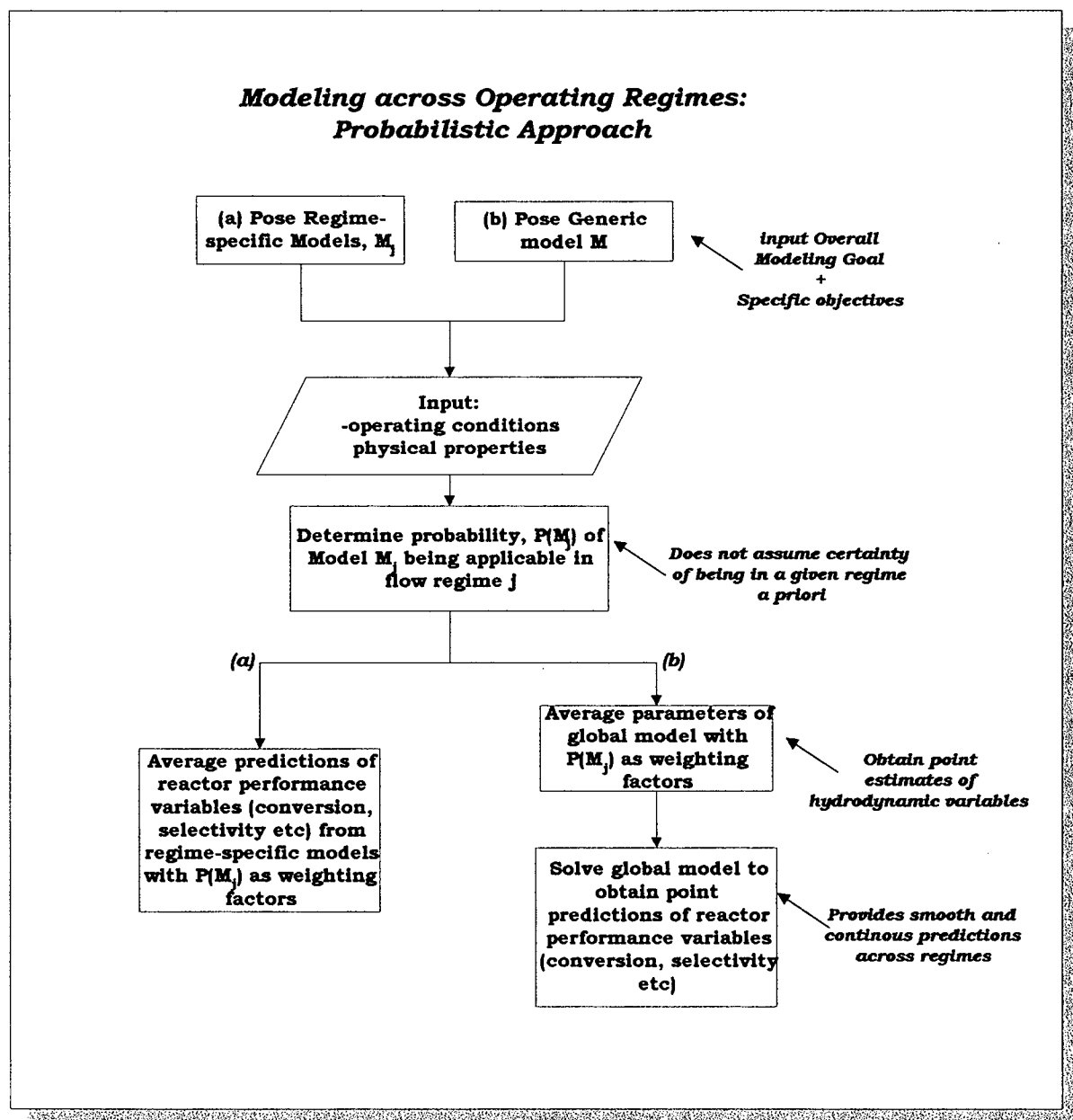
Figure 2.4. Illustration of modeling across flow regimes via probabilistic approach.

globally constructed generic model. Note that this global model reduces to the regime-specific models at any operating point at which any local model is 100% probable. Since this approach, rather than averaging point predictions of the regime-specific models, interpolates at the model parameter level, it can be ensured that the model equations are satisfied at all points regardless of the type of reaction kinetics. Symbolically

$$\hat{\theta}(x) = \sum_{j=1}^{N_{regime}} \theta_j(x) \times P(M_j | x, H)$$

where the global point estimate of the hydrodynamic parameter $\hat{\theta}$ (e.g. interphase mass transfer) is the average of the values of θ in regime j, θ_j, weighted by the respective probabilities $P(M_j | x, H)$.

Because of the robust interpolation at the finest possible resolution (parameter level), the latter approach is adopted in this work. In so doing, we are faced with the problem of accurately determining the probabilities of the regime-specific models being applicable in the various operating regimes. Probability theory provides a means of addressing this issue. The following section briefly overviews the probabilistic concepts and outlines the steps in the GFBR model development.

2.3.2 Probabilistic Paradigm

2.3.2.1 Introduction and Scope of Application

We noted in the probabilistic approach above the need to accurately estimate the weighting factors to carry out the model averaging. Because of the uncertainties in the flow regime transition boundaries and the correlations to estimate them, we are faced with the problem of making decisions/inferences under uncertainty. Probability density functions (pdfs) capture and represent the inherent uncertainties in correlations, model structure, assumptions etc. Combining this knowledge base represented in the pdfs and available data, probability theory provides means of making rational inferences under uncertainty.

The Bayesian probabilistic approach has been successful in synthesizing robust models for chemical processes (Thompson, 1996), interpolating between linear models for process control (Murray-Smith and Johansen, 1997; Banerjee et al., 1997),

uncertainty analyses of fuel biodegradation (McNab and Dooher, 1998), etc. The main idea lies in Baye's theorem (see Bernardo and Smith, 1994), which is essentially a mechanism for updating a prior probability of A, $P(A|H)$ to a posterior probability $P(A|B,H)$, when additional information B under hypothesis H, $P(B|A,H)$ becomes available. Symbolically

$$P(A \mid B,H) = \frac{P(A \mid H) \times P(B \mid A,H)}{P(B \mid H)}$$

Considerable literature exists describing this concept from both theoretical and applied perspectives (e.g. Berger, 1985; Loredo, 1990; Bernardo and Smith, 1994; Johansen, 1995; Thompson, 1996; Banerjee et al., 1997; Hoeting et al., 1998). However, because of the complexity of implementing the complete Bayesian analysis, we limit the scope of the probabilistic application to probabilistic averaging of hydrodynamic variables. This means that we are implicitly assuming certainty in the operating conditions, hydrodynamic correlations (except the regime boundary correlations), kinetic parameters etc. used in the model equations. As a result, our implementation does not take advantage of updating our prior knowledge to the posterior. In other words, Baye's theorem is not applied in this work. The simplified approach adopted here is as follows: Given a regime boundary correlation and the uncertainty associated with it, the probabilities of the flow regime being above or below the boundary is computed by imposing an appropriate pdf. These probabilities are then used as proxies for the probabilities that the regime-specific models are applicable in the respective regimes. The steps are outlined below.

2.3.2.2 Steps in Probabilistic Approach to GFBR modeling

A complete algorithm is as follows.

(i) Formulate generalized model equations applicable over the fluidization regimes of interest (sections 2.3.3 to 2.3.5 below)

(ii) Represent the uncertain regime boundaries as probability density functions (pdfs) using appropriate distributions.

(iii) Determine the probability of being in regime j given the operating conditions and model parameters (i.e., $P(H = H_j | x)$).

(iv)   Establish bounds "θ_j" in the hydrodynamic parameters (transition variables) central to the flow regime transitions for each flow regime j (e.g. $u_L = u_{L,turb} = U$, when the flow regime is turbulent).

(v)   Average the transition parameters probabilistically at the bounds established in step (iv), and obtain point estimates as:

$$\hat{\theta} = \sum_{1}^{3} \theta_j \times P(H = H_j \mid x) \cdot$$

(vi)   Finally, utilize these estimates in model equations posed in step (i) and solve together with the phase/bed balances, energy and pressure equations to obtain performance variables "y".

The remainder of this chapter presents in detail the steps outlined above.

2.3.3 Generalized Model Equations

From the various reactor models written specifically for the three fluidization flow regimes (reviewed in Chapter 1), three regime-specific models are chosen to represent the limiting behavior of the GFBR model at the fully bubbling, turbulent and fast fluidization conditions: (i) generalized version of Grace (1984) two-phase bubbling bed model (expanded to include dispersion in both phases) at low gas velocities, (ii) dispersed (axially and radially) flow model for turbulent beds at intermediate velocities, and (iii) a generalized version of the Brereton et al. (1988) core-annulus model (expanded to include reaction terms as well as dispersion terms in both the core and annulus regions) at higher velocities. After these generalizations, the three regime-specific models are then fully compatible with each other, and therefore a single model formulation each for the L and H-phase can describe the phenomena in all three flow regimes.

2.3.3.1 Mole Balance for the Two-Phases/Regions

Steady state two-phase/region mole balances represent the two-phase bubbling bed model in the low velocity limit, dispersed flow model at intermediate gas velocities where the turbulent fluidization regime is predominant, and the core-annulus model in the high velocity limit:

$$\psi_L u_L \frac{\partial C_{iL}}{\partial z} - \psi_L \mathcal{D}_{zg,L} \frac{\partial^2 C_{iL}}{\partial z^2} - \frac{\psi_L \mathcal{D}_{rg,L}}{r} \frac{\partial}{\partial r}\left(r \frac{\partial C_{iL}}{\partial r}\right)$$
$$+ k_{LH} a_I \psi_L \left(C_{iL} - C_{iH}\right) + \psi_L \rho_L \, Rate_{iL} = 0 \tag{2.1}$$

$$\psi_H u_H \frac{\partial C_{iH}}{\partial z} - \psi_H \mathcal{D}_{zg,H} \frac{\partial^2 C_{iH}}{\partial z^2} - \frac{\psi_H \mathcal{D}_{rg,H}}{r} \frac{\partial}{\partial r}\left(r \frac{\partial C_{iH}}{\partial r}\right)$$
$$+ k_{LH} a_I \psi_L \left(C_{iH} - C_{iL}\right) + \psi_H \rho_H \, Rate_{iH} = 0 \tag{2.2}$$

Overall balances: $\qquad\qquad C_i = q_L C_{iL} + q_H C_{iH}$ $\qquad\qquad\qquad$ (2.3)

The boundary conditions are

$$\text{at } z = 0 \qquad \begin{aligned} -\mathcal{D}_{zg,L} \frac{\partial C_{iL}}{\partial z} &= u_L \left(C_{iL}\big|_{o^-} - C_{iL}\big|_{o^+}\right) \\[2mm] -\mathcal{D}_{zg,H} \frac{\partial C_{iH}}{\partial z} &= u_H \left(C_{iH}\big|_{o^-} - C_{iH}\big|_{o^+}\right) \end{aligned} \tag{2.4}$$

$$\text{at } z = L \qquad \begin{aligned} \frac{\partial C_{iL}}{\partial z} &= 0 \\[2mm] \frac{\partial C_{iH}}{\partial z} &= 0 \end{aligned} \tag{2.5}$$

$$\text{at } r = 0 \qquad \begin{aligned} \frac{\partial C_{iL}}{\partial r} &= 0 \\[2mm] \frac{\partial C_{iH}}{\partial r} &= 0 \end{aligned} \tag{2.6}$$

$$\text{at } r = R \qquad \begin{aligned} \frac{\partial C_{iL}}{\partial r} &= 0 \\[2mm] \frac{\partial C_{iH}}{\partial r} &= 0 \end{aligned} \tag{2.7}$$

The net rate of consumption of component i in jth phase participating in N_r reactions can be written

$$Rate_i = \sum_{k=1}^{N_r} \nu_{ik} r_k(\mathbf{c})\Big|_j$$

where the stoichiometric coefficients ν_{ik} are positive for products, negative for reactants and zero for non-reacting species.

2.3.3.2 Energy Balance

The steady state energy balance equation for the fluid bed reactor with cooling can be written (neglecting any temperature differences between the L- and H-phases at a given level):

$$\frac{d}{dz}\left(k_e \frac{dT}{dz}\right) - C_{pg}\rho_g U \frac{dT}{dz} + \phi \sum_{k}^{N_r}\left(\Delta H_{k,i=base\,rxt} \times Rate_{i=base\,rxt}\right) - hA_s\left(T - T_{cool}\right) = 0 \quad (2.8)$$

The boundary conditions are

$$\text{at } z = 0 \qquad\qquad -k_e \frac{dT}{dz} = UA\rho_g C_{pg}\left(T_o - T\right) \qquad\qquad (2.9)$$

$$\text{at } z = L \qquad\qquad \frac{dT}{dz} = 0 \qquad\qquad (2.10)$$

2.3.3.3 Pressure Balance

The pressure, assuming the only contribution to the axial pressure drop is the hydrostatic head of solids (i.e. ignoring accelerational effects and friction at the walls), is given by

$$-\frac{dP}{dz} = \rho_p g(1 - \varepsilon) \qquad\qquad (2.11)$$

The boundary condition is

$$\text{at } z = 0 \qquad\qquad P = P_o \qquad\qquad (2.12)$$

2.3.4 Freeboard Region

Solids are continuously ejected into the freeboard as bubbles/voids erupt at the dense bed surface where the larger solids fall back to the bed and fines are entrained. Although the solids holdup in the freeboard, a function of gas velocity, is lower than in the dense bed, reactions continue in the freeboard, and can play a significant role, especially at high U. Accounting for the freeboard in the GFBR model is also important for properly extending the probabilistic modeling approach to the fast fluidization regime by fixing the height of integration to cover the total column/reactor height and evaluate the dense bed height iteratively as outlined below. The following assumptions are made in implementing the freeboard region:

(i)   Solids concentration in the freeboard decays exponentially with height.

(ii) The gas flow in the freeboard is well represented by a single-phase dispersed flow.

(iii) Dispersion of gas in the freeboard is a function of solids concentration as represented by the correlation of Li and Wu (1991).

(iv) Particles in the freeboard are of the same mean size as those in the dense bed.

2.3.4.1 Distribution of Solids Concentration

Consider the schematics of the dense and freeboard regions shown in Fig. 2.1. Decay of the solids concentration in the freeboard is given (Kunii and Levenspiel, 1991) by:

$$\phi = \phi^* + (\phi_d - \phi^*)e^{-a\,z_f} \tag{2.13}$$

where z_f is the freeboard axial coordinate. The saturation carrying capacity, ϕ^*, is obtained from

$$\phi^* = MIN(\phi_1^*, \phi_2^*) \tag{2.14}$$

where the value for low and intermediate velocities, ϕ_1^*, is correlated (Morikawa et al., 2001) by

$$\phi_1^* = 0.022(U - U_{mb})^{3.64} \tag{2.15}$$

while at high gas velocities, ϕ_2^*, can be obtained (assuming $v_t \ll U$) from

$$\phi_2^* = G_s / \rho_p (U - v_t) \tag{2.16}$$

The net solid circulation rate, G_s, is obtained by weighting with the respective regime probabilities, the solids entrainment, E_∞, (Choi et al., 1998) at low and intermediate superficial velocities, and the average solids flux, G_{so}, in the high velocity limit, so that

$$G_s = E_\infty(1 - P_{fast}) + G_{so}P_{fast} \tag{2.17}$$

where P_{fast} is the probability of being in the fast fluidization regime, described in detail below. The product of the decay constant, a, and the gas velocity, U, has been determined to be a constant (see Kunii and Levenspiel, 1991; 1997), such that for group A and B particles, a value of "3" reasonably fits measured solids concentration for a wide range of data in the freeboard pooled by Kunii and Levenspiel (1991). A slightly modified form of the relation is

$$a = \frac{3}{(U - U_{mf})} \tag{2.18}$$

The total solids inventory in the column is

$$M_s = A\rho_p \left(L_d \phi_d + L_f \overline{\phi}_f \right) \tag{2.19}$$

where $\overline{\phi}_f$ is the average hold-up of solids in the freeboard given by

$$\overline{\phi}_f = \frac{1}{L_f} \int_0^{L_f} \phi \, dz_f = \phi^* + \frac{\phi_d - \left(\phi^* + (\phi_d - \phi^*)e^{-aL_f}\right)}{aL_f} \tag{2.20}$$

The freeboard and dense bed heights are obtained by iteratively solving equations (2.19) and (2.20), noting that $L_t = L_d + L_f$.

2.3.4.2 Modeling the Freeboard as Dispersed Flow

The freeboard has sometimes been modeled as a plug flow reactor because of the relatively low solids concentration (e.g. Han and Chung, 2001). Although plug flow is a reasonable representation at very low gas velocities, it becomes inadequate at higher gas velocities as the solids concentration increases. Here, we model the freeboard as a dispersed flow region. There are two possible routes to accomplishing this within the GFBR model framework:

(a) Represent the dense region of the reactor with the generalized 2-phase/region equations, but set up different single-phase dispersed flow equations for the freeboard region.

(b) Model the entire reactor with the GFBR model caused to switch to fully single-phase dispersed flow when the axial coordinate reaches the dense bed surface. (This is achieved in practice by setting the turbulent regime probability to "1" in the GFBR model. A salient feature of the GFBR model is the ability to model a fluidized bed as fully two-phase bubbling, single-phase dispersed flow or two-region core-annular by setting the respective regime probabilities to "1" in the model. For example, by setting the probability of being in the turbulent fluidization regime equal to 1, the GFBR model simulates the single-phase dispersed flow model by forcing all variables in the two phases to merge into each other, thereby predicting identical concentrations in both phases.)

The second approach is adopted here, underscoring the utility of the probabilistic approach. To complete the specifications in the freeboard, we need to specify the gas dispersion. The correlation of Li and Wu (1991) for gas dispersion based on voidage, covering turbulent, fast fluidization and the dilute transport flow regimes is used, i.e.

$$D_{zg,f} = 0.195\varepsilon_f^{-4.12} \tag{2.21}$$

2.3.5 Bed and Phase Balances

Consider the schematic of the fluidized bed showing both dense and freeboard regions given in Fig. 2.5. The phase balances relate only to the dense region where there are two distinct phases, while the bed material balances apply to the entire column. The dense bed volume fractions in the L and H phases must add up to 1, i.e:

$$\psi_L + \psi_H = 1 \tag{2.22}$$

where

$$\psi_L = \frac{V_L}{V}; \qquad \psi_H = \frac{V_H}{V} \tag{2.23}$$

The gas flows through the phases add up to the total gas flow through bed, i.e.

$$Q = Q_L + Q_H \tag{2.24}$$

Fractional gas flow through the phases add up to 1, i.e:

$$q_L + q_H = 1 \tag{2.25}$$

where

$$q_L = \frac{Q_L}{Q} = \frac{\psi_L u_L}{U}; \qquad q_H = \frac{Q_H}{Q} = \frac{\psi_H u_H}{U} \tag{2.26}$$

Combining eqs. (2.25) and (2.26), the gas flow balance can be written in terms of gas velocities as

$$U = \psi_L u_L + \psi_H u_H \tag{2.27}$$

The sum of the solids hold-up in the two phases equals the bed average.

$$1 - \varepsilon = \psi_L (1 - \varepsilon_L) + \psi_H (1 - \varepsilon_H) \tag{2.28}$$

so that

$$\varepsilon = \psi_L \varepsilon_L + \psi_H \varepsilon_H \tag{2.29}$$

Solids densities in the two phases add up to the bed average, i.e.

$$\rho = \psi_L \rho_L + \psi_H \rho_H \tag{2.30}$$

Gas and solids volume fractions in each phase as well as the column add up to one, i.e:

L-phase: $\qquad\qquad\qquad\qquad \varepsilon_L + \phi_L = 1 \tag{2.31}$

H-phase: $\qquad\qquad\qquad\qquad \varepsilon_H + \phi_H = 1 \tag{2.32}$

Column average: $\qquad\qquad\quad \varepsilon + \phi = 1 \tag{2.33}$
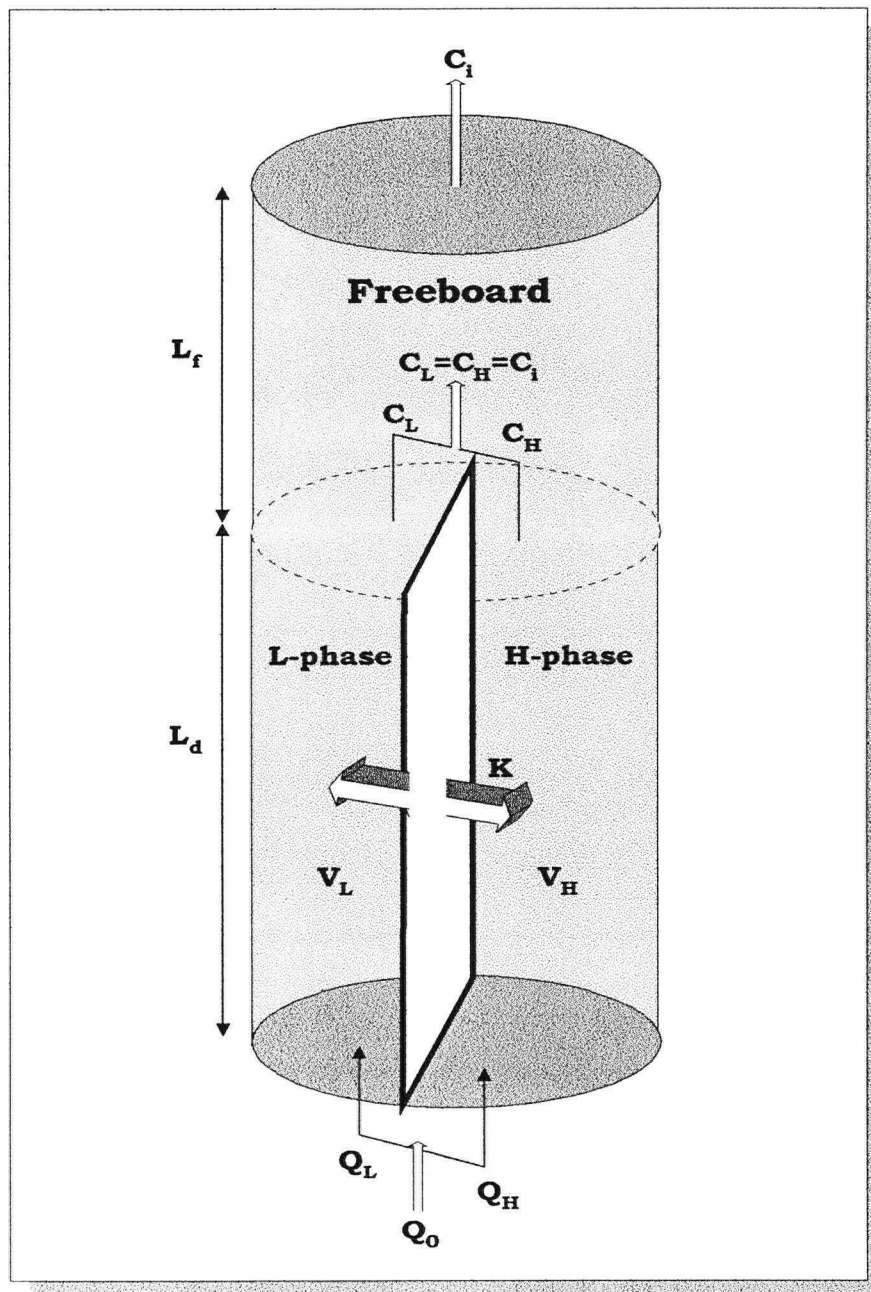
Figure 2.5. Schematic of generalized two-phase/region model with freeboard

The bed average axial gas dispersion coefficient can be distributed to the two phases by representing the dispersion in the two phases as resistances in parallel (ignoring the interphase mass transfer)
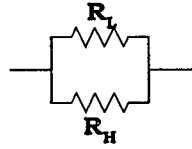
so that the total resistance, R, satisfies the equation

$$1/R = 1/R_L + 1/R_H$$

The resistances can be considered here to represent dispersion (or mass transfer) resistances and are given by

$$R_L = L_d/\mathcal{D}_{zg,L}A_L; \quad R_H = L_d/\mathcal{D}_{zg,H}A_H$$

$$\Rightarrow \mathcal{D}_{zg}A/L_d = \mathcal{D}_{zg,L}A_L/L_d + \mathcal{D}_{zg,H}A_H/L_d$$

If all terms in the above are multiplied by L_d / A, we obtain

$$\mathcal{D}_{zg} = \psi_L\mathcal{D}_{zg,L} + \psi_H\mathcal{D}_{zg,H} \qquad (2.34)$$

Note that significant interphase mass transfer would lead to different weighting of the dispersion coefficients, but eq. (2.34) has been used throughout as a reasonable approximation. Table 2.1 summarizes the pertinent bed and phase material balances in the GFBR model.

Table 2.1. Summary of bed and phase balances

Phase volume allocation	$\psi_L + \psi_H = 1$
Phase gas hold-up allocation	$\varepsilon = \psi_L\varepsilon_L + \psi_H\varepsilon_H$
Phase velocity allocation	$U = \psi_L u_L + \psi_H u_H$
Phase density allocation	$\rho = \psi_L\rho_L + \psi_H\rho_H$
L-phase volume allocation	$\varepsilon_L + \phi_L = 1$
H-phase volume allocation	$\varepsilon_H + \phi_H = 1$
Bed volume allocation	$\varepsilon + \phi = 1$

2.3.6 Representing and Quantifying the Uncertainty in Regime Boundaries

The probabilities of being above or below the boundaries are computed by imposing appropriate probability density functions, using the U_c and U_{se} regime boundary correlations and the uncertainty associated with them. These probabilities are then used as proxies for the probabilities of the applicability of the regime-specific models in the different flow regimes. The following notations are defined. Let:

- $p_i(U|Ar)$ = pdf representing the uncertainty in regime correlation for U_i given the gas and particle properties embodied by the Archimedes number, Ar. (Subscript "i" is used to denote either "c" or "se".)

- P_{bubb}, P_{turb}, P_{fast} = probabilities of being in the bubbling, turbulent and fast fluidization flow regimes respectively, with the sum always equal to 1.

The gamma probability density function has been determined to be the most appropriate pdf satisfying all the constraints: uncertainty/error "e_i" in correlations normally distributed with mean "0" and variances σ_i^2 and $U_{se} > U_c > 0$ (Thompson, 1996; Thompson et al., 1999). If the transition velocity, U_i, is far enough from zero, the pdfs can also be assumed to be normally distributed with the same means and variances. For example, the uncertainty in regime correlation for U_{se} represented by the Gaussian pdf is:

$$p_{se}(U \mid Ar) = \frac{1}{\sigma_{se}\sqrt{2\pi}} \exp\left(-\frac{(U - U_{se})^2}{2\sigma_{se}^2}\right) \tag{2.35}$$

For ease of computation, sigmoid-shaped logistic regression functions (LRFs) were fitted to the cumulative distributions evaluated from the Gaussian function:

$$P_{fast} = P(U > U_{se}) = \left(1 + e^{-\beta v_{se}}\right)^{-1} \equiv \int_U^\infty p_{se}(U \mid Ar) dU \tag{2.36}$$

where

$$v_{se} = \frac{(U - U_{se})}{\sigma_{se}} \tag{2.37}$$

It was found that $\beta = 1.7$ fitted both the Gaussian and gamma distributions within a 1% tolerance. Complete assignment of all the probabilities is specified below.

In constructing the regime probability diagram for our probabilistic approach, we need to specify some minimum $U = U_{min}$ below which there is zero probability of turbulent fluidization. The rationale for this is briefly examined. The probability of bubbling fluidization must be "1" at the onset of bubbling and should reach zero asymptotically with increasing gas velocity. To achieve this, U_c must be sufficiently far from zero, which may not be satisfied always. To ensure that turbulent fluidization does not co-exist with bubbling at the onset of bubbling, we impose the following constraint: for U just above U_{mb} ($U_{mb} < U < U_{min}$), P_{bubb} must be 1 and $P_{turb} = P_{fast} = 0$. U_{min} is assigned as a reasonable multiple of U_{mb}. Here, we assigned $U_{min} = 2U_{mb}$ or $U_c/10$, whichever is lower. The same problem could arise with respect to some minimum velocity below which the bed has 0 probability of being in the fast fluidization regime. This could be to avoid the coexistence of bubbling and fast fluidization conditions. However, given that the mean of the U_{se} distribution is well above zero, we do not impose such a constraint. Overall, the set of constraints $U_{se} > U_c > U_{min} > U_{mb} > 0$ are satisfied for all cases.

Central to the probability predictions in the GFBR model is a reliable estimate of the standard deviation of the error, σ_i. In earlier work (Thompson et al., 1999), a reasonable value of 0.2 m/s was adopted for σ_c and the need to estimate this parameter from actual hydrodynamic data was noted. Here, with the aid of the raw data used to determine the flow regime transition correlations for U_c and U_{se} (Bi et al., 1995) and additional data from Bi (1994), improved correlations with a reduced level of dispersion have been developed. Estimates of the normalized standard deviations, σ_i^*, at the regime boundary correlations are summarized in Table 2.2. Note that σ_i^* is assumed to be invariant to operating conditions and particle properties. This assists generic model development, obviating the need for determining case-specific σ_i's. With these controls and by invoking the axioms of probability theory, the probabilities of being in each of the three flow regimes are expressed as

$$P_{bubb} = 1 - P\left(U^* > U_c^*\right) = 1 - [1 + e^{-\beta v_c^*}]^{-1} \tag{2.38}$$

$$P_{fast} = P\left(U^* > U_{se}^*\right) = [1 + e^{-\beta v_{se}^*}]^{-1} \tag{2.39}$$

and from the summation rule

$$P_{turb} = 1 - P_{fast} - P_{bubb} \qquad (2.40)$$

where

$$U_c^* = \mathrm{Re}_c / Ar^{1/3}; \quad v_c^* = \frac{\left(U^* - U_{\min}^*\right) - U_c^*}{\sigma_c^*}; \quad \sigma_c^{*2} = \frac{1}{n-1}\sum_{j=1}^{n}\left[U_{c,\exp,j}^* - U_c^*(Ar)_j\right]^2 \qquad (2.41)$$

$$U_{se}^* = \mathrm{Re}_{se} / Ar^{1/3}; \quad v_{se}^* = \frac{U^* - U_{se}^*}{\sigma_{se}^*}; \quad \sigma_{se}^{*2} = \frac{1}{n-1}\sum_{j=1}^{n}\left[U_{se,\exp,j}^* - U_{se}^*(Ar)_j\right]^2 \qquad (2.42)$$

Figure 2.6 shows regions of uncertainty in the correlations for U_c^* and U_{se}^* depicted by error bars (corresponding to $2\sigma_i^*$ in the correlations). Figure 2.7a plots the pdfs representing the uncertainties in the regime transition correlations. The corresponding probabilities of operating within each of the three flow regimes appear in Fig. 2.7b. As expected bubbling conditions dominate for low U, turbulent conditions at intermediate U and fast fluidization at large U, with smooth transitions in-between.

Table 2.2. Summary of correlations for regime transition velocities

Source	Regime boundary Correlation	Normalized standard deviation, σ_i^*
Bi and Grace (1995)	$\mathrm{Re}_c = 0.56\,Ar^{0.461}$ $\mathrm{Re}_{se} = 1.53\,Ar^{0.51}$	$\sigma_c^* = 0.358$ $\sigma_{se}^* = 0.517$
This work	$\mathrm{Re}_c = 0.74\,Ar^{0.426}$ $\mathrm{Re}_{se} = 1.68\,Ar^{0.469}$	$\sigma_c^* = 0.292$ $\sigma_{se}^* = 0.448$

2.3.7 Flow Regime Transition Equations

With the probabilities of being in each flow regime determined, the next critical step is to use these probabilities as weighting factors to obtain point estimates of the hydrodynamic parameters. The transition equations are essentially the weighted averages of the model parameters (coefficients in the mole and energy balance equations for each separate fluidization regime), computed as follows:
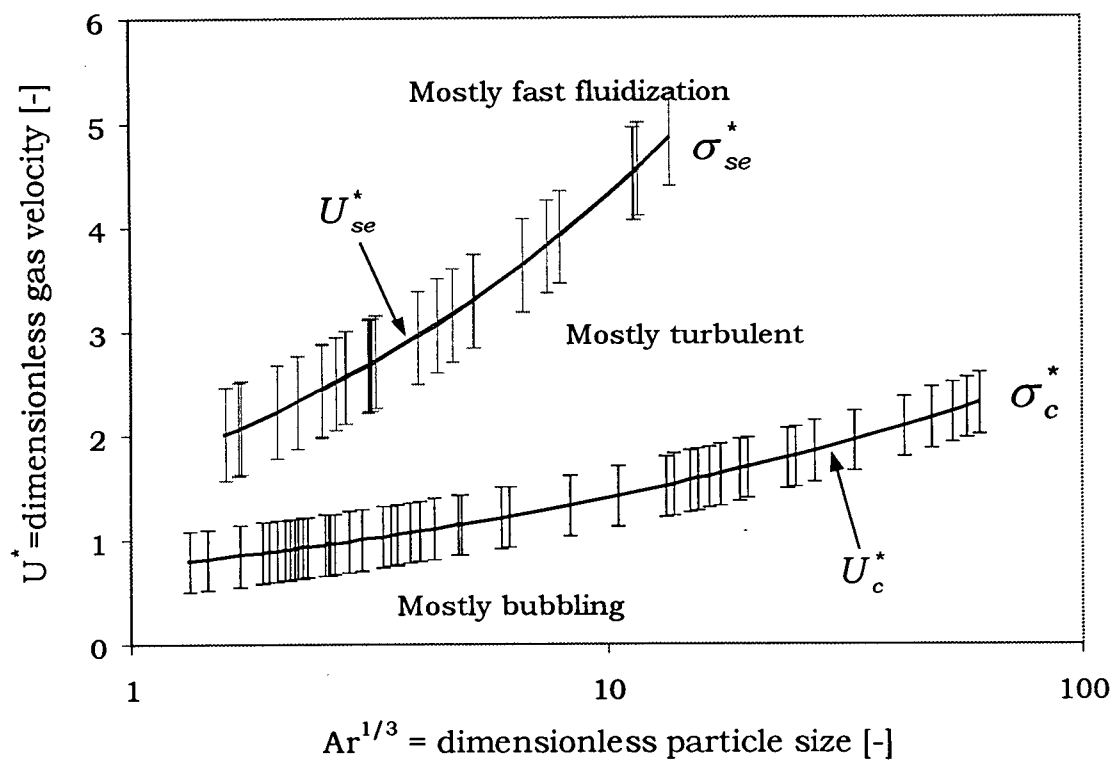
Figure 2.6. Regime diagram boundaries and regions of uncertainty. Correlations used, from Table 2.2, are: $U_c^* = \mathrm{Re}_c / Ar^{1/3} = 0.74 Ar^{0.093}$ and $U_{se}^* = \mathrm{Re}_{se} / Ar^{1/3} = 1.68 Ar^{0.136}$.
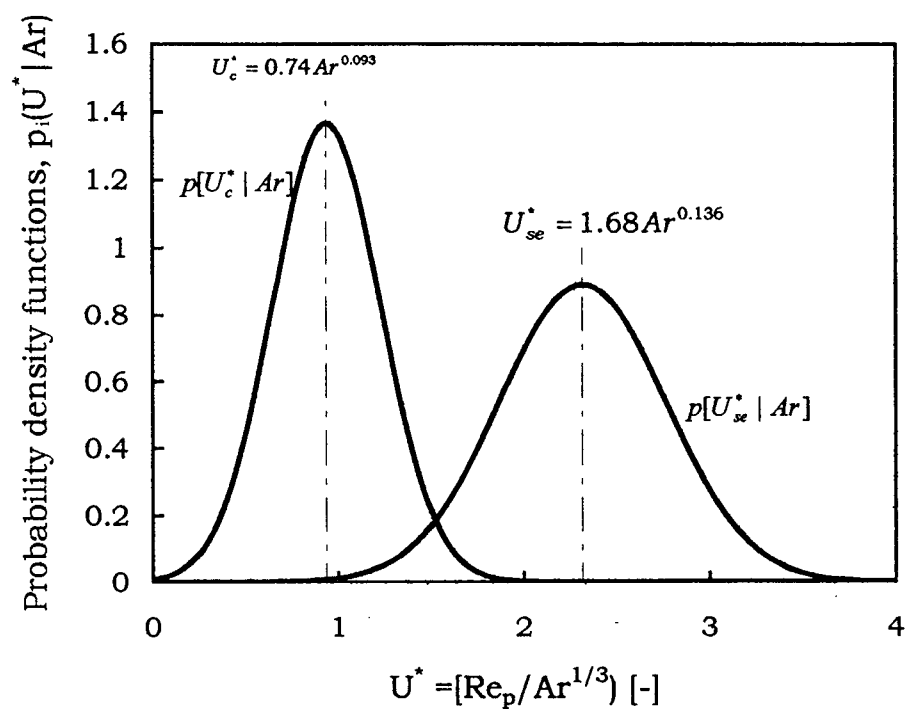
(a)
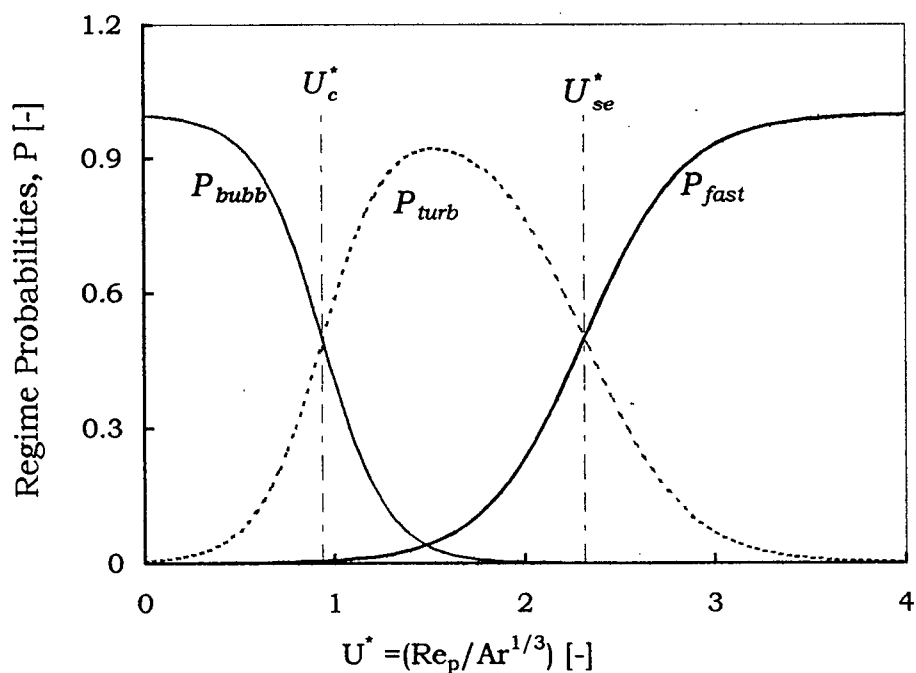
(b)

Figure 2.7 (a) Uncertainties in flow regime boundary correlations; b) Probability of being in each regime as a function of dimensionless superficial gas velocity. [Ar = 10.]

$$\hat{\theta} = \sum_{j=1}^{3} \theta_j P_j \qquad (2.43)$$

where θ_j is the value of θ in regime j and P_j is the probability of being in regime j. The values of j represent: 1 = bubbling fluidization, 2 = turbulent fluidization and 3 = fast fluidization. For example, consider the bed average voidage ε. The point estimate $\hat{\varepsilon}$ from the expected values of ε in each regime is obtained as

$$\hat{\varepsilon} = \varepsilon_{bubb} P_{bubb} + \varepsilon_{turb} P_{turb} + \varepsilon_{fast} P_{fast} \qquad (2.44)$$

where ε_{bubb}, ε_{turb} and ε_{fast} are the voidages in the bubbling, turbulent and fast fluidization flow regimes given in Table 2.3; the table also lists all the averaged variables and the equations used to evaluate them in the three flow regimes. Correlations for other hydrodynamic parameters for each of the three regimes such as u_{br}, d_b, r_C etc. appearing in Table 2.3 are summarized in Appendix A, while Appendix B presents the schemes used to evaluate thermophysical properties such as gas mixture diffusivity, thermal conductivity etc. Note that it should be straightforward to replace correlations currently listed with better ones as these become available through future work.

2.4 Current Limits of GFBR Model

The GFBR model is explicitly developed for the three principal fluidization flow regimes: bubbling, turbulent and fast fluidization. While it would be possible to extend this model to other flow regimes, at present its applicability is limited to those three regimes. Therefore, we note the following limits of the model:

(a) $U > U_{mb}$, i.e. the gas velocity is at least sufficient enough to initiate bubbling;

(b) A large or shallow enough column that slug flow conditions are avoided over the entire range of flow conditions;

(c) $U < U_{CA}$ or $G_s > G_{s,CA}$ (Grace and Bi, 1997) in the high gas velocity limit to avoid the dilute-phase transport flow regime;

(d) $U < U_{DSU} = 0.0113 G_s^{1.192} \rho_g^{-1.064} [\mu g(\rho_p - \rho_g)]^{-0.064}$ to ensure that the system is not operating in the dense suspension upflow regime (Grace et al., 1999).

Table 2.3. Summary of regime bounds and transition equations.

Point estimate, θ	Regime-specific parameter values, θ_j		
	j = Bubbling	j = Turbulent	j = Fast fluidization
ε	$\dfrac{1-(1-\varepsilon_{mf})}{\left(1+\dfrac{U-U_{mf}}{0.711\sqrt{gd_b}}\right)}$ (Clift and Grace, 1985)	$\dfrac{U+1}{U+2}$ (King, 1989)	$\left[1+\dfrac{G_{so}\Psi_{slip}}{\rho_p U}\right]^{-1}$ (Patience et al., 1993)
$k_{LH}a_I$	$\left\{\dfrac{U_{mf}}{3}+2\left[\dfrac{\mathcal{D}_{mix}\varepsilon_{mf}u_{br}}{\pi\,d_b}\right]^{1/2}\right\}\times\dfrac{6}{d_b}$ (Sit and Grace, 1981)	$1.631\,Sc^{0.37}U$ (Foka et al., 1996)	$\left[\dfrac{4\mathcal{D}_{mix}\bar{\varepsilon}_a U}{\pi\,L_t}\right]^{1/2}\times\dfrac{2}{r_c}$ (Pugsley et al., 1992)
ψ_L	$(\varepsilon-\varepsilon_{mf})/(\varepsilon_{L0}-\varepsilon_{mf})$ $\{$in limit $\varepsilon_H\rightarrow\varepsilon_{mf}$ & $\varepsilon_L\rightarrow\varepsilon_{L0}=(1-\phi_{Lo})\}$		r_c^2/R^2
$\mathcal{D}_{zg\_L}$	$\mathcal{D}_{mix}$	$UL_d/Pe_{z1}{}^*$	$0.184\bar{\varepsilon}_c{}^{(-4.445)}$
$\mathcal{D}_{rg\_L}$	$0.1\times\mathcal{D}_{zg\_L}$		
$\mathcal{D}_{zg}$	$UL_d/Pe_{z1}{}^*$	$UL_d/Pe_{z1}{}^*$	$UL_t/Pe_{z2}{}^+$
$\mathcal{D}_{rg\_H}$	$0.1\times\mathcal{D}_{zg\_H}$		
u_L	$MIN(\varepsilon_L u_{br},\,(U-U_{mf})/\psi_L)$	U	U/ψ_c
ϕ_L	ϕ_{L0}	$1-\varepsilon$	$1-\bar{\varepsilon}_c$
Point estimate $\hat{\theta}$ in column 1 is obtained by weighting θ_j with P_j as: $\hat{\theta}=\sum\limits_{j=1}^{3}\theta_j P_j$			

$${}^*Pe_{z1}=3.472\,Ar^{0.149}Re^{0.023}Sc^{-0.232}\left(\frac{L_d}{D_t}\right)^{0.285}$$ (Bi et al., 2000)

$${}^+Pe_{z2}=UL_t/(0.184\bar{\varepsilon}^{(-4.445)})$$ (Li and Wu, 1990)

2.5 Numerical Solution Approach

The differential equations resulting from the mole, energy and pressure balances, coupled with the set of algebraic and integral equations in the model, render the problem an integro-differential algebraic equation system (IDAEs). For such systems, the dispersed boundary conditions introduce a complexity that requires careful choice of solution approach. Most existing IDAEs solvers (*Mathlab, Mathmatica, Mathcad* etc) do not fully handle boundary value problems. Where such solvers do exist, the extent of flexibility is severely limited by the built-in bounds within the solvers leading to convergence problems (e.g. in the *Microsoft Fortran Developer Studio with IMSL*).

As a result of the above limitations, solution to complex boundary value problems are sought either through in-house development of coding with "*Programming Languages*" (e.g. *Fortran, C++* etc.) employing one of a variety of finite difference /element techniques, or by using advanced modeling languages such as *MODEL.LA* (Stephanopoulos, et al., 1990), *gPROMS* (Pantelides and Barton, 1993), or *LCR* (Han et al., 1995). These modeling languages are called "*Equation-based*" and "*Phenomenological Languages*", the latter being a variant of the former, differing only in some implementation aspects. Their development has made possible a shift from traditional programming languages such as *Fortran*. Equation-based languages are easier to use while sacrificing some flexibility, as illustrated in Fig. 2.8

2.5.1 general PROcess Modeling System (*gPROMS*)

The modeling language employed in this study is *gPROMS* from Process Systems Enterprise Limited, London, UK. Detailed description of the *gPROMS* language, its features and capabilities are given in the *gPROMS* Users Guide, readily accessible at www.psenterprise.com. It is possible using *gPROMS* to switch among a variety of solution techniques (e.g. finite difference discretization schemes of different order, orthogonal collocation, robust algebraic solvers etc.) to solve the set of equations. Modeling languages, with gPROMS at the forefront, are considered as the emerging programming paradigm for the 21st century (Stephanopoulos and Han, 1996).
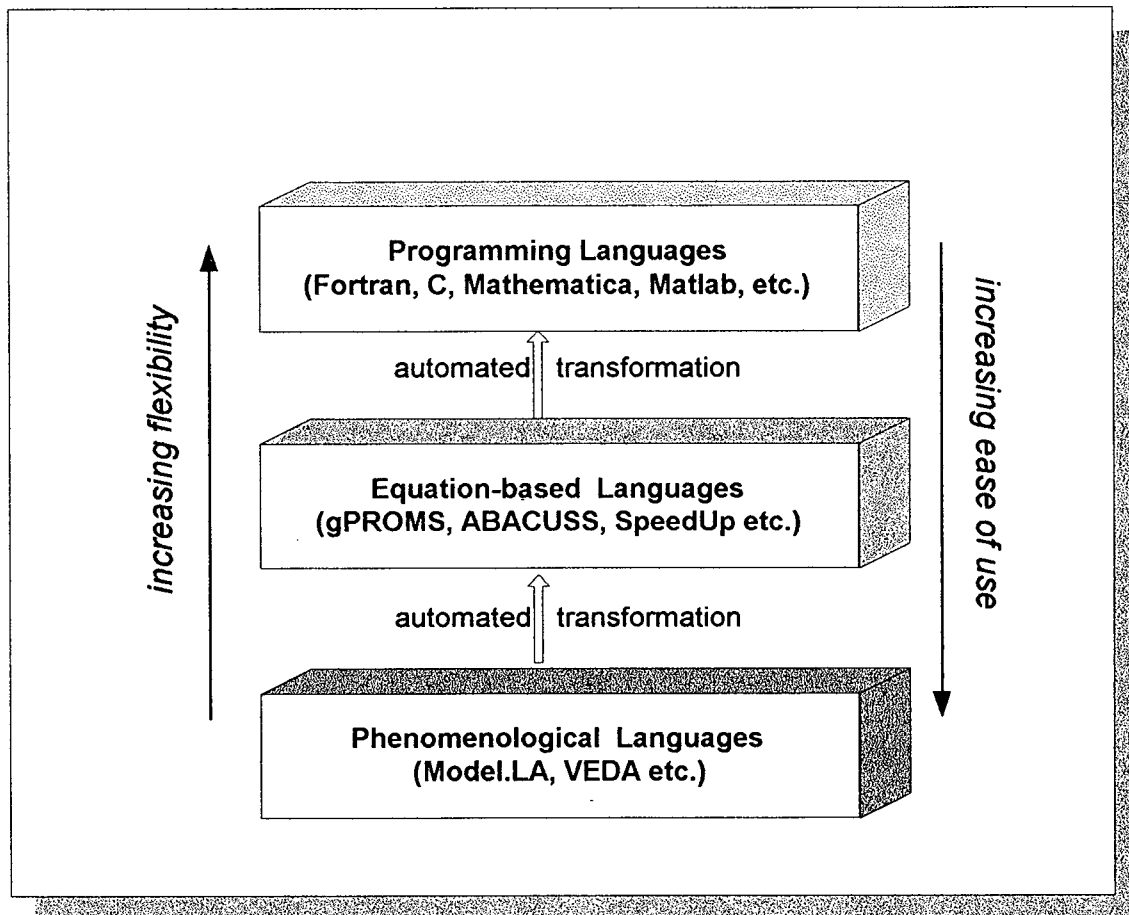
Figure 2.8 Hierarchical structure of modeling languages (adapted from Park, 1998)

2.5.2 Implementing the GFBR Model in gPROMS

Equation-based modeling languages generally have several segmented components as shown in Fig. 2.9. Each such component must be defined separately. Solution is attained through compilation of the model and process sections followed by execution. The versatility of the language lies in its ability to handle several process sections using only one main model section as a backbone, while allowing a foreign process/object (e.g. Fortran code, Excel worksheet) to be incorporated by interfacing. As a result, a variety of different processes can be modeled using a single model section containing the fundamental equations.

Within the context of the GFBR model, the main equations in the "model section" of gPROMS are: mole, energy and pressure balance equations, phase and bed balance equations, hydrodynamic regime transition equations, probability equations, reactor performance equations (performance variables, kinetics etc.), hydrodynamics equations/correlations and physical properties evaluation equations/correlations. In other words, the complete sets of IDAEs are contained in this section. The "process section" allows a so-called "simulation experiment" to be performed, so that the model section is used to study the behaviour of the system under different circumstances. For our system, this is the section where process-specific information such as kinetic parameters, physical properties not computed within the model section (e.g. particle density, mean particle size), operating conditions (e.g. inlet temperature and pressure) etc. are specified.

An important feature of gPROMS is the dynamic interfacing with foreign programs such as C++, Fortran and EXCEL. Taking advantage of this feature, we constructed a template in EXCEL containing most of the input information required under the process section. Figure 2.10 presents a typical EXCEL screen showing the different worksheets for the reactor data, physical properties etc. The reactor schematic within the Figure is constructed in EXCEL using a combination of graphing and drawing tools such that real time changes in bed properties, such as expanded bed height, regime probabilities, etc. can be directly monitored from the user interface created in EXCEL as the simulation proceeds.
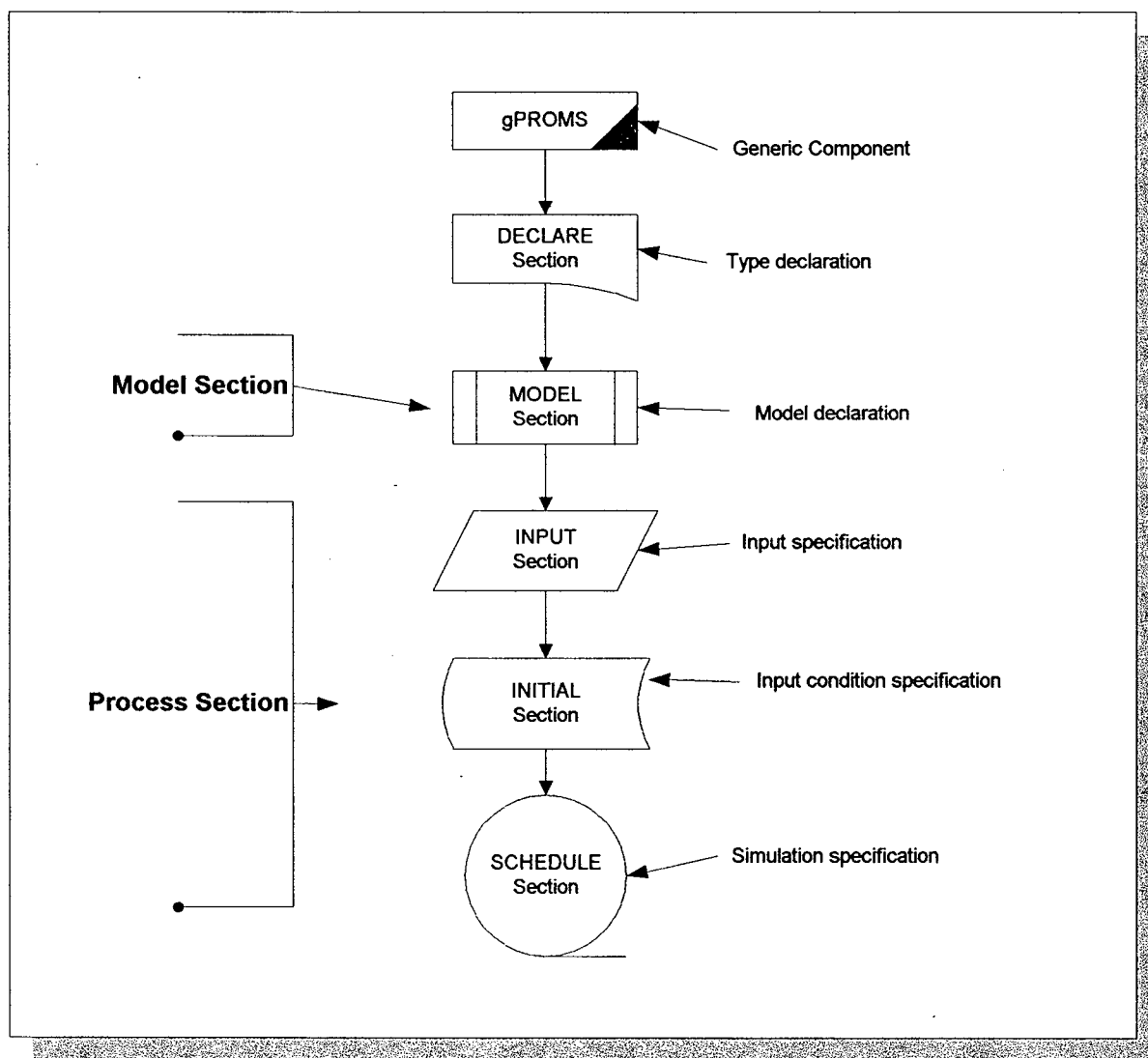
Figure 2.9 Components of the equation-based modeling language "gPROMS"
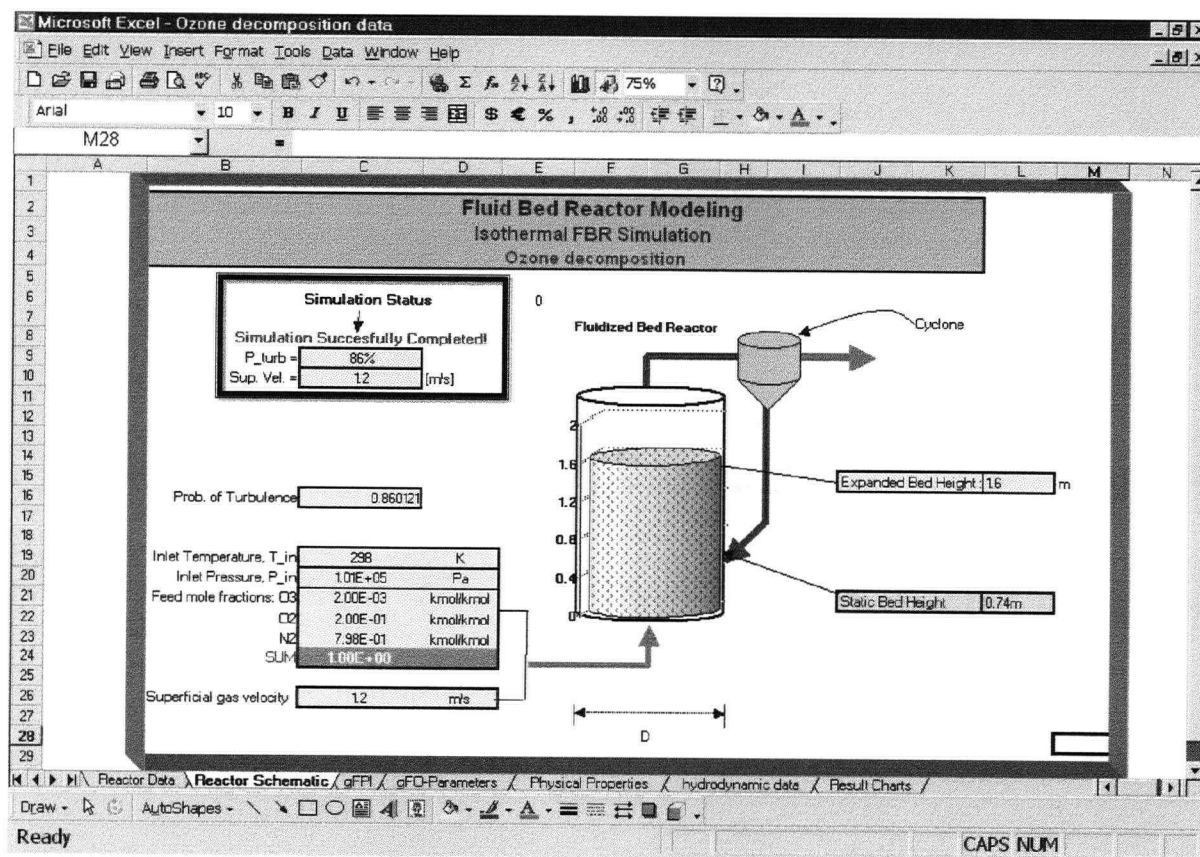
Figure 2.10 Typical EXCEL screen illustrating the foreign-process-interfacing feature of gPROMS.

Typical gPROMS simulation involving eight gaseous species and three reactions for the oxy-chlorination process, for example, takes about eight minutes to complete using a second order central finite difference discretization scheme.

2.6 Remarks on the Application of GFBR Model

A number of aspects have been considered in the GFBR model, namely: probabilistic averaging of hydrodynamic variables; inclusion of the freeboard region; energy and pressure variations along the reactor. In most commercial processes operated at high enough gas velocities, it is important to apply the complete model outlined above. However, in certain cases, some of these aspects can be ignored in order reduce computer processing time when their inclusion will not significantly change the model predictions or the overall model utility. (For example, when the reactor is operated at superficial gas velocities of a few multiples of U_{mb} for group A catalysts, it is safe to ignore the contribution from the freeboard region.)

Additional complexities are considered in subsequent chapters; specifically: (i) extension to simulate gas-solid reactions by coupling the GFBR model with a single particle model (Chapter 5c); (ii) implementation of volume change with reaction for systems accompanied by a change in molar flowrate (Chapter 6). The application of the GFBR model in this thesis is therefore structured as follows:

1 Isothermal and isobaric cold model version (without the reaction terms) is applied in the interpretation of gas mixing experiments in Chapter 3.

2 Isothermal, isobaric version of the model is applied to case studies for ozone decomposition (Chapter 4), phthalic anhydride process (Chapter 5a), and zinc sulfide roasting (Chapter 5c).

3 Chapter 6 implements the full capability of the GFBR model, accounting for volume change with reaction, energy and pressure variations along the reactor, and the influence of the freeboard region. The oxy-chlorination process is used to illustrate and validate the approach.

2.7 Conclusion

A new generic fluid bed reactor model is presented, applicable across the fluidization flow regimes most commonly encountered in industrial scale fluid bed reactors: bubbling, turbulent and fast fluidization. The model interpolates between three regime-specific models – the generalized two-phase bubbling bed model, dispersed plug flow model and the generalized core-annulus model – by means of probabilistic averaging of hydrodynamic and dispersion variables based on the uncertainty in the flow regime transitions. It is shown that the probabilistic approach captures salient features of the limiting models at any given operating point across the operating regimes and adequately describes phenomena within each flow regime. Applications of this model using *gPROMS* ® software is demonstrated in the following chapters.

Chapter 3

Gas Mixing in Bubbling-Turbulent Fluidized Bed

3.1 Introduction

Gas mixing in fluidized beds is strongly affected by the gas-solid interaction between the low- and high-density phases. Knowledge of the extent of mixing is important not only to provide a description of the gas flow pattern, but also to evaluate reactor performance. While results of several lab-scale investigations, usually carried out in columns of ID ~100 mm, have been reported in the literature, data for gas mixing in the turbulent and transition flow regimes are scarce (Bi et al, 2000). Existing correlations for the axial and radial dispersion coefficients mostly developed for the bubbling and slugging flow regimes, can provide only gross estimates at best for the turbulent flow regime.

This study was therefore undertaken to further study gas mixing using a commercial catalyst to help characterize the gas flow pattern in the bed for the operating conditions considered and to estimate dispersion and interphase mass transfer coefficients from the experimental data. Results from this study are intended to provide better understanding of the effects of dispersion in each phase with increasing velocities and at regime boundaries.

3.2 Experimental Studies

3.2.1 Experimental Apparatus and Instrumentation

The Plexiglas column used in this study, shown schematically in Fig. 3.1, is 4.4 m high and 0.286 m in inside diameter with a distributor plate composed of two perforated aluminum plates supporting the catalyst. There are 98 holes in each perforated plate, each 4.4 mm in diameter with a 30 mm pitch giving a fractional open area of 1.7 %. Two external cyclones in series with return leg diameters of 51 mm are used to capture entrained particles, while a baghouse filter removes fine particles not captured by the cyclones. A Roots blower supplies air as the fluidizing gas, with its flowrate
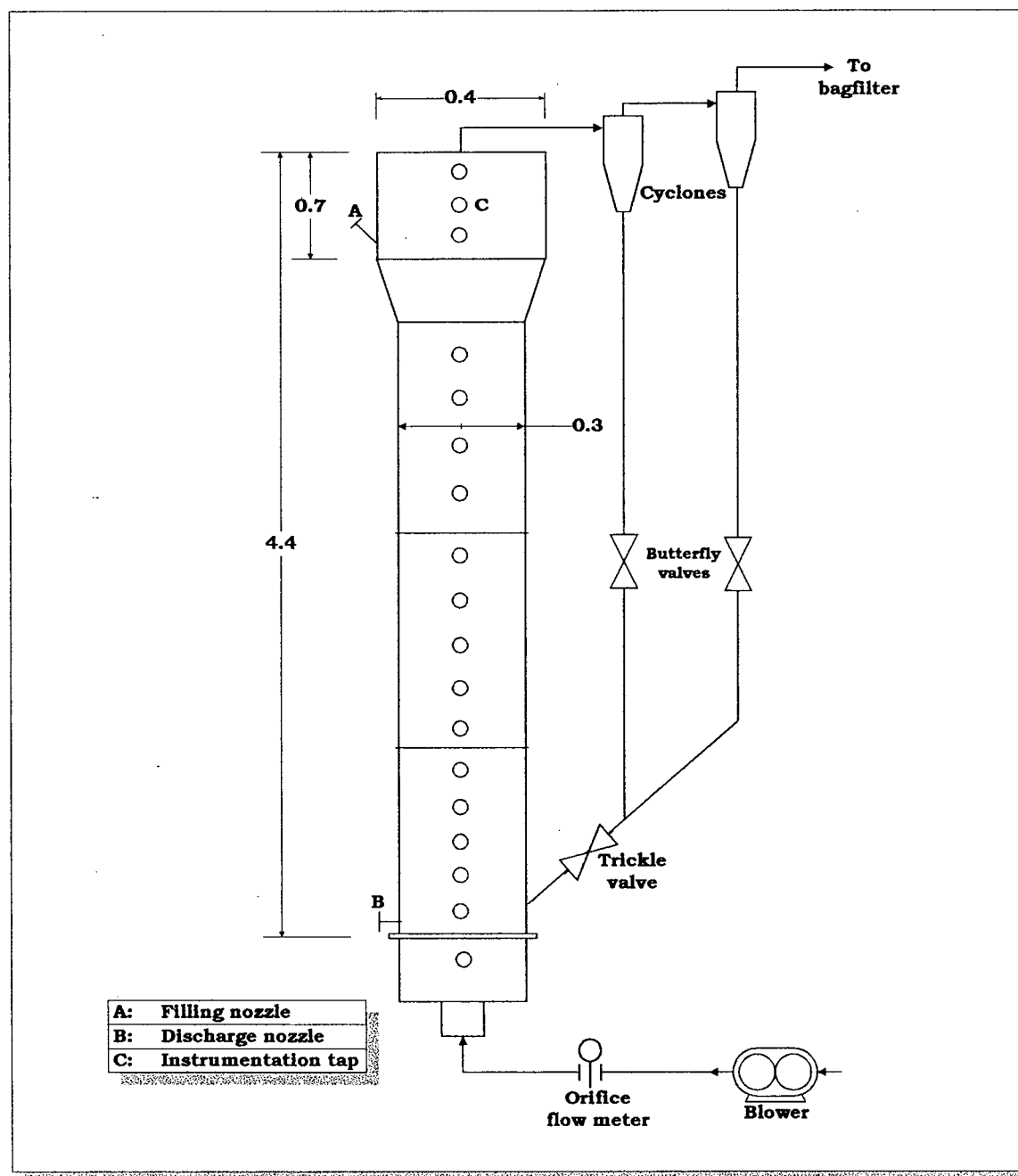
Figure 3.1. Schematic diagram of the pilot scale cold model unit. All dimensions in m (not to scale)

controlled by a ball valve. Pressure transducers (Omega PX142) positioned on the column wall are used to log pressure data through an EXP-32 Computer Board into a DAS08 card in a Pentium 233 computer using Labtech Notebook 10.1 data acquisition software. All transducers were calibrated before use to obtain information on the offset and scale factor values.

3.2.2 Gas Mixing Experiments

Commercial catalyst particles supplied by the Mitsubishi Chemical Corporation with mean diameter 48 μm and density 1580 kg/m^3 were used as bed material. A number of gases have been used as tracers (e.g. CO_2, H_2, He, CH_4 etc.) for such studies using transient (step or pulse) injection or continuous injection along the axis. Merits and de-merits of the different injection approaches have been summarized by Arena (1997). The tracer gas must be inert, readily detectable, and mix intimately with the flowing gas; it should also have physical properties similar to those of the fluidizing gas or be present in small enough concentration that the RTD of the tracer is representative of the flowing fluid. Helium gas was used as the tracer in this study since it possesses all these pertinent qualities; it is also non-adsorbing on the catalyst surface at the prevailing conditions. A known amount of helium gas was introduced into the air-fluidized bed, and the resulting tracer concentrations at pre-chosen positions were monitored using thermal conductivity detectors.

3.2.2.1 Calibration of Thermal Conductivity Detectors

The two thermal conductivity detectors (TCDs) were calibrated for different known concentrations of the He tracer gas (~ 0.5 to 6% He by volume) in order to establish optimal sampling conditions and obtain calibration equations. A schematic of the calibration set-up is shown in Fig. 3.2. The bypass on the sample line is to prevent pressure build up in the flask as the total flow into the flask is increased while maintaining a constant TCD sampling flowrate.

The calibration procedure was as follows: Using the He and air flowmeters, controlled flows of He and air were introduced into the flask. To ensure good mixing in the flask, the tips of the tubes used to introduce the gases were situated close to the bottom of the flask, while the tip of the tube used to withdraw the sample was located

near the top. A sample of known concentration (from ratio of He flow to total flow) was drawn from the He-Air mixture into the TCD using a vacuum pump. The response voltage was then amplified and sent to the data acquisition system. Results obtained by changing sampling flow rate through the TCD, the signal amplification ratio, and the current through the TCD, show that the response signal is highly dependent on these parameters. The optimal sampling conditions for our experiments that maximizes the detected signals with minimal fluctuations were found to correspond to: current of 95 mA, signal amplification ratio of 100 and sampling flow rate of 0.1 *lpm* (1.67×10^{-6} m^3/s). The final TCD calibration curves are presented in Fig. 3.3.
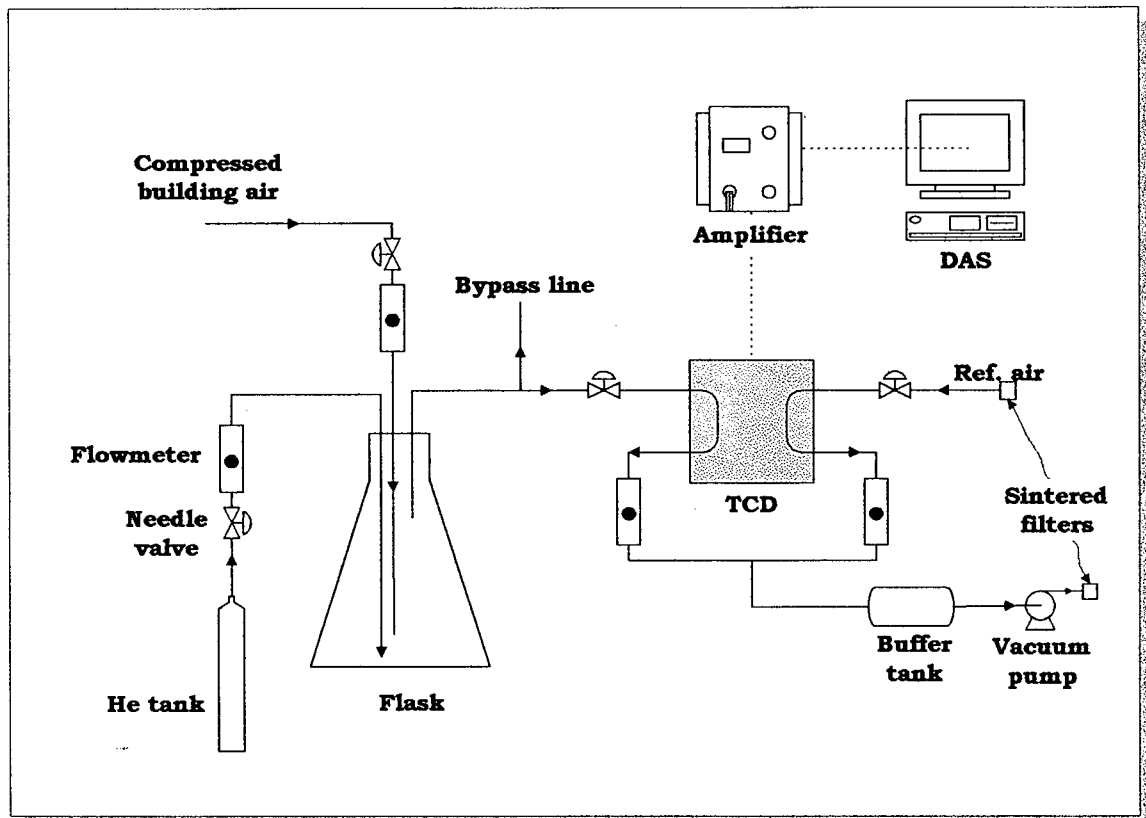
Figure 3.2. Schematic of TCD calibration set-up.
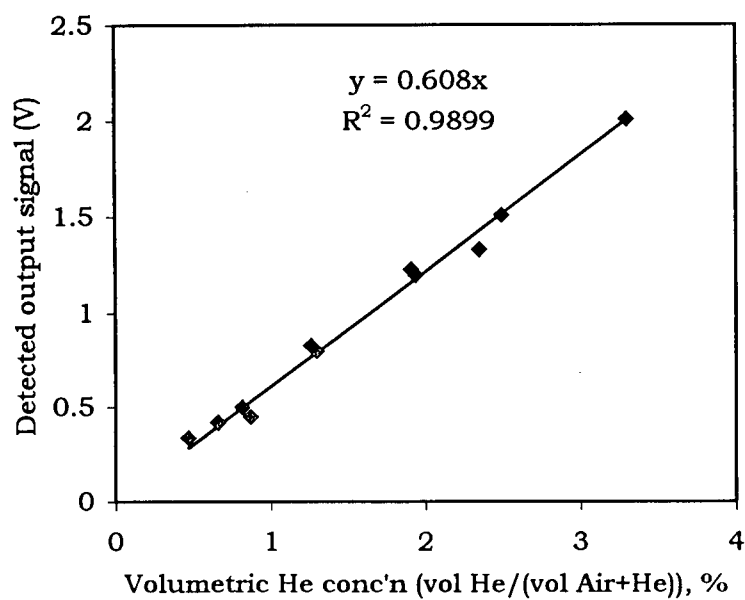
(a)
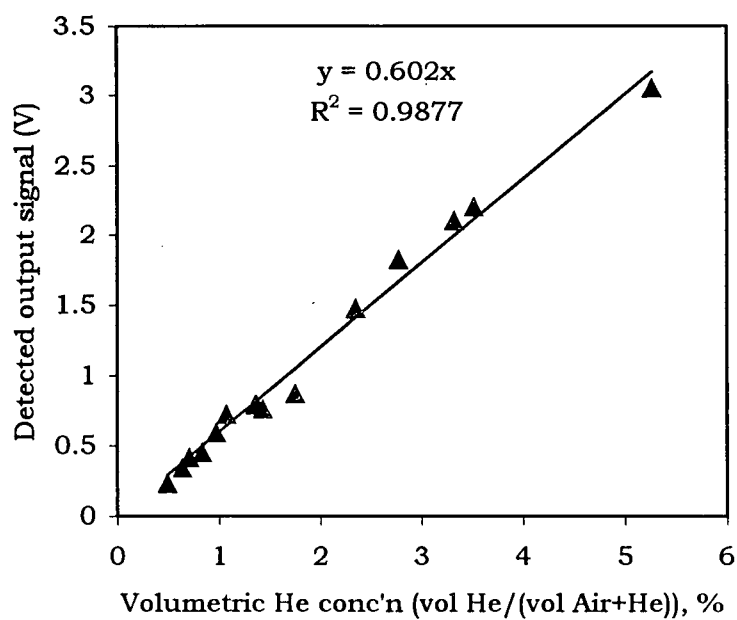
(b)

Figure 3.3. Plot of detected signals as a function of volume percent He injected
for a) TCD#1, and b) TCD#2. [Signal amplification ratio = 100; Current
= 95 mA; TCD sample flow rate = 1.67×10^{-6} m³/s.]

3.2.2.2 Steady State Measurements

A steady stream of He tracer was injected at a single point 654 mm above the distributor at r = 0 using a radially directed injection probe made of 20 mm ID aluminum tube with a 15 μm sintered filter soldered to the tip. Four traversing detection probes above and four below the injection probe could be moved from the centerline to the wall while the system was operating. The helium signal at the exit of the column, V_∞, which was confirmed to be radially uniform, was used to normalize the signals within the bed. It was measured by switching the sampling positions between the bed and the column exit using a 3-way valve. A schematic of the set-up is shown in Fig. 3.4. The samples and reference air were drawn into two thermal conductivity detectors connected to a Labtech Notebook data acquisition system. The output signals from the TCD's were converted to He concentration (volume %) using the calibration equations in Fig. 3.3.

Radial concentration profiles for a static bed height, L_0 of 1.0 m at four vertical positions upstream and four downstream of the injection point are shown in Figs. 3.5 to 3.8 for superficial gas velocities from 0.2 to 0.5 m/s. As expected, the concentrations of He at the axis are higher than at the wall for all downstream levels. For the upstream measurements, a decrease in concentration with increasing distance from the wall is observed. Figure 3.9 shows typical contours of the downstream and upstream dimensionless He concentration as functions of bed height and radius for a superficial gas velocity of 0.5 m/s.

3.2.2.3 Unsteady State Measurements

RTD experiments were conducted using positive and negative step tracer inputs for a static bed height of 1.5 m. When the He was first introduced into the windbox using a solenoid valve, large fluctuations were found in the detected signals, primarily due to inadequate mixing of the tracer in the windbox with the fluidizing gas. To enable proper mixing of the He tracer with the fluidizing air before entering the bed, the injection tip of the 1/4" (6.3 mm) dia. tube was moved upstream of the 90° elbow (1 m from the distributor) of the 6" (150 mm) air line. As shown in Fig. 3.10, two TCDs were set up to detect the He tracer, one immediately below the distributor in the windbox and the other near the expanded bed surface (at z = 660 mm).
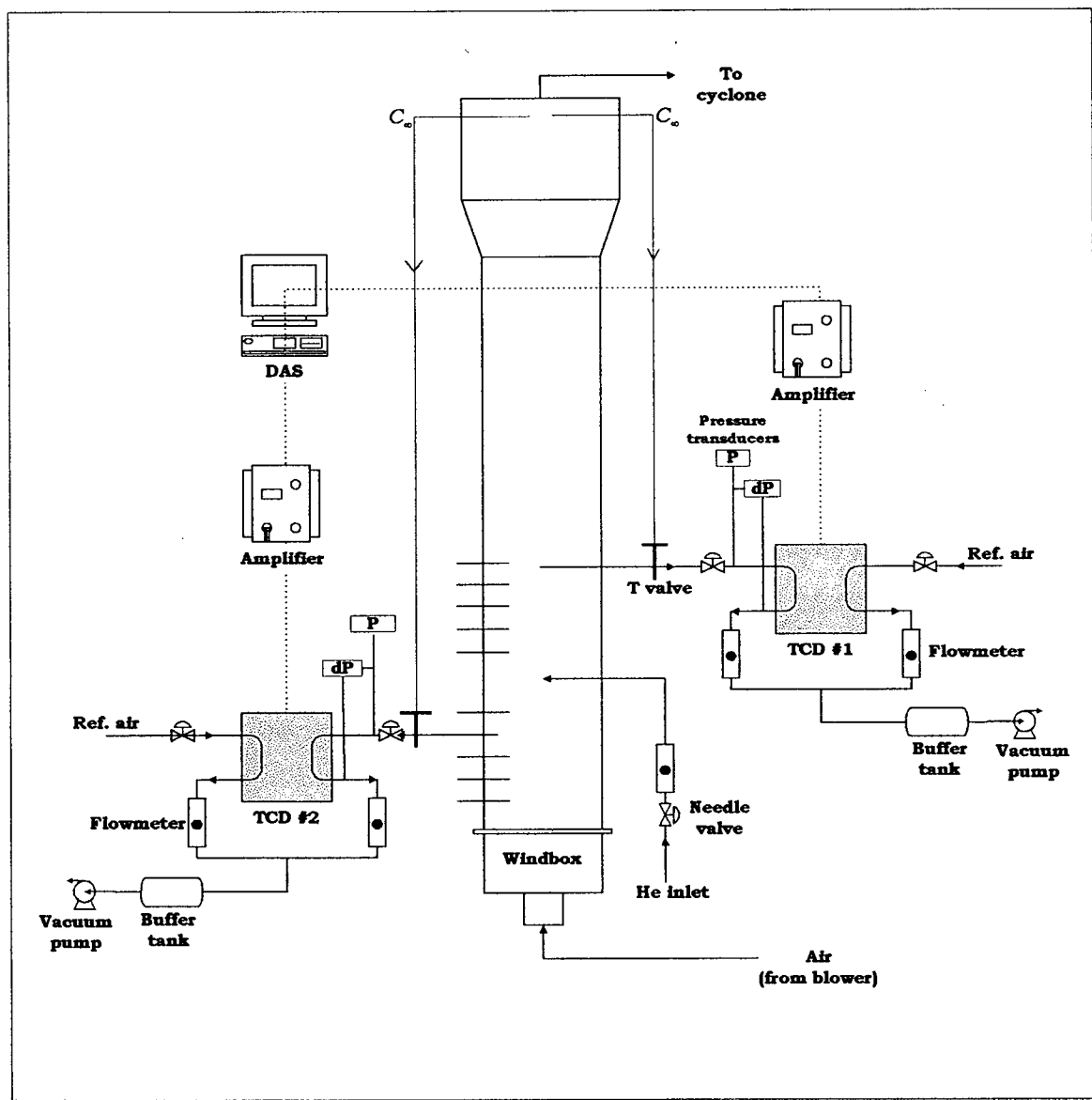
Figure 3.4. Schematic diagram of steady state tracer injection/detection set-up.
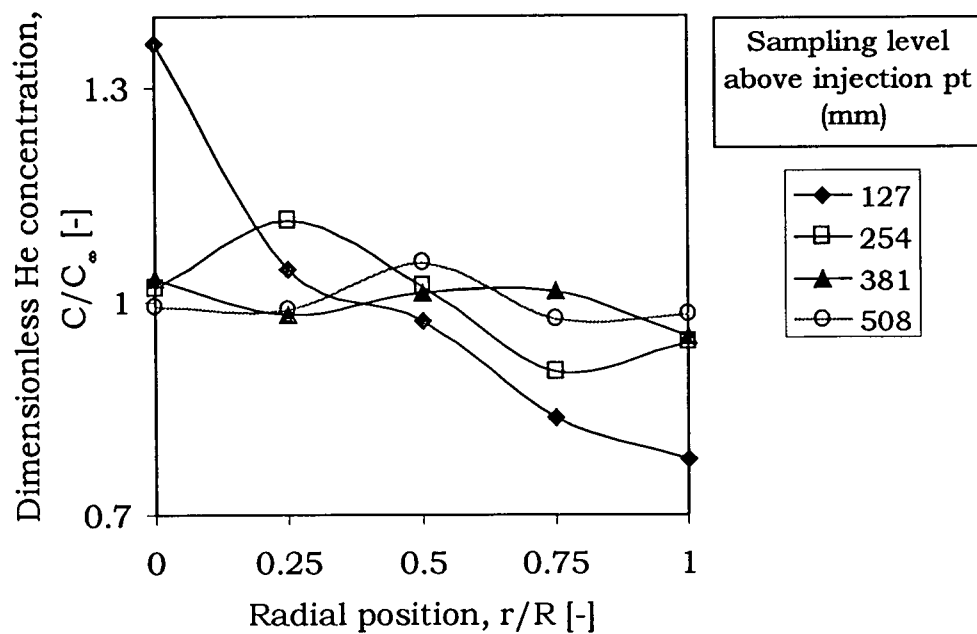
(a)
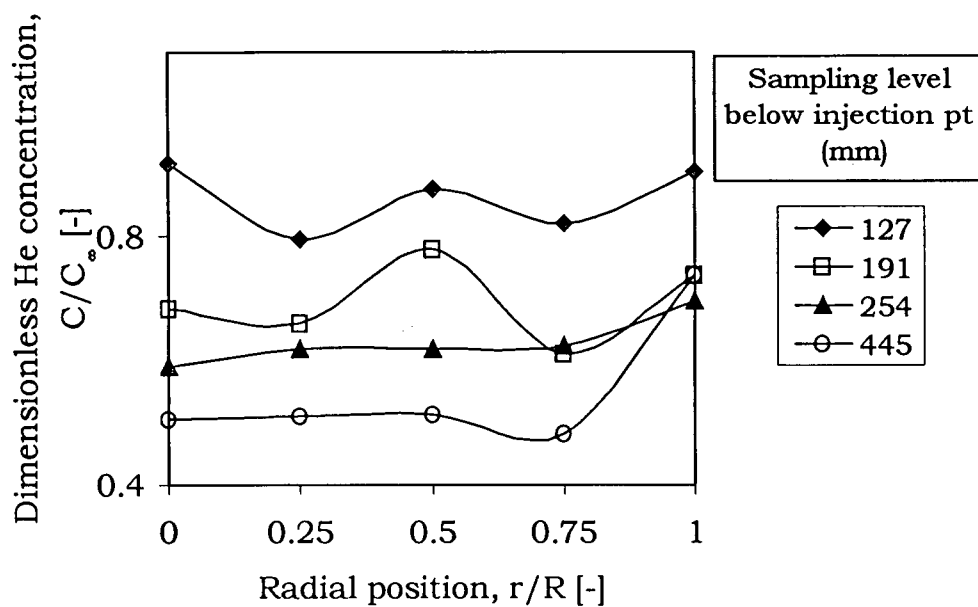
(b)

Figure 3.5. Radial concentration profiles for tracer: (a) downstream, (b) upstream of injection point. [L_o = 1.0 m, U = 0.2 m/s, tracer injection level 0.654 m above distributor.]
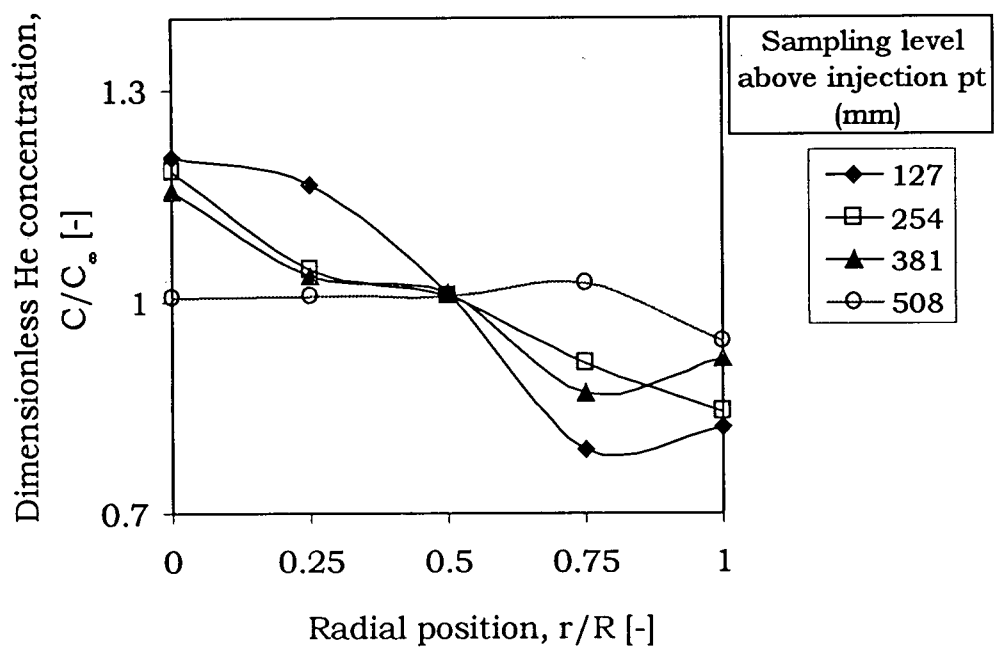
(a)
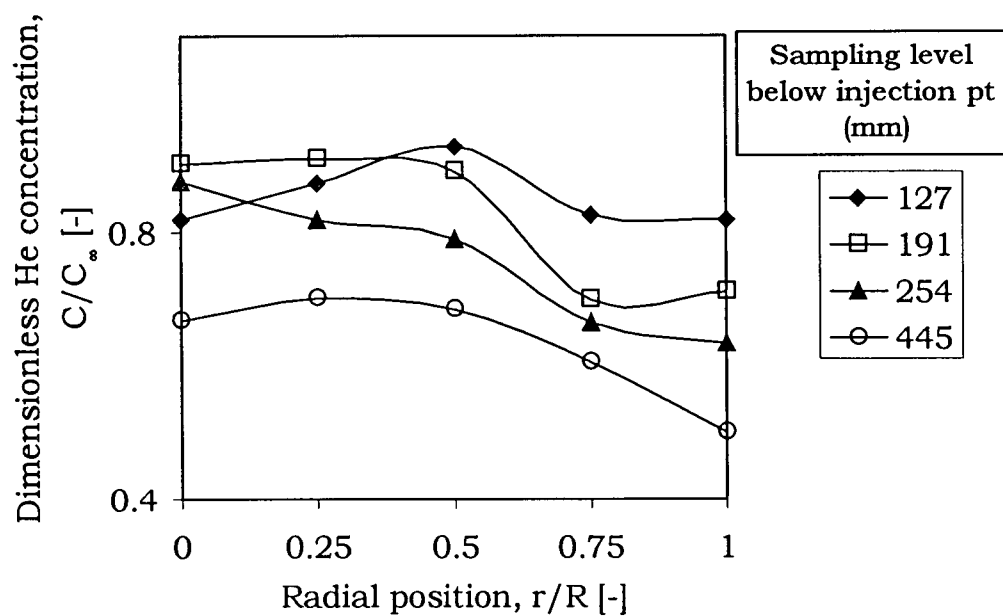
(b)

Figure 3.6. Radial concentration profiles for tracer: (a) downstream, (b) upstream of injection point. [L_o = 1.0 m, U = 0.3 m/s, tracer injection level 0.654 m above distributor.]
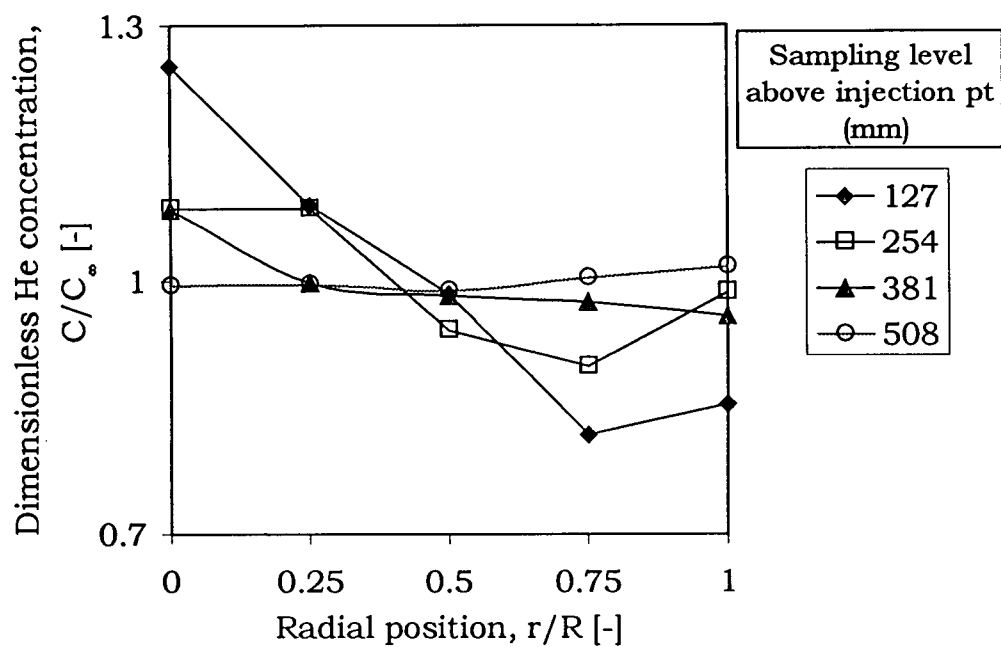
(a)
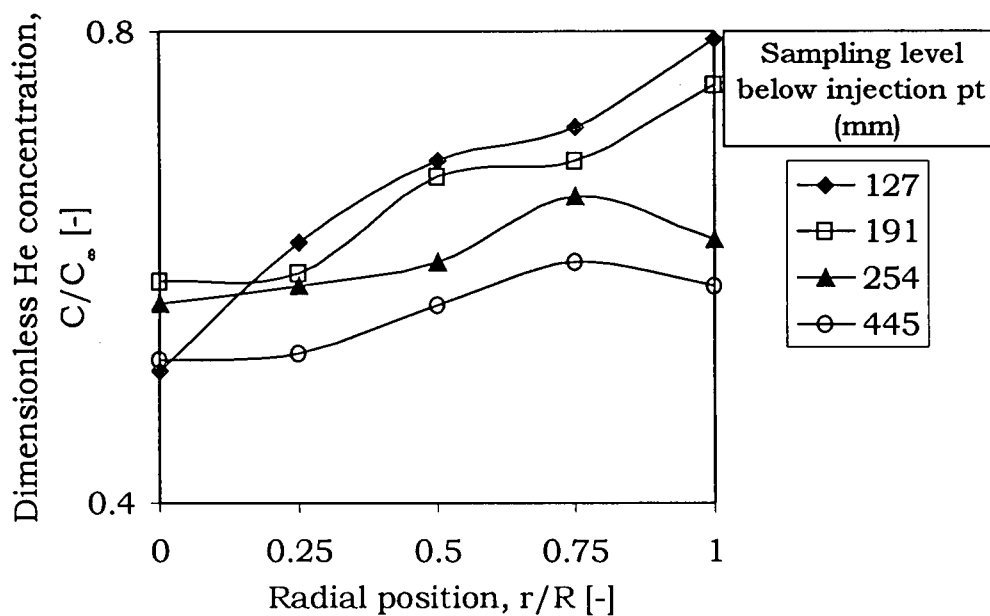
(b)

Figure 3.7. Radial concentration profiles for tracer: (a) downstream, (b) upstream of injection point. [L_o = 1.0 m, U = 0.4 m/s, tracer injection level 0.654 m above distributor.]
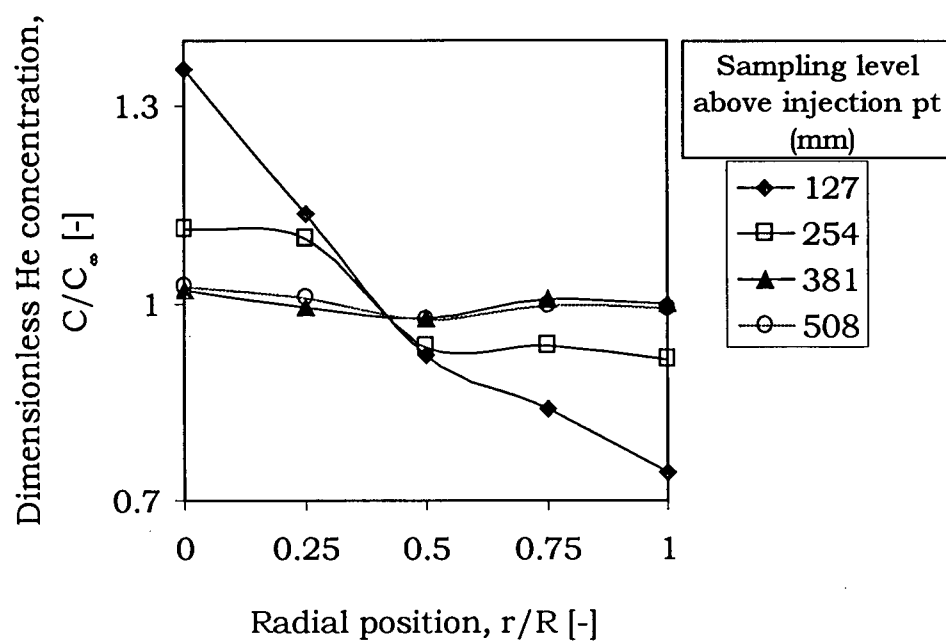
(a)
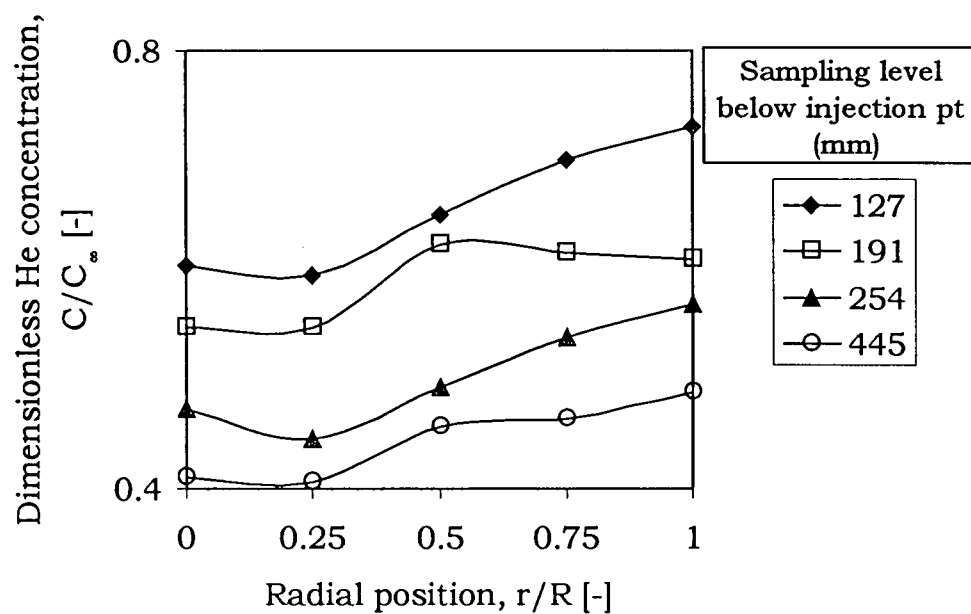
(b)

Figure 3.8. Radial concentration profiles for tracer: (a) downstream, (b) upstream of injection point. [L_o = 1.0 m, U = 0.5 m/s, tracer injection level 0.654 m above distributor.]
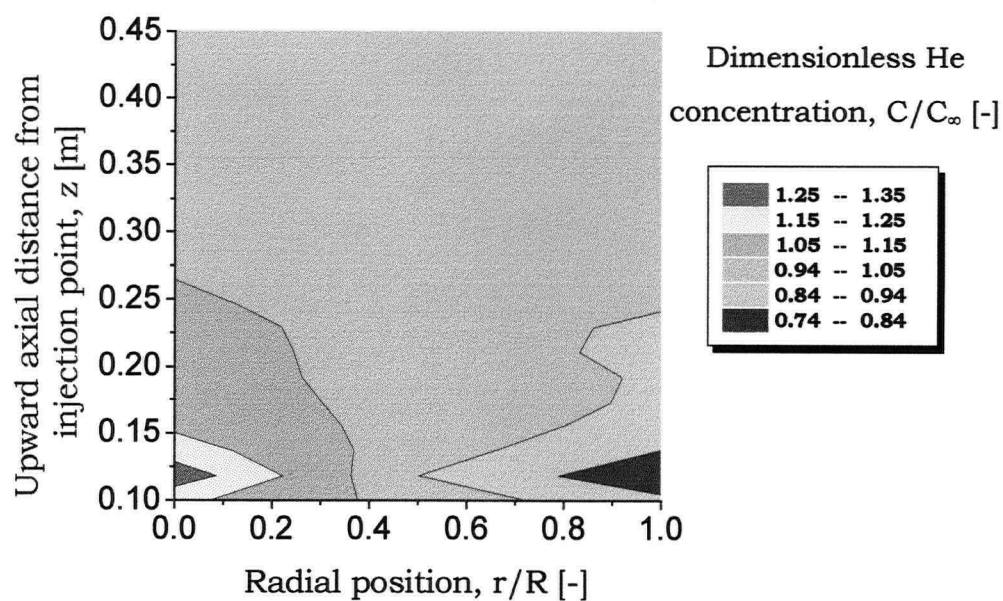
(a)
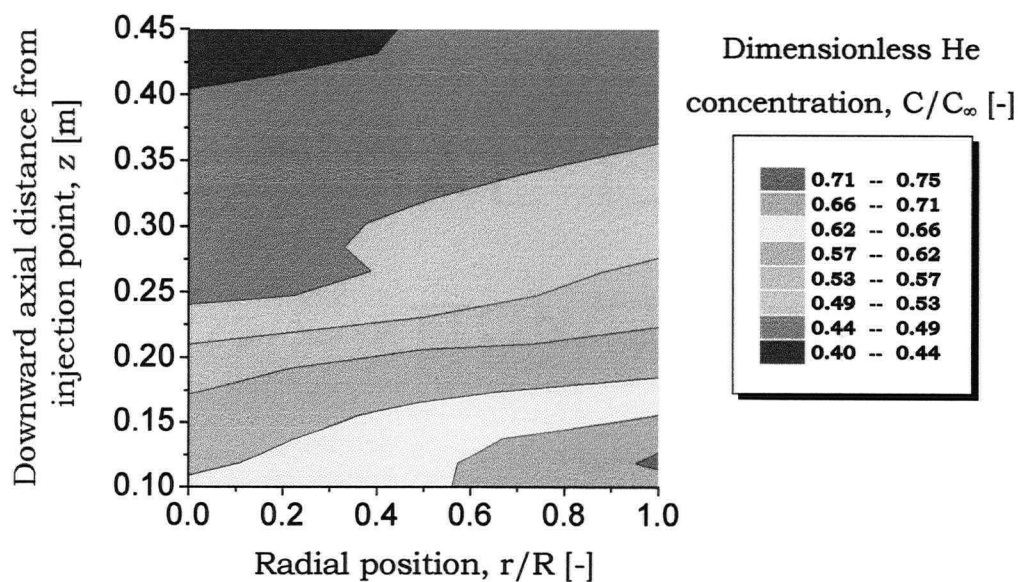
(b)

Figure 3.9. Contours for the dimensionless He concentration as functions of bed height and radius: (a) downstream, (b) upstream of injection point. [L_o = 1.0 m, U = 0.5 m/s, tracer injection level 0.654 m above distributor.]
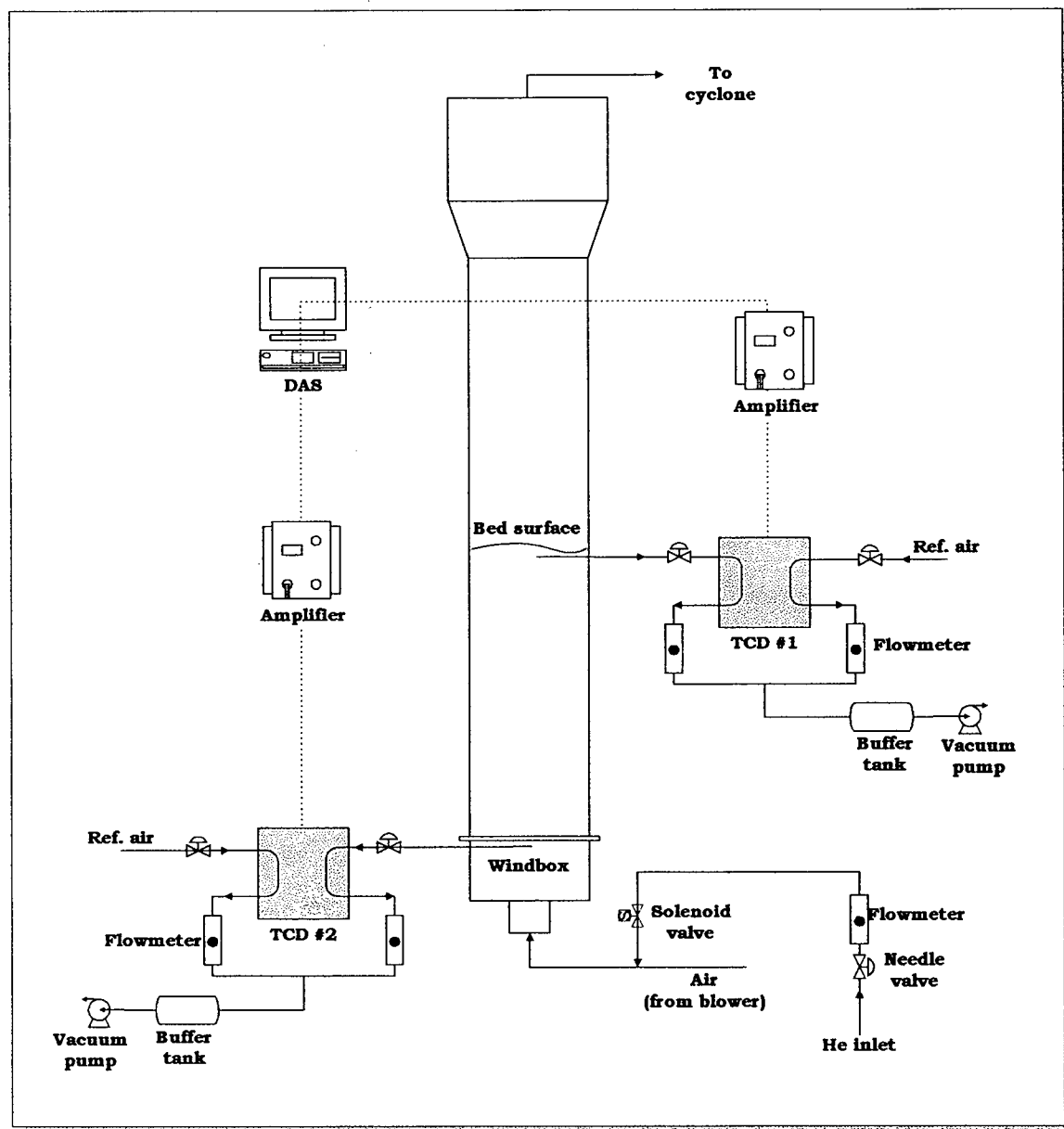
Figure 3.10. Schematic of unsteady state tracer injection/detection set-up.

The injection and the detection systems were synchronized using Labtech notebook software such that data logging began at the moment when the solenoid valve opens. The samples and reference air were drawn continuously into the two TCDs. Using the Labtech Notebook software, three separate data sets were logged for 60 s sampling periods at a frequency of 10 Hz to test the reproducibility of the data. One set of experimental F-curves for the downstream measurements (detection) for different superficial gas velocities is shown in Fig. 3.11. Representative F and E-curves for both the injection and the detection systems are plotted in Fig. 3.12.

3.3. Interpretation of Gas Mixing Data

Results from both steady and unsteady state tracer measurements can be interpreted in various ways. The goal here is to estimate the dispersion and interphase mass transfer coefficients using both the single-phase and the two-phase dispersion models. The results are intended to provide better understanding of the effects of dispersion in each phase with increasing velocities.

The effective axial dispersion coefficient, $\mathcal{D}_{zg}$, a measure of the intensity of the overall gas dispersion in the direction of flow, is related (Schügerl, 1967) to the backmixing coefficient, $\mathcal{D}_{zg,b}$, and the radial dispersion coefficient, $\mathcal{D}_{rg}$, by $\left(\mathcal{D}_{zg} = \mathcal{D}_{zg,b} + \beta U^2 D_t^2 / \mathcal{D}_{rg}\right)$. The dimensionless constant β characterizes the non-uniformity of the flow profiles and can be assumed to be in the range $5 \times 10^{-3} < \beta < 5 \times 10^{-4}$. Schügerl (1967) found $\beta = 0$ for small particles of $\approx 40 \mu m$. In general, $\mathcal{D}_{zg}$, can be approximated by $\mathcal{D}_{zg,b}$ if the radial velocity gradient is considered negligible or when mixing in the radial direction is rapid. This tends to be a reasonable approximation for group A particles (Yerushalmi and Avidan, 1985).

3.3.1 Steady State Measurements

3.3.1.1 Single-Phase One-Dimensional Dispersion Model

Results from the upstream measurements can be interpreted using a 1-D dispersion model to back out the backmixing coefficient, $\mathcal{D}_{zg,b}$:
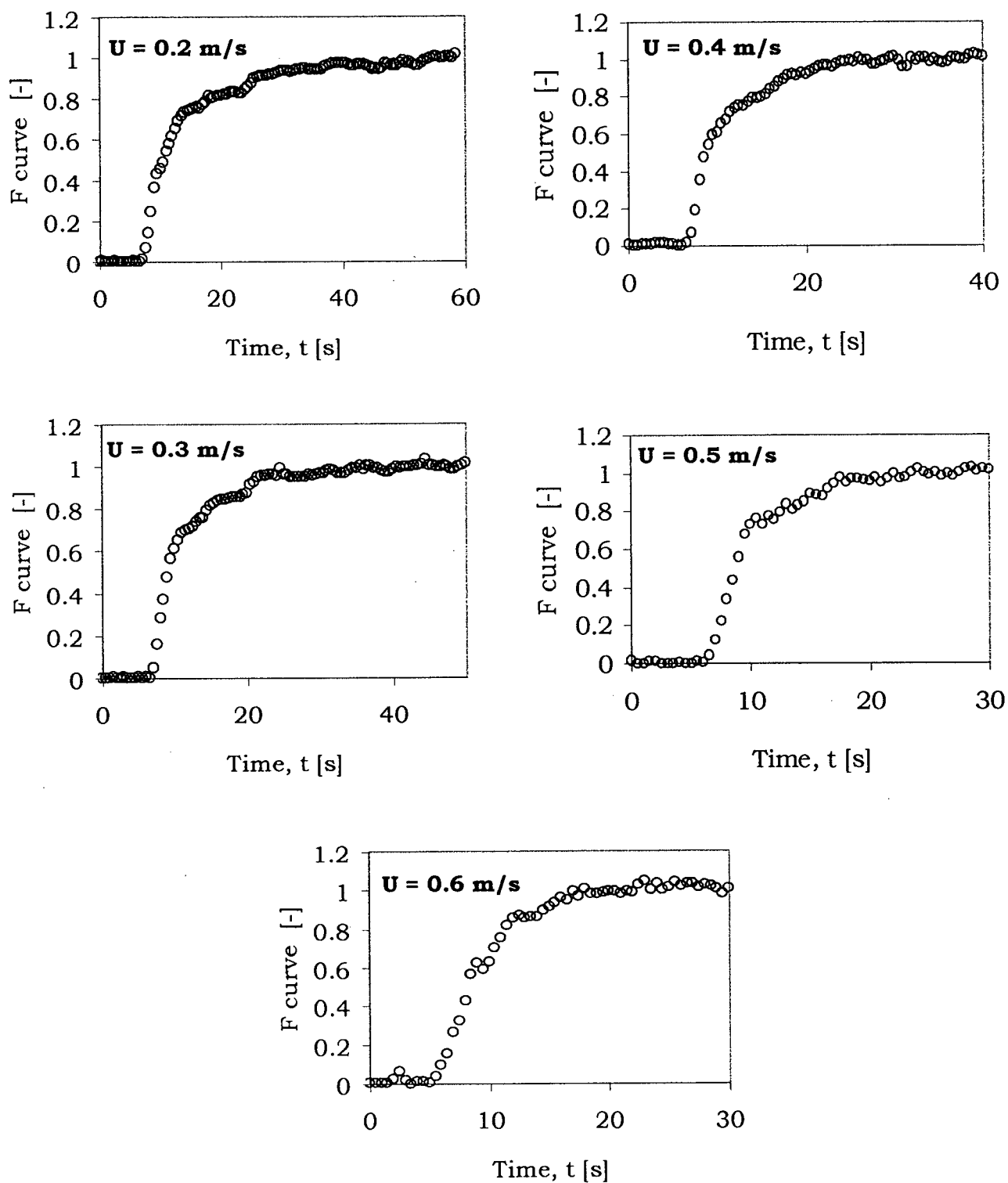
Figure 3.11. Experimental F curves for downstream (detection) measurements for different superficial gas velocities. [L_o = 1.5 m.]
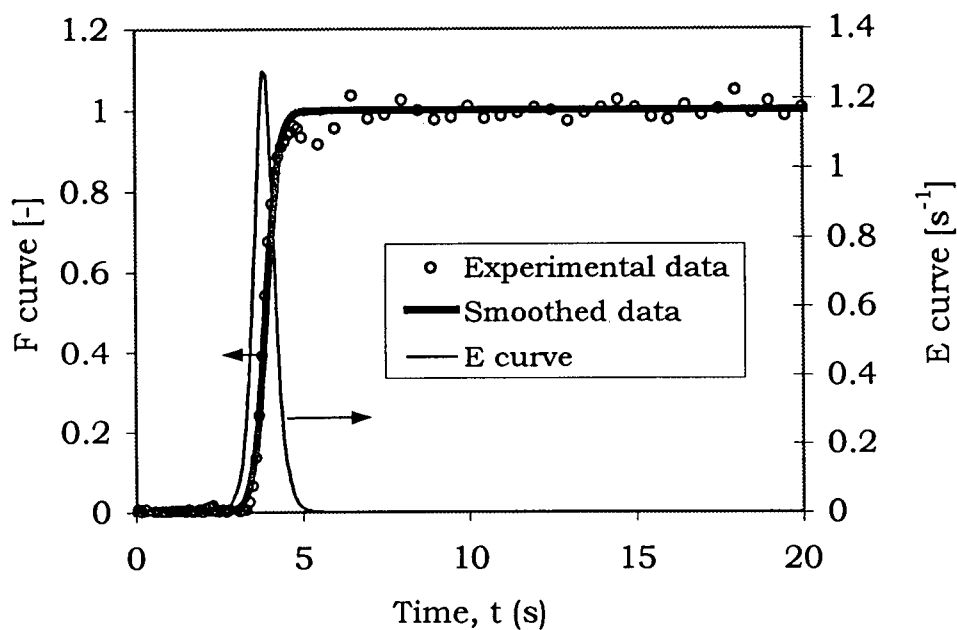
(a)
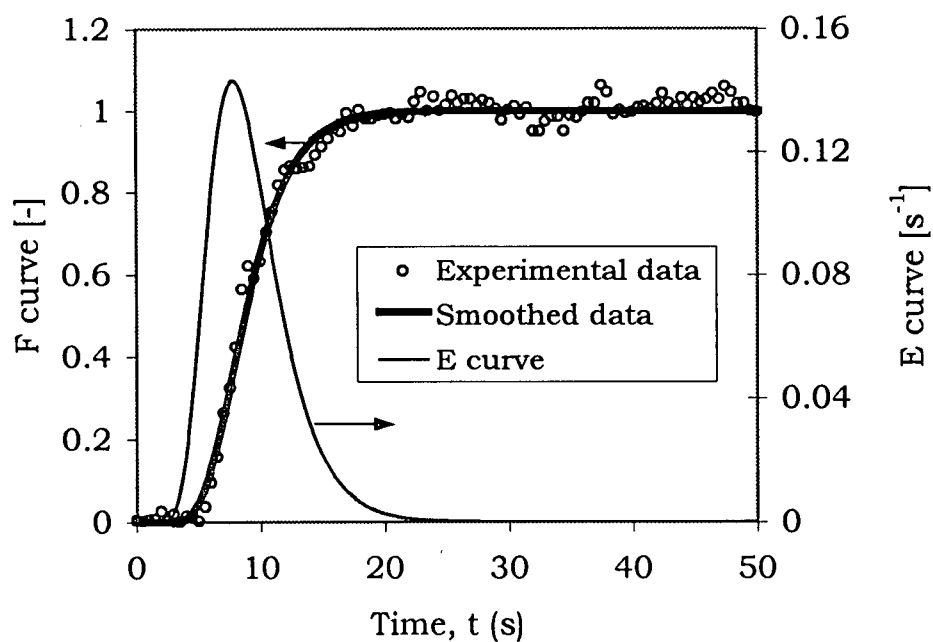
(b)

Figure 3.12. F and E curves for a) windbox measurements (near entrance to column), b) downstream measurements (near bed surface). [L_o = 1.5 m, U = 0.6 m/s; tracer injection is just upstream of 90° elbow (1 m from the distributor) of 6″ (150 mm) air line leading to windbox.]

$$\frac{U}{\varepsilon}\frac{dC}{dz} - \mathcal{D}_{zg,b}\frac{d^2C}{dz^2} = 0 \tag{3.1}$$

Equation (3.1) can be solved with the boundary conditions ($@z = 0, C = C_o$; $@z = -\infty, C = 0$) to obtain $\mathcal{D}_{zg,b}$. In this case it is required that concentrations at all upstream levels first be cross-sectionally averaged, such that (assuming the superficial radial velocity profile is flat)

$$C(z) = \frac{2}{\pi R^2}\int_0^R \pi r C(z,r)dr \tag{3.2}$$

This was achieved here using EXCEL by averaging the measured concentration along the radius. Using the 1-D dispersion model, the backmixing coefficients for $L_o = 1$ m over a range of superficial gas velocities were obtained from the analytical solution of eq. (3.1)

$$\frac{C}{C_o} = \exp\left[\frac{-U}{\varepsilon\mathcal{D}_{zg,b}}z\right] \tag{3.3}$$

by plotting the logarithm of concentration vs. axial distance upstream of the injection point. Different slopes can be obtained depending on whether the boundary condition at z = 0 is included as shown in Fig. 3.13. The poor correlation in Fig. 3.13a arises because the dispersion of gas at the point of injection is not accounted for by the simple boundary condition, as discussed below. Gas backmixing results of Won and Kim (1998) typify the poor correlation that results when the boundary condition at z = 0 is included. Similar results were obtained from a non-linear regression analysis performed using EXCEL. The resulting dispersion coefficients from the two linear-regression approaches are plotted in Fig. 3.14. Note the decrease in the backmixing coefficients at higher U. Although, there are too few data points to be certain of the trend, the point at which $\mathcal{D}_{zg}$ begins to decrease has been argued as marking the onset of turbulent fluidization (Lee and Kim, 1989; Foka et al., 1996). The results are, in general, comparable to, and in the same range as, those reported in the literature (see Bi et al, 2000).

Using the gPROMS parameter estimation algorithm (following the maximum likelihood approach, in which the goal is to obtain the parameters that maximize the probability that the model will predict the experimental values), we attempted to reproduce the above results in order to establish the reliability of the numerical approach, especially for the two-phase equations with complex boundary conditions. The numerical
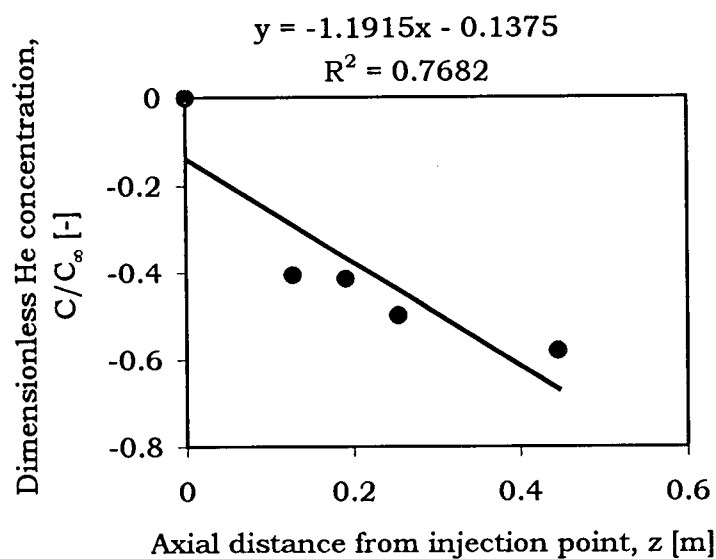
(a)
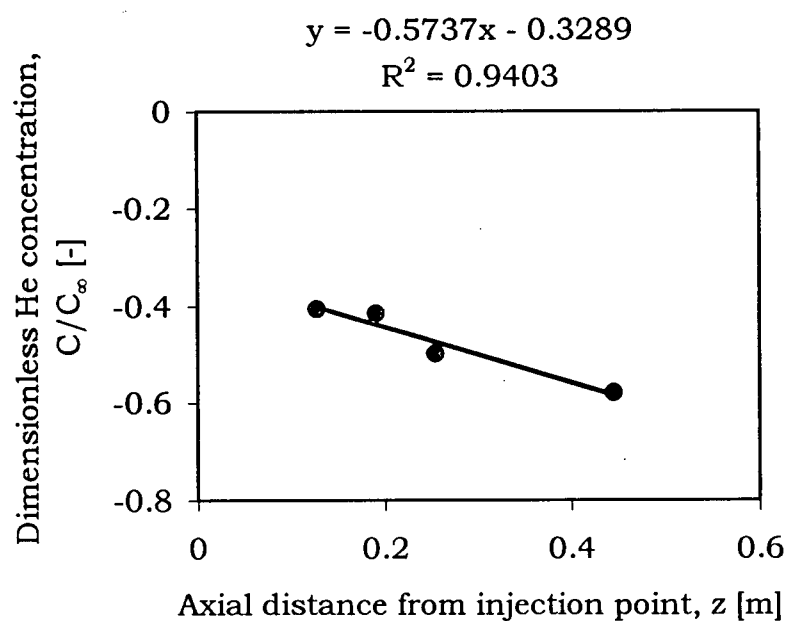
(b)

Figure 3.13. Plot of log of dimensionless concentration vs. superficial gas velocity for a commercial catalyst with boundary condition at z = 0: (a) included, (b) excluded. [U = 0.4 m/s, L_o = 1.0 m.]
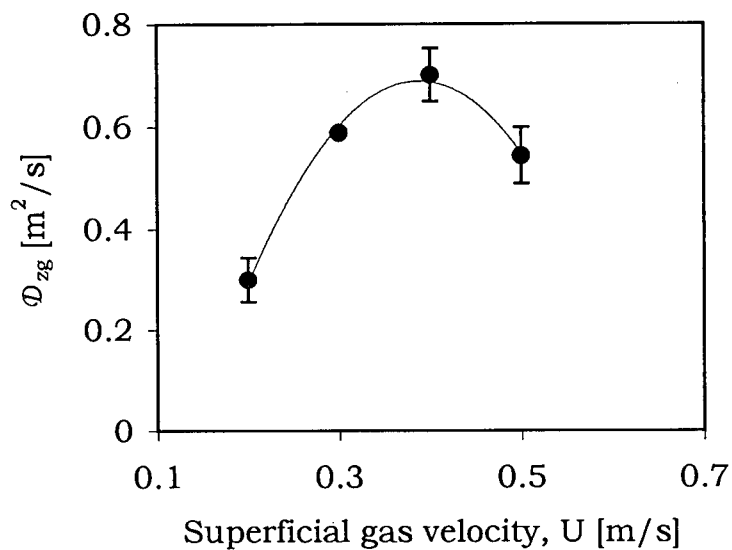
(a)
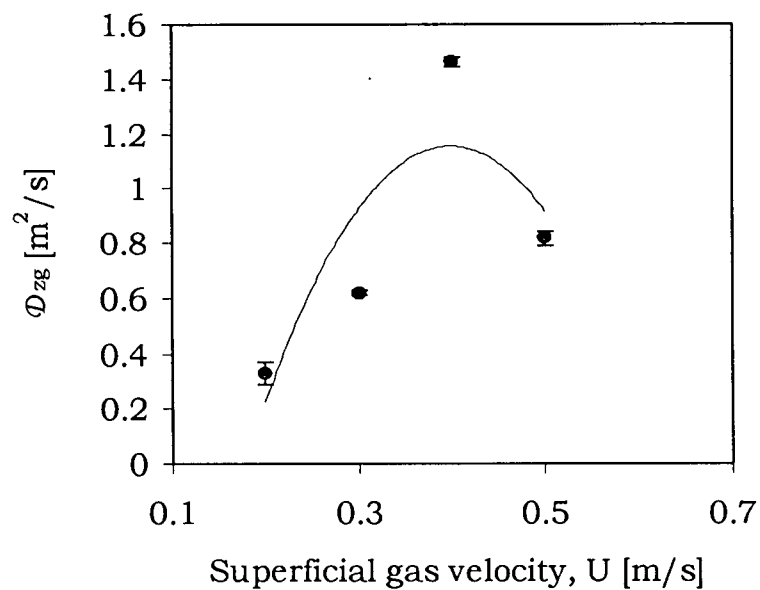
(b)

Figure 3.14. Backmixing coefficient as function of superficial gas velocity for a commercial catalyst: analytical solution obtained using Excel with boundary condition at z = 0: (a) included, (b) excluded. [L_o=1.0 m; lines show trends only.]

solution for the 1-D model, shown in Fig. 3.15, compares well with the least squares fitted curve based on the analytical solution of the 1-D model when the boundary condition at z = 0 is not considered. Note that the dispersed boundary condition was used in the numerical solution as discussed in the next section.

3.3.1.2 One-Dimensional Two-Phase Model with Dispersion

The single-phase dispersion model can give reasonable results for fluidized beds operated in the turbulent flow regime where homogeneity in the bed can be assumed. However, it is inadequate for lower gas velocities up to the transition region, as it does not account for the difference in the extent of dispersion between the two phases, nor for gas interchange between them. In this section, we attempt to estimate the dispersion coefficients in the two phases as well as the interphase mass transfer coefficient over a range of gas velocities using the generalized two-phase model with dispersion. The one-dimensional steady state two-phase mass balances (without the source term) can be written:

L-phase:
$$\psi_L u_L \frac{dC_L}{dz} - \psi_L \mathcal{D}_{zg,L} \frac{d^2 C_L}{dz^2} + K_{LH}(C_L - C_H) = 0 \tag{3.4}$$

H-phase:
$$\psi_H u_H \frac{dC_H}{dz} - \psi_H \mathcal{D}_{zg,H} \frac{d^2 C_H}{dz^2} + K_{LH}(C_H - C_L) = 0 \tag{3.5}$$

Overall:
$$C_i = q_L C_{iL} + q_H C_{iH} \tag{2.3}$$

where $K_{LH} = k_{LH} a_I \psi_L$. The phase volume fractions (ψ_L and ψ_H) and the fractional gas flows (q_L and q_H) are computed from eqs. (2.22), (2.25) and Table 2.3. Equations (3.4) and (3.5) must be solved together to back out the model parameters ($\mathcal{D}_{zg,L}, \mathcal{D}_{zg,H}$ and K_{LH}). Both an analytical solution to a simplified form of the above equations and a numerical approach that retains all terms in the equations are possible. One approach would be to measure the He concentration in the L- and H-phases (which is very difficult) and simplify the above equations by assuming $\mathcal{D}_{zg,L}$ to be negligible relative to $\mathcal{D}_{zg,H}$, while the interphase mass transfer coefficient is significant (van Deemter, 1961). Another approach would be to use a robust parameter estimation technique to determine the interphase mass transfer coefficient and the L- and H-phase dispersion coefficients while retaining all the terms in the equations. The former approach is most common because of its simplicity. Using this approach, eqs. (3.4) and (3.5) can be reduced to a
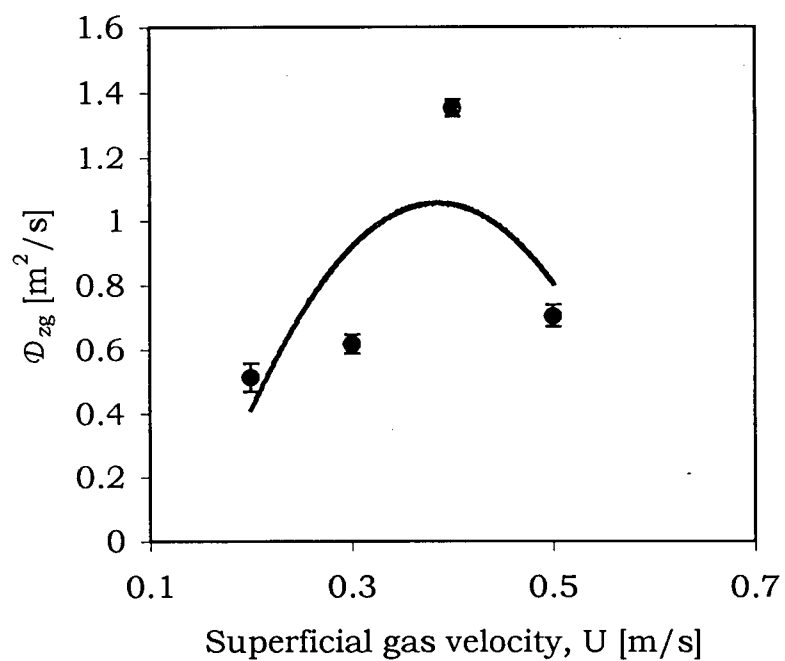
Figure 3.15. Backmixing coefficient as function of superficial gas velocity for a commercial catalyst: Solution from gPROMS parameter estimation function [L_o=1.0 m; line shows trend only.]

form similar to the dense phase axial dispersion model of Van Deemter (1961):

$$\psi_L u_L \frac{dC_L}{dz} + K_{LH}(C_L - C_H) = 0 \tag{3.6}$$

$$\psi_H u_H \frac{dC_H}{dz} - \psi_H \mathcal{D}_{zg,H} \frac{d^2 C_H}{dz^2} + K_{LH}(C_H - C_L) = 0 \tag{3.7}$$

Equations (3.6) and (3.7) can be solved together with the boundary condition ($@ z = -\infty$, $C_H = 0$) and the additional assumption that for $U > U_{mf}$, most of the gas passes through the dispersed or L-Phase such that $\psi_H u_H$ may be neglected relative to $\psi_L u_L$. The solution (van Deemter, 1961) is then:

i) for $z < 0$ (i.e. below injection level):

$$\frac{C_H}{C_o} = \left(\alpha \frac{\varpi^2 - 1}{4\varpi} + \frac{\varpi + 1}{2\varpi} \right) \exp\left[\frac{\varpi - 1}{2} \frac{K_{LH} \times z}{U} \right] \tag{3.8}$$

$$\frac{C_L}{C_o} = \left(\alpha \frac{\varpi - 1}{2\varpi} + \frac{1}{\varpi} \right) \exp\left[\frac{\varpi - 1}{2} \frac{K_{LH} \times z}{U} \right] \tag{3.9}$$

ii) for $z > 0$ (i.e. above injection level):

$$\frac{C_H}{C_o} = 1 + \left(\alpha \frac{\varpi^2 - 1}{4\varpi} + \frac{\varpi - 1}{2\varpi} \right) \exp\left[\frac{\varpi + 1}{2} \frac{K_{LH} \times z}{U} \right] \tag{3.10}$$

$$\frac{C_L}{C_o} = 1 + \left(\frac{1}{\varpi} - \alpha \frac{\varpi + 1}{2\varpi} + \right) \exp\left[- \frac{\varpi + 1}{2} \frac{K_{LH} \times z}{U} \right] \tag{3.11}$$

where

$$\varpi = \sqrt{1 + 4U^2 / (\psi_H \mathcal{D}_{zg,H} K_{LH})} \tag{3.12}$$

Here $\alpha = 1$ when the tracer is injected into the H-phase, and $\alpha = 0$ when the tracer is injected into the L-phase. Note that z is the upward positive axial distance from the injection level. The challenge of this approach is injecting the tracer gas into one of the L- or H-density phase. However, since it is expected that tracer injection at the wall will give more backmixing than injection along the axis of the column, it may be possible to inject the tracer at the wall, detect He concentrations below the injection point at different axial locations and use eq. (3.8) to obtain the parameters by optimization.

A superior approach employs a robust parameter estimation technique to calculate all three parameters. We accomplished this using the gPROMS parameter estimation feature.

The possible boundary conditions for eqs. (3.4) and (3.5) are:

$$at \ z = 0 : \begin{cases} C_H = C_o \\ q_L C_L + q_H C_H = C_o \end{cases} \qquad (a)$$

$$OR \quad at \ z = 0 : \begin{cases} -\mathcal{D}_{zg,L} \dfrac{dC_L}{dz} = u_L(C_o - C_L) \\ -\mathcal{D}_{zg,H} \dfrac{dC_H}{dz} = u_H(C_o - C_H) \end{cases} \qquad (b)$$

$$at \ z = -\infty : \begin{cases} C_L = 0 \\ C_H = 0 \end{cases} \qquad (c)$$

$$OR \quad at \ z = L^- : \begin{cases} -\mathcal{D}_{zg,L} \dfrac{dC_L}{dz} = u_L C_L \\ -\mathcal{D}_{zg,H} \dfrac{dC_H}{dz} = u_H C_H \end{cases} \qquad (d)$$

(3.13)

The choice of boundary condition strongly influences the estimated parameters. Boundary conditions (a) and (c) are commonly employed in gas mixing studies; they are reasonable approximations when the same concentration of tracer is injected into both phases, and for long columns in which the concentration in both phases at the distributor can be neglected. In this study, tracer was injected at the column axis. We consider that the tracer is dispersed in both phases right at the point of injection as represented by boundary condition (b). The boundary condition at the distributor is obtained by assuming that all gas that diffuses downward to the distributor is carried back upward by the up-flowing gas through convection. A simple mass balance at the distributor then results in the boundary condition represented by eq. 3.13d. The parameter estimator then compares experimental data with the model predictions at the corresponding axial positions. Agreement between model prediction and experiment is reasonable as shown in Fig. 3.16. The Optimal parameter estimates for the interphase mass transfer coefficient, and the L- and H-phase dispersion coefficients for superficial velocities in the range 0.2 to 0.5 m/s and boundary conditions (b) and (d) are presented in Table 3.1 and Fig. 3.17. The results are reasonable and of the same order of magnitude as those obtained from the analytical and numerical solutions of the 1-D model. While the dispersion coefficients in both phases increased with increasing gas velocity as expected, the phase dispersion ratio, $\mathcal{D}_{zg,L} / \mathcal{D}_{zg,H}$, differed considerably from its expected value of 1, even as U approached U_c. The observed increase of interphase mass transfer with increasing gas velocity
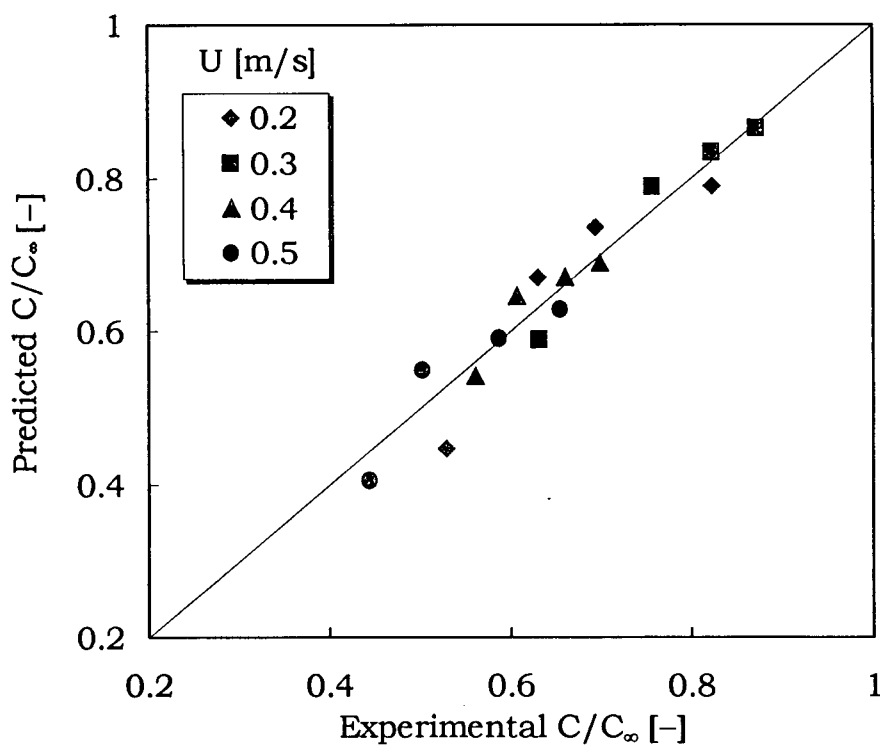
Figure 3.16. Two-phase dispersion model predictions of dimensionless concentration vs. experimental data for different superficial gas velocities. [L_o = 1.0 m.]
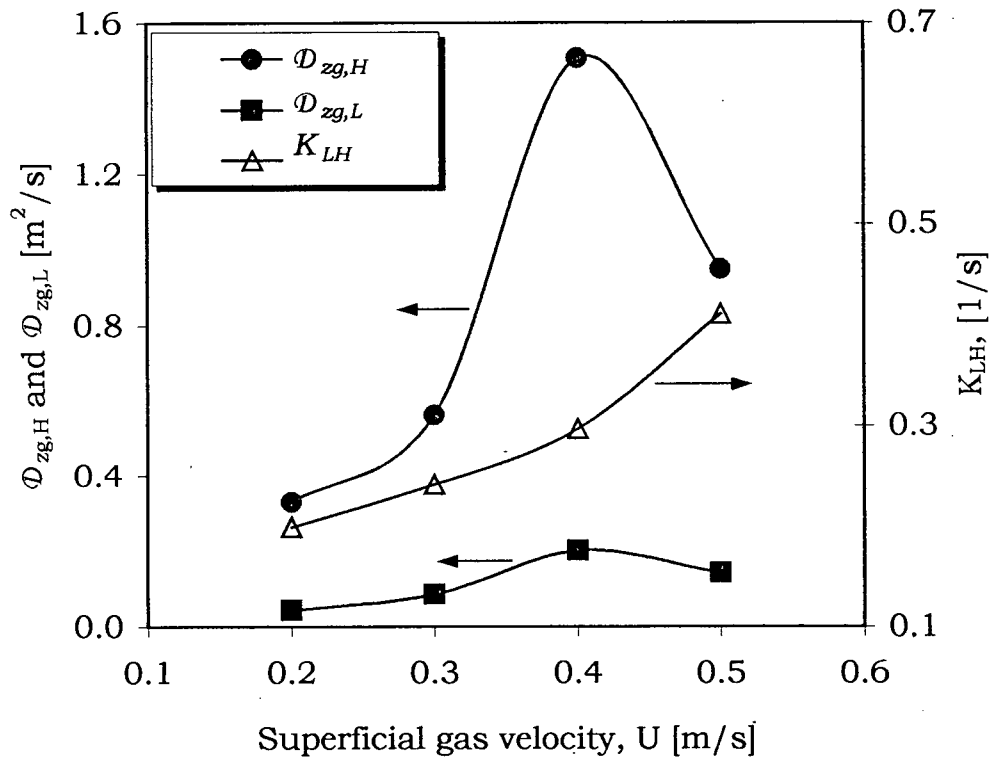
Figure 3.17. Axial dispersion and interphase mass transfer coefficients as functions of superficial gas velocity: Solution through gPROMS parameter estimation function [L$_o$ = 1.0 m, L^- = 664 mm.]

and the range of values obtained are consistent with previously published results (see Bi et al., 2000).

Table 3.1. Fitted values of interphase mass transfer and L- and H-phase axial dispersion coefficients

U (m/s)	$\mathcal{D}_{zg,L}$ (m²/s)	$\mathcal{D}_{zg,H}$ (m²/s)	K_{LH} (1/s)
0.2	0.044	0.330	0.199
0.3	0.087	0.562	0.241
0.4	0.202	1.507	0.297
0.5	0.143	0.947	0.411

3.3.2. Unsteady State Measurements

3.3.2.1 Single-Phase Dispersion Model

The analytical solution to the single-phase 1-D transient dispersion model

$$\frac{\partial C}{\partial t} = \mathcal{D}_{zg} \frac{\partial^2 C}{\partial z^2} - \frac{U}{\varepsilon} \frac{\partial C}{\partial z} \tag{3.14}$$

for closed-closed boundary conditions is quite cumbersome. For a small extent of gas dispersion, however, the dispersion coefficient can be determined by evaluating the mean residence time, t_m, and the variance, σ^2, of the tracer gas in the bed, obtained here from the residence time distribution data. The pertinent equations are:

$$E(t) = \frac{dF(t)}{dt} \tag{3.15}$$

$$t_m = \int_0^\infty tE(t)dt \tag{3.16}$$

$$\sigma^2 = \int_0^\infty (t - t_m)^2 E(t)dt \tag{3.17}$$

$$\frac{\sigma^2}{t_m^2} = \frac{2}{Pe_z} - \frac{2}{Pe_z^2}[1 - \exp(-Pe_z)] \tag{3.18}$$

The mean residence times and the spread of the RTD based on this approach as a function of superficial gas velocity are plotted in Fig. 3.18. As expected, both the mean, and the
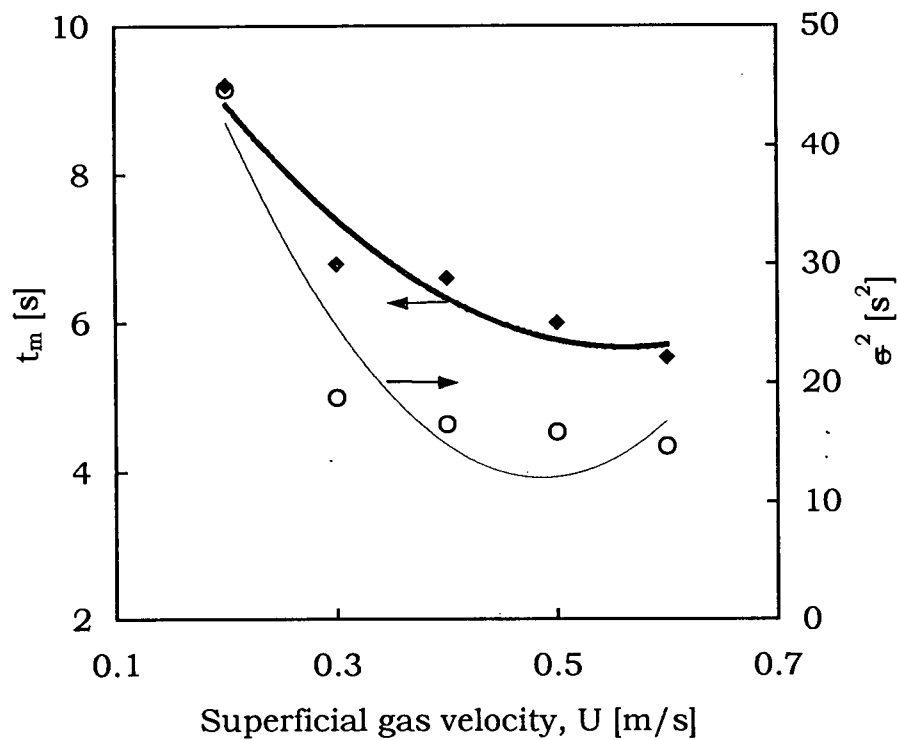
Figure 3.18. Mean residence time and variance of tracer gas as function of superficial gas velocity [L_o=1.5 m.]

spread of the residence time distribution decrease with increasing gas velocity. However, as seen from the figure, given the breath of the RTD ($\sigma^2 \approx t_m^2$), the variance approach is not valid for estimating the dispersion coefficient. Therefore we sought a numerical solution. The complete initial and boundary conditions for eq. (3.14) are

$$at \quad t = 0 \qquad C = 0$$

$$at \quad z = 0 \qquad -\mathcal{D}_{zg}\frac{\partial C}{\partial z} = U\left(C\big|_{o^-} - C\right) \tag{3.19}$$

$$at \quad z = L \qquad \frac{\partial C}{\partial z} = 0$$

where the imperfect step input for t > 0 is represented by the logistic regression function

$$C\big|_{o^-} = C_o(1 + a_1 e^{-a_2 t})^{-1} \tag{3.20}$$

fitted to the input RTD data (see Fig. 3.12a) measured with TCD#2, shown in Fig. 3.10. Because the tracer was injected farther from the distributor, eq. (3.20) corrects for the delay associated with the tracer injection setting explained above. The constants a_1 and a_2 are functions of the superficial gas velocity.

The dispersion coefficients were estimated using gPROMS by solving eq. (3.14) together with the initial and boundary conditions given by eqs. (3.19) and (3.20). As seen in Fig. 3.19, the agreement between model prediction and experiment is reasonable. The estimated parameters are shown in Fig. 3.20 as a function of superficial gas velocity. Note the difference between these coefficients and the backmixing coefficients given in Fig. 3.15. This difference is due to a combination of factors: different types of coefficients as discussed above, different bed depths, and, possibly, different experimental techniques. Note, also, that there is no maximum as the gas velocity is increased beyond the transition velocity, $U_c = 0.52$ m/s (obtained from the U_c correlation in Table 2.2). This may be due to an increase in U_c with increasing static bed height as reported by Ellis et al. (2000) from an experimental study using the same catalysts, an aspect not captured in the U_c correlations. In particular, U_c was reported to be ~0.62 m/s (based on differential pressure fluctuations) and 0.45 m/s (from absolute pressure fluctuations) for $L_o = 1.5$ m. The onset of turbulent fluidization, therefore, may well fall around 0.6 m/s, explaining the lack of a maximum in the dispersion coefficient. The values of $\mathcal{D}_{zg}$ are between 0.2 and 1.9 m²/s, consistent with the range obtained from the backmixing studies above, while noting that the dispersion coefficients computed
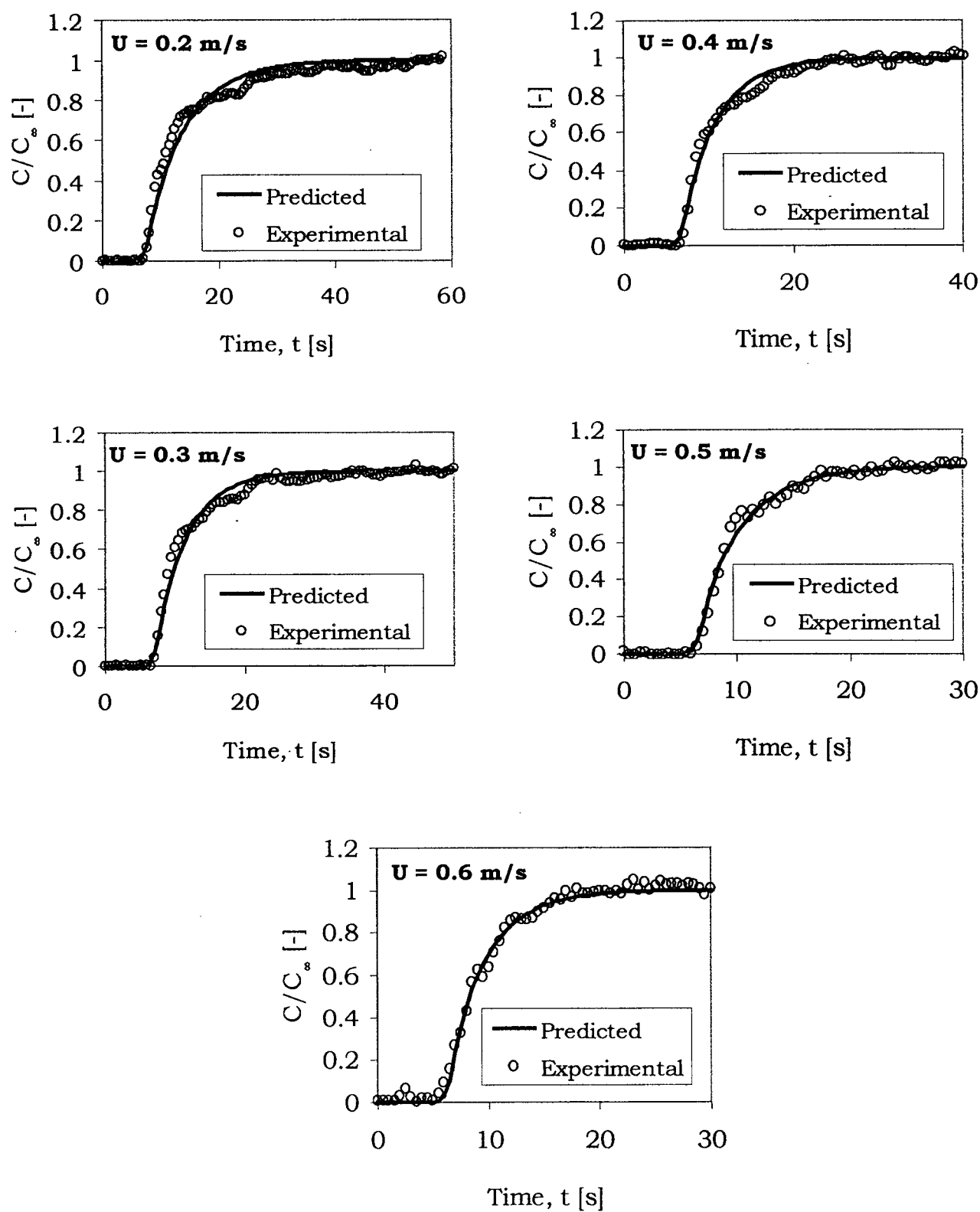
Figure 3.19 1-D dispersion model predictions of transient dimensionless concentration (F curves) compared with experimental data for different superficial gas velocities. [L_o = 1.5 m.]
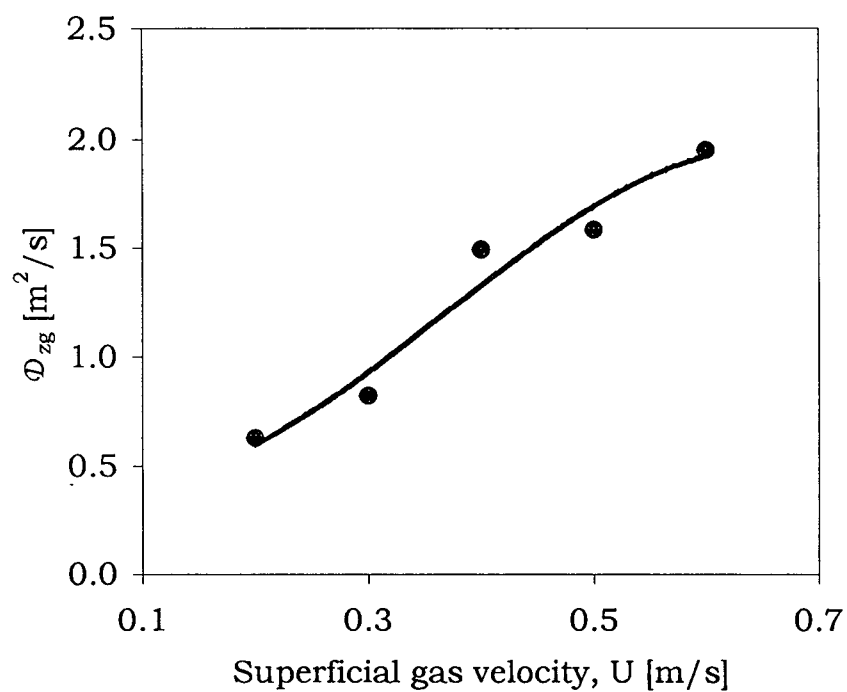
Figure 3.20. Axial dispersion coefficient obtained from gPROMS parameter estimation function as a function of superficial gas velocity for a commercial catalyst. [L_o=1.5 m; line shows trend only.]

using the RTD measurements reflect the extent of axial mixing of the gas, which is a function both of the backmixing coefficient, a strong function of the downward movement of the solids, and the radial gas mixing coefficient. As mentioned above, however, the axial dispersion coefficient, $\mathcal{D}_{zg}$, can be approximated by the backmixing coefficient, $\mathcal{D}_{zg,b}$, if the radial velocity gradient is neglected or when radial mixing is rapid.

3.3.2.2 Two-Phase Model with Dispersion

RTD measurements can also be interpreted using the unsteady state form of eqs. (3.4) and (3.5) to determine the dispersion coefficients in the L- and H-phases together with the interphase mass transfer coefficient. The mass balances can be written:

L-phase: $\qquad \varepsilon_L \dfrac{\partial C_L}{\partial t} = \mathcal{D}_{zg,L} \dfrac{\partial^2 C_L}{\partial z^2} - u_L \dfrac{\partial C_L}{\partial z} + K_{LH}(C_L - C_H)/\psi_L \qquad (3.21)$

H-phase: $\qquad \varepsilon_H \dfrac{\partial C_H}{\partial t} = \mathcal{D}_{zg,H} \dfrac{\partial^2 C_H}{\partial z^2} - u_H \dfrac{\partial C_H}{\partial z} + K_{LH}(C_H - C_L)/\psi_H \qquad (3.22)$

The initial and boundary conditions (closed-closed) are given in Table 3.2.

Figure 3.21 shows the L- and H-phase axial dispersion coefficients and interphase mass transfer coefficient as functions of the superficial gas velocity. As expected, the extent of dispersion in both phases and the mass transfer all increase with increasing gas velocity. As in the analytical solution to the 1-D dispersion model, no maximum is observed. However, the ratio $\mathcal{D}_{zg,L}/\mathcal{D}_{zg,H}$, which is also seen to increase with increasing gas velocity, remains far from unity, even as U approaches U_c.

Table 3.2. Initial and boundary conditions for eqs. (3.21) and (3.22).

$at \quad t = 0$	$\begin{cases} C_L = 0 \\ C_H = 0 \end{cases}$	
$at \quad z = 0 \quad \begin{cases} -\mathcal{D}_{zg,L} \dfrac{\partial C_L}{\partial z} = u_L(C\mid_{o^-} - C_L) \\ -\mathcal{D}_{zg,H} \dfrac{\partial C_H}{\partial z} = u_L(C\mid_{o^-} - C_H) \end{cases}$	$at \quad z = L$	$\begin{cases} \dfrac{\partial C_L}{\partial z} = 0 \\ \dfrac{\partial C_H}{\partial z} = 0 \end{cases}$
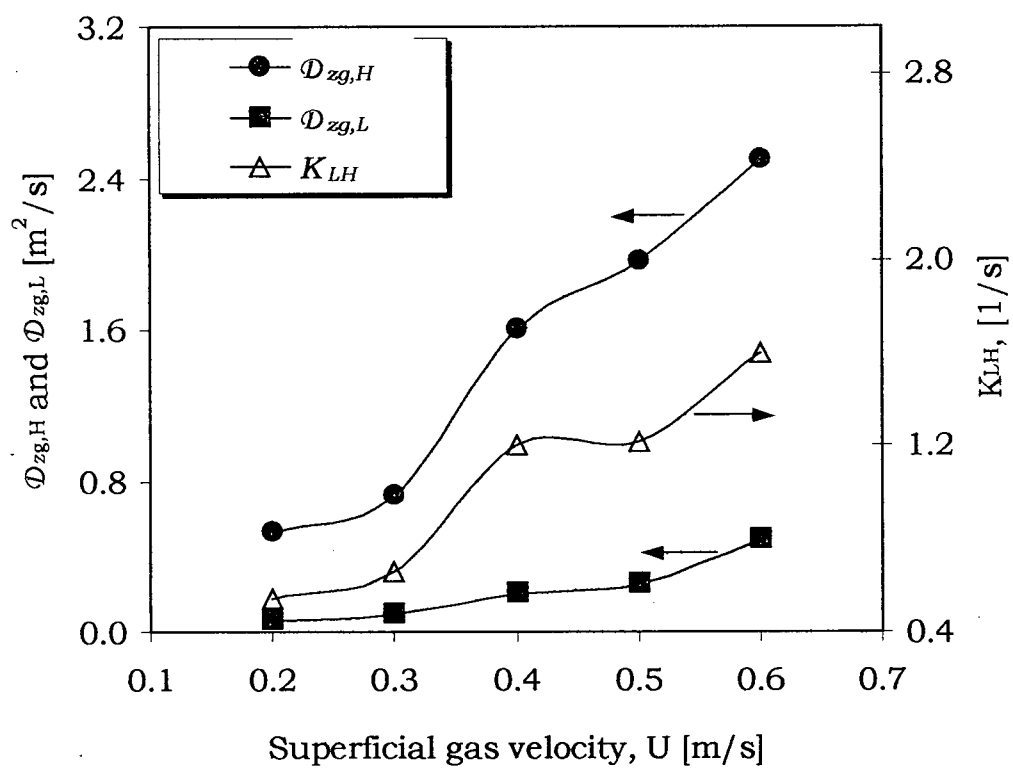
Figure 3.21. L- and H-phase axial dispersion coefficients and interphase mass
transfer coefficient as functions of superficial gas velocity: Solution via
gPROMS parameter estimation [L_o=1.5 m.]

3.4. Comments on Correlations for Pe$_z$

The dispersion in the dilute or the L-phase is commonly assumed negligible relative to that in the dense or H-phase, or approximated by using the molecular diffusivity of the gas. Consequently, none of the numerous dispersion correlations attempted to delineate the dispersions in the L- and the H-phases. Results from this study indicate that the dispersion coefficients differ widely in the two phases at low gas velocities, with the difference narrowing as the gas velocity increases. The effect of the initial solid inventory, which affects the interfacial area available for gas interchange between the two phases, and also affects the gas diffusion through the dense phase, has significant impact on dispersion and interphase mass transfer. In addition, the column size also has considerable impact on gas dispersion (Cho et al., 2000), but most reported correlations do not account for this effect. Given the scarcity of data reported in the literature on the effect of column size and static bed height on the Peclet number (Bi et al, 2000), it is difficult to pin down the influence of such factors.

Unfortunately, because there are few results from our experiments, reliable correlations cannot be developed at this point. In view of this, these results are not used in later chapters; the correlations for Pe$_z$ listed in Table 2.3 are used in conjunction with equation (2.34) throughout the later chapters. It should be possible, however, when more results from similar studies become available, to develop separate correlations for the dispersion coefficients in the separate phases while accounting for the above factors.

3.5. Conclusions and Recommendations

Gas mixing experiments were conducted in a 4.4 m high by 0.286 m diameter column with commercial catalyst particles as bed material for superficial gas velocities from 0.2 to 0.6 m/s. Data from both steady state and step change tracer injection experiments were interpreted using a one-dimensional dispersion model and a generalized 2-phase model with dispersion. The results are, in general, comparable to, and in the same range as, those reported in the literature (see Bi et al., 2000). They also fall in the same range with predictions from the correlations for interphase mass transfer and axial dispersion given

in Table 2.3. The generalized 2-phase model effectively captures the expected trends of increasing dispersion in both the low- and high-density phases as gas velocity is increased. Beyond the transition velocity, U_c, however, the overall dispersion decreased for $L_0 = 1.0$ m. Results for the different gas velocities and aspect ratios suggest that the dispersion coefficients, and interphase mass transfer coefficient between the low- and high-density phases depend on the initial solids inventory.

To provide further information for scale-up, the following are recommended:

(i) Conduct further gas mixing experiments at different static bed heights, preferably in longer columns for the same or similar column diameters.

(ii) Conduct experiments in columns of different diameters for the same static bed height, i.e. changing the aspect ratio, L_0/D_t, while keeping L_0 constant. Results from this and (i) above, when treated together with the results from this study and available literature data, will help establish the effect of the aspect ratio on both the interphase mass transfer and gas dispersion in the bed.

(iii) It would be helpful to conduct experiments in columns of similar geometry for superficial gas velocities beyond the range considered in this study. Specifically, it would be valuable to study the effect of increasing velocity on the ratio $\mathcal{D}_{zg,L} / \mathcal{D}_{zg,H}$, which is expected to approach unity when the gas velocity is close to U_c.

(iv) Using the combined information from above, it would be valuable to develop separate correlations for the dispersion coefficients in the two phases.

Chapter 4

Validation of GFBR Model with Ozone Decomposition Data

4.1 Introduction

Although the new GFBR model is based on sound theoretical underpinnings, its true utility lies in how well it predicts specific performance measures such as conversion, selectivity and hydrodynamic trends. As shown in Chapter 2, the model provides a means of covering the complete range of gas velocities and flow conditions from minimum bubbling right up to fully fast fluidization conditions. The capability of the model in eliminating discontinuities at the boundaries, while giving improved predictions of particle and gas dynamics and of reactor performance, is demonstrated using experimentally investigated ozone decomposition data from Sun (1991), covering a wide range of superficial gas velocities and catalyst activities. The wide range of conditions allows us to test the model across all three flow regimes considered.

4.2 Case study: Ozone Decomposition Reaction

4.2.1 Reaction Kinetics and Model Parameters

The ozone decomposition reaction is represented by

$$O_3 \rightarrow 1.5O_2 \qquad (4.1)$$

This reaction has been commonly employed in laboratory investigation of the performance of fluidized beds by several workers (e.g. Chavarie and Grace, 1975; Sun, 1991; Jiang et al., 1991, Ouyang et al., 1995) for a number of reasons: it proceeds at atmospheric temperature and pressure; reaction kinetics are pseudo-first order; there is negligible heat of reaction because of the low concentrations involved; and ozone is readily determined using UV absorption. Ozone conversion data from experimental investigation of the effect of PSD on FBR performance covering superficial gas velocities in the range 0.1 to 1.8 m/s are used to validate the GFBR model. The particle properties

and operating conditions employed in the investigation are shown in Table 4.1. The velocity range covers bubbling, turbulent and fast fluidization flow regimes (with U_c = 0.55 m/s and U_{se} = 1.38 m/s respectively, estimated from the correlations in Table 2.2).

4.2.2 Other Considerations in Applying the GFBR Model to Sun's Data

(a). It is assumed, for the ozone decomposition process, that temperature variations along the column height are negligible, since the ozone decomposition reaction is conducted at atmospheric conditions with a very small inlet concentration of ozone. Also, the column is shallow enough (L_t = 2 m) that pressure gradients are not very significant, and pressure changes are neglected. Therefore, to reduce CPU time, both energy and pressure balances in the GFBR model code were turned off at this stage using the selector section of the gPROMS code.

(b). Sun (1991) estimated that about 20% of the solids were in the solids return system during the experiments. The exact quantity may have varied widely over the course of the investigation, but lacking any systematic measurements that could tie the entrainment rate to the gas velocity, the solids inventory was adjusted in all cases so that M_s = 0.8×M_{so}.

(c). The voidage at minimum fluidization, ε_{mf}, was taken as 0.48 from Grace and Sun (1991) who reproduced experimental measurements of Ip (1989) for different PSDs of FCC particles.

(d). Three parameters appearing in the transition equations (Table 2.3), crucial to correctly predicting the behavior at the limiting conditions in the GFBR model, were first estimated by comparing model predictions with experimental data: In particular, the (i) initial volume fraction of solids in L-phase at bubbling conditions, ϕ_{Lo}, was estimated to be 0.0355 by matching model predictions with data under bubbling conditions using the two-phase bubbling bed model. (ii) The average solids flux under fast fluidization conditions, G_{so}, was estimated by matching model predictions with data using the GFBR model for the intermediate gas velocities between turbulent and fast fluidization conditions giving G_{so} = 120 kg/m^2s. This value was used throughout the simulations. (iii) Widely varying

estimates of gas dispersion coefficients result from different correlations (Bi et al., 2000). The parameter, f_{pe}, was estimated by matching model predictions with data using the dispersed flow model for turbulent conditions, leading to a fitted value of 0.071. The adjusted Peclet number is then $Pe_z' = f_{Pe} \times Pe_z$.

Table 4.1. Operating conditions, hydrodynamic properties and reactor geometry (Details are given by Sun, 1991).

Parameter	Value
Inlet temperature, T_o	298 K
Inlet pressure, P_o	101 kPa
Inlet superficial gas velocity, U_o	Varied (0.1 to 1.75 m/s)
Expanded bed height, L_d	Varied (~ 0.56 to 2.0 m)
Average particle diameter, $\overline{d}_p$	60 μm
Initial solids inventory, M_{so}	5 kg
Catalyst density, ρ_p	1580 kg/m³
Catalyst activity, k_r	Varied (8.95, 4.62 and 2.41 s⁻¹)
Inside diameter of reactor, D_t	0.105 m
Column height, L_t	2.0 m

4.2.3 Results and Discussion

4.2.3.1 Hydrodynamics

Figure 4.1 shows exponential decay of solids hold-up in freeboard according to eq. (2.12) for different gas velocities and the other conditions given in Table 4.1. As expected, at low gas velocities ($U = 0.03$ m/s $= 5 \times U_{mb}$), the model predicts a small fraction of solids in the freeboard. Solids hold-up in the freeboard is predicted to increase with increasing gas velocity, while the column-average value decreases. The height at which the decay starts corresponds to the bed height, L_d. The predicted solids hold-up at $U \cong 1.5$ m/s $> U_{se}$ indicates that the dense bed height, L_d, approached the total column height ($L_t = 2$ m). Beyond this point, solids are significantly entrained. Thus solids hold-up from that point becomes a strong function of the solids flux.

Figures 4.2 and 4.3 show predicted phase gas velocities and densities for the low-density (L) and high-density (H) phases as well as the bed average gas velocity and density in the bed with increasing superficial gas velocity for the conditions appearing in Table 4.1. The phases seem to be quite distinct at low velocities where the L (bubble) phase accommodates most of the gas flow, while the H (dense) phase, composed of solids and interstitial gas, occupies most of the volume. Hence, as seen in Fig. 4.2, u_H trails u_L as almost all the excess gas, $U-U_{mf}$, flows via the low-density phase. As U increases, however, the two phases merge, i.e. become almost identical, corresponding to the nearly homogeneous behavior encountered within the turbulent fluidization flow regime. With further increase in U, the bed begins to segregate into a continuous dilute core surrounded by a dense annular region, especially for fully developed conditions. The predicted fractional gas allocation in the L-phase, shown in Fig. 4.4, further portrays this trend. Note that the fractional allocation is seen to approach 1 asymptotically in the fast fluidization limit because of the assumption in the core-annulus model that gas flows upward in the core only, with zero net flow of gas in the annulus.
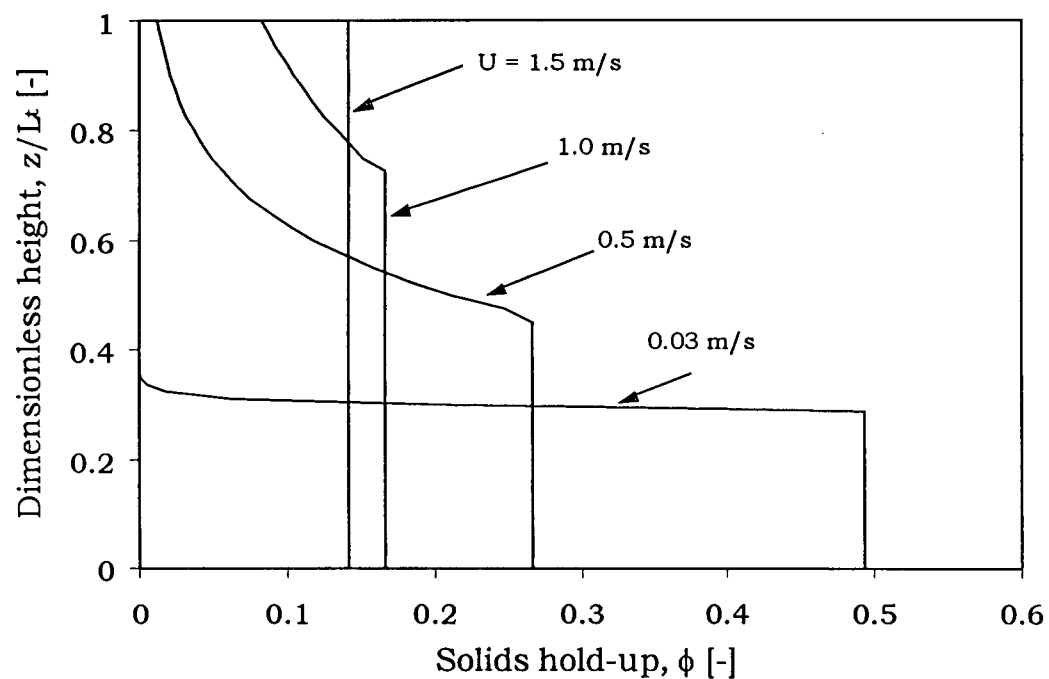
Figure 4.1. Axial profiles of solids hold-up in column at different superficial gas velocities. Conditions are listed in Table 4.1.
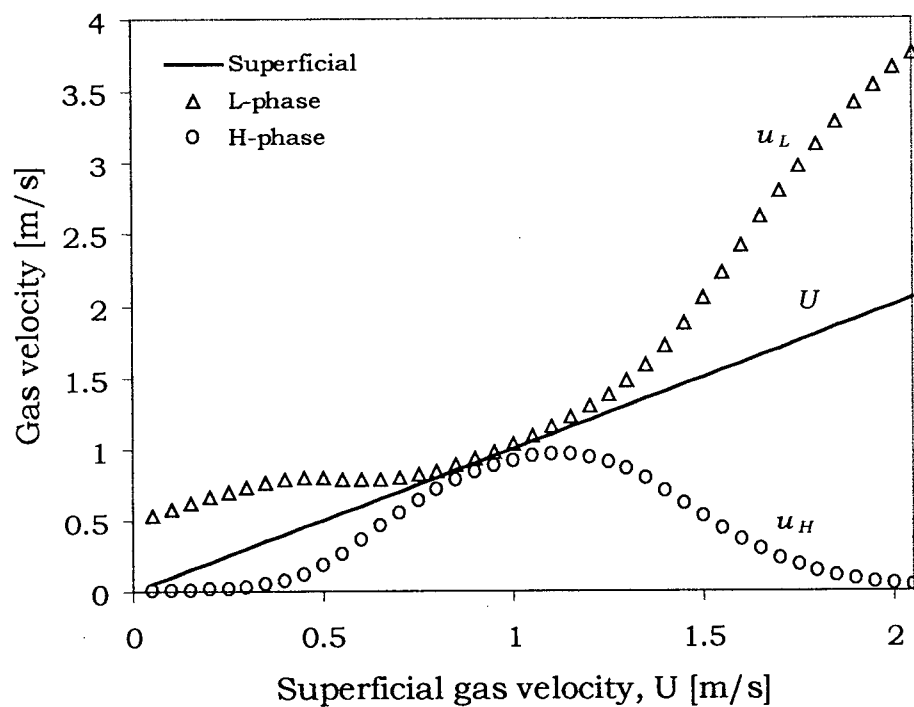
Figure 4.2. Predicted gas velocities in low- and high-density phases and bed average with increasing superficial gas velocity in the dense bed. Conditions are listed in Table 4.1.
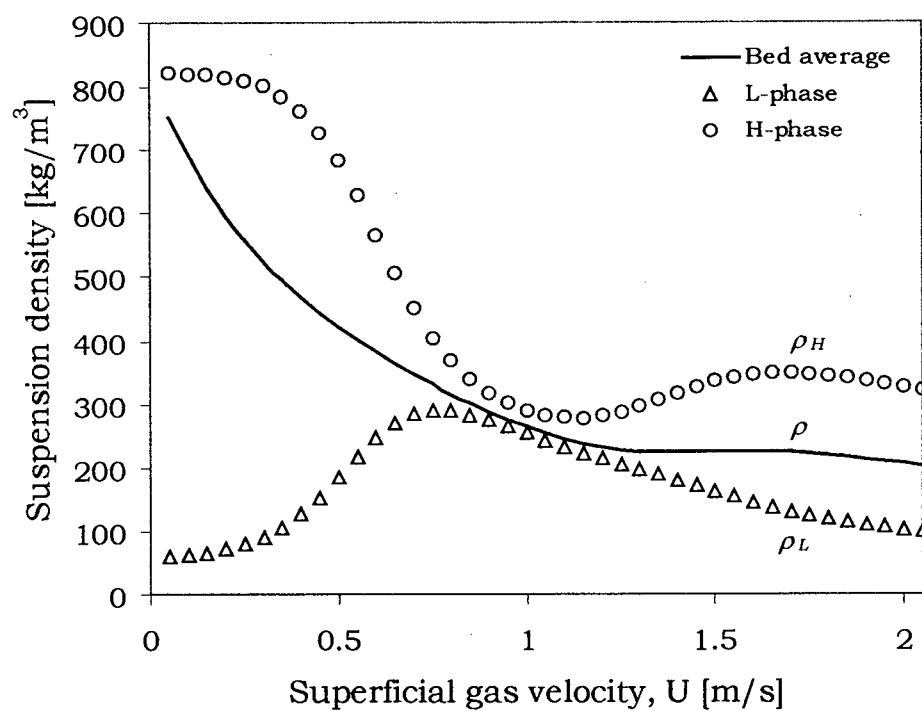
Figure 4.3. Predicted suspension densities in low- and high-density phases and bed average with increasing superficial gas velocity in the dense bed. Conditions are listed in Table 4.1.
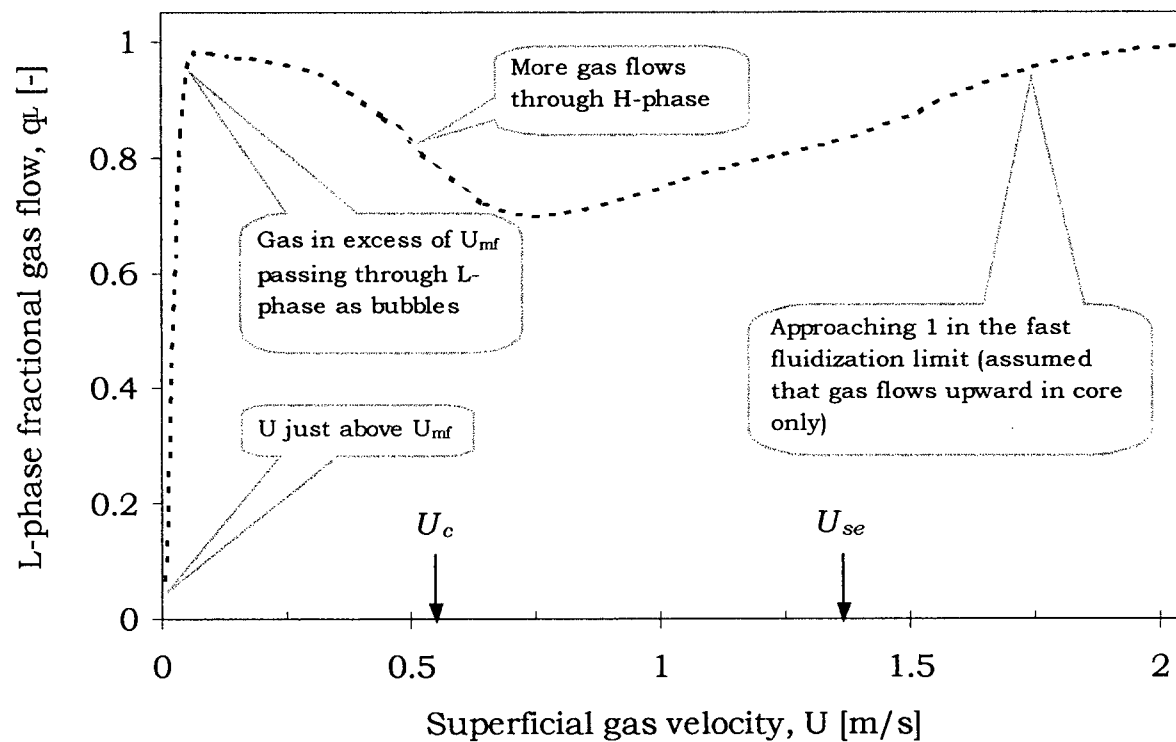
Figure 4.4. Predicted L-phase fractional gas flow allocation with increasing superficial gas velocity in the dense bed. Conditions are given in Table 4.1.

4.2.3.2 Reactor Performance

(a) Influence of Freeboard on Ozone Conversion

The performance of the GFBR model with the freeboard included (case1) is compared here with case 2 where the freeboard is ignored. We also explore how the contribution of the freeboard; (i) influences the overall conversion of ozone; and (ii) changes with increasing superficial gas velocity. But first, we examine the difference between the dense bed heights for the two cases (cases 1 and 2). Figure 4.5 shows the predicted dense bed height with increasing gas velocity for both cases, where the bed heights are computed based on

$$M_s = A\rho_p\left(L_d\phi_d + L_f\overline{\phi}_f\right) \tag{2.19}$$

For the case without the freeboard, the expanded bed height, L_d, is computed by assigning all the solids to the dense region, or equivalently by setting $\overline{\phi}_f = 0$ in eq. (2.19). As expected, the bed height for case 1 continues to trail that in case 2 until the predicted bed heights in both cases reach the column height, L_t.

Figure 4.6 shows predicted axial ozone conversions at different gas velocities for the two cases. At low U (sufficiently high for some solids to be ejected into the freeboard), because of the sharp exponential decay of solids hold-up, the additional freeboard reaction occurs just above the dense bed height with the remaining freeboard height showing a flat profile up to the column exit. Moreover, even for this low U, the computed bed height is slightly higher when the freeboard is ignored than when included, in line with eq. (2.19). With a further increase in U, the computed dense bed heights diverge even further until the freeboard disappears completely, from which point there is no difference in the predicted values for the two cases.

The performance of the GFBR model with and without the freeboard is tested by comparing model predictions with experimental data over a wide range of superficial gas velocities and catalysts activities in Figure 4.7. Predictions for the case with the freeboard included gives better agreement with the data in general. At high U ($U > 1.2$ m/s), predictions from the two cases merge for the reasons explained above. Overall, the freeboard is important in columns where the freeboard height constitutes a significant fraction of the total column height. For highly exothermic reactions, the dense region
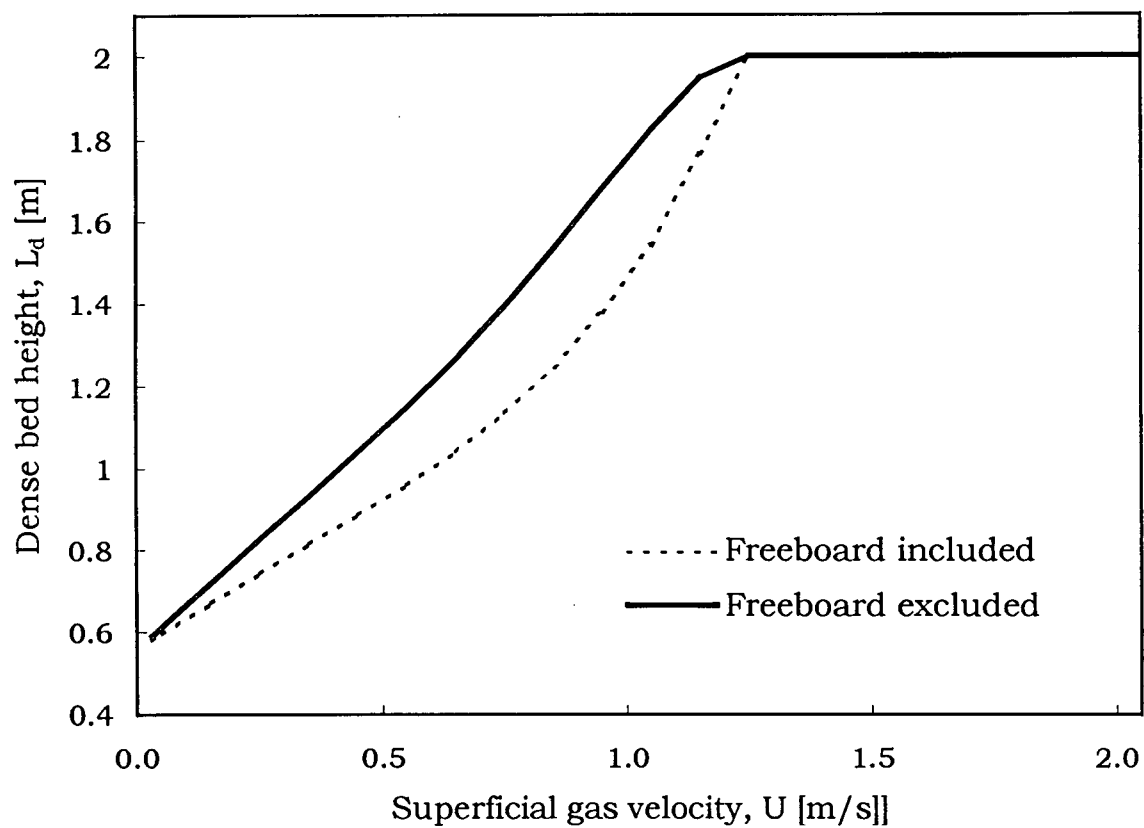
Figure 4.5. Comparison of computed expanded bed heights for the cases when freeboard is included and excluded in the GFBR model.
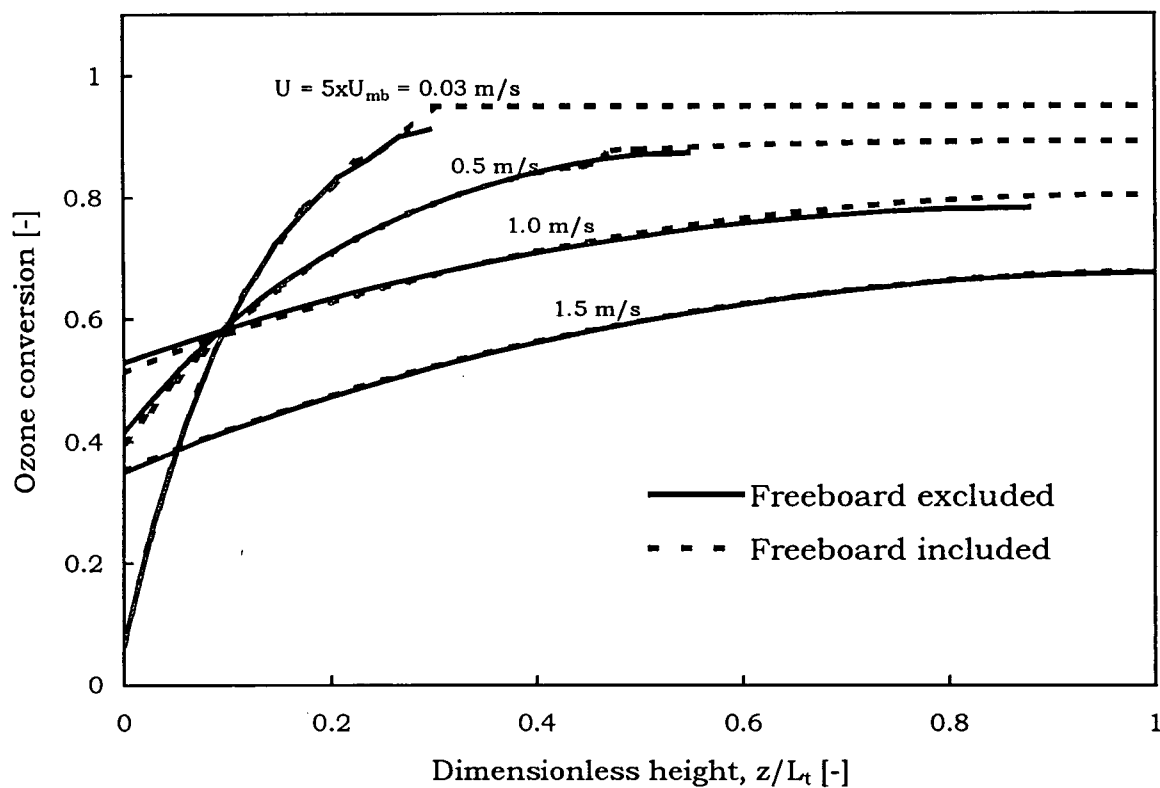
Figure 4.6. Predicted axial ozone conversions for the cases when freeboard is included and excluded in the GFBR model at different superficial gas velocities. (k_r = 8.95 s^{-1})
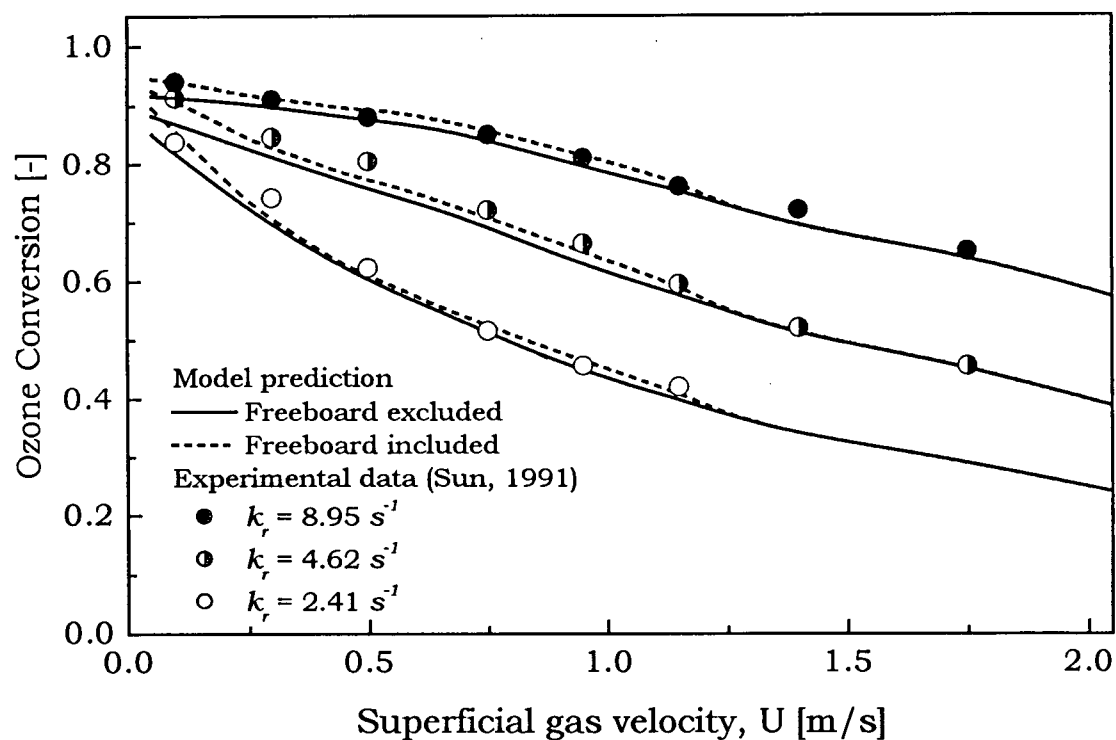
Figure 4.7. Comparison of predicted ozone conversions with experimental data for different catalyst activities for cases when freeboard is included and excluded in the GFBR model.

provides a mechanism for good temperature control (because of intense solids mixing and circulation), while the freeboard can be subjected to large temperature variations, and further reactions there can profoundly change the final species compositions, especially for complex reactions where selectivity is important.

(b) Comparison of Predictions from Regime-Specific and Probabilistic Models

As explained in section 2.3.1 above, there are two broad approaches to managing multiple models: the regime-specific and probabilistic models. Here, we examine the performance of the two approaches in relation to the experimental data of Sun (1991).

Figure 4.8 compares predictions from the individual regime-specific models – generalized two-phase bubbling bed at low U, dispersed flow at intermediate U and generalized core-annulus at high U - switched discretely at the regime boundaries U_c and U_{se} vs. experimental ozone decomposition data of Sun (1991). Sharp transitions at the U_c and U_{se} boundaries result in predicted discontinuities in conversion when the three separate regime-specific models are employed. Such discontinuities are not observed experimentally. Note that a salient feature of the GFBR model is that it reduces to the fully two-phase bubbling bed model, dispersed flow model or the core-annulus model by setting the respective regime probabilities to 1. This is possible because the system is represented by a single global mass balance for both the low- and high-density phases and a set of hydrodynamic bed and phase balances. Thus, all the balances are fully satisfied at all times. On the other hand, the *GFBR* model correctly predicts a smooth transition in the conversion (as well as other variables), while also giving improved agreement with the experimental data as shown in Figure 4.9. The advantage of the *GFBR* model compared with separate regime-specific models is clearly demonstrated in Fig. 4.10.

4.3 Conclusions

The new generic fluid bed reactor model, which interpolates between three regime-specific models by probabilistic averaging of hydrodynamic and dispersion variables based on the uncertainty in the flow regime transitions is compared with experimental data of Sun (1991). Predictions of hydrodynamic variables across the fluidization flow
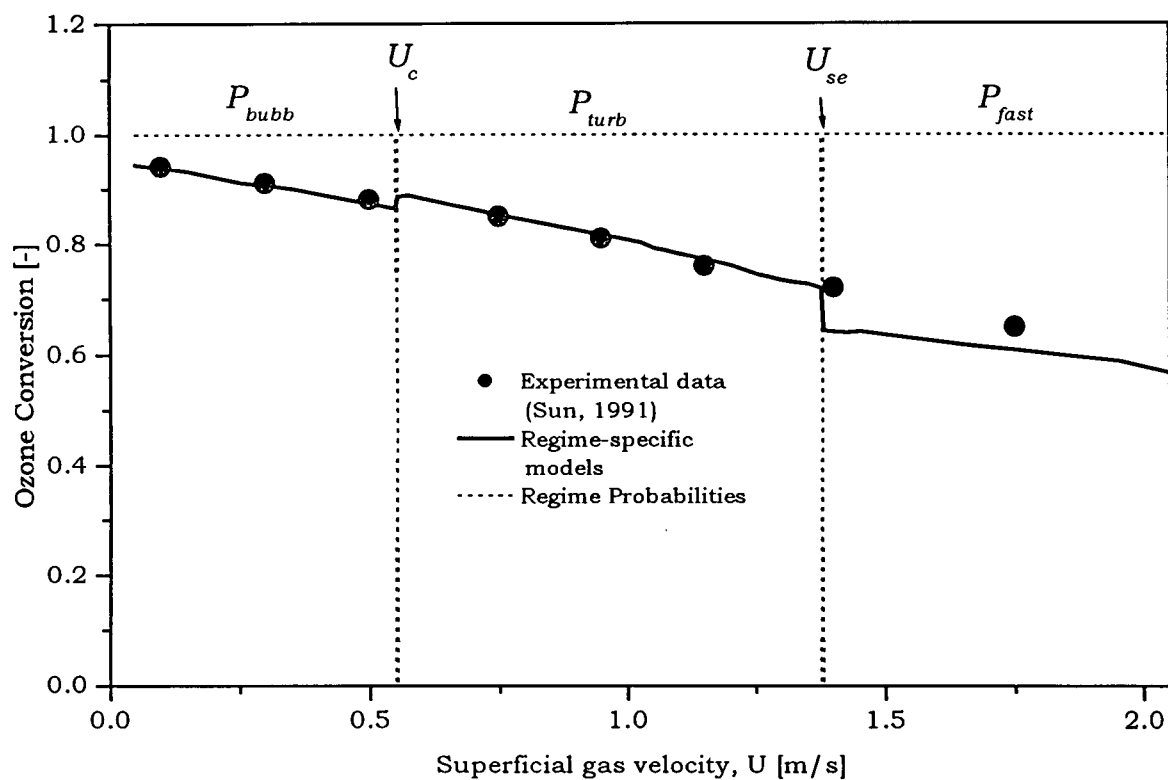
Figure 4.8. Comparison of predicted conversion trends from individual regime-specific models which switch sharply at regime boundaries with experimental data for $k_r = 8.95$ s⁻¹. Other conditions are given in Table 4.1.
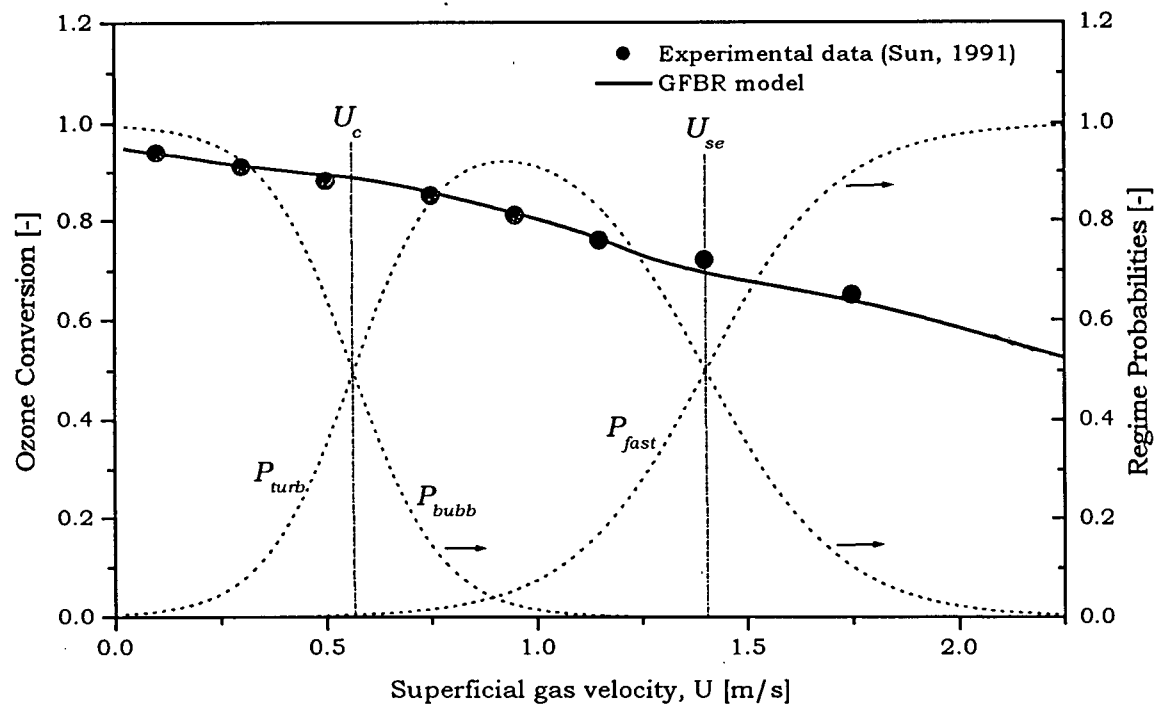
Figure 4.9 Comparison of predicted conversions (solid line) using GFBR model
with experimental results (points) for k_r = 8.95 s^{-1}. Other conditions are
given in Table 4.1.Regime probabilities (dots) are also indicated.
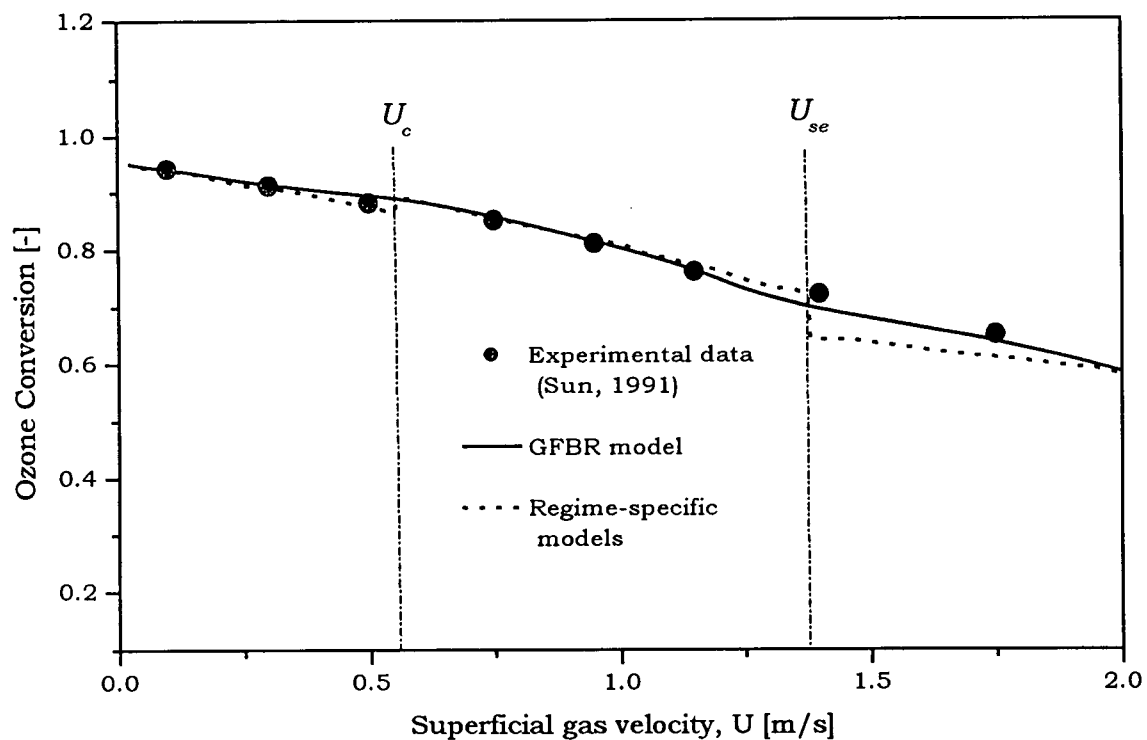
Figure 4.10 Predicted and experimental conversion trends: i) individual regime-specific models which switch sharply at regime boundaries; ii) GFBR model. $k_r = 8.95$ s^{-1}. Other conditions are given in Table 4.1.

regimes most commonly encountered in industrial scale fluid bed reactors - bubbling, turbulent and fast fluidization - are realistic, while conversion predictions are in good agreement with available experimental data. This approach leads to improved predictions of reactor performance compared with any of the three separate models for individual flow regimes, while avoiding discontinuities at the boundaries between the flow regimes. The contribution of the freeboard is shown to be important for reactors operated well beyond U_{mb} and for tall columns where the freeboard height represents a significant fraction of total column height. Although the preliminary results are encouraging, more validation with more complex reactions, significant energy effects and industrial-scale equipment is needed to consolidate this approach. This is the subject of Chapters 5 and 6.

Chapter 5

Application of GFBR Model to Industrial-Scale Processes

In this Chapter, the performance of the GFBR model is examined using two industrial-scale catalytic processes (oxy-chlorination of ethylene and oxidation of naphthalene to phthalic anhydride) and an industrial non-catalytic process (roasting of zinc sulfide). In addition to their scale of operation, the two catalytic processes are chosen because: (a) Plant measurements are available, accompanied by sufficient details of reactor configuration and operating conditions, providing an opportunity for validating the model with industrial-scale data, and for testing the model's ability to aid in "simulation experimentation" over a wide range of operating conditions. (b) The two catalytic processes are complex so that selectivity[1] can be used as a reactor performance indicator. (c) The reactors operate around the U_c boundary (phthalic anhydride: $P_{bubb} \cong P_{turb} \cong 50\ \%$; oxy-chlorination: $P_{bubb} \cong 20\%$, $P_{turb} \cong 80\ \%$), making it possible to assess the performance of the GFBR model, as well as the limiting cases of dispersed plug flow and the two-phase bubbling bed model.

Section 5.3 extends the GFBR model to gas solid reactions. A single particle model is coupled with the fluid bed reactor model to create a combined model, with the zinc sulfide roasting process addressed as a case study.

5.1 Phthalic Anhydride Process

Phthalic anhydride (PA) is an important organic chemical used mainly in the preparation of diesters, which are widely applied as plasticizers for polyvinyl chloride. It is also used in the preparation of alkyd and polyester resins and dyes. Until the late 1950's, manufacture of PA was based on the oxidation of naphthalene over vanadium oxide catalysts. The increasing demand for PA led to a search for alternative raw materials. At present, PA is made primarily by gas-phase oxidation of ortho-xylene, available in large

---

[1] Selectivity is defined as the ratio of moles of product formed to that of reactant consumed. (When plotted against height, the moles correspond to the values at that level.)

quantities from refineries, over fixed catalysts containing vanadium and titanium oxides. The technical difficulty associated with the development of long-life, attrition-resistant catalysts (Bolthrunis, 1989) has not allowed the development of fluidized bed process for the oxidation of o-xylene to PA. Dias et al. (1997) reviewed the catalysts, kinetics and modeling of both the o-xylene and naphthalene phthalic anhydride processes for fixed and fluidized beds.

Johnsson et al. (1987) published a detailed study on the naphthalene-based phthalic anhydride process. They compared data from an industrial reactor of 2.1 m diameter with a number of bubbling bed mechanistic models [Grace (1984) model, Kunii and Levenspiel (1969) model, Kato and Wen (1969) model and, Partridge and Rowe (1966) model]. The first three models all gave good overall prediction of the very limited data on reactor performance, provided that the bubble size and the fraction of solids in bubbles are estimated with reasonable accuracy. However, because the plant operates around the bubbling-turbulent regime boundary ($U \sim 0.4$ - 0.5 m/s, while $U_c = 0.436$ m/s, estimated from the correlation in Table 2.2), the use of the simple two-phase or three-phase models is only an approximation at best. No general conclusions can be drawn on the performance of the models, as their applicability to turbulent processes is questionable. The sensitivity analysis done by Johnsson et al. (1987) showed that, in general, the models performed better when the bubble size was decreased and more solids were allocated to the bubbles – effectively approximating more homogeneous behavior as in turbulent flow regime. This led Bolthrunis (1989) to suggest the dispersed plug flow model rather than the bubbling bed models, to capture the shift away from the bubbling behaviour. It is clear from the foregoing discussions that the PA process is an ideal "candidate process" to test the performance of the GFBR model.

Here, we use plant data from an industrial-scale naphthalene-based fluidized bed reactor, accompanied by sufficient information (Johnsson, 1986; Johnsson et al., 1987) to assess the performance of the GFBR model. Predictions from the limiting cases of the model at low U, i.e. the generalized two-phase bubbling bed model (2PBBM), and at intermediate U, i.e. the dispersed plug flow model (DPFM), are also compared with the GFBR model (GFBRM) and plant data. Sensitivity analysis is also carried out to assess

the influence of the freeboard region, interphase mass transfer, gas dispersion, reaction rate constants and gas flow.

5.1.1 Model Parameters and Reaction Kinetics

A summary of the bed hydrodynamics and operating conditions is given in Table 5.1. All other hydrodynamic properties needed in the models not included in the table are evaluated within the program using the correlations in Appendix A.

The oxidation of naphthalene is complex and involves several byproducts and intermediates. In addition to PA, naphthaquinone (NQ), maleic anhydride and carbon oxides, here lumped together as oxidation products (OP), have been detected as reaction products (Wainwright and Foster, 1979). Several reaction networks consisting of a combination of parallel and consecutive steps have been applied to the reaction. Johnsson et al. (1987) evaluated several kinetic schemes including those proposed by De Maria et al. (1961) and Westerman (1980) and concluded that the De Maria et al. kinetics better capture the conditions in the actual industrial reactor in general. The reaction scheme proposed by De Maria et al. is represented in Fig. 5.1. Johnsonn (1986) gives a detailed discussion of the uncertainties of these kinetics. A pseudo first order form of the rate law and a summary of the reaction rate constants for all of the separate reactions are given in Table 5.2
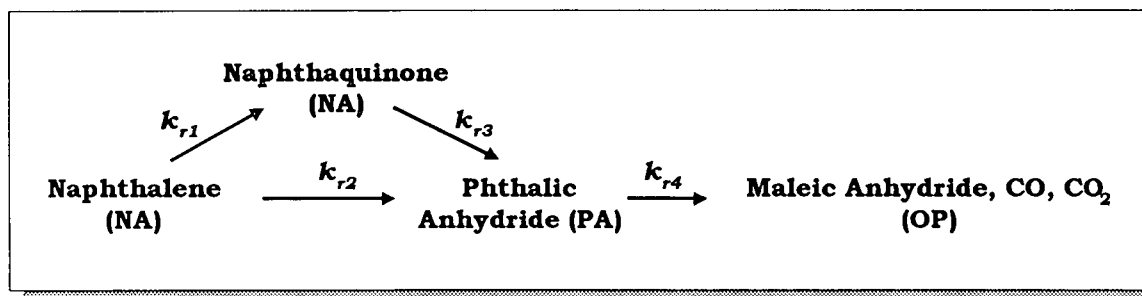
Figure 5.1. Reaction pathway for naphthalene oxidation to phthalic anhydride proposed by De Maria et al. (1961).

Table 5.1 Operating conditions and hydrodynamic properties for the phthalic anhydride process

Parameter	Value
Temperature, T	636 K
Pressure, P	2.66×10^5 Pa
Expanded bed height, L_d	7.9 m
Expanded bed density, ρ	350 kg/m^3
Superficial gas velocity, U	0.43 m/s
Mean particle diameter, $\bar{d}_p$	53 µm
Catalyst bulk density, ρ_{bulk}	770 kg/m^3
Catalyst density, ρ_p	1200 kg/m^3
Total inlet gas flowrate, F_{To}	254.7 kmol/hr
Inlet flowrate of naphthalene, $F_{NA,o}$	5.21 kmol/hr
Bed voidage at minimum fluidization, ε_{mf}	0.36 [-]
Inside diameter of reactor, D_t	2.13 m
Total reactor height, L_t	13.7 m

Table 5.2. Reaction kinetics for the naphthalene-based phthalic anhydride process

Reaction	Assumed True Kinetics	Assumed Pseudo First Order Rate Constants
$NA \rightarrow NQ$	$r_1 = k'_{r1} C_{NA} C_{O_2}$	$k_{r1} = k'_{r1} C_{O_2} = 1.8\ s^{-1}$
$NA \rightarrow PA$	$r_2 = k'_{r2} C_{NA} C_{O_2}$	$k_{r2} = k'_{r2} C_{O_2} = 1.8\ s^{-1}$
$NQ \rightarrow PA$	$r_3 = k'_{r3} C_{NQ}$	$k_{r3} = k'_{r3} = 4.6\ s^{-1}$
$PA \rightarrow OP$	$r_4 = k'_{r4} C_{PA} C_{O_2}$	$k_{r4} = k'_{r4} C_{O_2}^{0.8} = 0.023\ s^{-1}$

5.1.2 Simulation and Comparison with Plant Data

The following assumptions are adopted for the present simulation: (i) Molar flow rates of gas entering and leaving the reactor are very nearly equal (Johnsson et al., 1987). Hence volume changes due to reaction are neglected. (ii) Temperature variations along the bed are neglected. The system is modeled as an isothermal process because of insufficient information regarding cooling of the reactor. In addition, excellent temperature uniformity was observed within the dense region in the industrial unit and no significant temperature rise was observed in the freeboard (Johnsson et al., 1987, Bolthrunis, 1989). Moreover, no information is given regarding the temperature dependence of the rate constants in Table 5.2.

Figure 5.2 shows the GFBR model predictions of axial concentration (computed from eq. 2.3) profiles of naphthalene (NA), phthalic anhydride (PA), naphthaquinone (NQ) and oxidation products (OP). Both PA and NQ concentrations are predicted to pass through maxima at different heights, while that of NQ is predicted to approach zero at the bed surface.

Figure 5.3 compares predictions from the GFBR model (GFBRM) with those from the generalized two-phase bubbling bed model (2PBBM) and the dispersed plug flow model (DPFM). It is seen that all three models predict almost identical exit conversions of NA and PA selectivity. While the predicted exit values of the NA conversion and the PA yield[2] from all models closely match the plant data (Table 5.3), possibly because the exit NA conversion is nearly complete (100%), predictions of the NQ and OP yields are unsatisfactory. The poor prediction of the OP yield and particularly that of NQ may be due to uncertainties regarding key model parameters such as bubble size, gas dispersion coefficients, reaction rate constants etc. None of these parameters was adjusted to fit the plant data so that we examine below the impacts of each of these parameters as well as the freeboard region on the reactor performance.

---

[2] Yield is defined as the ratio of moles of product formed to that of reactant fed.
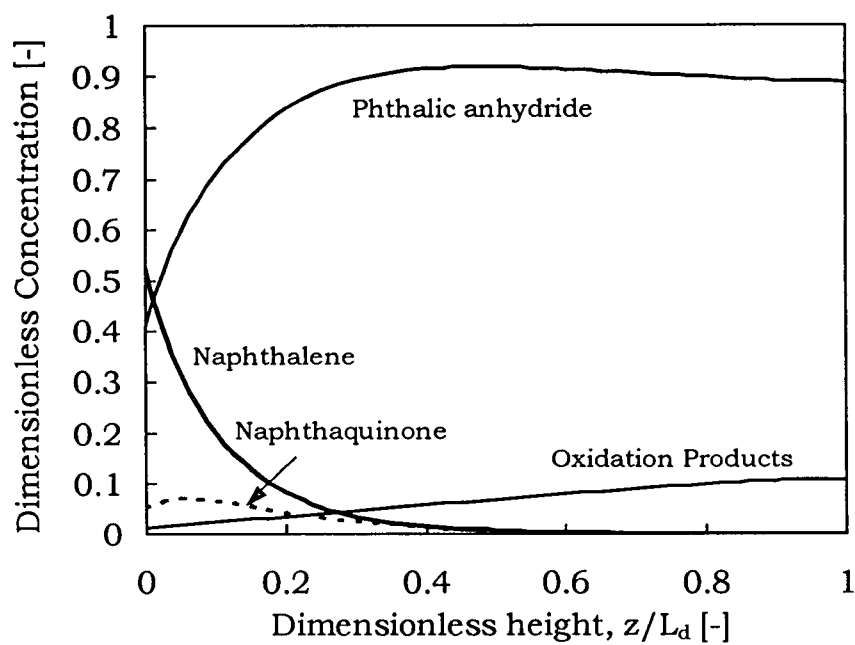
Figure 5.2 Axial concentration profiles of naphthalene (NA), naphthaquinone (NQ), phthalic anhydride (PA) and oxidation products (OP) predicted by the GFBR model. Conditions are given in Tables 5.1 and 5.2.
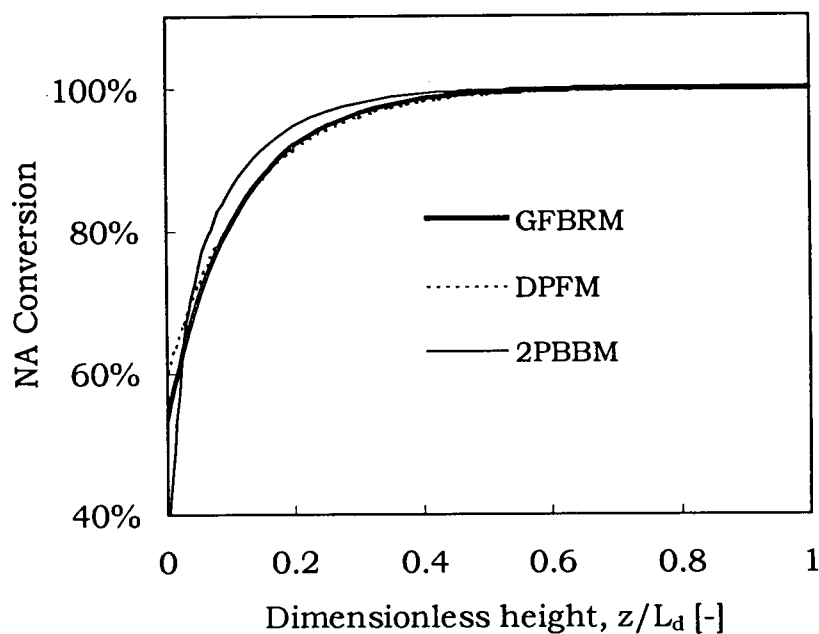
(a)
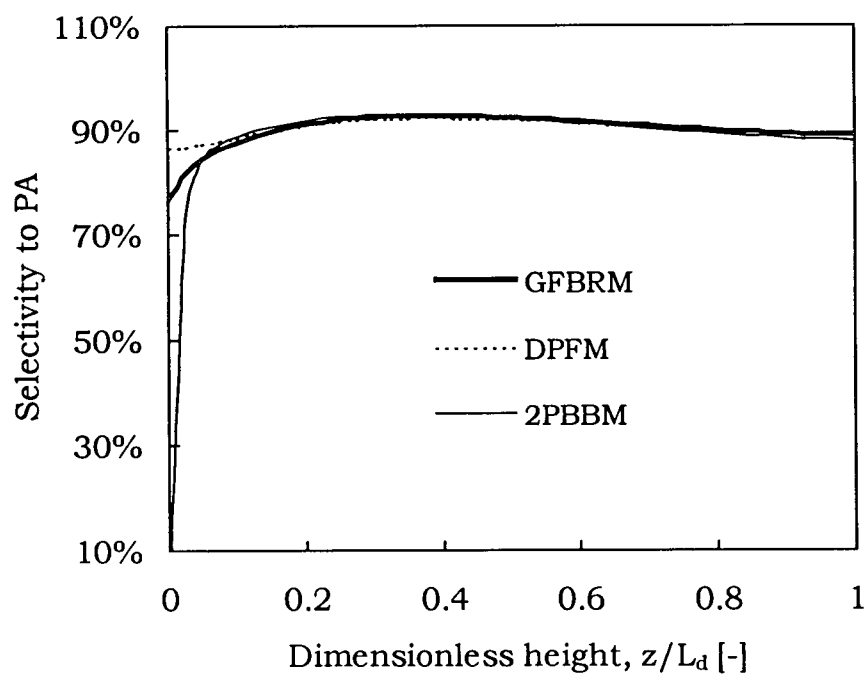
(a)

Figure 5.3 Predictions of axial profiles of (a) NA conversion and (b) selectivity to PA from the three models: GFBRM, 2PBBM and DPFM for conditions given in Tables 5.1 and 5.2.

Table 5.3 Comparison of model exit predictions with plant data

Model	NA Conversion (%)	PA Yield (%)	NQ yield (%)	OP Yield (%)
GFBRM	99.99	88.96	0.02	11.01
DPFM	99.97	89.23	0.04	10.70
2PBBM	99.99	88.01	0.00	11.99
Plant data	**~100 (> 98)**	**88.90**	**1.31**	**~9.8**

5.1.3 Sensitivity Analysis

5.1.3.1 Influence of Freeboard

The performance of the GFBR model with the freeboard included (case1) is compared with case 2 where the freeboard is ignored in order to assess the impact of the freeboard on the reactor performance. The expanded bed heights for both cases are computed in the manner described in Chapter 4. The predicted dense bed heights with increasing gas velocity for both cases are shown in Fig. 5.4.

Figure 5.5 shows predicted axial profiles of NA and PA concentrations at different gas velocities for the two cases. The predictions for the two cases are nearly identical at all gas velocities, mostly because of the rapid and nearly complete conversion of NA before the bed surface is reached. Even at U approaching 1 m/s, NA nearly attains complete conversion before reaching the bed surface. Temperature in the freeboard is assumed to be the same as in the dense bed so that the freeboard reactions are not subjected to temperature variations. The observed increase in predicted PA yield with increasing gas velocity is expected, as the decrease in gas residence time allows less oxidation of PA to oxidation products. It is seen for both cases that because of the rapid conversion of NA at low U, the increased gas residence time leads to further oxidation of PA, with predicted small concentrations of NQ at the exit. The predictions at high U for both cases are dependent on the average solids flux, G_{so}, to which a value of 120 kg/m^{2}s was arbitrarily assigned in this simulation, as in Chapter 4, since the goal of the simulation at high U is to capture the trend, rather than match plant data.
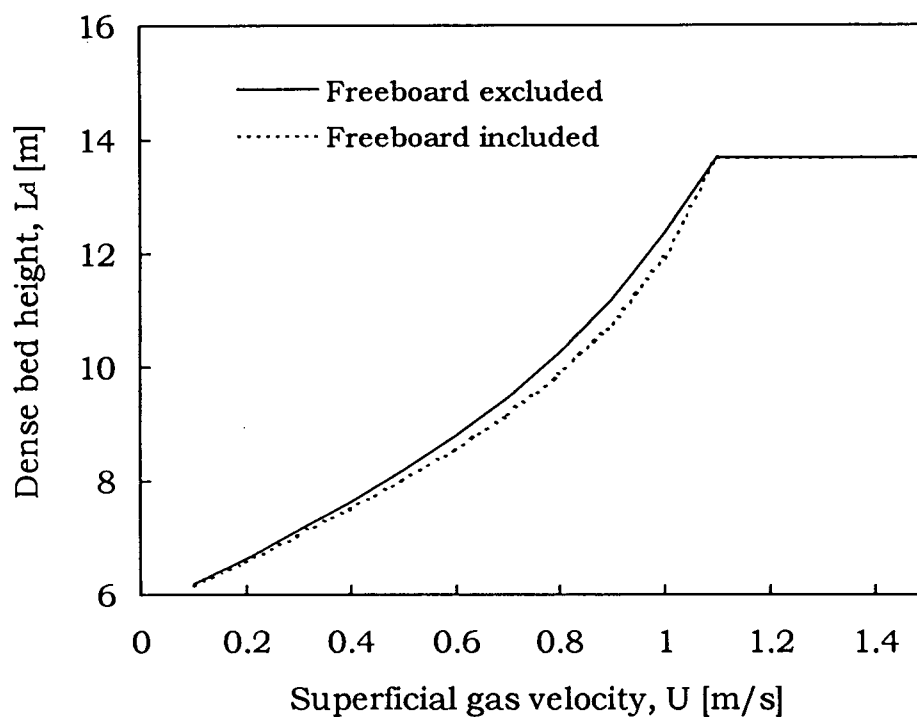
Figure 5.4. Comparison of computed expanded bed heights for cases when freeboard is included and excluded in the GFBR model. [Operating velocity, $U = 0.43$ m/s; Total reactor height, $L_t = 13.7$ m.]
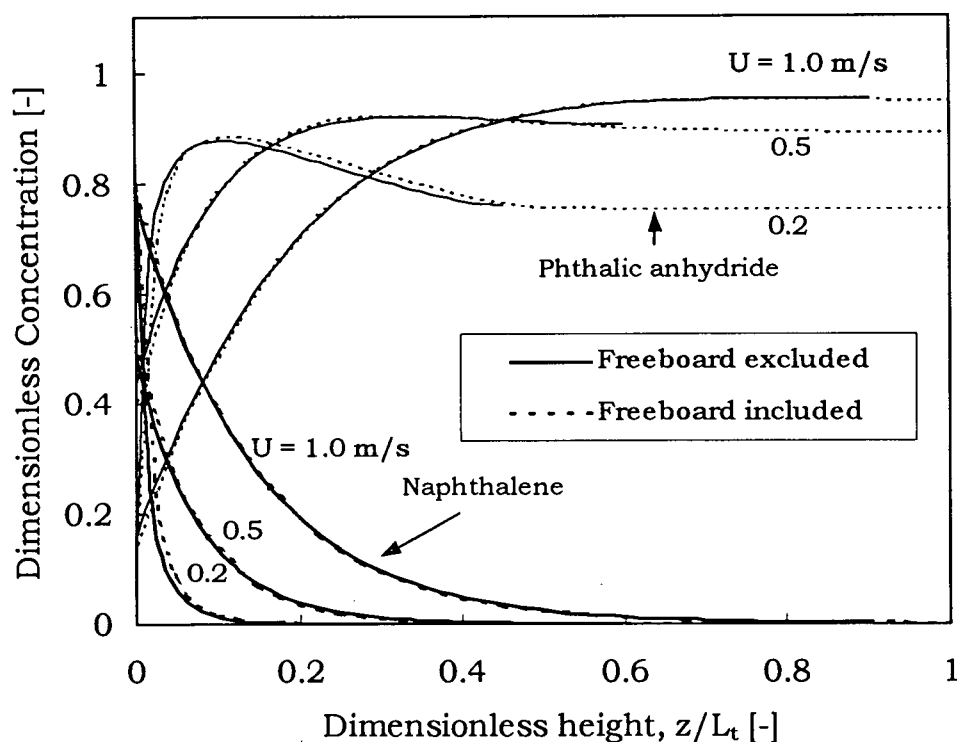
Figure 5.5. Predicted axial profiles of naphthalene and phthalic anhydride concentrations for cases when freeboard is included in the GFBR model and when it is ignored at different superficial gas velocities. Conditions are given in Tables 5.1 and 5.2.

Exit predictions from the GFBR model with and without the freeboard are compared with plant data in Table 5.4. Predictions from the two cases are nearly identical, with that for case 2 showing a slightly better agreement with the plant data for the PA yield. Overall, for the conditions simulated here, the freeboard does not have a significant influence on the model predictions. Note, however, that because the freeboard could be subjected to large temperature variations, further reactions there at elevated temperatures could profoundly change the final product compositions. Given the above observations, all subsequent simulation results are based on the dense bed region so that the axial profiles and in particular, the positions of occurrence of the maximum PA yield can be emphasized without being obscured by the freeboard.

Table 5.4 Comparison with plant data of exit predictions from GFBR model for cases when the freeboard is included and excluded.

	Without freeboard (%)	With freeboard (%)	Plant data (%)
NA Conversion	99.99	100	~100(>98)
NQ Yield	0.02	0.00	1.31
PA Yield	88.96	88.62	88.90
OP Yield	11.01	11.38	~9.80

5.1.3.2 Effect of Interphase Mass Transfer

Figure 5.6 shows predicted PA axial concentration profiles for different values of the dimensionless interphase mass transfer group, X [$=k_{LH}a_I\psi_L L_d /U$]. As expected, for the GFBR model, the effect of the interphase mass transfer on the predicted yield (Fig. 5.6a) is not high since the resistances due to the gas dispersion and interphase mass transfer are of similar importance at the prevailing operating conditions. The influence is clearly much greater for the 2PBBM (Fig. 5.6b). Figure 5.7 compares the effect of interphase mass transfer on the exit predictions of PA yield from the GFBRM,
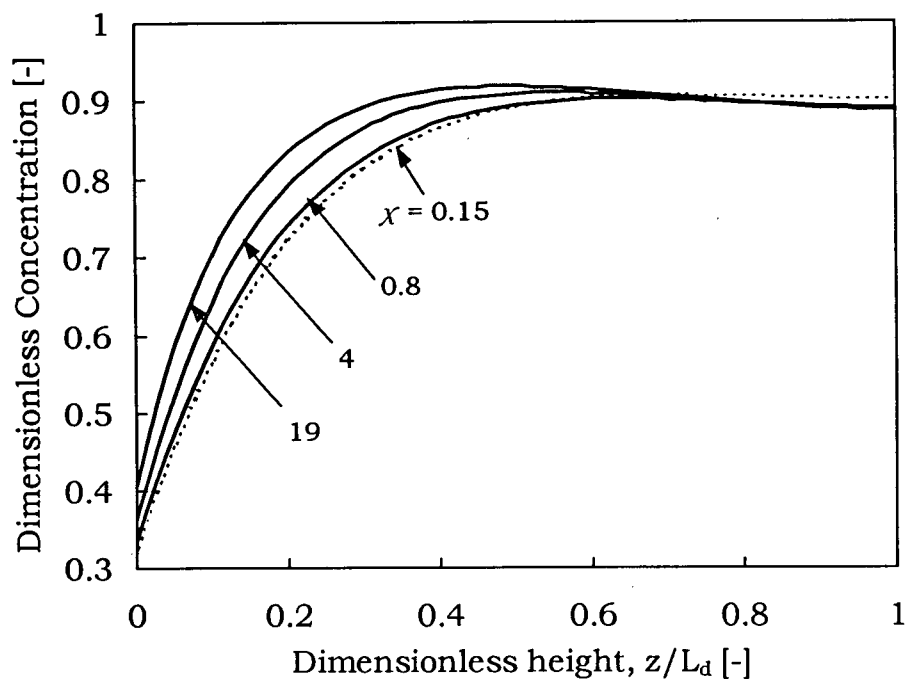
(a)
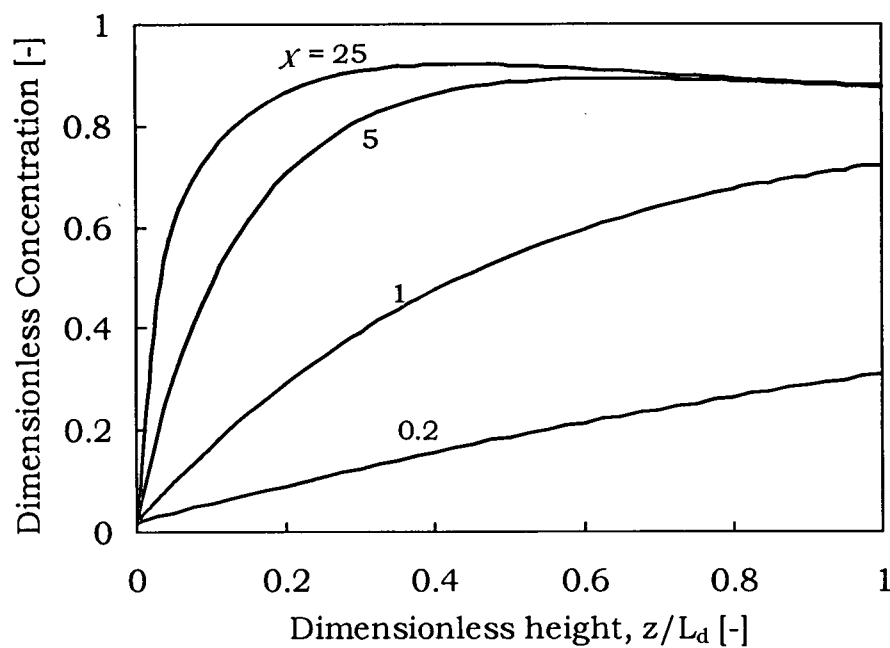
(b)

Figure 5.6. Axial profiles of PA concentrations predicted by (a) GFBR model (b) 2PBBM at different values of the dimensionless interphase mass transfer coefficient for conditions given in Tables 5.1 and 5.2.
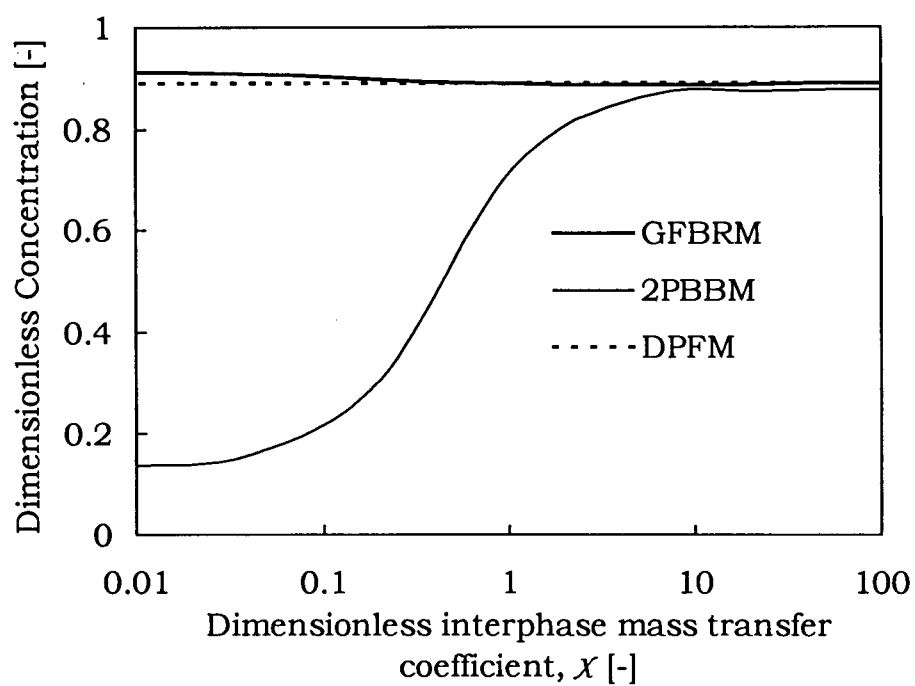
Figure 5.7. Predictions of exit PA concentrations from the GFBRM, 2PBBM and DPFM as function of dimensionless interphase mass transfer coefficient for the conditions given in Tables 5.1 and 5.2.

and the DPFM. As expected, a decrease in the interphase mass transfer between the two phases leads to poor prediction of reactor performance by the 2PBBM, while predictions by the DPFM, being a single phase model is completely insensitive to interphase mass transfer. Results from the GFBR model show only a slight sensitivity to variations in the interphase mass transfer.

An interesting trend is seen in Fig. 5.7 in which the GFBR model predicts higher PA yield than the DPFM as X approaches zero. At very low X, gas exchange between the L- and the H-phases is virtually eliminated, so that the GFBR model essentially reduces to two "dispersed plug flow models" for the two phases in parallel. The predicted bed average concentration is then the average of the individual phase concentrations, weighted by the fractional gas flow through each phase. Because the gas dispersion in the L-phase is less than in the H-phase and because the gas flow through the L-phase is higher than through the H-phase, it is possible to predict NA conversions greater than would be obtained from the DPFM. As X tends to infinity, however, the GFBR model reduces to a single-phase dispersed plug flow model, with identical concentrations predicted in both phases. Therefore, as expected, at high X, predictions of PA yield from all three models are nearly identical.

5.1.3.3 Effect of Gas Dispersion

A decrease in axial dispersion of gas (i.e. an increase in Pe_z) results in an increase in the predicted PA yield, with the influence diminishing beyond a Pe_z $[=UL_d / \mathcal{D}_{zg}]$ of about 4 as shown in Fig. 5.8. The consequence of increasing the gas dispersion coefficient is a reduction in NA conversion in both the low- and high-density phases resulting in decreased yield of the intermediate products. Predictions from the limiting cases of single phase perfectly mixed reactor (CSTR) and plug flow reactor (PFR), shown in the Figure, are obtained from the GFBR model by first letting the interphase mass transfer go to infinity, and then letting the Pe_z go either to infinity (PFR) or zero (CSTR). It is seen that at very low Pe_z, the GFBR model predicts lower product yield than the CSTR model because of interphase mass transfer limitations.
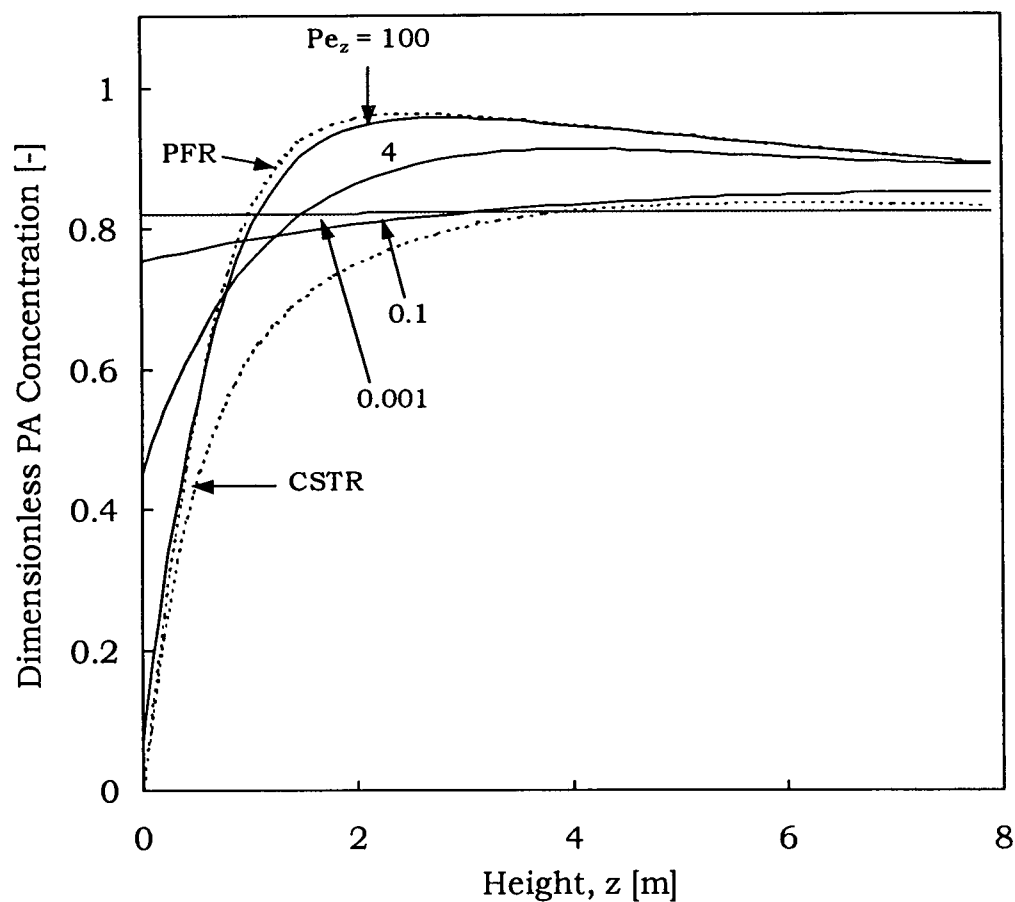
Figure 5.8. Axial profiles of PA concentration predicted by the GFBR model at different values of the axial Peclet number for conditions given in Tables 5.1 and 5.2.

5.1.3.4 Influence of Reaction Rate Constants

To illustrate the effect of the reaction rate constants on the model predictions, the base case values (Table 5.2) were varied over reasonable ranges as listed in Table 5.5. One rate constant was varied for each simulation, while the others retained their base case values. Figures 5.9 to 5.11 show the effect of the rate constants on the reactor performance. As seen from Fig. 5.9, although the exit NA conversion remain unchanged over the range of k_{r1} and k_{r2} varied, the height at which the maximum for the selectivity to PA occurs is seen to decrease with increasing k_{r1} and k_{r2} because of the more rapid conversion of NA to the intermediate products at higher values of the rate constants. Similar trends can be observed for the variations in k_{r3} (Fig. 5.10) for the NA conversion. Decreasing k_{r3} from the base value is seen to result in a decrease of both PA and OP yields, while that of NQ is seen to increase (Fig. 5.10b). The impact of the kinetics was further assessed by arbitrarily varying the base case values of the rate constants (Table 5.2) by ± 20%. The results, summarized in Table 5.6, show a profound influence of the rate constants on the oxidation products and the PA yields. The observed trend is that decreases in the rate constants favour higher PA yield while decreasing both the NQ and OP yields. An increase in the rate constants results in more rapid conversion of NA thereby giving more opportunity for further conversion of PA to oxidation products. Given the sensitivity of the model predictions to the reaction kinetics, it is possible to predict significantly different results from the model depending on the kinetic scheme adopted.

Table 5.5. Reaction rate constants and the range of variation for the sensitivity analysis

Reaction Rate Constant	Base Case Value (s^{-1})	Range explored (s^{-1})
k_{r1}	1.8	0.18 - 10
k_{r2}	1.8	0.18 – 10
k_{r3}	4.6	0.25 - 20
k_{r4}	0.023	0.003 – 0.1
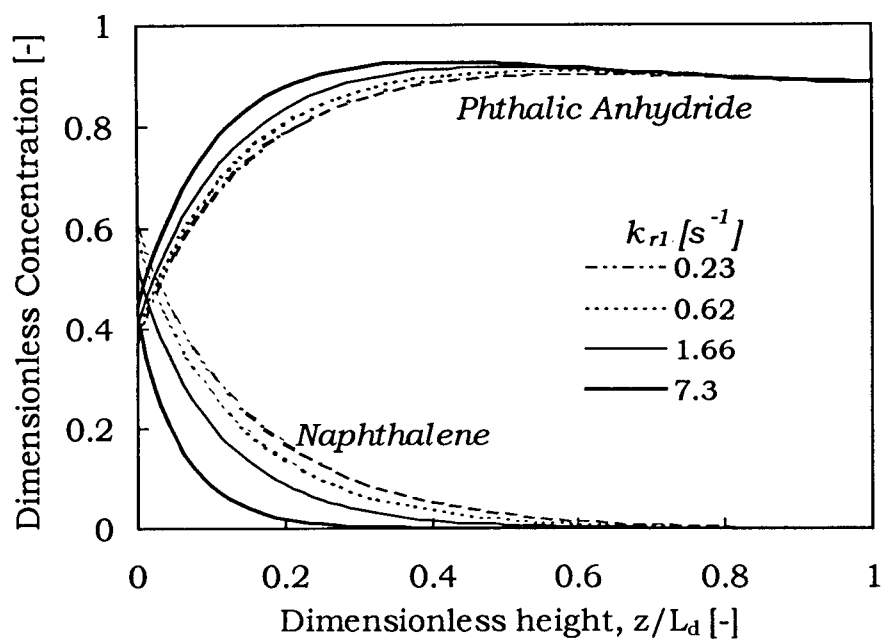
(a)
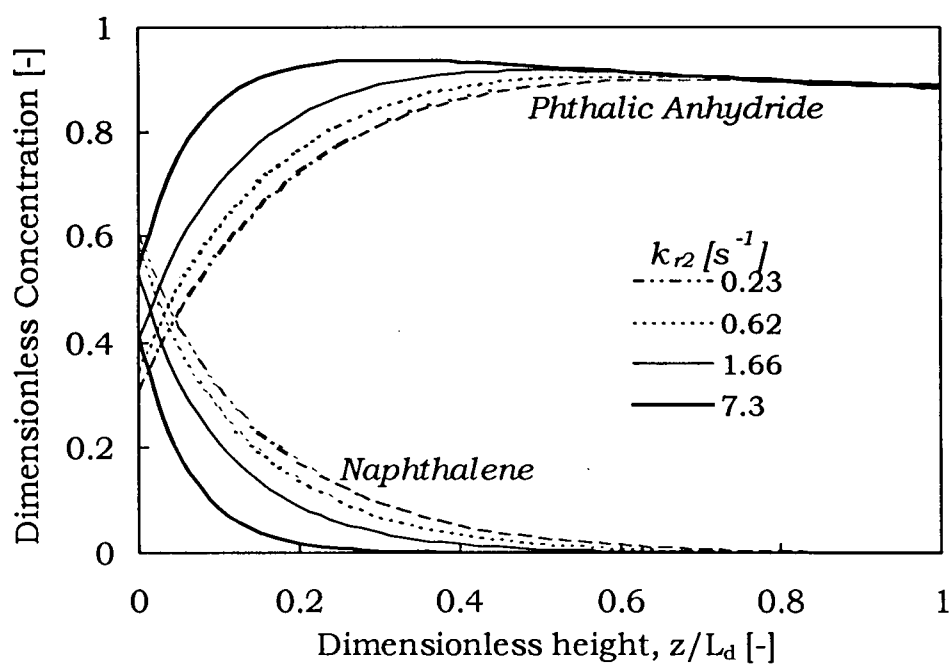
(b)

Figure 5.9. Axial profiles of PA and NA concentrations for different values of the reaction rate constants varied one at a time: (a) reaction 1, k_{r1}; (b) reaction 2, k_{r2}. Base case conditions are given in Tables 5.1 and 5.2.
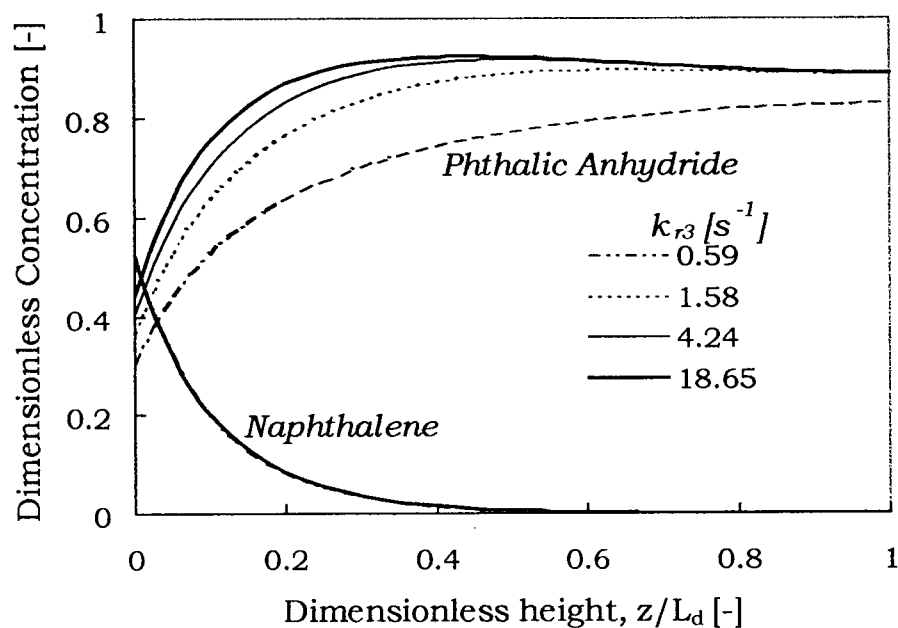
(a)
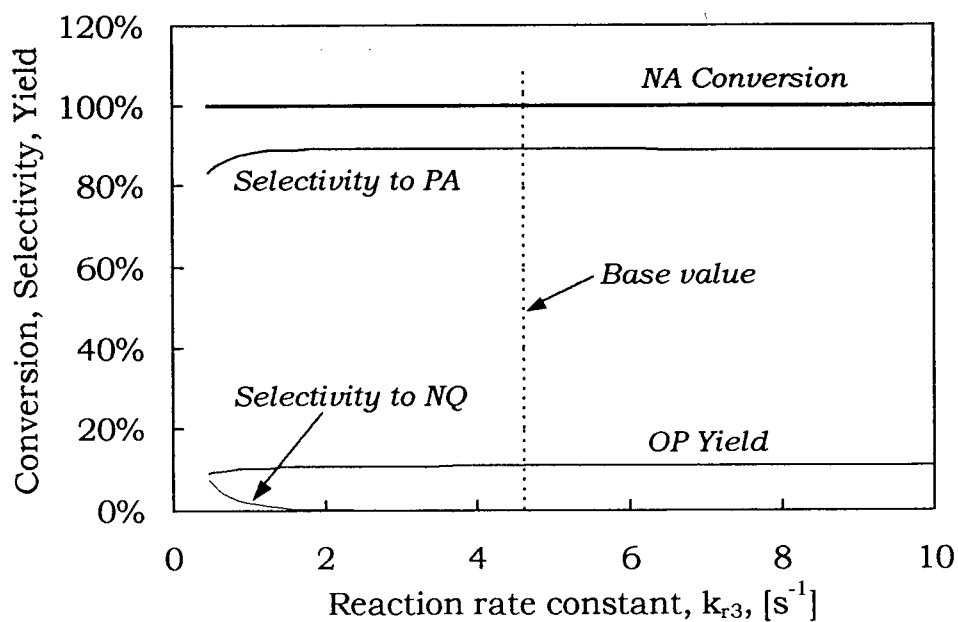
(b)

Figure 5.10. (a) Axial profiles of PA and NA concentrations at different values of the reaction rate constant, k_{r3}; (b) NA conversion, OP yield and selectivities to PA and NQ as a function of k_{r3}. Base case conditions are given in Tables 5.1 and 5.2.
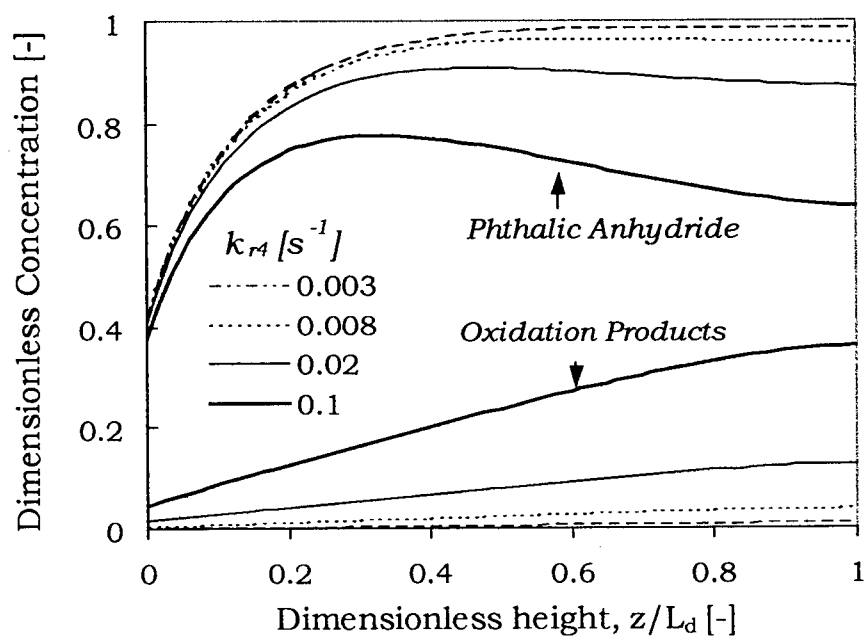
(a)
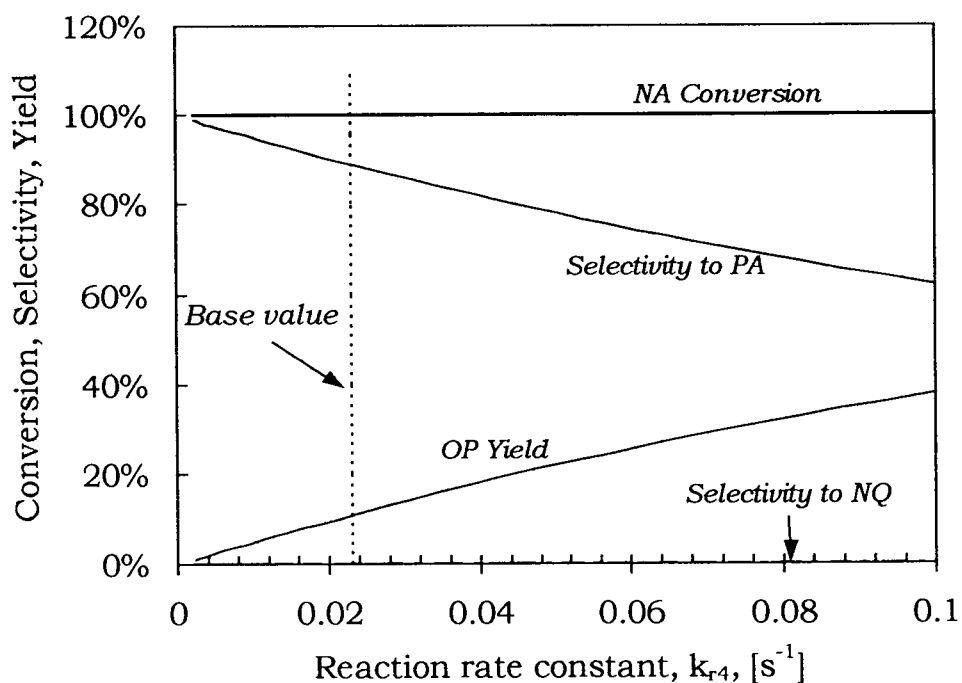
(b)

Figure 5.11. (a) Axial profiles of PA and NA concentrations at different values of the reaction rate constant, k_{r4}; (b) NA conversion, OP yield and selectivities to PA and NQ as a function of k_{r4}. Base case conditions are given in Tables 5.1 and 5.2.

Because of the uncertainties in the estimation of the individual reaction rate constants in the De Maria et al. (1961) kinetics, Johnsson et al. (1987) also explored an alternative kinetic scheme reported by Westerman (1980), and showed very different predictions of exit concentrations of all species, further highlighting the strong influence of the reaction kinetics on the performance of the models. It is clearly imperative to use accurate reaction kinetics to obtain reliable predictions from reactor models.

Table 5.6 Sensitivity of the GFBR model predictions to variations in kinetic rate constants. (Results shown are exit values.)

	Kinetic rate constants in Table 5.2			Plant data
	Decreased by 20%	Increased by 20%	Unchanged (Base case)	
NA Conversion (%)	99.96	100	99.99	~100(>98)
NQ Yield (%)	0.06	0.01	0.02	1.31
PA Yield (%)	91.19	86.92	88.96	88.90
OP Yield (%)	8.70	13.07	11.01	~9.80

5.1.3.5 Influence of Gas Flow

The influence of superficial gas velocity on the reactor performance is shown in Fig. 5.12. It is seen that increasing the gas velocity beyond the base case value has the desired effect of increased selectivity to PA and reduced OP yield, with the decreased conversion of NA. The industrial reactor is operated at lower superficial gas velocity than would maximize the predicted selectivity to PA without compromising NA conversion (Fig. 5.12). This may arise due to other design considerations and constraints such as the capacity of the solids return system, friability of the catalysts etc.
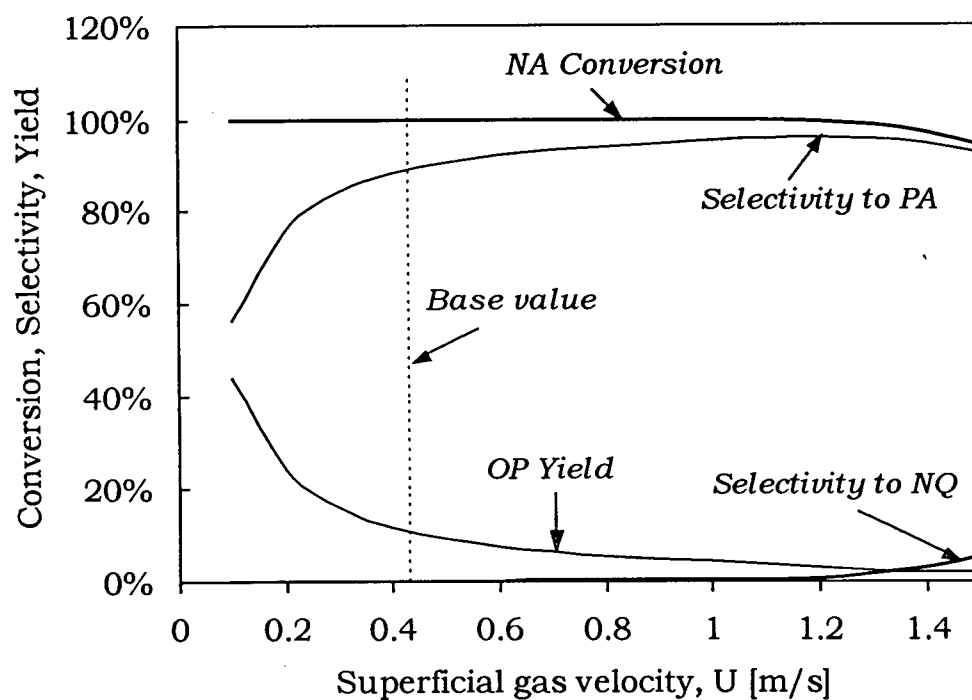
Figure 5.12. Predictions of NA conversion and selectivities to PA, NQ and OP
from the GFBR model as a function of superficial gas velocity for conditions
given in Tables 5.1 and 5.2.

5.1.4 Conclusions

The performance of the GFBR model is assessed using an industrial-scale phthalic anhydride process as a case study. The phthalic anhydride (PA) process operates near the bubbling-turbulent regime boundary, which makes it an ideal candidate to test the performance of the GFBR model. Predictions from the model for naphthalene (NA), PA and oxidation products (OP) are seen to be reasonable and compare favourably with the plant data within the constraints of the uncertainties in the estimation of the various parameters (hydrodynamic, kinetic, property estimation, etc.), while the agreement for the naphthaquinone (NQ) is poor. From the sensitivity analysis performed, it is shown that the predictions from the GFBR model are strongly influenced by the reaction kinetics, gas dispersion and superficial gas velocity, while the freeboard influence is relatively small for the range of conditions covered. The NQ yield is predicted to be ≈ 0 ($<<$ plant data) in all simulations, except when the reaction rate constant for the third reaction, kr_3, is varied, further emphasizing the strong influence of the reaction kinetics on the model performance. Clearly, accuracy of the model predictions depends strongly on utilizing reliable estimates of the model parameters. Use of the GFBR model to perform simulation experiments over a wide range of conditions is demonstrated.

5.2 Oxy-Chlorination Process

The oxy-chlorination (OC) process is part of the balanced process for the production of vinyl chloride used as a precursor for polyvinyl chloride and a wide variety of copolymers. Detailed description of the balanced process is outside our scope and is given elsewhere (Cowfer and Magistro, 1984).

In the OC process, ethylene reacts with hydrogen chloride and either air (air-based) or pure oxygen (oxygen-based) in a fixed or fluidized bed reactor over a cupric chloride catalyst to produce ethylene dichloride, together with oxidation by-products and traces of chlorinated impurities. Nearly all OC reactors built since 1990 are oxygen-based, and many existing air-based units are being re-designed for pure oxygen feed. As illustrated in Fig. 5.13, a key advantage of the oxygen-based process over the air-based operation is the drastic reduction in the volume of vent gas discharge, since N_2 is no longer present in the feedstream; a small fraction of the off-gas is, however, continuously purged to prevent accumulation of impurities. Moreover, in the O_2-based process, because any unconverted ethylene is compressed after purification, and recycled back to the reactor, ethylene is generally fed in large excess of the stoichiometric requirements. This makes it possible to operate the reactor at lower temperatures leading to improved product yields, since high ETY conversion is not a design requirement.

Here, we use industrial-scale data for the air-based oxy-chlorination process of Mitsubishi Chemical Corporation (MCC) of Japan to assess the performance of the GFBR model. For confidentiality reasons, all data specific to the MCC process such as conversions, yields, operating conditions, reactor geometry etc. are presented here in normalized form. For an idea of the magnitude of the results presented here, the following information should serve as useful guide: Typical conversions are 94 - 99% for ETY and 98 - 99.5 % for HCl, while EDC selectivities are in the range 94 – 97 %, with typical operating temperatures of 220 – 245 °C and reactor average pressures of 250 – 600 kPa (Cowfer & Magistro, 1984).

5.2.1 Model Parameters and Reaction Kinetics

A summary of the typical bed hydrodynamics, operating conditions and reactor geometry
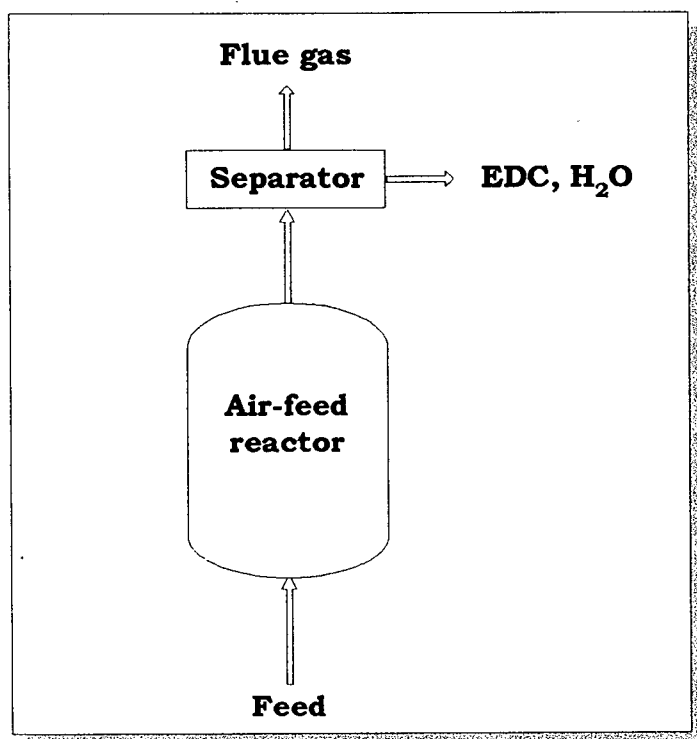
(a)
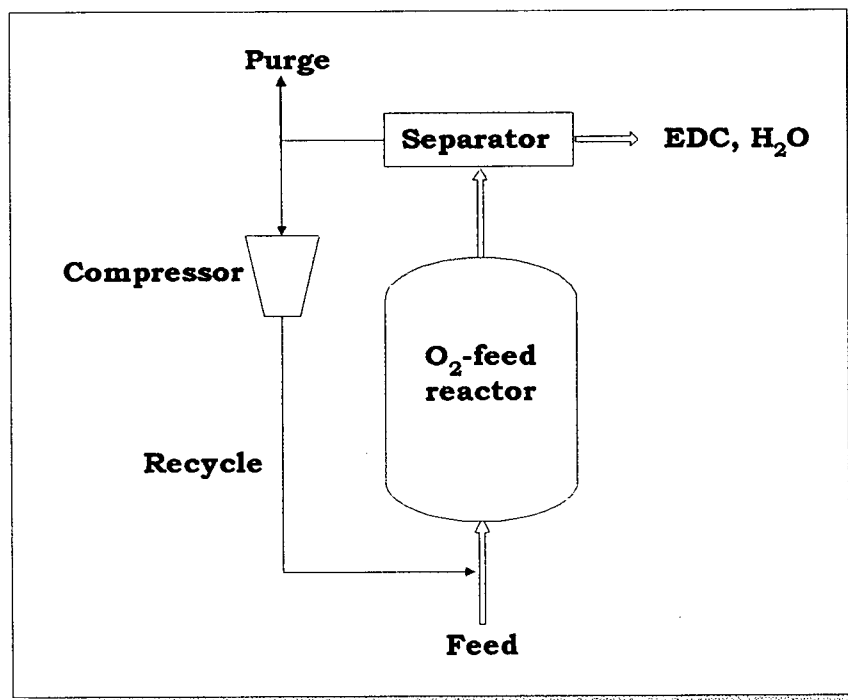
(b)

Figure 5.13. Schematics of the oxy-chlorination processes: (a) air-feed, (b) O_2-feed operation.

used for the simulation, corresponding to the *base case*, is given in Table 5.7. All other hydrodynamic properties not shown in Table 5.7 are evaluated within the *gPROMS* code using the correlations in Appendix A.

Table 5.7. Typical operating conditions, hydrodynamic properties and reactor geometry for the air-based oxy-chlorination process. (All quantities are shown in normalized form; ρ_g and μ are based on inlet temperature and pressure.)

Dimensionless Parameter	Value
Inlet temperature, T_o / T_{ave}	0.84
Expanded bed height, L_d / L_t	0.41
Gas flow, $\rho_g U_o \overline{d}_p / \mu$	3.2
Feed composition, y_{in}/y_{air} [HCl/ETY/AIR]	[0.63/0.33/1]
Particle size, $\rho_g(\rho_p - \rho_g)g\overline{d}_p^3 / \mu^2$	17
Expanded bed density, ρ / ρ_p	0.38
Reactor aspect ratio, L_t / D_t	7.1

The ethylene oxy-chlorination process involves complex reactions with non-linear temperature-dependent kinetics. The feed stream to the air-based OC reactor consists of oxygen/nitrogen, hydrogen chloride (HCl) and ethylene (ETY). The main product is ethylene dichloride (EDC). By-products include a few percent of carbon oxides (CO and CO_2, combined here as CO_x) and less than one percent chlorinated hydrocarbons excluding EDC (lumped together here as "impurities", IMP) (see Cowfer & Magistro, 1984). The reaction pathways considered are shown in Fig. 5.14 based on a simple lumped reaction scheme. The reaction rates are expressed in Langmuir-Hinshelwood form, while the reaction rate and the adsorption constants are considered to be of Arrhenius type. The detailed kinetic rate expressions, together with the values of the activation energies and pre-exponential constants, are based on extensive small-scale fluid bed studies and are proprietary (Ellis et al., 2000).
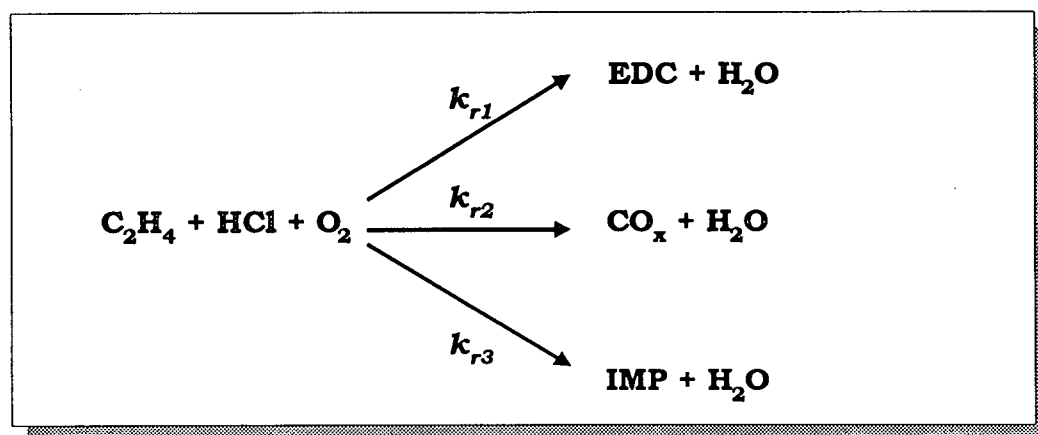
Figure 5.14. Reaction pathways for oxy-chlorination reactions.

5.2.2 Simulation and comparison with commercial data

The oxy-chlorination reaction is accompanied by a significant change in gas volume due to change in the number of moles, as well as temperature and pressure effects. Here, we crudely approximate the extent of gas volume reduction by making the restriction that the volume flow varies linearly with conversion of the main reactant, ETY, so that for a reactor of constant cross section (ignoring temperature and pressure effects)

$$U = U_o(1 + \gamma X_{ETY})$$

where X_{ETY} is the conversion of ETY and γ is the reduction factor, estimated here to be ~ 0.25 from the stoichiometry of the main reaction (ETY to EDC). Given that ETY attained almost complete conversion immediately above the distributor, we assign $X_{ETY} = 1$ so that $U = 0.25U_o$. The adjusted U, set as the base case superficial gas velocity, is used as a simplification throughout the simulations presented in this section. This form of estimating the extent of gas density change is only an approximation for the oxy-chlorination. Therefore, Chapter 6 addresses volume change due to reaction in a detailed and more rigorous manner, accounting for the change in the number of moles as well as the effects of temperature and pressure variations.

The model prediction of axial temperature profile in the bed based on conditions in Table 5.7 is shown in Fig. 5.15. It is in reasonable agreement with the averaged plant data in both the cooled and uncooled regions. The predicted temperature profile and the

magnitude of the temperature strongly depend on the effective thermal diffusivity, k_e, (see eq. 2.8) determined here using the analogy between solid and thermal dispersions (Matsen, 1985). The analogy and the pertinent correlations are presented in Appendix B. Note that heat losses to the surrounding are neglected, i.e. it is assumed that the system is well insulated.

Unless stated otherwise, conversions, selectivities and yields in this section and in Chapter 6 are normalized by dividing the model predictions at that level with the plant exit data corresponding to the base case conditions given in Table 5.7. Figure 5.16 shows the predicted conversions of ETY, HCl and O_2 for the base case. Rapid conversions of all reactants are observed, with the limiting reactant, HCl, reaching complete conversion almost immediately above the distributor. The axial profiles of the selectivities and yields of EDC, IMP and CO_x relative to the ETY converted at that level, are shown in Fig. 5.17. Predicted impurities are less than 1% relative to EDC and remain nearly flat throughout the bed. However, the observed decrease in EDC selectivity with height is due to the increased conversion of ETY leading to formation of more oxidation products. Overall, as expected, both EDC and CO_x yields increase along the bed with increasing ETY conversion.

Average values of plant data collected over several months for different bed temperatures, pressures and initial solid inventories (their values varied over ~10°C, 150 kPa and 2.8 kg/s respectively, from the base case values) for six cases, are compared with model predictions in Table 5.8 and Fig. 5.18. Average values rather than individual daily data were used to minimize the uncertainty, variation and errors associated with the plant data. Model predictions for the base case conditions are also shown. The agreement between model predictions and plant data is excellent for the ETY and HCl conversions. The predicted EDC yields are also close to the plant data. However, the model consistently underpredicts the IMP yield while usually overpredicting the CO_x yield.

There was uncertainty (Ellis et al., 2000) regarding the rate constant, k_{r2}, for the reaction leading to the formation of CO_x, which in this simulation was used as an adjustable parameter. An increase of k_{r2} by a factor of 10, which increased the CO_x yield by about an order of magnitude, may have contributed to the overprediction of CO_x yield by the model. When a smaller factor was used to multiply k_{r2}, however, conversions of

both ETY and O_2 dropped appreciably. Thus, the factor of 10 was taken as the optimal adjustment factor for k_{r2} and used throughout. The influence of k_{r2} on the model predictions is explored in more detail below. In general, the simulation results are in reasonable agreement with the plant data.

Table 5.8. Per pass exit model predictions for all cases including the base case (normalized by corresponding plant exit data).

Case*	Conversion (-)		Yield (-)			Selectivity (-)		
	ETY	HCl	EDC	CO_x	IMP	EDC	CO_x	IMP
1:↑T, ↑P, ↓I	1.002	1.002	0.999	1.124	0.859	1.015	1.142	0.873
2:↔T, ↓P,↓I	0.997	1.003	0.996	1.124	0.730	1.022	0.961	0.797
3: ↑T, ↓P,↓I	0.996	1.002	0.994	1.113	0.690	1.010	1.294	0.811
4:↔T, ↑P,↔I	1.004	1.003	1.000	1.191	0.841	1.019	1.011	0.874
5: ↑T, ↓P,↓I	0.998	1.002	0.986	1.388	0.820	1.006	1.416	0.836
6:↓T,↑P, ↔I	0.996	1.003	0.996	1.003	0.860	1.027	0.773	0.777
0 (Base case)	1.005	1.003	0.997	1.345	0.770	0.993	1.339	0.767

*Symbols denote variations in average temperature (T), pressure (P) and, solids inventory (I) from the base case values: ↔: Approximately unchanged; ↓ decreased; ↑ increased.

5.2.3 Sensitivity analysis

5.2.3.1 Influence of Freeboard

Normalized exit predictions from the GFBR model for the cases when the freeboard is included and when it is ignored are compared in Table 5.9. Overall, for the base case conditions, the freeboard does not exhibit a significant influence on the model predictions, except that its inclusion slightly favours further oxidation of ETY, mostly leading to formation of oxidation products. As for the PA process above, all further simulations are, therefore, based on the dense bed region.
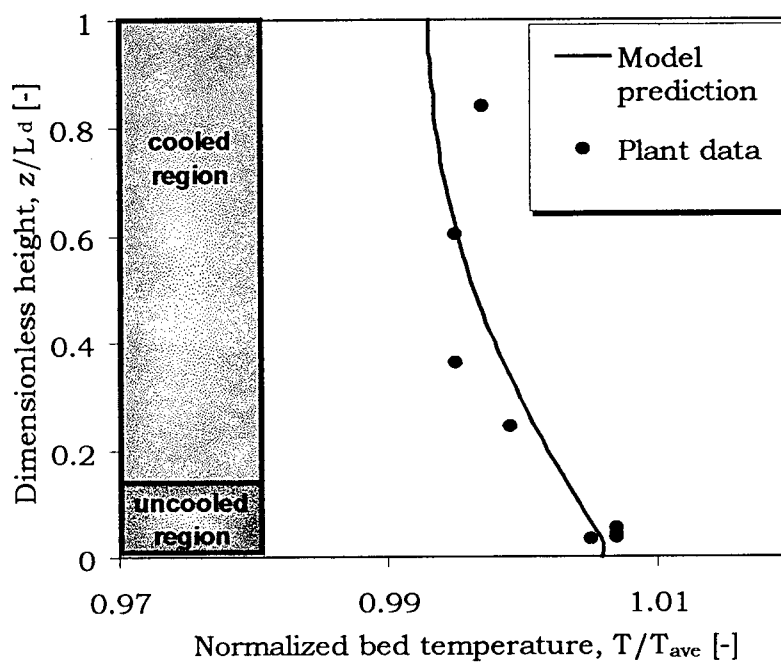
Figure 5.15. Axial bed temperature profile normalized by bed-average plant data, T_{ave}, based on conditions in Table 5.7.
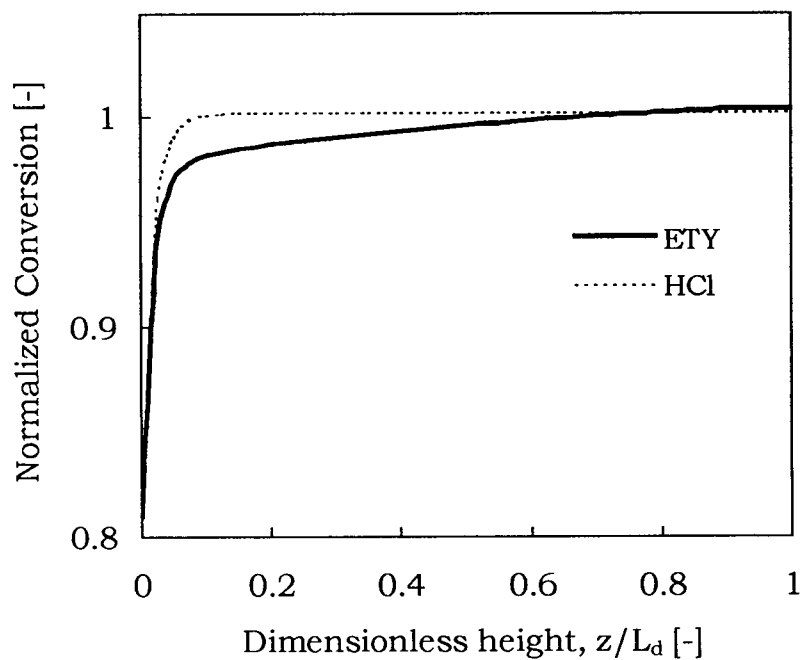
Figure 5.16. Axial conversion profiles of ETY and HCl normalized by exit plant data for conditions given in Table 5.7.
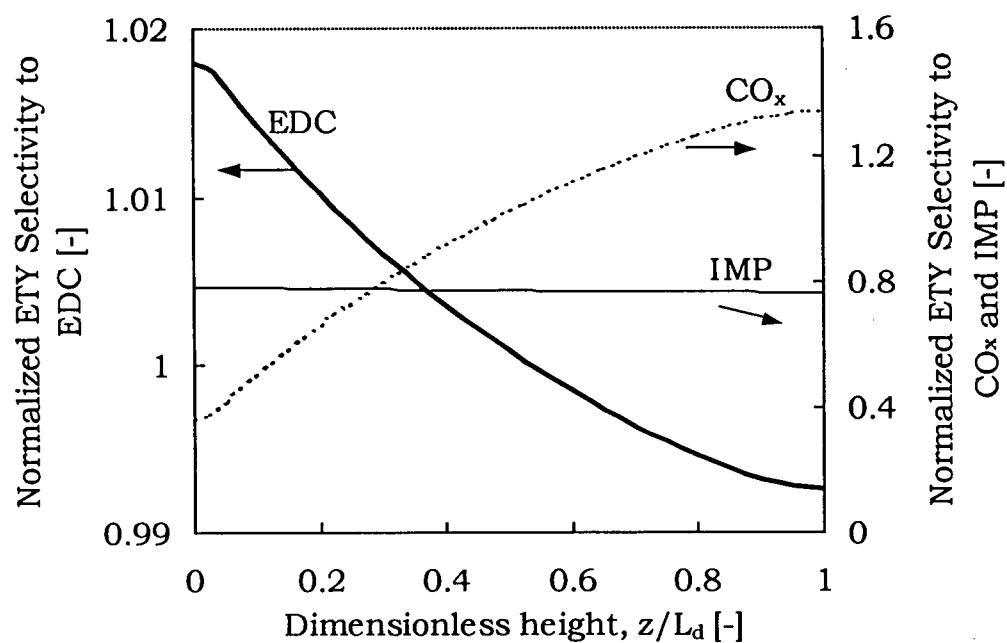
(a)
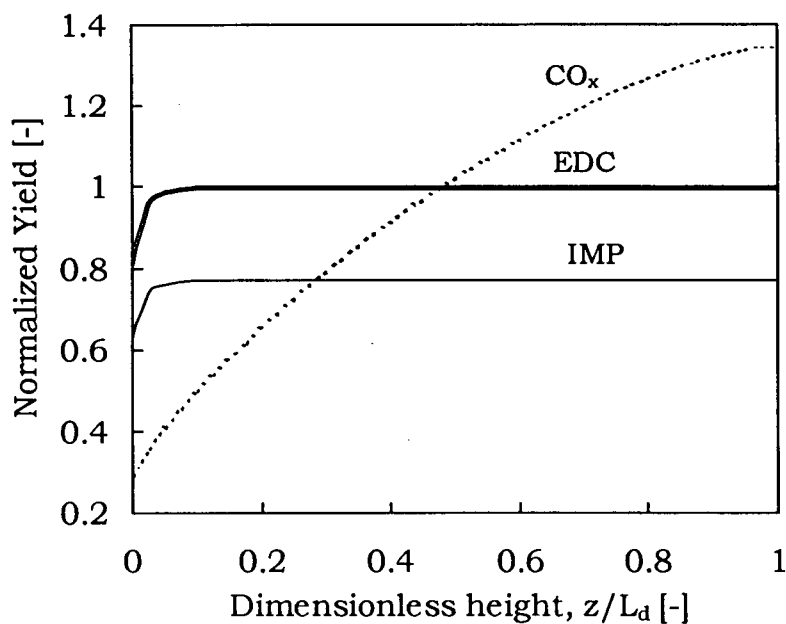
(b)

Figure 5.17. Axial profiles normalized by exit plant data: (a) selectivities of ETY to EDC, CO_x and IMP, (b) yields of EDC, CO_x and IMP for conditions in Table 5.7.
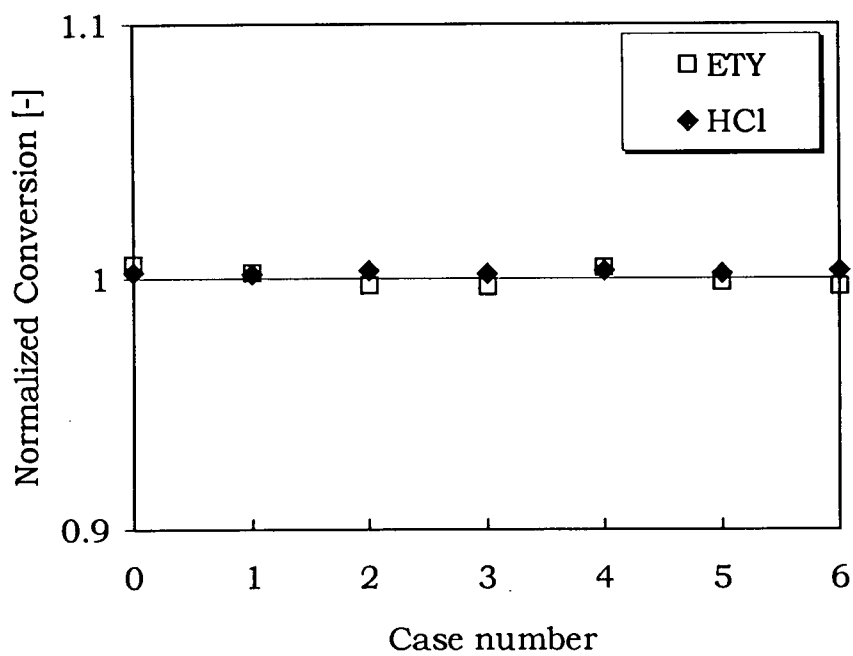
(a)
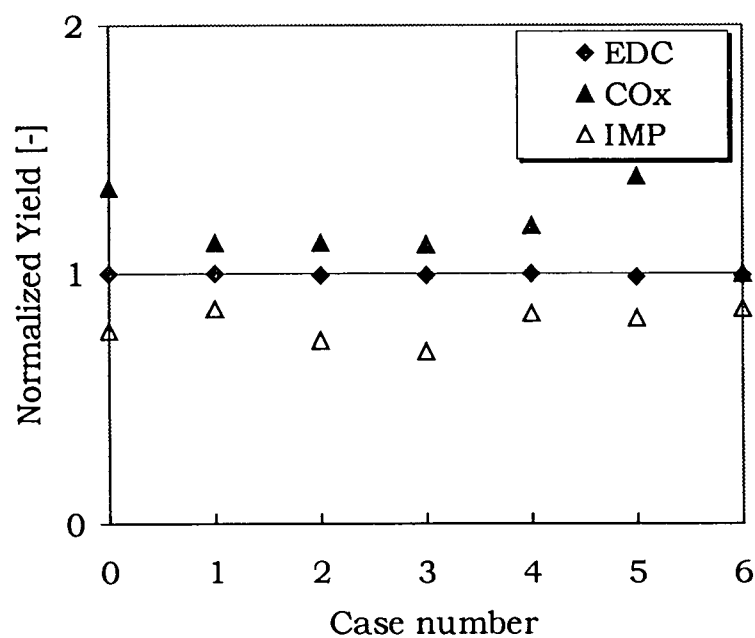
(b)

Figure 5.18. Normalized model predictions for the six cases in Table 5.8: (a) ETY and HCl conversions, (b) yields of EDC, COx and IMP. Case 0 is the base case in Table 5.8.

Table 5.9 Comparison of per pass exit predictions from the GFBR model for the cases when the freeboard is included and when it is ignored (normalized by exit plant data).

	Without freeboard (-)	With freeboard (-)
ETY Conversion	1.004	1.006
HCl Conversion	1.003	1.003
EDC Yield	0.997	0.997
COx Yield	1.329	1.389
IMP Yield	0.766	0.763

5.2.3.2 Effect of Temperature

The effects of temperature on the conversions of ETY, HCl and on the yields of EDC, CO_x and IMP are shown in Fig. 5.19. An increase in reactor temperature not only favours conversion of ETY leading to the formation of more CO_x, but also accelerates the undesirable cracking of the main product, EDC, towards chlorinated impurities. Both CO_x and IMP yields are predicted to almost quadruple as the operating temperature is increased by 60 K. This trend is consistent with the data from the commercial air-feed oxy-reactor. Good temperature control of this highly exothermic reaction is essential for efficient production of EDC. Note also that higher temperatures can also cause catalyst deactivation through increased sublimation of cupric chloride. Moreover, because of their small particles sizes, OC catalyst particles are known to stick together at elevated temperatures leading to increased interparticle agglomeration.

5.2.3.3 Influence of Gas Flow

Figure 5.20 shows the model exit predictions as a function of the superficial gas velocity. Both the EDC and IMP yields are insensitive to increases in U, while the resulting decrease in gas residence time causes a decrease in ETY conversion leading to reduced CO_x yield. Clearly, the additional ETY conversion due to the increase in gas residence time with decreasing U leads exclusively to the formation of oxidation products.
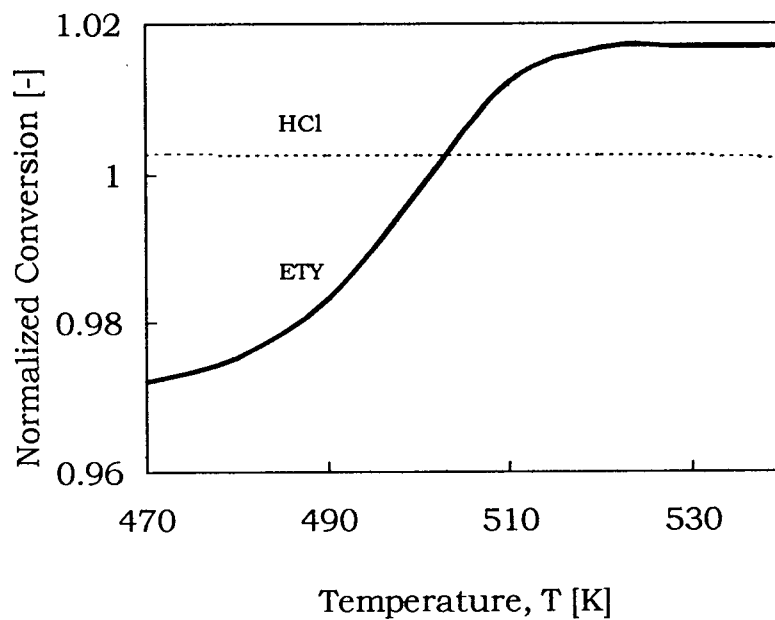
(a)
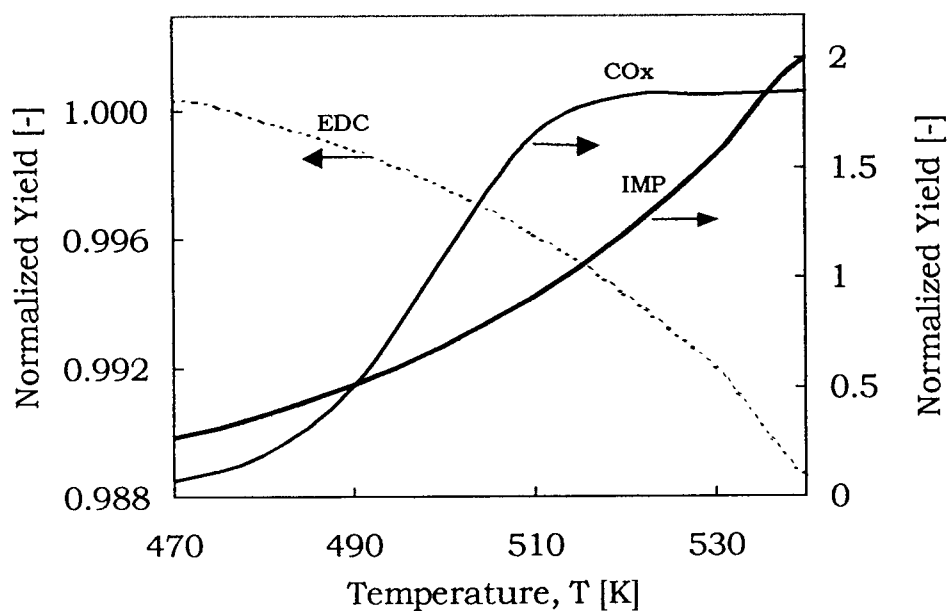
(b)

Figure 5.19. Effect of temperature on reactor performance: (a) Normalized conversion of ETY and HCl, (b) Normalized yields of EDC, CO_x and IMP. (Base case conditions are given in Table 5.7.)
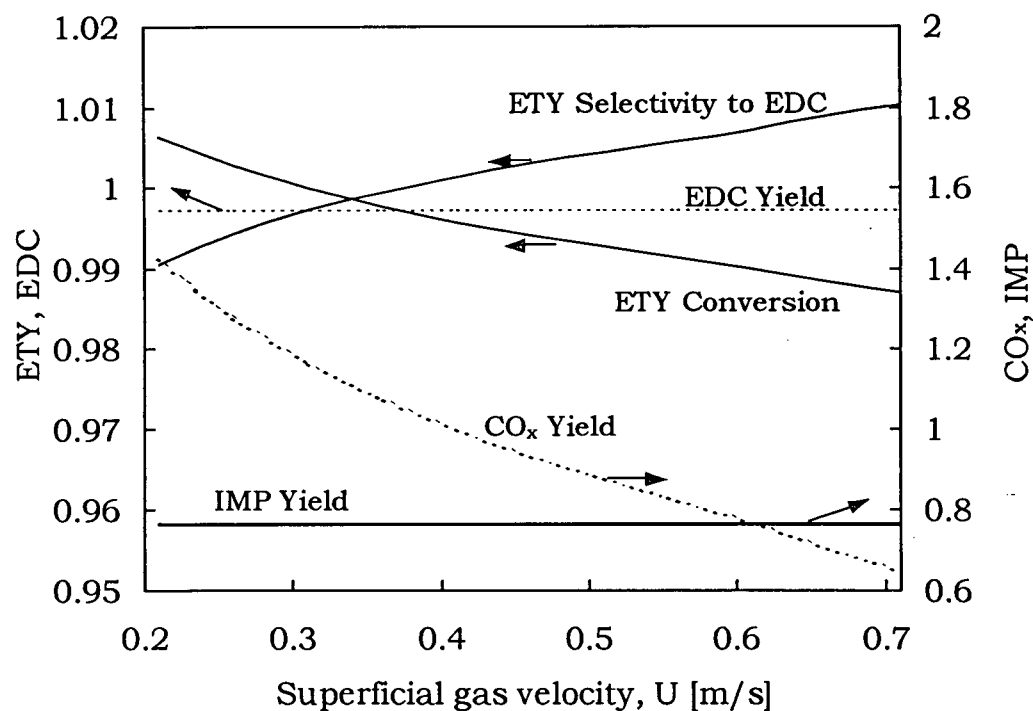
Figure 5.20. Predicted ETY conversion and EDC, IMP and CO_x yields as a function of superficial gas velocity for base case conditions in Table 5.7.

Increasing U is seen to favour the selectivity of ETY to EDC at the expense of ETY conversion. In the air-based OC process, ETY is fed in slight excess of stoichiometric requirements to ensure high conversion of HCl and to minimize losses of the excess ethylene that remains after product condensation. Therefore, the reduced ETY conversion with increasing U is not favorable for the air-based operation. The observed higher selectivity to EDC at reduced ETY conversion is, however, desirable for the O_2-feed oxy-chlorination reactor, where virtually all unreacted ETY is recycled back to the reactor.

5.2.3.4 Effect of Interphase Mass Transfer and Gas Dispersion

Figure 5.21 shows the effect of interphase mass transfer on reactor performance. Since the bed operates, under the prevailing conditions outlined in Table 5.7, mostly in the turbulent regime (P_{turb} being about 80%), the effect of mass transfer between the low-density and high-density phases is minimal. As a result, the interphase mass transfer coefficient is predicted to have almost no effect on the reactor performance in this case.

As expected, increasing Pe_z (i.e. decreasing the gas axial dispersion coefficient) enhances the ETY conversion (Fig. 5.22a). It also causes more CO_x to be formed, while HCl conversion as well as EDC and IMP yields are predicted to remain unchanged (Fig. 5.22b). Since the mass transfer resistance is negligible under the prevailing conditions, the model effectively functions as a dispersed plug flow model, with the limiting cases of the perfect mixing and plug flow approached at low and high Pe_z, respectively. Notwithstanding the slight change in ETY conversion over the range of Pe_z shown, the CO_x yield is predicted to increase by about 17% and remains overpredicted throughout.

5.2.3.5 Influence of Reaction Rate Constants

Given the uncertainty regarding the rate constant, k_{r2}, for the second reaction leading to the formation of CO_x and the observed consistent overprediction of the oxidation products by the model, we next examine its effect as well as the combined influence of all three rate constants on the model predictions. As shown in Fig. 5.23, the exit ETY conversion is predicted to increase with increasing k_{r2}, with the additional converted ETY going almost entirely to CO_x. As expected, the EDC and IMP yields are insensitive to variations in k_{r2}. As for the phthalic anhydride process, the impact of the kinetics was
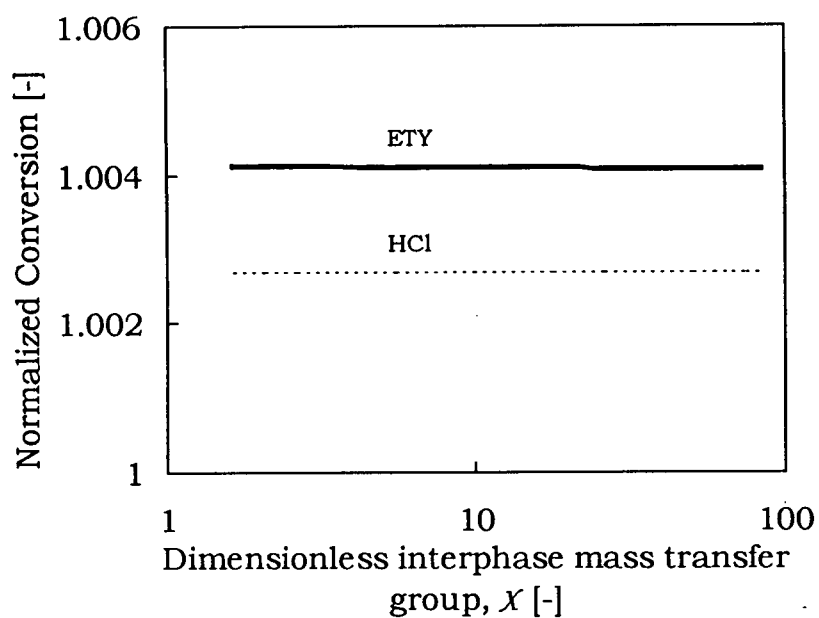
(a)
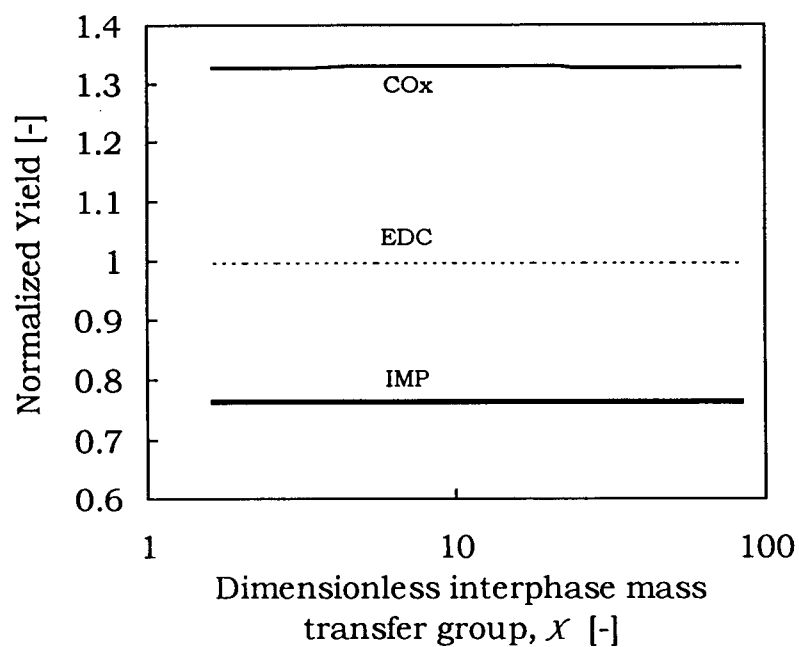
(b)

Figure 5.21. Effect of interphase mass transfer on reactor performance for base case conditions given in Table 5.7: (a) Normalized conversion of ETY and HCl, (b) Normalized yields of EDC, CO_x and IMP.
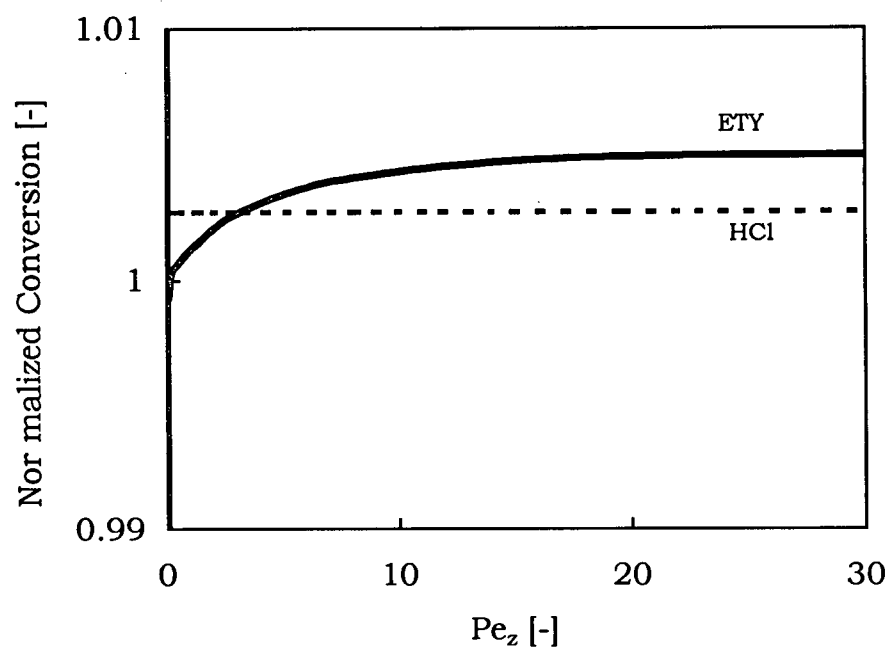
(a)
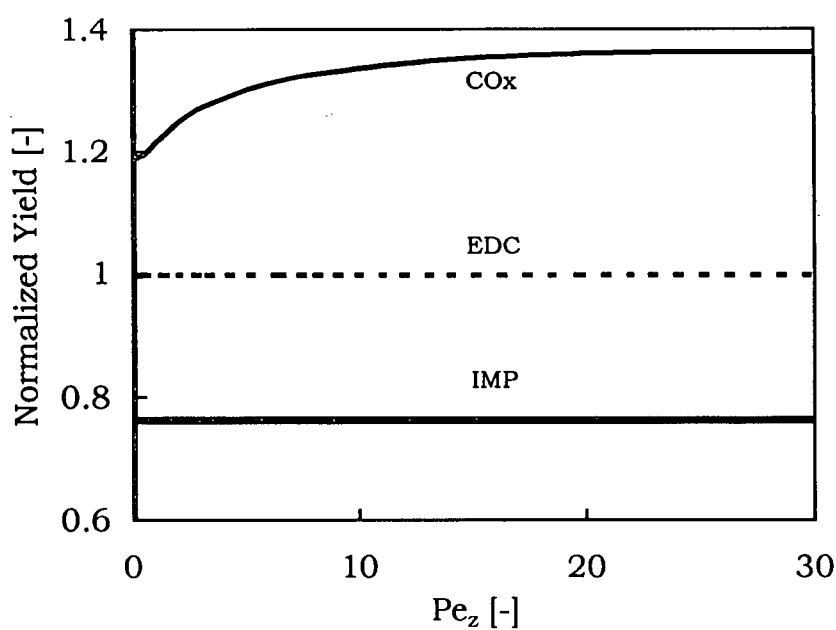
(b)

Figure 5.22. Effect of gas dispersion on reactor performance for base case conditions given in Table 5.7: (a) Normalized conversion of ETY and HCl, (b) Normalized yields of EDC, CO_x and IMP.
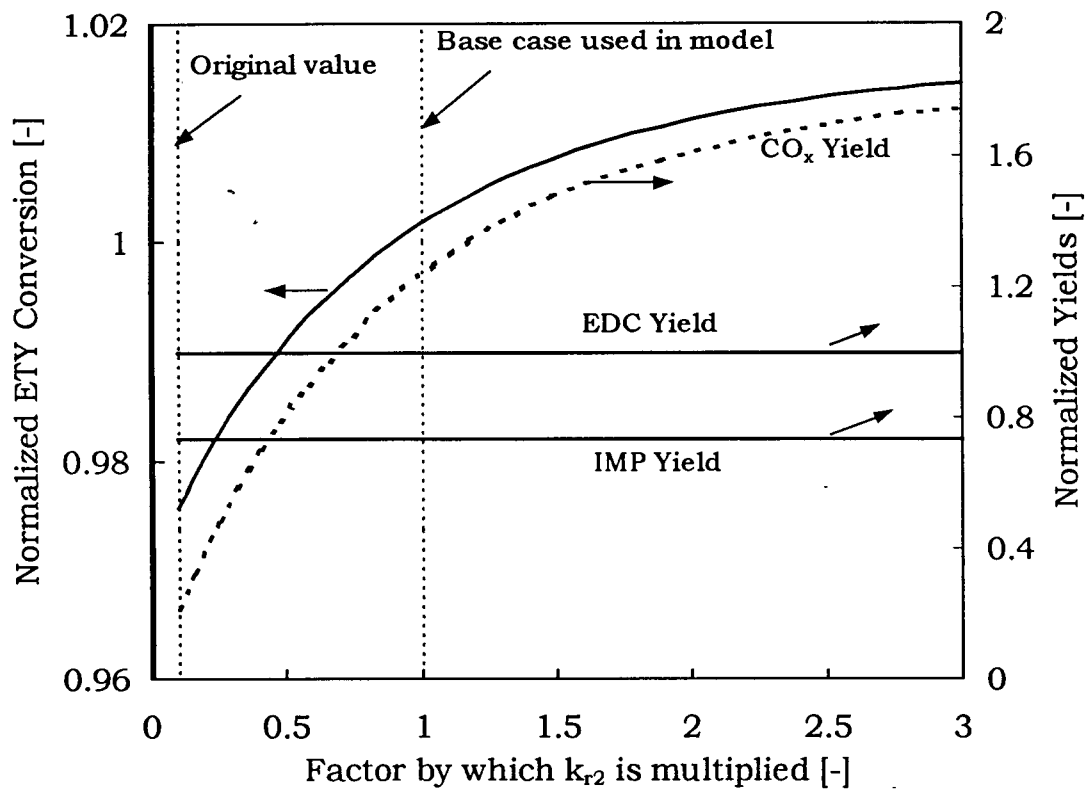
Figure 5.23. Normalized conversion and yields as a function of reaction rate constant, k_{r2}, for base case conditions given in Table 5.7.

further assessed by varying the base case reaction rate constants. It is seen in Table 5.10 that increasing the rate constants favours higher ETY conversion, leading to further oxidation to CO_x. Both EDC and IMP yields are seen to be insensitive to variations in the rate constants. Clearly, the reliability of the model predictions is again dependent on the accuracy of the reaction kinetics.

Table 5.10 Sensitivity of the model predictions to variations in kinetic rate constants. (Results shown are the exit values normalized by exit plant data.)

	All three kinetic rate constants		
	Decreased by 20%	Increased by 20%	Unchanged (Base case)
ETY Conversion	1.000	1.007	1.004
HCl Conversion	1.003	1.003	1.003
EDC Yield	0.997	0.997	0.997
COx Yield	1.181	1.442	1.329
IMP Yield	0.760	0.769	0.766

5.2.4 Conclusions

The simulation results show reasonable agreement between the model predictions and the commercial air-based oxy-chlorination reactor data over a range of conditions. In general, model predictions of the ethylene (ETY) and HCl conversions as well as the yield of ethylene dichloride (EDC) were satisfactory, while the impurities (IMP) yields were consistently underpredicted and the carbon oxides (CO_x) yields were overpredicted. It is very likely that this is primarily due to deficiencies in the chemical kinetic parameters, and possibly even in the mechanisms upon which the kinetics are based. It is clearly imperative to use accurate reaction kinetics in the model for reliable predictions. In addition, a sensitivity analysis shows that even small variations in reactor temperature

profoundly influence the CO_x and IMP yields, underscoring the need to accurately capture the reactor temperature profile through the energy balance in the model. Further analysis shows that gas flow and gas dispersion both significantly influence the reactor performance, while the effect of interphase mass transfer is predicted to be negligible for the conditions prevailing in the industrial reactor.

5.3 Gas-Solid Reactions

5.3.1. Introduction

The GFBR model has so far been applied to gas phase catalytic processes. Application of this model to non-catalytic processes requires coupling it with a single particle model. The goal here is to demonstrate the application of the model for non-catalytic gas-solid reactions in fluidized bed by coupling it with the "grain-particle model" (GPM). This can be achieved in two ways depending on the operating conditions and particle properties:

A. Low velocity flow regimes

- *Approach A1*: Generally for bubbling and turbulent regimes of fluidization with limited entrainment, the solids in the low-density (L) and high-density (H) phases can be considered to be exposed to gaseous species of average concentration $\overline{C_{iL}}$ and $\overline{C_{iH}}$ respectively through the particle boundary layers. The overall conversion of solids leaving the reactor, $\overline{\overline{X}}$, is then a function of the individual particle conversion in the L- and H-phases, $\overline{X}_L$ and $\overline{X}_H$, the solids residence time distributions, E_L, and E_H, and the phase volume allocations, ψ_L and ψ_H.

- *Approach A2*: Alternatively, the solids in the bed can be considered to be exposed to gaseous species of bed-average concentration $\overline{C_i}$ through the gas film surrounding the individual particles. The overall conversion of solids leaving the reactor, $\overline{\overline{X}}$, is then a function of the individual particle conversion, $\overline{X}$, and the solids RTD, E. This is essentially a simplification of approach A1, likely to work better when the particle mean residence time in bed >> time spent within either phase before being transferred to the other phase.

B. High velocity flow regimes

- *Approach B:* For flow systems with significant entrainment (typical of the fast fluidization regime) with net solid circulation flux G_s, the particle conversion should be tracked as a function of both time and space. To achieve this, an equation of particle motion as a function of time must be included. The overall solids conversion

is then calculated by integrating the individual particle conversion with an appropriate compartment-in-series solids RTD model.

Approach A is presented here, which is subsequently reduced to sub-case A2 below. In the following sections, we present the equations for the single particle and the methodology adopted for coupling the reactor model with the particle model. The combined model is then assessed using the zinc sulfide roasting process as a case study. To avoid confusion, the following distinction is made in this section: *reactor model* refers to the fluidized bed reactor model - the GFBR model in this case; *particle model* refers to the grain particle model for a single particle - the GPM in this case.

5.3.2. Single Particle Model

5.3.2.1 Introduction

A number of models have been developed for single particle reactions, including the Shrinking Core Model, Crackling Core Model, Pore Model, Volume Reaction Model, Grain Particle Model, Network Model, among others (Ramachandran and Doraiswamy, 1982). The Shrinking Core Model (SCM), also referred to as the Sharp Interface Model or Topochemical Model, is one of the earliest. It considers the solid reactants to be non-porous and, thus, assumes that the reaction takes place at a sharp interface that divides the exhausted outer shell (ash layer) from the unreacted core of the solid. Although the SCM has the advantage of mathematical simplicity and is widely used, its applicability is limited to non-porous or barely porous solids. In the GPM, the solids are considered to be comprised of compacted grains of uniform size, usually of submicron dimensions. Reaction of the solid is considered to take place at the surface of the grains according to the SCM. Figure 5.23 shows the SCM and GPM schematically. The GPM is often considered realistic for physical systems where the solid particles are agglomerates of grains.

5.3.2.2 Model Equations[3]

In general, a gas-solid reaction can be written in compact form as

---

[3] All symbols are defined in the notation
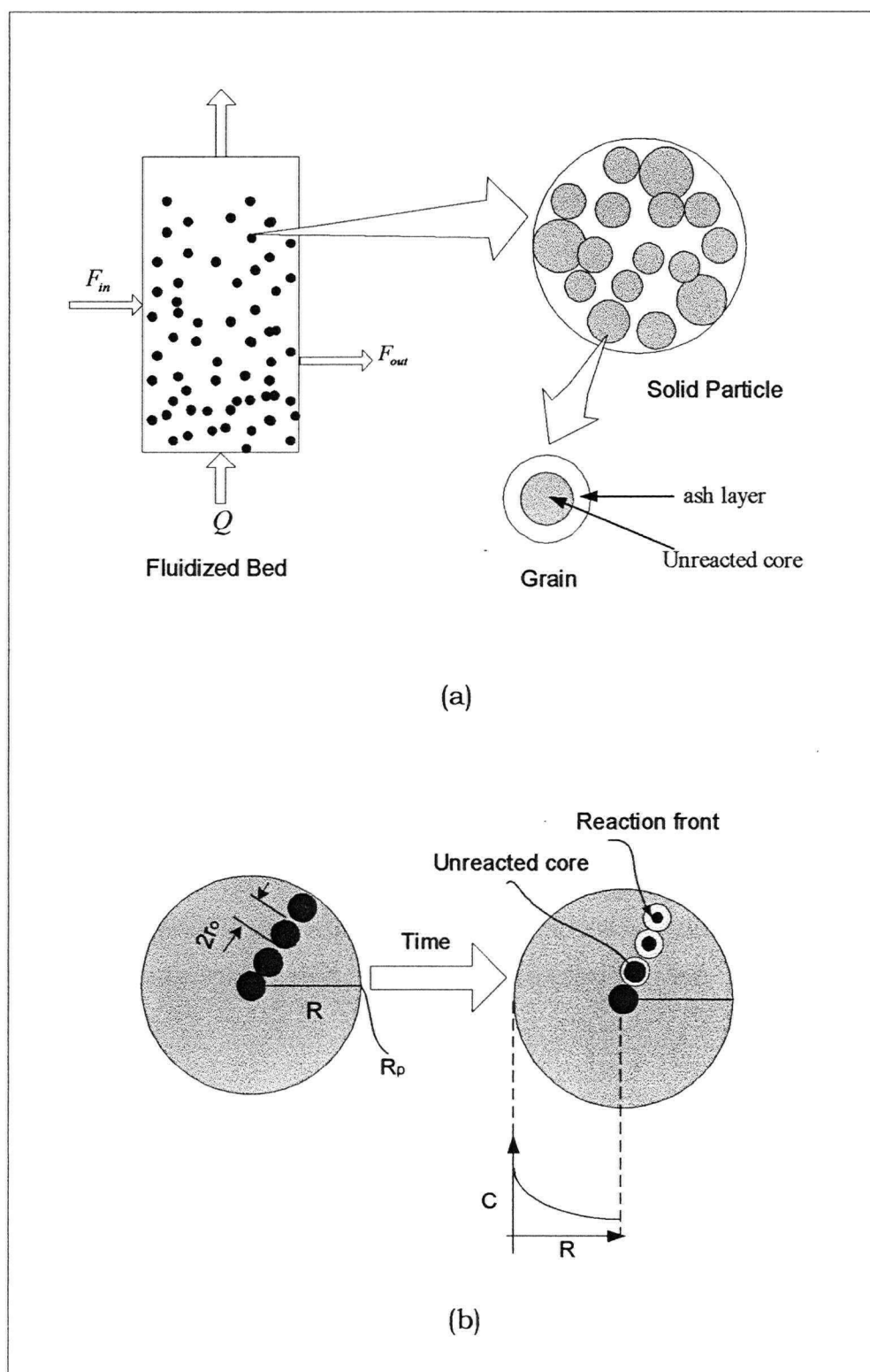
Figure 5.23. (a) Schematic of bed, particle and grain (three different scales of space), (b) Schematic of reaction progression for the GPM.

$$\sum_{i=1}^{N_g} a_{ki} A_i + \sum_{l=1}^{N_s} b_{kl} B_l = 0 \qquad k = 1, \ldots\ldots, N_r \tag{5.1}$$

The conservation equation for gaseous species i in solid l within the j-phase is:

$$\frac{\partial(\varepsilon_j^P C_{ij}^P)}{\partial t} = -\nabla N_{ij} - \sum_k^{N_r} (A_X)_k \times a_{ki} f_k(\mathbf{C}^P)\Big|_j \tag{5.2}$$

where

$$(A_X)_k = F_G(1 - \varepsilon_o^P) \frac{r_{c_l}^{F_G-1}}{r_{o_l}^{F_G}} \tag{5.3}$$

Using the Fickian flux relation to approximate diffusion through the product layer, eq. (5.2) reduces to:

$$\frac{\partial(\varepsilon_j^P C_{ij}^P)}{\partial t} = \mathcal{D}_e \left[\frac{\partial^2 C_{ij}^P}{\partial R^2} + \frac{(F_p - 1)}{R} \frac{\partial C_{ij}^P}{\partial R} \right] - F_G(1 - \varepsilon_o^P) \frac{r_{c_l,j}^{F_G-1}}{r_{o_l}^{F_G}} \sum_k^{N_r} a_{ki} f_{kj}(\mathbf{C}^P) \tag{5.4}$$

The initial and boundary conditions for the j-phase are:

$$at \ t = 0 \qquad C_{ij}^P = \overline{C}_{ij} \qquad 0 \le R \le R_p$$

$$at \ R = 0 \qquad \frac{\partial C_{ij}^P}{\partial R} = 0 \tag{5.5}$$

$$at \ R = R_p \qquad -\mathcal{D}_e \frac{\partial C_{ij}^P}{\partial R} = k_{c,j}\left(C_{ij}^P - \overline{C}_{ij}\right)$$

The effective diffusivity of gas through the product layer, $\mathcal{D}_e$, and the external mass transfer coefficient, $k_{c,j}$ are evaluated from the correlations summarized in Appendix A. The average concentration of the gaseous species i in the j-phase is obtained by integrating the concentration over the bed height and radius:

$$\overline{C}_{ij} = \frac{1}{L_d} \frac{1}{R_c} \int_{z=0}^{L_d} \int_{r=0}^{R_c} C_{ij} dr dz \tag{5.6}$$

Figure 5.24 shows the complete bed-particle coupling mechanism in the two phases. Reactant gases in each phase must diffuse through the gas boundary layer surrounding a particle and through a product layer surrounding the unreacted cores of the compacted grains. The gases then react at the surface of the unreacted cores, and the product gases counter-diffuse back to the bulk of the gas in the L- and H-phases.
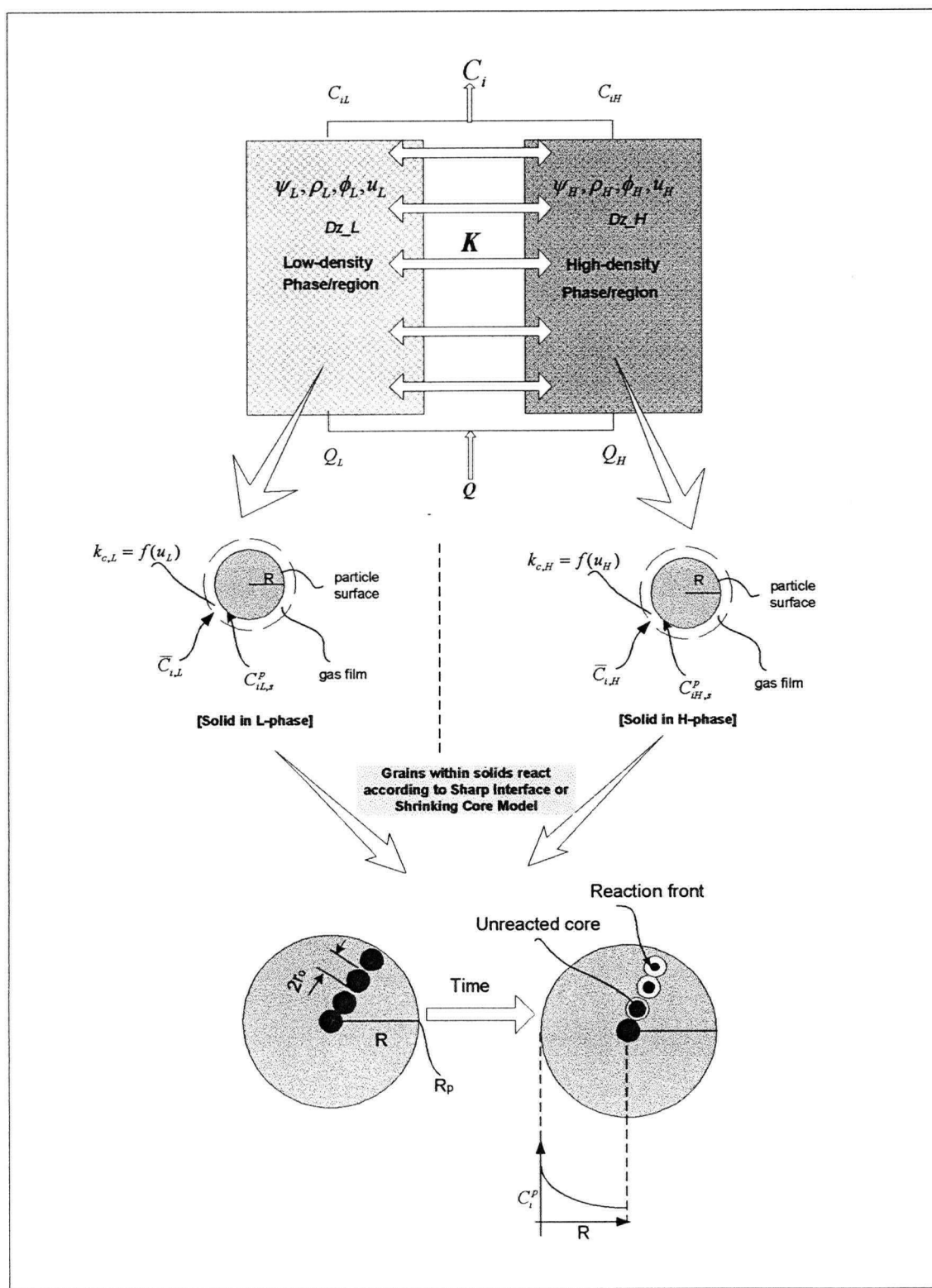
Figure 5.24. Complete visualization of gas-solid contact in the bed

The conservation equations for solid reactant l (grain) can be written for reaction k (based on stochiometry) with particles and grains assumed to be spherical:

$$\frac{1}{b_{kl}}\frac{dn_l}{dt} = \frac{1}{a_{ki}}\frac{dn_i}{dt} \tag{5.7}$$

where

$$n_l = \frac{4}{3}\pi r_{c_l}^3 \frac{\rho_l}{M_l} \tag{5.8}$$

$$\frac{dn_l}{dt} = 4\pi r_{c_l}^2 \frac{\rho_l}{M_l}\frac{dr_{c_l}}{dt} \tag{5.9}$$

$$\frac{dn_i}{dt} = -4\pi r_{c_l}^2 \sum_k a_{ki} f_{kj}(\mathbf{C}^P) \tag{5.10}$$

Therefore the equation governing the movement of the reaction front in the j-phase, obtained by substituting eqs. (5.9) and (5.10) into eq. (5.7) is

$$\frac{dr_{c_l,j}}{dt} = -\frac{M_l}{\rho_l}\sum_k^{Nr} b_{kl}a_{ki}f_{kj}(\mathbf{C}^P) \tag{5.11}$$

The initial condition is:

$$at \quad t = 0 \qquad r_{c_l,j} = r_{o_l} \qquad 0 \le R \le R_p \tag{5.12}$$

The local conversion of solid reactant, l, is evaluated as a function of the volume change as:

$$x_{l,j}(R,t) = 1 - \left[\frac{r_{c_l,j}}{r_{o_l}}\right]^{Fg} \tag{5.13}$$

The overall particle conversion in the j-phase is obtained by integrating the individual local grain conversion (for solid species l) over the particle:

$$X_{l,j}(t) = \frac{\int_0^{R_p} R^{F_p-1}x_{l,j}(R,t)dR}{\int_0^{R_p} R^{F_p-1}dR} \tag{5.14}$$

5.3.3 Coupling the Reactor and Particle Models

5.3.3.1 Overall Conversion of Solids Leaving the Bed

The overall conversion of solids in the j-phase leaving the bed, $\overline{X}_{l,j}$, is a function of the duration of stay of the individual solids in that phase. As in the analysis of Kunii and

Levenspiel (1991), this is accounted for by integrating the conversion of the individual particles with the solids RTD according to

$$1 - \overline{X}_{l,j} = \int_0^t [1 - X_{l,j}(t)] \times E_j(t)dt \tag{5.15}$$

Assuming that solids mixing in the bed can be represented as N compartments in series, the solids RTD in the j-phase can be written:

$$E_j(t) = \frac{t^{N-1}}{(N-1)! \, \overline{t}_j^N} e^{-t/\overline{t}_j^N} \tag{5.16}$$

where $\overline{t}_j = M_{s,j} / \dot{m}_{out}$ is the mean residence time of particles in the j-phase. Here, solids are assumed to be perfectly mixed (N = 1) in both phases. In some cases, it may be better to allow for separate RTDs in the two phases; the mixing pattern in the H-phase is likely to be closer to perfect mixing, especially for bubbling fluidization while a compartment-in-series model, closer to plug flow, is likely to be more representative of the mixing pattern in the L-phase. However, the total residence time of particles in fluidized bed reactors used for gas-solid reactions is usually so long (typically hours) that the assumption of perfect mixing in each phase is reasonable.

5.3.3.2 Accounting for Solids Interchange between the L- and H-Phases

In order to calculate the final overall conversion of solids at the exit of the reactor, one must account for the extent of solids interchange between the two phases. Let P_L and P_H be the probabilities of solids being in the L- and H-phases, respectively, at any instant ($P_L + P_H = 1$); also let f_L and f_H be the volume-averaged solid fractions in the two phases [$f_L + f_H = 1$]. The phase-averaged conversion of solids leaving the bed, $\overline{\overline{X}}_l$, is then given by

$$\overline{\overline{X}}_l = f_L P_L \overline{X}_{l,L} + f_H P_H \overline{X}_{l,H} \tag{5.17}$$

where

$$f_L = \psi_L \phi_L / \phi; \qquad\qquad f_H = \psi_H \phi_H / \phi \tag{5.18}$$

The above reasoning seems logical with the challenge being the assignment of probabilities of solids having passed from one phase to the other or conversely. Given the assumption of perfect mixing of solids adopted here, it is immaterial how the

probabilities are assigned. If different RTDs of solids in the L- and H-phase were to be considered, however, their assignment would become important.

5.3.3.3 Overall Material Balance

To relate the conversion of gaseous reactant to that of solid reactant, an overall material balance is performed over the entire bed. For k reactions, this becomes:

$$\sum_i \frac{1}{a_{ik}} (total\ moles\ of\ gaseous\ reactants\ consumed)$$
$$= \sum_l \frac{1}{b_{lk}} (total\ moles\ of\ solid\ reactants\ consumed) \tag{5.19}$$

$$\sum_i \frac{1}{a_{ik}} \Delta F_i = \sum_l \frac{1}{b_{lk}} \Delta F_l \tag{5.20}$$

For the ZnS process, for example, eq.(5.20) can be written:

$$\frac{1}{a_{O_2}} [AUC_{in} - AUC_{out}]_{O_2} = \frac{1}{b_{ZnS}} [F_{in} - F_{out}]_{ZnS} \tag{5.21}$$

or

$$\frac{1}{a_{O_2}} AUC_{in} \left[1 - \frac{C_{out}}{C_{in}}\right]_{O_2} = \frac{1}{b_{ZnS}} F_{in} \left[1 - \frac{F_{out}}{F_{in}}\right]_{ZnS} \tag{5.22}$$

5.3.4 Case Study: Zinc Sulfide Roasting

Zinc is found in nature as a sulfide. Part of the extraction process involves converting the sulfide to zinc oxide in a process called roasting. The main reaction is:

$$ZnS + 3/2O_2 = ZnO + SO_2 \tag{5.23}$$

$$[\Delta H = -444 \times 10^3\ kJ/kmol\ ZnS \qquad (800 - 1000°C)]$$
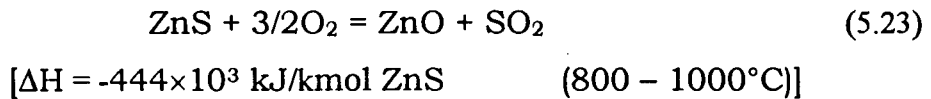
This reaction produces sulfur dioxide which is used for the production of sulfuric acid, but is also a precursor of acid rain. Roasting is the oldest pyrometallurgical process commonly employed in treating such concentrates. There is currently no simple, cost-effective alternative to remove sulfur from the sulfide on a commercial scale. However, as environmental restrictions tighten, newer ways of treating the zinc sulfide ores are being explored.

5.3.4.1 Assumptions, Model Parameters and Reaction Kinetics

In applying the combined model to the roasting of zinc sulfide, the following additional assumptions are made: (i) Solid concentrate is assumed to be 100% ZnS. (In practice, it is usually about 80%, with a significant fraction of FeS and other sulphides and oxides in

trace quantities); (ii) Particles are assumed to be monosized. (In practice, there is commonly a wide PSD.); (iii) Solids are assumed to be perfectly mixed in the bed; (iv) The operation is assumed to be isothermal. (In practice, the temperature close to the grid is somewhat lower than close to the bed surface.) For a more realistic representation of the system, these assumptions clearly need to be relaxed. Some of these issues are well documented (see Avedesian, 1974).

Table 5.11 summarizes the operating conditions and particle properties for the process simulated. These are typical of industrial conditions.

The kinetics of the ZnS reaction have been studied by several workers (e.g. Natesan and Philbrook, 1970; Fukunada et al., 1976). The rate of reaction is reported to be first order with respect to oxygen concentration. Fukunada et al. (1976) reported the following Arrhenius equation for the surface rate constant:

$$k_r = 2.96 \times 10^{13} \exp\left[-\frac{3.14 \times 10^5}{RT}\right] \qquad \text{m/s}$$

Table 5.11 Summary of operating conditions and hydrodynamic properties for the zinc sulfide roasting process corresponding to the base case (from Avedesian, 1974; Grace, 1986)

Parameter	Value
Temperature, T	1233 K
Pressure, P	1.013×10^5 Pa
Superficial gas velocity, U	0.78 m/s
Average particle diameter, $\bar{d}_p$	60 μm
Particle density, ρ_p	4100 kg/m^3
Inlet/Initial gas composition, y_{in}	0.21/0.78999/0.000001[O$_2$/N$_2$/SO$_2$]
Mass of solids in bed, M_{so}	30,000 kg
Solids feed rate, $\dot{m}_{in}$	2.48 kg/s
Initial grain radius, r_{o_l}	5 μm
Initial particle porosity, ε_o^p	0.4
Reactor diameter, D_t	6.38 m

5.3.4.2 Results and Discussion

Results from approach A2 are presented here, noting that this approach is essentially a sub-case of approach A1 in which the bed-averaged gas concentration is obtained as:

$$\overline{C_i} = \frac{1}{L_d}\frac{1}{R_c}\int_{z=0}^{L_d}\int_{r=0}^{R_c}C_i drdz \tag{5.24}$$

where

$$C_i = q_L C_{iL} + q_H C_{iH} \tag{2.3}$$

Equation (5.24) is then substituted for eq. (5.6) and all phase subscripts drop out leading to bed-averaged profiles.

Figure 5.25 shows the grain conversion along the radius of a particle as a function of time for single particles of diameter 60 and 200 μm. As expected, the grains closer to the particle surface, exposed to more of the reactant-rich gaseous species, are converted more than grains towards the center of the particle. Therefore, one observes a drop in the extent of grain conversion as the reactant concentration becomes depleted towards the center of the particle (Fig. 5.26), consistent with the expected prediction from the GPM. This is especially the case, for the larger particle (b) in which diffusional mass transfer is seen to be limiting. Figure 5.27 compares the particle conversion as a function of time for the same two particle sizes. As expected, it takes much longer for larger particles to completely react. (A similar trend can be seen in Fig. 5.25b.) A snapshot of the overall exit conversion of gas and solids together with other transport and hydrodynamic quantities for the 60 μm particles is given in Table 5.12. It is seen that the solids mean residence time is much greater than the time for complete conversion of particles so that the vast majority of particles leaving the bed are nearly fully converted.

The influence of the particle size on the time required for complete conversion of individual particles, as well as the overall solids conversion, is assessed in Fig. 5.28. The overall conversion is seen to drop only slightly with increasing particle size even though the time for conversion significantly increased. In the commercial operations, solids taken out of the main product stream (overflow) of the fluidized bed roasters are converted slightly more than those, mostly fines, which spend less time in the reactor and are entrained (carried over) (Magoon et al., 1990). Based on the analysis of the residual sulfide sulfur in the overflow stream, the average commercial values of solids conversion
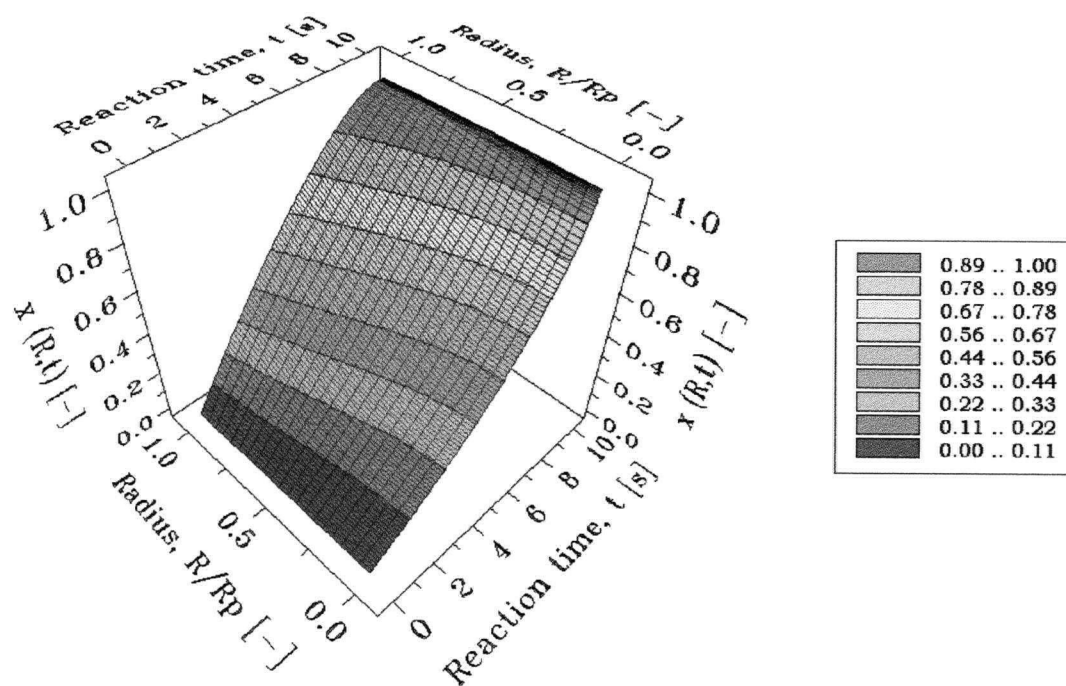
(a)
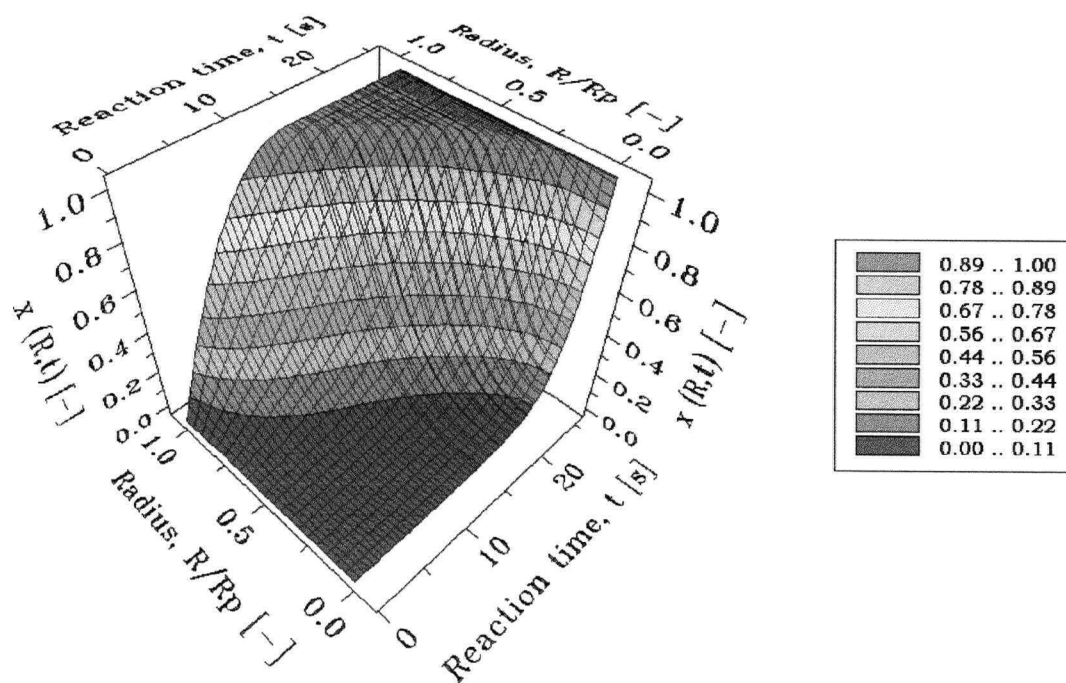
(b)

Figure 5.25. Local conversion of grain, x, as function of dimensionless radius and reaction time for: (a) **60** μm; (b) **200** μm particles. Other conditions as in Table 5.11.
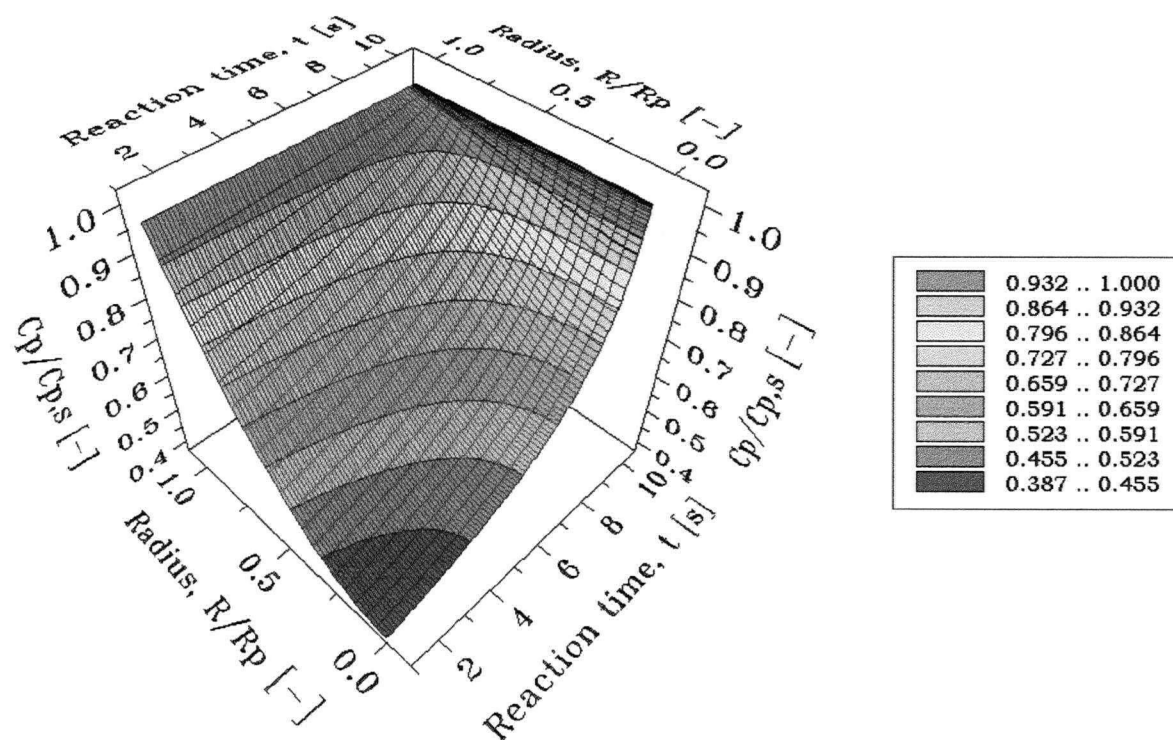
[4]Figure 5.26. Dimensionless radial concentration profile of O_2 as a function of time for particle of **d_p=60 μm**;. Other conditions as in Table 5.11.

---

[4] The normalizing concentration $C_{p,s}$ is the prevailing surface concentration at each reaction time.
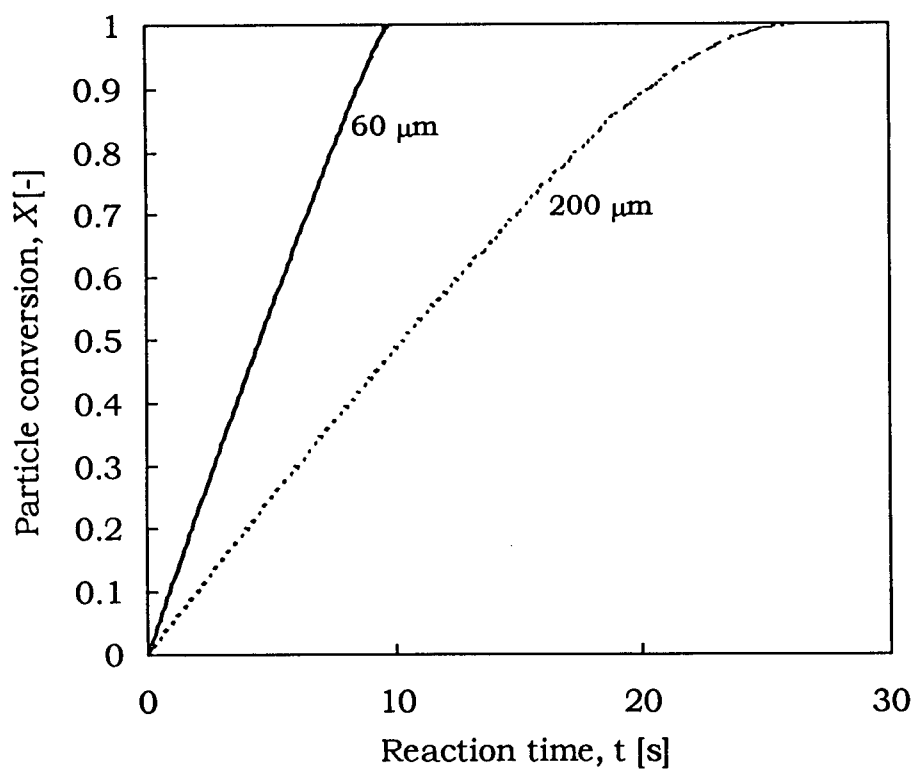
Figure 5.27. Comparison of particle conversion with time for two particles sizes for the conditions given in Table 5.11
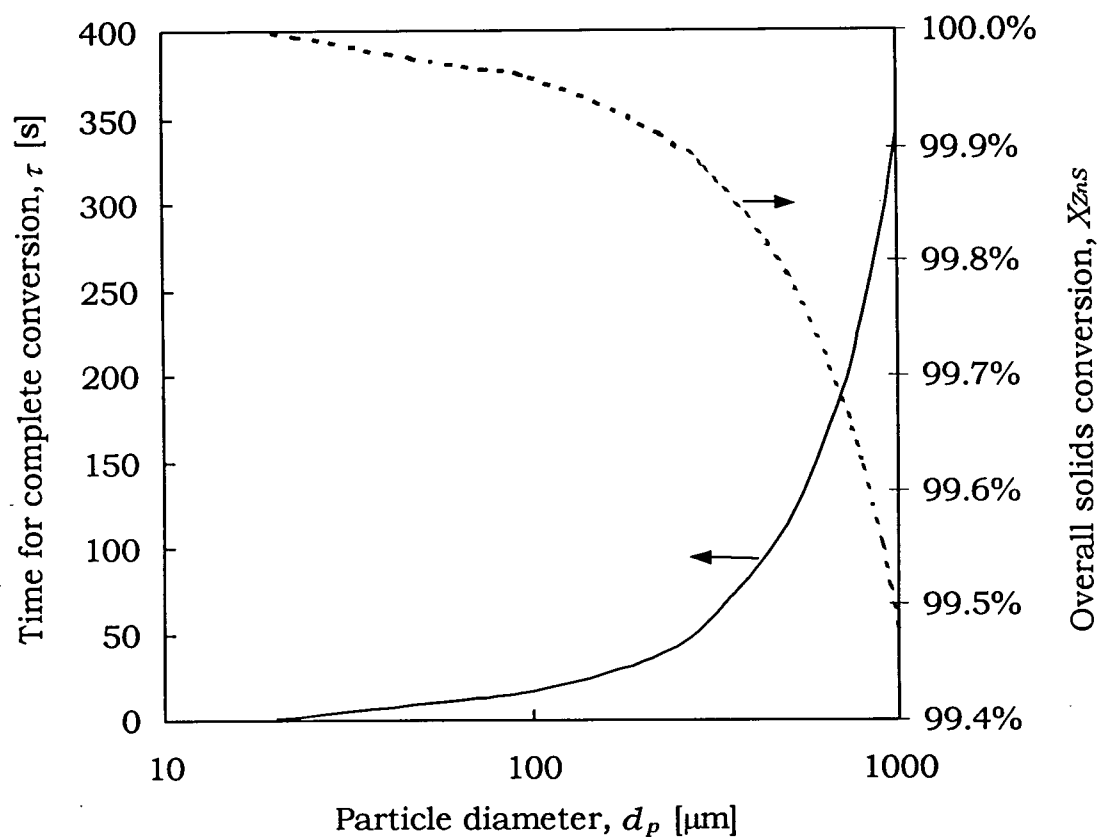
Figure 5.28. Time for complete conversion of individual particles and overall conversion of solids leaving the bed as a function of particle size. Other conditions as in Table 5.11.

are in the range 98 – 99.9% (see Magoon et al., 1990; Kunii and Levenspiel, 1991; Nyberg, et al., 2000). The predicted conversions here compare reasonably with this commercial range.

Clearly, for cases where $\bar{t} \gg \tau$, the overall conversion is much more dependant on the solids RTD than on the dynamics within individual particles. For cases where the solids mean residence time is close to the time for complete conversion of particle, however, the particle model becomes as important in contributing to the overall conversion.

Table 5.12. Summary of pertinent variables at reaction completion for 60 μm particles. Other properties as in Table 5.11.

Variable	Value	Remarks
τ	10.2 s	Time for complete conversion of particle
$\bar{t}$	14,500 s	Solids residence time ($M_{so}/\dot{m}_{out}$)
$\bar{X}_{ZnS}$	99.97 %	Overall solid conversion at exit
X_{O_2}	74.6 %	Overall O_2 conversion at exit
U_c	2.1 m/s	High because of temperature effect (estimated from correlation in Table 2.2)
U_{mf}	7×10^{-3} m/s	Close to experimental value of 10mm/s obtained by Avedesian (1974)
U	0.74 m/s	$U_c > U \gg U_{mf}$
P_{bubb}	94%	Probability of bubbling
q_L	0.97	Almost all gas passes through L-phase as bubbles
k_c	0.38 m/s	External mass transfer coefficient based on U (estimated from correlation in Appendix B)
k_r	1.47 1/s	Reaction rate constant

5.3.3 Concluding Remarks

Application of the GFBR model to gas-solid reactions has been demonstrated using the zinc sulfide roasting process as a study case. Preliminary model predictions at the single particle level for the zinc sulfide roasting process are reasonable. In order to fully realize the potential of the model, several modifications and extensions could be made to the combined model at both the particle and the fluid bed levels, namely: (i) Allow for separate solid RTDs in the L- and H-phases; (ii) Refine the approach of solids interchange between phases for proper implementation of approach A1; (iii) Consider a wide particle size distribution in bed; (iv) Consider a variable area freeboard region. (v) Account for change in particle porosity with time depending on whether the solids expand, shrink or retain their original shapes as they react; (vi) Incorporate energy balances to track temperature history in the bed and within the particles. However, these modifications/extensions, particularly at the particle level, are not likely to change the overall result significantly for cases where the particle mean residence time is much greater than the time for complete conversion of individual particles (i.e. for $\bar{t} \gg \tau$), as in the ZnS roasting case. In such systems, the overall conversion is much more a function of the solid RTD (which may be a function of the PSD) than the reaction model used to describe the gas-solid reaction.

Chapter 6

Implementation of Volume Change with Reaction

6.1 Introduction

A number of industrial gas phase reactions are accompanied by significant volume change (reduction or expansion) due to reaction. Examples include oxy-chlorination and steam methane reforming. The volume change can cause significant change in the hydrodynamic behavior of the bed, as well as variations in reactor performance indicators such as conversion, selectivity and yield. Volume reduction in a fluidized bed reactor leads to a decrease in the gas velocity with the possibility of de-fluidization. The decrease in the volumetric gas flow can directly affect hydrodynamics throughout the bed. It also results in increased gas residence time leading to increased conversions and yields, but with the possibility of decreased selectivities for desired intermediates. An increase in the number of moles can lead not only to increased entrainment, but also to decreased gas residence time resulting in reduced conversions, yields and selectivities.

Few fluidized bed reactor-models in the literature consider volume changes with reaction. When such effects have been considered, models have been limited to single reactions with simple first order kinetics (Irani et al., 1980; Kai and Furusaki, 1984; Shiau and Liu, 1993) or single reactions with non-linear kinetics (Tafreshi et al., 2000). Adris et al. (1997) examined the impact of volume increase for a fluidized bed membrane steam methane reforming process with multiple reactions and non-linear kinetics. In all of these cases, the investigations were limited to the bubbling flow regime of fluidization and to isothermal, isobaric conditions. No attempts have been reported to assess the impact of volume changes on the performance of a commercial-scale reactor.

In this chapter, we treat the effect of volume change with reaction, accounting for the changes in both temperature and pressure, as well as total molar flow rate, along the reactor height. Multiple reactions with non-linear kinetics for the oxy-chlorination process treated in Chapter 5 are considered to assess the impact of the volume change on the hydrodynamics and reactor performance.

6.2 Modeling Approach

The total volumetric flowrate Q can be expressed as a function of the total molar flow rate, temperature and pressure using the basic equation of state,

$$\frac{F_T}{Q} = \frac{P}{ZRT} \tag{6.1}$$

At height $z = 0|^-$, i.e. just below where the reaction is initiated,

$$\frac{F_{To}}{Q_o} = \frac{P_o}{Z_o RT_o} \tag{6.2}$$

Combining eqs. (6.1) and (6.2) and assuming that the compressibility factor does not change significantly, the volumetric flowrate at any height z is

$$Q = Q_o \frac{F_T}{F_{To}} \frac{T}{T_o} \frac{P_o}{P} \tag{6.3}$$

For a column of constant cross-section, eq. (6.3) can be written in terms of gas velocity:

$$U = U_o \frac{F_T}{F_{To}} \frac{T}{T_o} \frac{P_o}{P} \tag{6.4}$$

For a two-phase/region system with low- and high-density phases or regions (which we label the L- and H-phases as before), eq. (6.4) can be written (neglecting any temperature or pressure difference between the phases at a given level):

$$u_L = u_{Lo} \frac{F_{T,L}}{F_{To}} \frac{T}{T_o} \frac{P_o}{P} \tag{6.5}$$

$$u_H = u_{Ho} \frac{F_{T,H}}{F_{To}} \frac{T}{T_o} \frac{P_o}{P} \tag{6.6}$$

$$U = \psi_L u_L + \psi_H u_H \tag{6.7}$$

For *single reactions*, the effect of change in the number of moles due to reaction in the *j*th phase can be related to the conversion of the base reactant A

$$\frac{F_{T,j}}{F_{To}} = (1 + \gamma X_{A,j}) \tag{6.8}$$

where the expansion/reduction factor γ is obtained from

$$\gamma = y_{Ao} \sum_{i=1}^{N_c} \nu_i \tag{6.9}$$

In this way, the continuity equations can be written in terms of species concentration with the effect of the volume change captured through the superficial gas velocity. For example, for a single reaction

$$aA + bB \rightarrow cC + dD \qquad (6.10)$$

The low and high-density phase variables can be written for a base reactant A (with the implicit assumption that extra moles of gas generated within one phase remain with that phase)

$$u_L = u_{Lo}(1 + \gamma X_{A,L})\frac{T}{T_o}\frac{P_o}{P} \qquad (6.11)$$

$$u_H = u_{Ho}(1 + \gamma X_{A,H})\frac{T}{T_o}\frac{P_o}{P} \qquad (6.12)$$

where

$$X_{A,L} = \frac{1 - C_{A,L}/C_{Ao}}{1 + \gamma C_{A,L}/C_{Ao}} \qquad (6.13)$$

$$X_{A,H} = \frac{1 - C_{A,H}/C_{Ao}}{1 + \gamma C_{A,H}/C_{Ao}} \qquad (6.14)$$

$C_{A,L}$ and $C_{A,H}$ are obtained by solving the continuity equations for species A together with the energy and pressure equations and appropriate boundary conditions. The concentrations of the other species (B, C, D) are then given by

$$C_{i,L} = \frac{C_{Ao}(\theta_{i,L} + \frac{v_i}{a}X_{A,L})}{1 + \gamma X_{A,L}} \qquad (6.15)$$

$$C_{i,H} = \frac{C_{Ao}(\theta_{i,H} + \frac{v_i}{a}X_{A,H})}{1 + \gamma X_{A,H}} \qquad (6.16)$$

$$\theta_{i,j} = C_{io,j}/C_{Ao} \qquad (6.17)$$

$$U_o = \psi_L u_{Lo} + \psi_H u_{Ho} \qquad (6.18)$$

$$u_{Lo} = \sum_{j=1}^{N_{regime}} u_{Lo,j} \times P_j \qquad (6.19)$$

For *multiple reactions*, it is generally impossible to express the volumetric flowrate in terms of the conversion of single species because of the complexity of the reactions. Therefore, the continuity equations and the reaction rates must be written in terms of the

species molar flowrates F_i and solved together with the volumetric flowrate from eqs. (6.5) to (6.7). This general approach handles single reactions as well.

For the variable density generalized modeling approach, the steady state two-phase/region mole balances representing the two-phase bubbling bed model in the low velocity limit, dispersed plug flow model at intermediate velocities and the core-annulus model in the high velocity limit presented in Chapter 2 for constant gas density systems (eqs. 2.1 to 2.3) can then be re-written in terms of molar flow rates, F

$$L\text{-phase:} \quad \frac{\partial (F_{iL})}{\partial z} - \mathcal{D}_{zg,L} \frac{\partial^2 (F_{iL}/U)}{\partial z^2} - \mathcal{D}_{rg,L} \frac{1}{r} \frac{\partial}{\partial r}\left(r \frac{\partial (F_{iL}/U)}{\partial r}\right) \qquad (6.20)$$
$$+ K(F_{iL} - F_{iH})/(U \times \psi_L) + A\rho_L Rate_{iL} = 0$$

$$H\text{-phase:} \quad \frac{\partial (F_{iH})}{\partial z} - \mathcal{D}_{zg,H} \frac{\partial^2 (F_{iH}/U)}{\partial z^2} - \mathcal{D}_{rg,H} \frac{1}{r} \frac{\partial}{\partial r}\left(r \frac{\partial (F_{iH}/U)}{\partial r}\right) \qquad (6.21)$$
$$+ K(F_{iH} - F_{iL})/(U \times \psi_H) + A\rho_H Rate_{iH} = 0$$

$$\text{Overall balances:} \qquad F_i = q_L F_{iL} + q_H F_{iH} \qquad (6.22)$$

$$F_{T,L} = \sum_{i=1}^{N_c} F_{iL}; \qquad\qquad F_{T,H} = \sum_{i=1}^{N_c} F_{iH} \qquad (6.23)$$

where $K = k_{LH} a_I \psi_L$. The species conversions, yields, selectivities, etc are computed based on the molar flowrates, F_i. The concentration of the individual species i in phase j can be obtained from

$$C_{i,j} = \frac{F_{i,j}}{Q} \qquad (6.24)$$

We assume here that exchange of gas between the L- and H-phases occurs solely via interphase mass transfer. The effect of bulk transfer between phases is discussed below. This system of equations is solved together with the energy and pressure balance equations (eqs. 2.8 and 2.11) and the material balances (Table 2.1) for a given set of reactor conditions.

6.3 Case Study: Oxy-Chlorination Process

As discussed in Chapter 5, the oxy-chlorination process is described by complex reactions with non-linear temperature-dependent kinetics and is accompanied by a significant change in the total number of moles. Using this process as a case study, the

impacts of the volume change on both the hydrodynamic and reactor performance are examined for the four different cases listed in Table 6.1, with reactor physical conditions as given in Table 5.8.

Table 6.1. Four different cases considered for simulating the effects of changes in the number of moles, temperature and pressure on reactor performance.

➤ **Case 1***	$u_j = u_{jo}$ $(j = L \text{ and } H)$	-Neglects volume change due to reaction -Effects of T and P on U are ignored -All thermophysical properties are based on average values of T and P.
➤ **Case 2**	$u_j = u_{jo} \dfrac{F_{T,j}}{F_{To}}$	-Accounts for change in number of moles -Effects of T and P on U are ignored -Thermophysical properties vary with T and P.
➤ **Case 3**	$u_j = u_{jo} \dfrac{F_{T,j}}{F_{To}} \dfrac{T}{T_o}$	-Accounts for change in number of moles and T -Effect of P on U is ignored -Thermophysical properties vary with T and P.
➤ **Case 4**	$u_j = u_{jo} \dfrac{F_{T,j}}{F_{To}} \dfrac{T}{T_o} \dfrac{P_o}{P}$	-Accounts for change in number of moles -Accounts also for effects of both T and P on U -Thermophysical properties vary with T and P.
*Base case		

6.4 Results and Discussion

6.4.1 Effect of volume change on the hydrodynamic variables

6.4.1.1 Gas velocity

The bed-average axial gas velocity profiles for all four cases listed in Table 6.1 are presented in Fig. 6.1. The gas velocity for case 1 is uniform, while for case 2, a decrease in gas velocity is observed immediately above the distributor owing to the rapid conversion of the reactants, resulting in a reduction in volumetric flow by about 25%. The nearly flat velocity profile over the rest of the expanded bed height occurs because the ethylene conversion is almost complete, with relatively little further conversion. The impacts of the temperature and pressure are shown in cases 3 and 4. The sharp decrease in case 4 immediately above the distributor is due to the rapid conversion of ethylene as above, while the subsequent increase stems from the decreasing hydrostatic pressure. Figure 6.2 shows the bed-average L- and H-phase axial gas velocity profiles for case 4. As expected, the velocities decrease rapidly immediately above the distributor where rapid reactions occur and then continue to increase over the rest of the bed.

6.4.1.2 Gas flow distribution and phase volume fractions

Similar trends as for the gas velocity profiles can be observed when the fractional gas flow allocation to the L-phase, q_L (= fraction of total flow passing through this phase) is plotted vs. height as shown in Fig. 6.3. Figure 6.4 shows the expected immediate decrease of the total gas flow through both phases due to reaction, with the relative decrease being more pronounced in the L-phase. Since more reaction take place in the H-phase than the L-phase ($P_{turb} \approx 94\%$), a slightly higher absolute decrease occurs for the gas flow through the H-phase. When the volumetric flow in the H-phase decreases faster, less gas is exchanged with the L-phase via interphase mass transfer. As a result, the volume occupied by the H-phase is predicted to increase while that of the L-phase decreases as shown in Fig. 6.5.

So far, we have ignored bulk transfer of gas between the phases, assuming that all gas exchange between phases occurs due to interphase mass transfer. The effect of bulk transfer between the phases is discussed below.
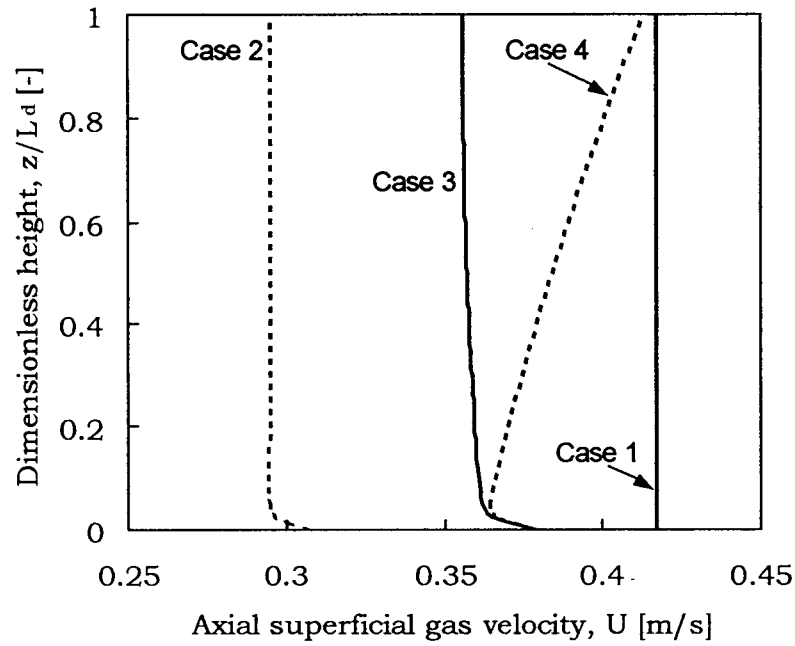
Figure 6.1. Predicted bed-average axial gas velocity profiles [Case 1: $u_j=u_{jo}$; Case 2: $u_j=u_{jo} \times F_{T,j}/F_{To}$; Case 3: $u_j=u_{jo} \times F_{T,j}/F_{To} \times T/T_o$; Case 4: $u_j=u_{jo} \times F_{T,j}/F_{To} \times T/T_o \times P_o/P$; $j = L$ & H]
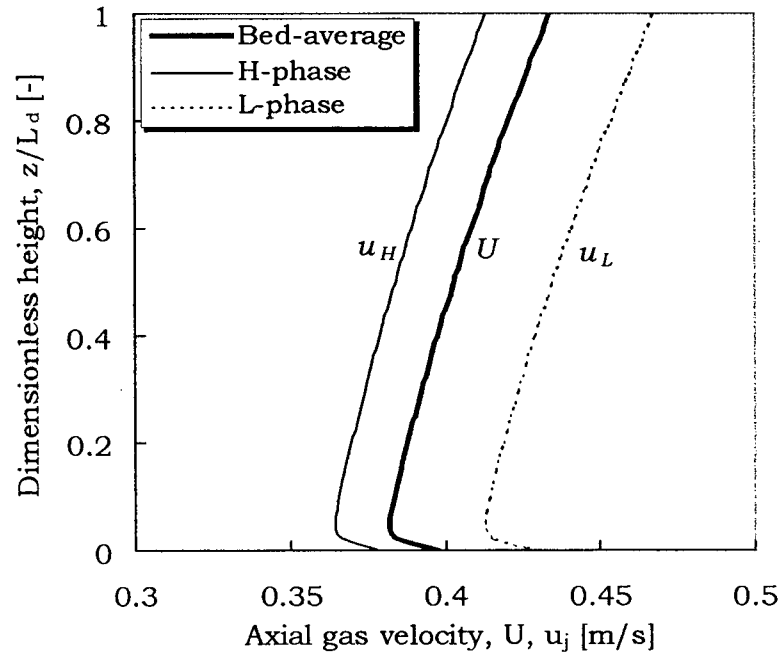
Figure 6.2. Predicted axial gas velocity profiles for case 4
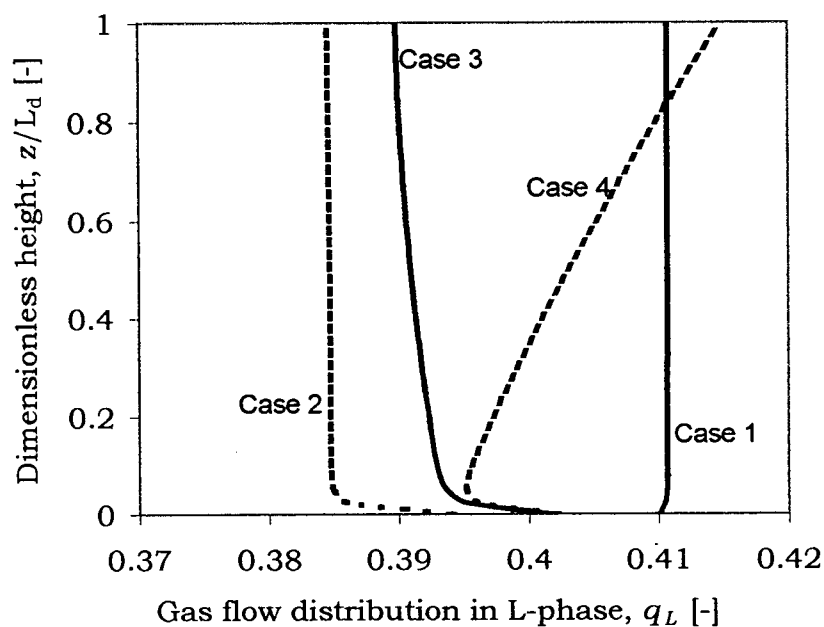
Figure 6.3. Predicted axial profiles of gas flow distribution in L-phase for conditions in Table 5.8 and cases in Table 6.1.
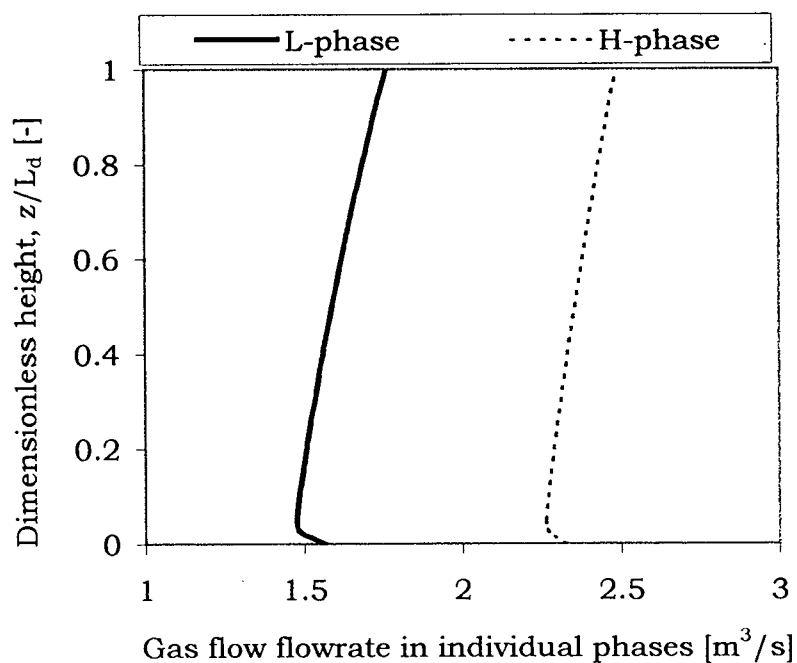
Figure 6.4. Predicted axial profiles of gas flow through both phases for case 4 in Table 7.1 and conditions given in Table 5.8.
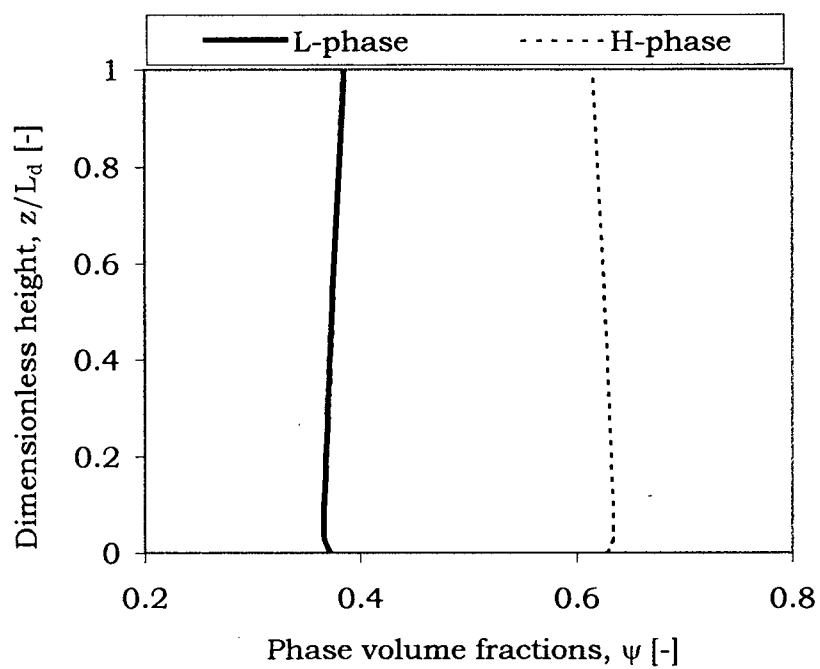
Figure 6.5. Predicted axial profiles for phase volume fractions, ψ, for case 4

6.4.1.3 Regime probabilities

Since the regime probabilities are functions of the superficial gas velocity, as well as of physical properties such as gas density and viscosity, the flow regimes within the bed may change causing the probabilities to vary with height. As shown in Fig. 6.6 for case 2, the probability of turbulent fluidization, P_{turb}, decreased sharply from nearly fully turbulent conditions ($P_{turb} \approx 93\%$) to approx. 83% immediately above the distributor (where the molar composition changes rapidly) and then continued to fall, with P_{turb} reaching about 75% at the bed surface. Note that although the effect of temperature and pressure on the gas velocity is not considered for this case, they affect the regime probabilities throughout the bed since all thermophysical properties are computed as functions of temperature and pressure. The influence on the gas velocity of the steep temperature rise (~85 K) at the distributor due to the strongly exothermic reactions and the subsequent mild temperature change of about 7 K (Fig. 6.7) along the rest of the bed is clearly captured by the plot for case 3. When the effect of pressure is also considered (case 4), an interesting trend is observed in Fig. 6.6. P_{turb} first decreases slightly, then increases gradually until near the bed surface it starts to decrease gradually again.

To explain the observed trend, consider the expanded version of the changes in the probabilities of all three flow regimes along the bed for case 4 presented in Fig. 6.8a. Figure 6.8b shows the generalized regime probability diagram based on the dimensionless gas velocity; the shaded area shows the approximate range of dimensionless gas velocity (U^* ranging from 1.3 to 1.7) along the bed height. The observed sharp change in the probabilities immediately above the distributor (Fig. 6.8a) is caused by volume increase due to rapid reactions, as discussed above, while the subsequent decrease can be attributed to the increase in gas velocity as the hydrostatic pressure decreases, partially offset by the small decrease in temperature. At about 80% of the total bed height, the probability of fast fluidization has increased enough to cause a decrease of the probability of turbulent fluidization after the turbulent plateau is passed.

Clearly, for operations in which there is a significant swing in the regime probabilities, multiple flow regimes can result (e.g., for an increase in the number of moles, predominantly bubbling around the grid and predominantly turbulent fluidization near the bed surface). The model accounts for such behaviour. It is also clear from the
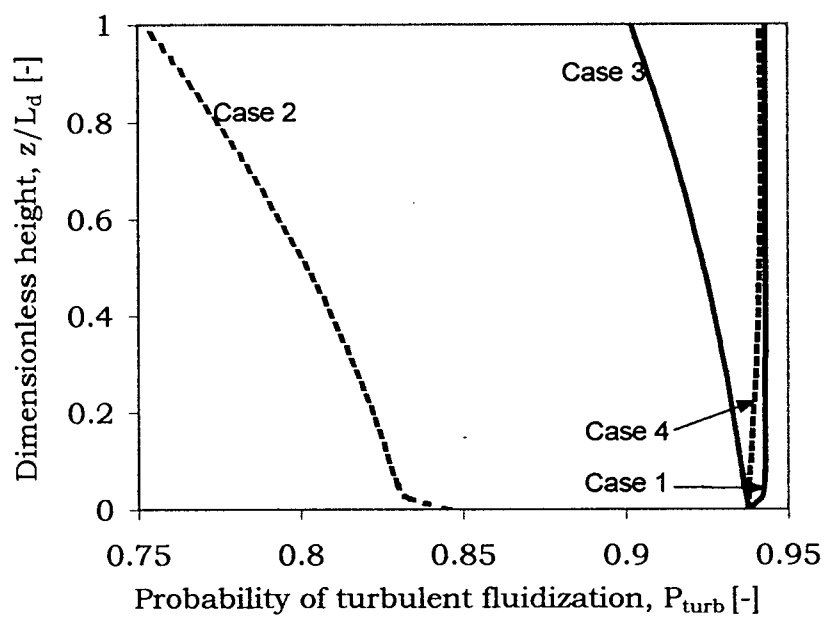
Figure 6.6. Axial profiles of probability of turbulent fluidization
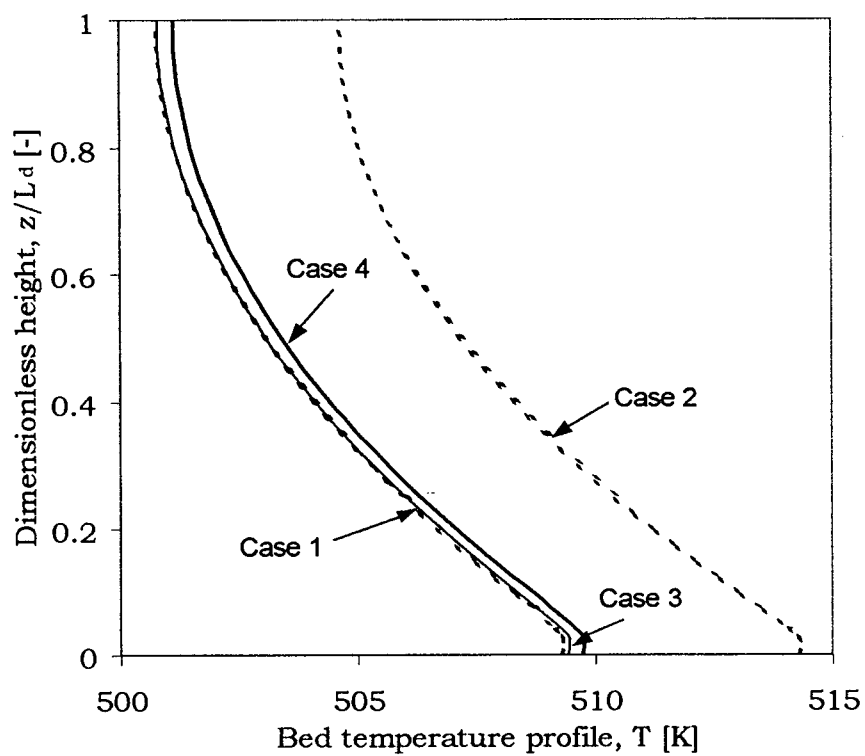
Figure 6.7. Axial profiles of bed temperature
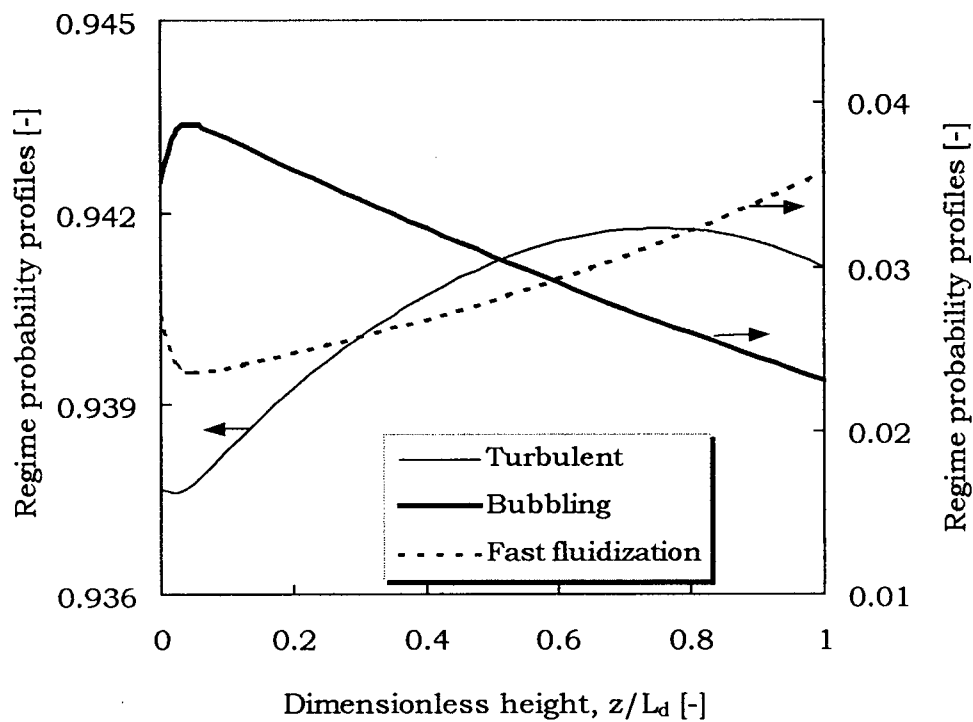
(a)
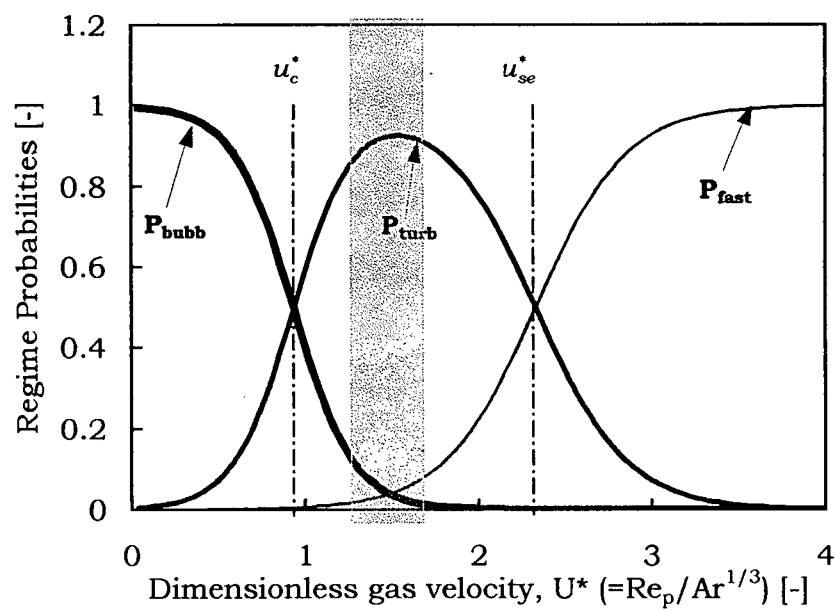
(b)

Figure 6.8. (a) Axial profiles of regime probabilities for case 4; (b) probability regime diagram based on dimensionless gas velocity

foregoing discussion that models that account for the effect of temperature and pressure in the computation of the thermophysical properties while neglecting their influence on the gas velocity, u (as in case 2), are prone to misrepresent the hydrodynamic conditions along the bed.

6.4.2 Effect of volume change on the reactor performance

Figure 6.9 shows the predicted conversion of ETY for the four cases identified in Table 6.1, normalized by the corresponding industrial conversion. Rapid conversion of ETY is observed immediately above the distributor, with the limiting reactant, HCl, approaching complete conversion in a short distance. The effect of the volume change can be seen by comparing case 1 with cases 2, 3 and 4. (Cases 3 and 4 are almost overlapping, with 3 slightly higher.) A decrease in the superficial gas velocity due to decreased molar flow leads to increased conversion of ETY because of the higher gas residence time in the bed, and this results in increased CO_x yield as shown in Fig. 6.10.

Table 6.2 compares the model predictions of reactor performance variables at the reactor exit for all four cases to the measured plant data. As expected, any decrease in superficial gas velocity results in increased conversion and increased CO_x yield. The decrease in EDC yield with decreasing bed-averaged velocity is due to formation of more oxidation products, as well as further oxidation of the EDC to impurities. In general, model predictions agree well with the plant data. Case 4 (with full allowance for volume change due to all three factors – change in total molar flow, temperature and pressure) appears to give the best overall agreement of the four cases considered.

Table 6.2. Comparison of per pass exit model predictions (normalized by exit plant data) for the four cases

	Conversion (-)		Yield (-)			Selectivity (-)		
	ETY	HCl	EDC	CO_x	IMP	EDC	CO_x	IMP
Case 1	0.999	1.003	0.997	1.126	0.766	0.998	1.127	0.768
Case 2	1.010	1.003	0.995	1.582	1.026	0.985	1.567	1.016
Case 3	1.002	1.003	0.996	1.239	0.897	0.994	1.237	0.896
Case 4	1.001	1.003	0.996	1.214	0.905	0.995	1.213	0.905
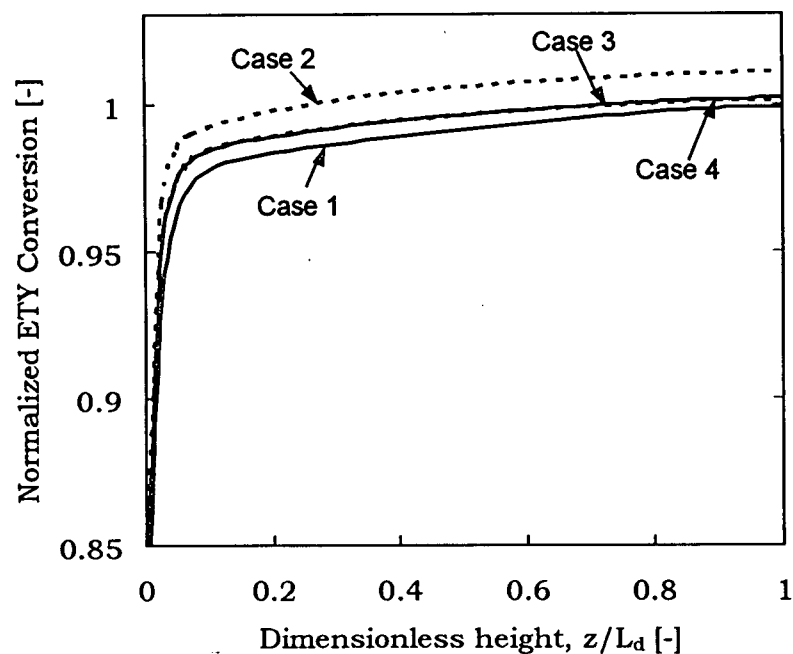
Figure 6.9. Axial profiles of ethylene conversion normalized by plant exit conversion for the four cases identified in Table 6.1.
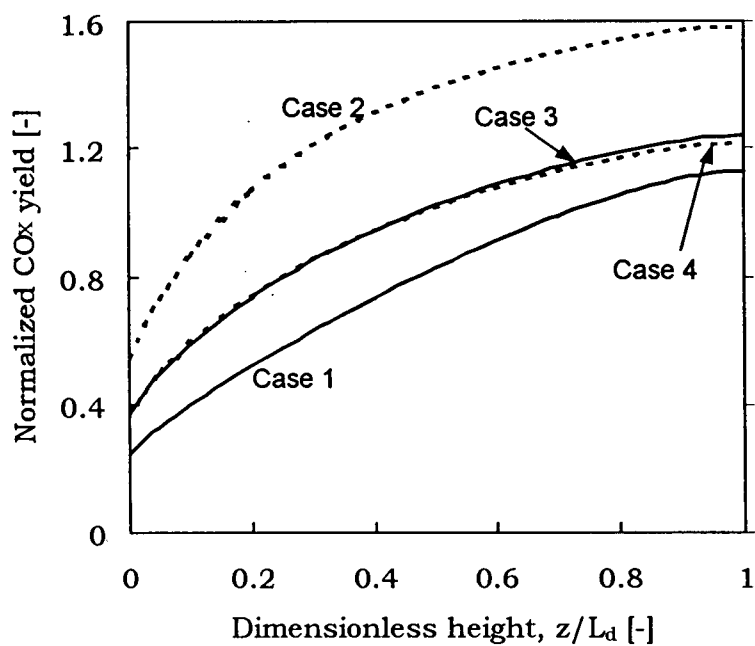
Figure 6.10. Axial profiles of CO_X yield normalized by plant exit value for the same cases as in Fig. 6.9.

6.4.3 Effect of bulk transfer of gas between phases

Results presented up to this point ignore any bulk transfer of gas between the two phases, implicitly assuming that extra moles of gas generated within one phase remain with that phase. The distribution of additional moles between phases when there is an increase or decrease presents a dilemma. While there is some experimental evidence (Adris et al., 1993) that at least some of the extra moles generated in the H-phase end up in the L-phase, it is not clear how quickly or to what extent this occurs. Also it is not clear whether redistribution is best handled via non-equimolar interphase mass transfer, or by assuming bulk flow of gas. One approach (e.g. Adris et al., 1997) is to take any extra moles generated in the H-phase and assign them directly to the L-phase as the reaction proceeds.

Here, we examine the impact of the interphase bulk flow of excess gas between phases on the hydrodynamics and reactor performance for cases 2 and 4. Consider the two-phase/region model shown schematically in Fig. 6.11. The change in volumetric flow with reaction in the jth phase can be represented by

$$Q_j^{'} = Q_j - Q_{jo} = Q_{jo}\Gamma_j \tag{6.25}$$

where

$$\Gamma_j = \left(\frac{F_{T,j}}{F_{To}} \frac{T}{T_o} \frac{P_o}{P} - 1 \right) \tag{6.26}$$

Mindful of the uncertainties regarding how the excess gas may be distributed and transferred between the phases, the following assumptions are made:

- Only a fraction $(1 - q_j)$ of the excess gas generated in the jth phase is transferred to the other phase such that the transfer flow is $(1 - q_j)Q_j^{'}$. The difference, $q_j Q_j^{'}$, remains in the phase in which it is generated. As a result, at every grid point, the net change in volumetric flow through the L-phase is $(Q_H^{'} - Q_L^{'} + q_L Q_L^{'} - q_H Q_H^{'})$. Similarly for the H-phase, the net change is $(Q_L^{'} - Q_H^{'} - q_L Q_L^{'} + q_H Q_H^{'})$.

- Bulk transfer of excess gas between the phases is assumed to occur immediately (at the level at which it is produced). In reality, the gas generated (when expansion
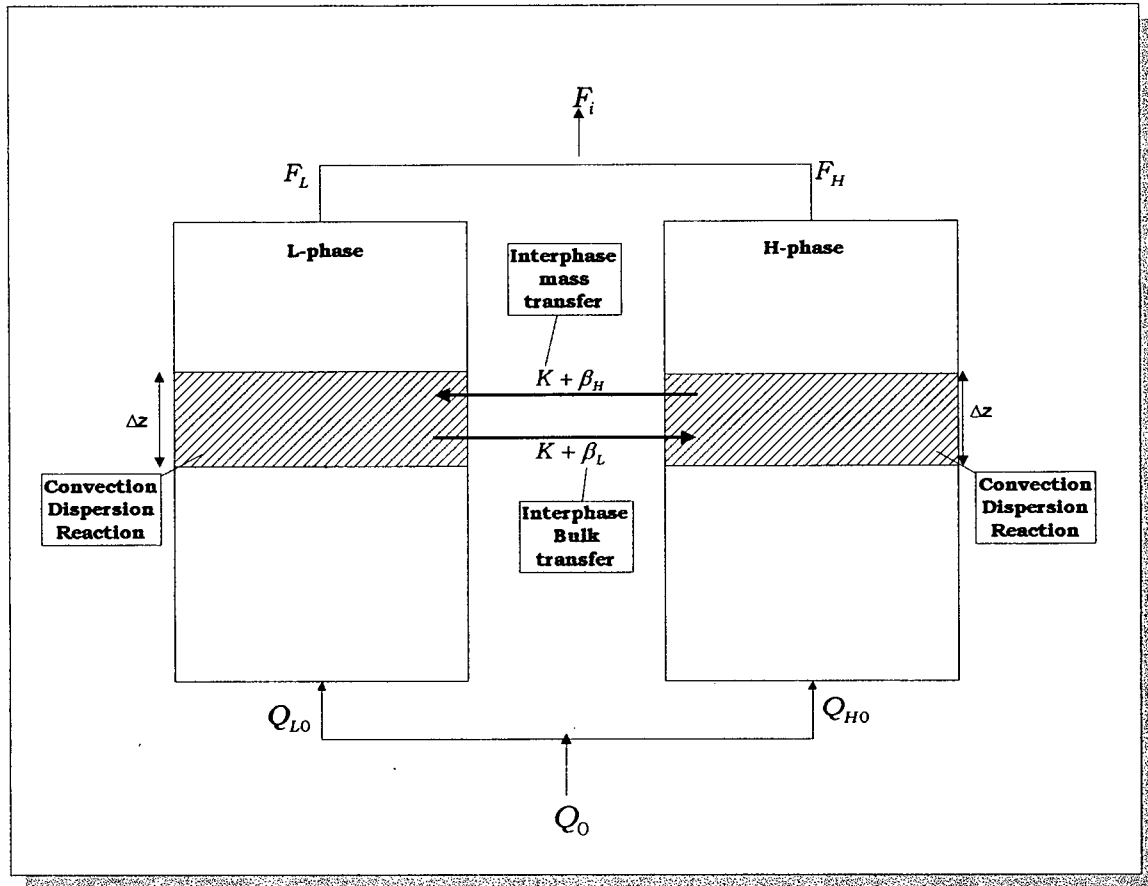
Figure 6.11. Schematic of generalized one-dimensional, two-phase/region model

occurs, for instance) may remain in the same phase for some distance before transferring to the other phase.

The excess gas flow transferred from the jth phase to the other phase is

$$Q'_{j,transferred} = (1 - q_j)Q_{jo}\Gamma_j \qquad (6.27)$$

The gas flow transferred from the jth phase per unit volume of the jth phase is

$$\beta_j = \frac{Q'_{j,transferred}}{\Delta V_j} = \frac{(1 - q_j)Q_{jo}\Gamma_j}{\psi_j A\Delta z} \qquad (6.28)$$

The interphase mass transfer is augmented by β_j so that eqs. (6.20) and (6.21) become:

L-phase:
$$\frac{\partial(F_{iL})}{\partial z} - \mathcal{D}_{zg,L}\frac{\partial^2(F_{iL}/U)}{\partial z^2} - \mathcal{D}_{rg,L}\frac{1}{r}\frac{\partial}{\partial r}\left(r\frac{\partial(F_{iL}/U)}{\partial r}\right)$$
$$+ [(K + \beta_L)F_{iL} - (K + \beta_H)F_{iH}]/U \times \psi_L) + A\rho_L Rate_{iL} = 0 \qquad (6.29)$$

H-phase:
$$\frac{\partial(F_{iH})}{\partial z} - \mathcal{D}_{zg,H}\frac{\partial^2(F_{iH}/U)}{\partial z^2} - \mathcal{D}_{rg,H}\frac{1}{r}\frac{\partial}{\partial r}\left(r\frac{\partial(F_{iH}/U)}{\partial r}\right)$$
$$+ [(K + \beta_H)F_{iH} - (K + \beta_L)F_{iL}]/(U \times \psi_H) + A\rho_H Rate_{iH} = 0 \qquad (6.30)$$

Figure 6.12 compares model predictions of volumetric flow through the two phases for cases 2 and 4 when the bulk flow between phases is considered and when it is ignored. The volumetric flow through the L-phase is increased, as more gas is bulk transferred to the L-phase. Note that the approach outlined here ensures that at all grid points along the bed height the phase flow ratio (i.e. ratio of volumetric flow through the H-phase to that through the L-phase, Q_H/Q_L) remains nearly constant. This approach also avoids potential phase defluidization even if there were to be substantial volumetric flow reduction.

The effect of the change in flow distribution on the reactor performance is shown in Fig. 6.13 for cases 2 and 4. Inclusion of allowance for bulk transfer makes prediction slightly worse. The effect can be appreciable well away from the turbulent fluidization flow regime where the extent of reaction in the two phases differs markedly and when the interphase mass transfer resistance is significant. The effect of bulk flow is, however, small in the present case because the reductions in volume in the two phases are comparable since the bed operates under almost fully turbulent conditions (where the phases become identical in the model). Given this insensitivity, the agreement between the plant data and model predictions is not changed appreciably by the treatment of the flow distribution between phases in the present case.
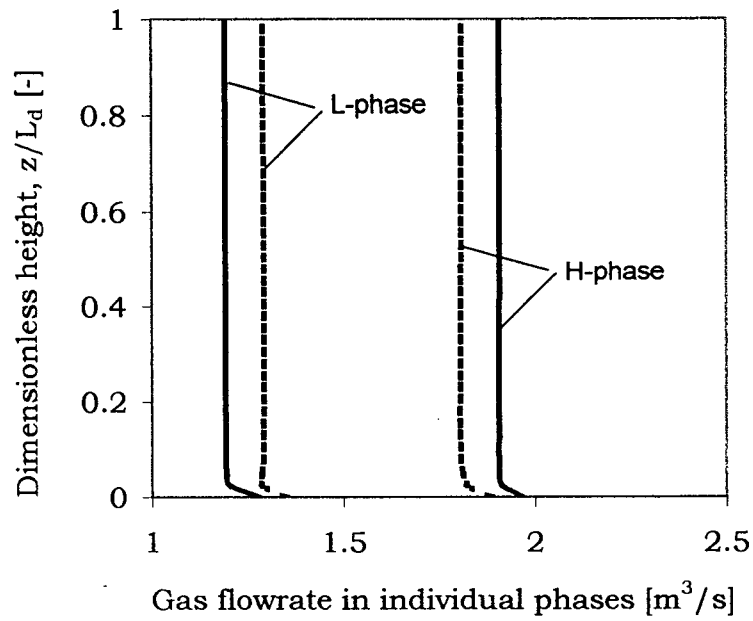
(a)
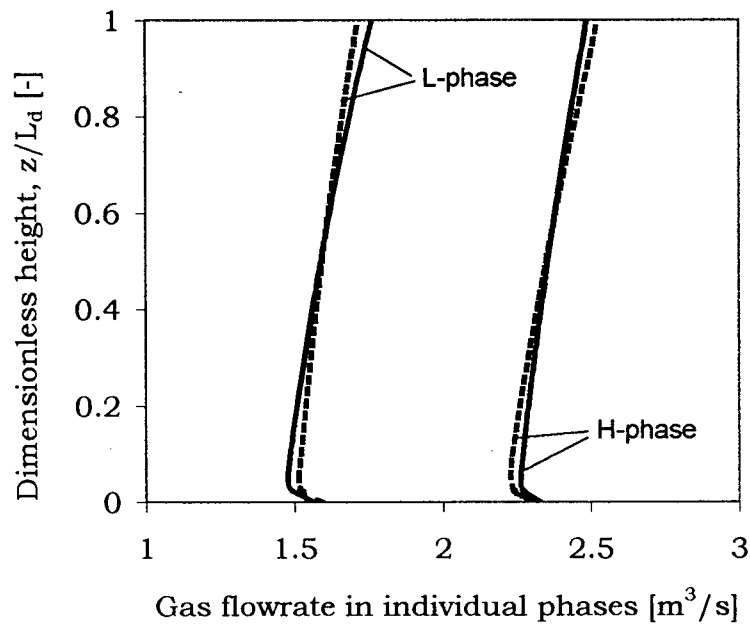
(b)

Figure 6.12. Axial profiles of the total gas flow Q for the L- and H-phases: (a) case 2, (b) case 4 [——: bulk transfer between phases ignored; -----: bulk transfer between phases considered]
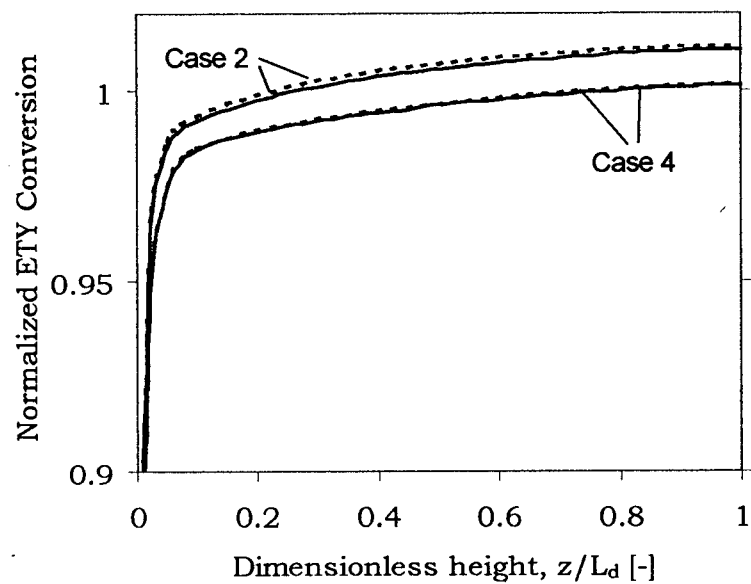
(a)
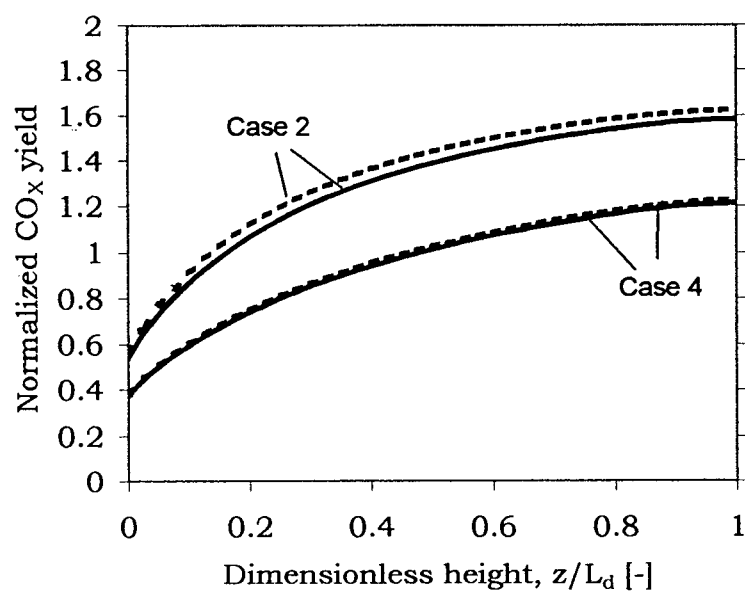
(b)

Figure 6.13. Axial profiles normalized by plant exit data for cases 2 and 4: (a) CO$_x$ yield, (b) ETY conversion[——: bulk transfer between phases ignored; -----: bulk transfer between phases considered]

Notwithstanding the lack of sensitivity to bulk flow in the present example, the bulk transfer of excess gas between phases should be included when considering reactions with volume change in fluid bed reactor models. This is especially important when operating well above, or well below, superficial velocities for maximum P_{turb}, since the interphase mass transfer resistance then plays a major role and the difference between phases is large when either the bubbling or fast fluidization probabilities are significant.

6.5 Conclusions

The generalized probabilistic fluidized bed reactor model is extended to cover variable-gas density systems. Using the air-based oxy-chlorination process as a case study, it is shown that a change in the number of moles due to reaction significantly affects the hydrodynamics, conversion, selectivity and yield. Multiple flow regimes can exist in the same reactor due to the changing volumetric flow. The impact of varying the temperature and pressure non-uniformity along the bed height on the gas velocity and, in turn, on the hydrodynamics and reactor performance is also examined. Allowing for the volume change due to reaction, temperature variations and the decrease in hydrostatic pressure with height improves the performance of the model somewhat in the oxy-chlorination case relative to industrial data, in particular, significantly improving the impurities predictions. Bulk transfer of gas between the phases influences both the hydrodynamics and the reactor performance. This influence is small when the fluidized bed operates primarily in the turbulent flow regime, but may be appreciable when bubbling or fast fluidization predominates.

The effects of volume change on reaction may be even more important for some other processes, e.g. where there is a larger change in the number of moles due to reaction. The version of the GFBR model incorporating allowance for the volume change is therefore recommended as the major product of this thesis.

Chapter 7

Overall Conclusions and Recommendations

7.1 Conclusions

The principal outcome of this research is the development of a new generic fluid bed reactor (GFBR) model applicable across the fluidization flow regimes most commonly encountered in industrial scale fluid bed reactors: bubbling, turbulent and fast fluidization. The model interpolates between three regime-specific models – the generalized two-phase bubbling bed model, dispersed flow model and the generalized core-annulus model – by means of probabilistic averaging of hydrodynamic and dispersion variables based on the uncertainty in the flow regime transitions.

Specific conclusions from the different aspects studied can be summarized as:

1) Model predictions of hydrodynamic variables across the three fluidization flow regimes are realistic, while conversion predictions are in good agreement with available experimental data. The probabilistic approach leads to improved predictions of reactor performance compared with any of the three separate models for individual flow regimes, while overcoming the difficulties in predicting the transition boundaries among these flow regimes and avoiding discontinuities at the boundaries between them.

2) The performance of the model is assessed using two industrial-scale catalytic processes: oxidation of naphthalene to phthalic anhydride and oxy-chlorination of ethylene. In both cases, model predictions were reasonable and compare favourably with available plant data within the constraints of the uncertainties in the estimation of the model parameters. Sensitivity analysis indicates that predictions from the model are strongly influenced by the reaction kinetics, gas dispersion, superficial gas velocity and reactor temperature. Accuracy of the model predictions depends strongly on utilizing reliable estimates of the model parameters. Ability of the model to aid in simulation experimentation over a wide range of conditions is also demonstrated.

173

3) The generic reactor model has been extended to cover systems accompanied by volume change due to a change in the number of moles, as well as variations in temperature and pressure along the reactor. Using the air-based oxy-chlorination process as a case study, it is shown that these changes significantly affect the hydrodynamics, conversion, selectivity and yield. Accounting for the volume changes improves the performance of the model relative to industrial data. Multiple flow regimes can exist in the same reactor due to the varying volumetric flow. The probabilistic modeling approach effectively tracks changes in flow regimes within the reactor. Moreover, bulk transfer of gas between the phases also influences both the hydrodynamics and the reactor performance. This influence is small when the fluidized bed operates primarily in the turbulent flow regime, but may be appreciable when bubbling or fast fluidization predominates.

4) Application of the GFBR model to gas-solid reactions is demonstrated using the zinc sulfide roasting process as a case study. Predictions from a combined model that couples a single-particle model with the generic fluid bed reactor model are reasonable. However, in order to fully realize the potential of the combined model, some extensions are suggested. Such extensions are likely to have significant impact on the model performance only for systems where the solids mean residence time is similar to the time for complete conversion of particles.

5) Gas mixing experiments were conducted in a Plexiglas column with commercial catalyst particles as bed material at superficial gas velocities from 0.2 to 0.6 m/s. Data from both steady state and step change tracer injection experiments are interpreted using a single-phase dispersion model and a generalized two-phase model with dispersion. The generalized two-phase model captures the expected trends of increasing dispersion in both the low- and high-density phases with increasing superficial gas velocity. Beyond the transition velocity, U_c, however, the overall dispersion decreased for $L_o = 1.0$ m. Results for different gas velocities and aspect ratios suggest that the dispersion coefficients and interphase mass transfer coefficient between the low- and high-density phases depends on the initial solids inventory.

6) The GFBR model provides a means of predicting hydrodynamics regimes and quantities in fluid bed reactors. For example, for a given set of particle properties, operating conditions and reactor geometry, it is possible to predict the fluidization regime(s) in which the reactor operates.

7.2 Recommendations for Future Work

1) Further gas mixing experiments are suggested to provide additional data for scale-up. Specifically, it is recommended to: (a) Conduct experiments at different static bed heights, preferably in taller columns for the same or similar column diameters as used in this study. (b) Conduct experiments in columns of different diameters for the same static bed height, i.e., changing the aspect ratio, L_o/D_t, while keeping L_o constant. Results from this and (a) above, when combined together with the results from this study and available literature data, would help establish the effect of the aspect ratio on both the interphase mass transfer and gas dispersion in the bed.

2) It would be helpful to conduct experiments in columns of similar geometry for superficial gas velocities beyond the range considered in this study. Specifically, it would be valuable to study the effect of increasing U on the ratio, $\mathcal{D}_{zg,L} / \mathcal{D}_{zg,H}$, which is expected to approach unity for $U \approx U_c$. It would also be valuable to develop separate correlations for the dispersion coefficients in the two phases using data from this and (1) above.

3) Several modifications and extensions could be made to the combined "fluid-bed-single-particle" model at both the particle and the fluid bed levels, namely: (i) Allow for separate solid RTDs in the L- and H-phases; (ii) Refine the approach for predicting solids interchange between phases for proper implementation of approach A1 presented in Chapter 5a; (iii) Consider a wide particle size distribution in the bed; (v) Account for changes in particle porosity with time depending on whether the solids expand, shrink or retain their original shapes as they react.

4) Apply the combined model to other gas-solids reactions, in particular, to polymerization processes. For this class of applications, it is possible to fully incorporate the particle size distribution through a particle population balance. Preliminary simulations performed for ethylene polymerization process show good promise. This extension, combined with the modifications in (3) above could create a valuable tool for simulating a wide range of fluid bed processes involving gas-solid reactions.

5) An alternative approach to constructing the generic model through probabilistic averaging would be to consider flow regime transition from a two-phase bubbling bed at low U to a homogeneous single-phase flow structure with both axial and radial non-uniformities at intermediate and high U (eliminating the core-annular consideration at the high-velocity limit). To implement this, the regime transition equations need to be modified to ensure that the global model interpolates between two limiting models (generalized two-phase bubbling bed model and the axially/radially dispersed flow model). The values of the dispersion parameters would need to be extrapolated among the limiting values of the three flow regimes as flow condition changes. In addition to the reported success of the single-phase two-dimensional model in the fast fluidization limit, this approach would have the advantage of reducing the number of model parameters.

6) It would be valuable to fine tune this model and to develop a better user interface to enable delivery of the research outcome to industry as well as other users without the demand of familiarity with the modeling language, while recognizing that a "standard-all-purpose-package" may lead to sub-optimal solutions in some cases because of varying objectives.

Nomenclature

a_I	Interphase transfer surface area per unit volume of gas in low-density phase	m^{-1}
a_{ki}, b_{kl}	Stoichiometric coefficients of gaseous species i and solid l, respectively, in reaction k	[-]
A	Bed cross-sectional area	m^2
A_i	Gaseous component i as reactant or product	[-]
Ar	Archimedes number, $\rho_g(\rho_p - \rho_g)g\overline{d}_p^3/\mu^2$	[-]
A_s	Covered heat transfer surface area per unit reactor volume	m^{-1}
A_X	Reaction surface or area per unit volume of reaction space	m^{-1}
B_l	Solid component l as reactant or product	[-]
C	Concentration of helium	Vol %
C_o	Concentration of helium at inlet	Vol %
C_∞	Concentration of helium at infinite mixing	Vol %
C_i	Concentration of species i	mol/m^3
$\overline{C}_i$	Bed-averaged (radially and axially) concentration of species i	mol/m^3
$C_{i,L}$	Concentration of species i in L-phase	mol/m^3
$C_{i,H}$	Concentration of species i in H-phase	mol/m^3
C_{pg}	Specific heat of gas	J/mol K
C_{Pp}	Specific heat of solids	J/mol K
d_b	Volume-equivalent bubble diameter	m
$\overline{d}_p$	Mean particle diameter	m
$\mathcal{D}$	Molecular diffusivity of gas	m^2/s
$\mathcal{D}_e$	Effective diffusivity of gases through product layer	m^2/s
$\mathcal{D}_{mix}$	Mixture diffusivity	m^2/s
D_t	Column/reactor diameter	m
$\mathcal{D}_{z,g}$	Axial gas dispersion coefficient	m^2/s
$\mathcal{D}_{r,g}$	Radial gas dispersion coefficient	m^2/s

$\mathcal{D}_{zg,b}$	Gas backmixing coefficient	m^2/s
e	Error or uncertainty in regime boundary estimation	m/s
$E(t)$	Exit age distribution function or residence time distribution	1/s
f_{pe}	Adjustable parameter in the expression for Peclet number	[-]
$f_k(\mathbf{C}^p)$	Intrinsic reaction rate per unit surface area for reaction k	-
F	Cross-sectional average molar flowrate	mol/s
$F_{i,L}, F_{i,H}$	Molar flowrate of species i in L- and H-phases	mol/s
$F(t)$	Cumulative distribution function	
F_G, F_P	Grain and particle shape factors [flat plate = 1; cylinder = 2; sphere = 3]	[-]
F_{in}, F_{out}	Feed, exit molar flow rates	mol/s
g	Gravitational acceleration	m/s^2
f_{pe}	Parameter used to adjust Peclet number	[-]
G_{so}	Average solids flux under fast fluidization conditions	$kg/m^2 s$
G_s	Net solids circulation rate	$kg/m^2 s$
h	Overall bed-to-surface heat transfer coefficient	$W/m^2.K$
H	Hypothesis (e.g., bubbling, turbulent, fast fluidization regimes etc.)	
ΔH_k	Heat of reaction k	kJ/kmol
$k_{c,j}$	External mass transfer coefficient in j-phase	m/s
k_e	Effective axial thermal conductivity of solids	W/m.K
k_{LH}	Gas interchange coefficient between L and H phases	m/s
k_r	Reaction rate constant	1/s
K	Interphase volumetric mass transfer coefficient	1/s
L	Column height at any level	m
L^-	Downwards axial distance from tracer injection level	m
L_d	Dense bed height	m
L_f	Freeboard height	m

L_o	Static bed height	m
L_t	Total column height	m
M_i	Molecular weight of gaseous species i	kg/mol
M_l	Molecular weight of solid l	kg/mol
M_s	Solids inventory	kg
$\dot{m}_{in}$	Solids feed rate	kg/s
$\dot{m}_{out}$	Solids exit rate	kg/s
n_i	Number of moles of gaseous species i	mol
n_l	Number of moles of solid species l	mol
N	Number of compartments in series	[-]
N_i	Flux of component i	mol/m^2.s
N_g	Number of gaseous components	[-]
N_r	Number of reactions	[-]
N_s	Number of solid components	[-]
P	Pressure	kPa
P_j	Probability of being in regime j	[-]
P_L, P_H	Probabilities of solids being in L- and H-phases (Chapter 5c)	[-]
P_o	Inlet pressure	kPa
$p(.)$	Probability density function (pdf)	s/m
$p(. \mid .)$	Conditional probability density function	[-]
Pe_H	H-phase Peclet number, $u_H L_d / \mathcal{D}_{zg,H}$	[-]
Pe_L	L-phase Peclet number, $u_L L_d / \mathcal{D}_{zg,L}$	[-]
Pe_z	Peclet number, $U L_d / \mathcal{D}_{zg}$	[-]
Pe_{z1}	Peclet number based on L_d, $U L_d / \mathcal{D}_{z,g}$	[-]
Pe_{z2}	Peclet number based on L_t, $U L_t / \mathcal{D}_{z,g}$	[-]
q	Gas flow fraction	[-]
Q	Gas flow rate	m^3/s
r	Radial coordinate	m

r_C	Core radius	m
r_{c_l}	Reaction front radius of grain l	m
r_k	Rate expression for reaction k	kmol/kg s (kmol/m^3 s)
r_{o_l}	Initial radius of grain l	m
R	Column radius	m
R_p	Radius of particle	m
Re$_c$	Reynolds number based on U_c, $\rho_g U_c \bar{d}_p / \mu$	[-]
Re$_p$	Particle Reynolds number, $\rho_g U \bar{d}_p / \mu$	[-]
Re$_{se}$	Reynolds number based on U_{se}, $\rho_g U_{se} \bar{d}_p / \mu$	[-]
t	Time	s
t_m	Mean residence time of gas	s
$\bar{t}_j$	Mean residence time of solids in j-phase	s
T	Reactor temperature	K
T_{ave}	Reactor average temperature	K
T_{cool}	Coolant temperature	K
T_o	Inlet temperature	K
u_{br}	Bubble rise velocity	m/s
u_j	Gas velocity in phase j	m/s
U	Superficial velocity of gas at any level	m/s
U^*	Dimensionless superficial gas velocity, $U[\rho_g^2 / \mu g(\rho_p - \rho_g)]^{1/3}$	[-]
U_c	Transition velocity from bubbling to turbulent fluidization	m/s
U_i	Transition velocity to regime i	m/s
U_{DSU}	Onset of dense suspension upflow	m/s
U_{se}	Transition gas superficial velocity to fast fluidization regime, corresponding to significant solids entrainment	m/s
v_c	Normalized transition velocity from bubbling to turbulent fluidization	[-]
v_{se}	Normalized transition velocity to fast fluidization regime, corresponding to significant solids entrainment	[-]

v_t	Terminal settling velocity of particles	m/s
x	Any hydrodynamic variable (e.g., k_q, ϕ_L, $\mathcal{D}_{z,g,L}$ etc.)	
x_l	Local conversion of grain l	[-]
X_{ETY}	Ethylene conversion	[-]
X_l	Conversion of particle l at a given time	[-]
X_i	Conversion of base gaseous reactant i	[-]
X_{O_2}	Overall oxygen conversion	[-]
$\overline{X}_{l,j}$	Overall conversion of particles in j-phase leaving bed	[-]
$\overline{\overline{X}}_l$	Phase-averaged conversion of particles leaving bed	[-]
y	Set of performance variables (e.g., conversion, selectivities etc.)	
z	Axial coordinate, positive upwards, measured from grid (in Chapter 3, from tracer injection level)	m
Z	Compressibility factor	[-]

Greek symbols

α, ϖ	Constants in eqs. (3.8)-(3.12)	[-]
β	Fitting parameter in logistic regression function	[-]
β	Gas transfer rate/control volume as defined in eq. (6.28)	1/s
ε	Voidage	[-]
$\overline{\varepsilon}$	Cross-sectional average voidage	[-]
ε^p	Particle porosity	[-]
γ, Γ	Expansion/reduction factor	[-]
μ	Absolute viscosity of gas	kg/m s
ϕ	Solids volume fraction	[-]
ϕ^*	Saturation carrying capacity	[-]
ρ	Density	kg/m^3
σ	Standard deviation of uncertainty in regime boundary correlation	m/s
σ	Standard deviation of RTD	s^2

ψ	Phase volume fraction	[-]
Ψ_{slip}	Slip factor $= 1 + 5.6/Fr^2 + 0.47 Fr_t^{0.41}$	[-]
θ	Set of operating conditions and physical properties (e.g., T_o, P_o, ρ_g, etc.)	
ν	Stoichiometric coefficient	[-]
χ	Dimensionless interphase mass transfer coefficient	[-]

Subscripts

a	Annular (outer) region
b	Bubble phase or bubble
$bubb$	Bubbling flow regime
c	Critical
C	Core region
CA	Type A or accumulative choking
d	Dense phase
f	Freeboard
$fast$	Fast fluidization flow regime
g	Gas
G	Grain
H	High density phase
L	Low density phase
mb	Minimum bubbling
mf	Minimum fluidization
o	Initial/Inlet
p	Particle
r	Radial
s	Surface
se	Significant entrainment

t	Total
$turb$	Turbulent flow regime
z	Axial

Superscript

*	Dimensionless variable

Abbreviations

CO_x	Carbon oxides (CO and CO_2)
$GFBR$	Generic fluid bed reactor
GPM	Grain particle model
IMP	Chlorinated by-products/impurities
MCC	Mitsubishi Chemical Corporation
NA	Naphthalene
NQ	Naphthaquinone
OC	Oxy-chlorination
OP	Oxidation products (primarily Maleic anhydride, CO, CO_2)
PA	Phthalic anhydride
PSD	Particle size distribution
RTD	Residence time distribution
UBC	University of British Columbia

References

Abed, R., The characterization of Turbulent Fluid Bed Hydrodynamics, in *Fluidization IV* (eds. Kunii, D. and R. Toei), Engineering Foundation, New York, pp. 137-144, (1984).

Abrahamsen, A.R. and D. Geldart, Behavior of Gas-Fluidized Beds of Fine Powders, Part I. Homogeneous Expansion, *Powder Tech.*, **26**, 35-46 (1980).

Adris, A.M., C.J. Lim and J.R. Grace, The Effect of Gas Volume Increase due to Reaction on Bed Expansion, Bubbling and Overall Conversion in a Fluidized Bed Reactor, *AIChE Annual Meeting*, St. Louis, November, pp. 7-12 (1993).

Adris, A.M., C.J. Lim and J.R. Grace, The Fluidized Bed Membrane Reactor for Steam Methane Reforming: Model Verification and Parametric Study. *Chem. Eng. Sci.*, **52**, 1609-1622 (1997).

Arena, U., Gas Mixing, Chap. 3, in Circulating Fluidized Beds, (eds. Grace, J.R., A.A. Avidan and T.M. Knowlton), Chapman and Hall, London (1997).

Arena, U., R. Chirone, M. D'Amore, M. Miccio and P. Salatino, Some Issues in Modeling Bubbling and Circulating Fluidized Bed Coal Combustors, *Powder Tech.*, **82**, 943-949 (1995).

Avedesian, M.M, Roasting Zinc Concentrates in Fluidized Beds – Practice and Principles, *24th CSChE Meeting*, Ottawa, October 1974.

Avidan, A.A., Future Prospects, Chap. 17, in Circulating Fluidized Beds (eds. J.R. Grace, A.A. Avidan and T.M. Knowlton), Chapman and Hall, London, pp. 568-577 (1997).

Avidan, A.A., Turbulent Fluid Bed Reactors Using Fine Powder Catalysts, *AIChE-CIESC.* Meeting, Chemical Industry Press, Beijing, pp. 411-423 (1982).

Banerjee, A., Y. Arkun, B. Ogunnaike and R. Pearson, Estimation of Nonlinear Systems Using Linear Multiple Models, *AIChE J.* **43**, 1204-1226 (1997).

Berg, D.A., C.L. Briens and M.A. Bergougnou, Reactor Development for the Ultrapyrolysis Reactor, *Can. J. Chem. Eng.*, **67**, 96-101 (1989).

Berger, J. O., Statistical Decision Theory and Bayesian Analysis, New York, McGraw-Hill (1985).

Bernardo, J. M. and A. F. M. Smith, Bayesian Theory, New York, Wiley (1994).

Berruti, F., J. Chaouki, L. Godfroy, T.S. Pugsley and G.S. Patience, Hydrodynamics of Circulating Fluidized Bed Risers: a Review, *Can. J. Chem. Eng.*, **73**, 579-602 (1995).

Bi, H.T., Ellis, N., Abba, I.A. and Grace, J.R., A State-of-the-art Review of Gas-Solid Turbulent Fluidization, *Chem. Eng. Sci.*, **55**, 4789-4825 (2000).

Bi, H.T. and J.R. Grace, Effects of Measurement Method on Velocities Used to Demarcate the Transition to Turbulent Fluidization, *Chem. Eng. J.*, **57**, 261-271 (1995b).

Bi, H.T. and J.R. Grace, Flow Regime Diagrams for Gas-Solids Fluidization and Upward Transport, *Int. J. Multiphase Flow*, **21**, 1229-1236 (1995a).

Bi, H.T., J.R. Grace and J.X. Zhu, Regime Transitions Affecting Gas-Solids Suspensions and Fluidized Beds, *Trans. I. Chem. Engr.*, **73**, 154-161 (1995).

Bi, H.T., J.X. Zhu, J. Qin and J.R. Grace, Annular Wall Layer Thickness in CFB Risers, *Can. J. Chem. Eng.*, **74**, 811-814 (1996).

Bolthrunis, C.O., An Industrial Perspective on Fluid Bed Reactor Models, *Chem. Engng. Prog.*,51-54, May 1989.

Brereton, C.H.M., J.R. Grace, and J. Yu, Axial Gas mixing in Circulating Fluidized Bed, in *Circulating Fluidized Bed Technology II* (eds. P. Basu and J.F. Large), Pergamon, Oxford, pp. 307-314 (1988).

Chaouki, J., D. Klvana, and C. Guy, Selective and Complete Catalytic Oxidation of Natural Gas in Turbulent Fluidized Beds. *K. J. Chem. Eng.*, **16**, 494-500 (1999).

Chavarie, C. and J.R. Grace, Performance Analysis of a Fluidized Bed Reactor II. Observed Reactor Behaviour Compared with Simple Two-Phase Models, *Ind. Eng. Chem. Fundam.*, **14**, 79-85 (1975).

Cho, H., Chung, C., Han, G., Ahn, G and Kong, J., Axial Gas Dispersion in a Fluidized Bed of Polyethylene Particles, *Korean J. Chem. Eng.*, **17**, 292-298 (2000).

Choi, J.H., Ryu, H.J., Shun, D.W., Son, J.E., & Kim, S.D, Temperature Effect on the Particle Entrainment Rate in a Gas Fluidized Bed, *Ind. Eng. Chem. Res.*, 37, 1130-1135 (1998).

Clift, R., Hydrodynamics of Bubbling Fluidized Beds, Chap. 4, in Gas Fluidization Technology, (ed. Geldart, D.), John Wiley and Sons Ltd., Chichester, pp. 53-96 (1986).

Clift, R. and J.R. Grace, Continuous Bubbling and Slugging, Chap.3 in Fluidization, 2nd ed., (eds. J. F. Davidson, R. Clift and D. Harrison), Academic Press, London, pp. 73-132 (1985).

Contractor, R.M., G.S. Patience, D.I. Garnett, H.S. Horowitz, G.M. Sisler and H.E. Bergner, A New Process for n-Butane Oxidation to Maleic Anhydride Using a

Circulating Fluidized Bed Reactor, in *Circulating Fluidized Bed Technology IV*, (ed. A.A. Avidan), AIChE, New York, pp. 387-389 (1994).

Cowfer, J.A. and A.J. Magistro, Vinyl Chloride. *Kirk-Othmer Encyclopedia of Chemical Technology*, vol. 23, pp. 865-885 (1984).

De Maria, F., J.E. Longfield and G. Butler, Catalytic Reactor Design, *Ind. Eng. Chem.*, **53**, 259-266 (1961).

Dias, C.R., Portela, M.F. and Bond, C.G., Synthesis of Phthalic Anhydride: Catalysts, Kinetics, and Reaction Modeling, *Catal. Rev.-Sci. Eng.*, **39**, 169-207 (1997).

Ding, J. and D. Gidaspow, A Bubbling Fluidization Model Using Kinetic Theory of Granular Flow, *AIChE J.* **36**, 523-538 (1990).

Edwards, M. and A. Avidan, Conversion Model Aids Scale-Up of Mobil's Fluid Bed MTG Process, *Chem. Eng. Sci.*, **41**, 829-835 (1986).

Ege, P., A. Grislingås and H.I. deLasa, Modeling Turbulent Fluidized Bed Reactors: Tracer and Fibre Optic Probe Studies, *Chem. Eng. J.*, **61**, 179-190 (1996).

Ellis, N., I.A. Abba, H.T. Bi and J.R. Grace, Modeling and Scale-Up of O_2-Feed Oxy-Chlorination Fluidized Bed Reactors, Internal Report Submitted to MCC, Fluidization Research Centre, University of British Columbia, Canada, August (2000).

Fane, A.G. and C.Y. Wen, Fluidized Bed Reactors, Chap. 8.4, in Handbook of Multiphase Systems (ed. G. Hetsroni), Hemisphere Publishing, Washington (1982).

Foka, J., C. Chaouki, D.K. Guy and D. Klvana, Natural Gas Conversion in a Catalytic Turbulent Fluidized Bed, *Chem. Eng. Sci.*, **49**, 4269-4276 (1994).

Foka, J., C. Chaouki and D. K. Guy, Gas Phase Hydrodynamics of a Gas-Solid Turbulent Fluidized Bed Reactors, *Chem. Eng. Sci.*, **55**, 713-723 (1996).

Fukunada, Y., Monta, T., Asaki, Z. and Kondo, Y., Oxidation of Zinc Sulphide in a Fluidized Bed, Metal. Trans., 7B, 307-314 (1976).

Fuller, E.N., P.D. Schettler and J.C. Giddings, A New method for Prediction of Binary Gas-Phase Diffusion Coefficients, *Ind. Eng. Chem.*, **58**, 19-27 (1966).

Geldart, D., ed., Gas Fluidization Technology, John Wiley and Sons Ltd., Chichester (1986).

Geldart, D. and A.R. Abrahamsen, Homogeneous Fluidization of Fine Particles Using Various Gases and Pressures, *Powder Tech.*, **19**, 133-136 (1978).

Geldart, D. and M.J. Rhodes, Survey of Current Worldwide Research in Gas Fluidization (January 1989 – December 1991), *Powder Tech.*, **71**, 1-46 (1992).

Grace, J.R., An Evaluation of Models for Fluidized Bed Reactors, *AIChE Symp. Ser.* **67**, 159-167 (1971).

Grace, J.R., Fluid Beds as Chemical Reactors, Chap. 11, in Gas Fluidization Technology, (ed. D. Geldart), John Wiley and Sons Ltd., Chichester (1986).

Grace, J.R., Fluidized Bed Hydrodynamics, Chap. 8 in Handbook of Multiphase Systems, (ed. G. Hetsroni), Washington Hemisphere Publishing (1982).

Grace, J.R., Generalized Models for Isothermal Fluidized Bed Reactors, *in Recent Advances in the Engineering Analysis of Chemically Reacting Systems*, (Ed. L.K. Doraiswamy), Wiley, New Delhi, pp. 237-255 (1984).

Grace, J.R., High Velocity Fluidized Bed Reactors, *Chem. Eng. Sci.* **45**, 1953-1966 (1990).

Grace, J.R. Modeling and Simulation of Two-Phase Fluidized Bed Reactors, *in Chemical Reactor Design and Technology* (ed. De Lasa, H.I.), Martinus Nijhoff Publishers, Dordrecht, The Netherlands, pp. 245-289 (1986).

Grace, J.R., I.A. Abba, H.T. Bi, and M.L. Thompson, Fluidized Bed Catalytic Reactor Modeling across the Flow Regimes, *Can. J. Chem. Eng*, **77**, 305-311 (1999).

Grace, J.R., A.A. Avidan and T.M. Knowlton, eds., Circulating Fluidized Beds, Chapman and Hall, London (1997).

Grace, J.R. and H.T. Bi, Introduction to Circulating Fluidized Beds, Chap. 1, in Circulating Fluidized Beds, (eds. Grace, J.R., A.A. Avidan and T.M. Knowlton), Chapman and Hall, London, pp. 1-20 (1997).

Grace, J.R., A.S. Issangya, D. Bai and H.T. Bi, Situating the High-Density Circulating Fluidized Bed, *AIChE J.*, **45**, 2108-2116 (1999).

Grace, J.R. and K.S. Lim, Reactor Modeling for High-Velocity Fluidized Beds, Chap. 15, in Circulating Fluidized Beds, (eds. Grace, J.R., A.A. Avidan and T. M. Knowlton), London, Chapman Hall, pp. 504-524 (1997).

Grace, J.R. and G. Sun, Influence of Particle Size Distribution on the Performance of Fluidized Bed Reactors, *Can. J. Chem. Eng.*, **69**, 1126-1134 (1991).

Han, I.S. and C.B. Chung, Dynamic Modeling and Simulation of a Fluidized Catalytic Cracking Process. Part I: Process Modeling, *Chem. Eng. Sci.*, 56, 1951-1971 (2001).

Hashimoto, O., T. Haruta, S. Mori, S. Hiraoka, I. Yamada, M. Kuwa and Y. Saito, Simulation Model of Turbulent Fluidized Bed Catalytic Reactor (in Japanese), *Kagaku Kogaku Ronbunshu*, **15**, 336-342 (1989).

Hoeting, J. A., D. Madigan, A. E. Raftery, and C. T. Volinsky, Bayesian Model Averaging, Technical Report # 9814, Department of Statistics, Colorado State University, Fort Collins (1998).

Ip, T., Influence of Particle Size Distribution on Fluidized Bed Hydrodynamics, M.A.Sc. Thesis, University of British Columbia, Vancouver, Canada (1989).

Irani, K.R., B.D. Kurkarni and L.K. Doraiswamy, Analysis of Fluid Bed Reactors for Reactions Involving a Change in Volume, *Ind. & Eng. Chem. Fund.*, **19**, 424-428 (1980).

Itoh, S., Y. Okada, G. Higuchi and K Furubayshi, Combustion Properties of Wide Range Fuels of Circofluid, in *Circulating Fluidized Bed Technology III*, (eds. P. Basu, M. Horio and M. Hasatani), Pergamon, Oxford, pp. 3-24 (1991).

Jackson, R., Transport in Porous Catalysts, Chem. Eng. Monograph, New York, Elsevier (1977).

Jiang, P, H. Bi, R.H. Jean and L.S. Fan, Baffle Effects on Performance of Catalytic Circulating Fluidized Bed Reactor, *AIChE J.*, **37**, 1392-1400 (1991).

Johanssen T.A and B.A. Foss, Operating Regime Based Modeling and Identification, *Comp. Chem. Eng.* **21**, 159-176 (1997).

Johnsson, J.E., Fluidized Bed Reactor Model Verification on a Reactor of Industrial Scale, Research Report DIAK-1986-1 (1986).

Johnsson, J.E., J.R. Grace and J.J. Graham, Fluidized Bed Reactor Model Verification on a Reactor of Industrial Scale, *AIChE J.*, **33**, 619-627 (1987).

Kagawa, H, H. Mineo, R. Yamazaki and K. Yoshida, A Gas-Solid Contacting Model for Fast Fluidized Bed, in *Circulating Fluidized Bed Technology III*, (eds. P. Basu, M. Horio and M. Hasatani), Pergamon, Oxford, pp. 551-556 (1991).

Kai, T. and S. Furusaki, Effect of Volume Change on Conversions in Fluidized Catalyst Beds. *Chem. Eng. Sci.*, **39**, 1317-1319 (1984).

Kato, K. and C. Wen, Bubble Assemblage Model for Fluidized Bed Catalytic Reactors, *Chem. Eng. Sci.*, **24**, 1351-1369 (1969).

King, D.F., Estimation of Dense Bed Voidage in Fast And Slow Fluidized Beds of FCC Catalyst, *in Fluidization VI* (eds. J.R. Grace, L.W. Schemilt, & M.A. Bergougnou), New York, Engineering Foundation, pp. 1-8 (1989).

Krambeck, F.J., A.A. Avidan, C.K. lee and M.N. Lo, Predicting Fluid Bed Reactor Efficiency Using Adsorbing Gas Tracers, *AIChE. J.*, **33**, 1727-1738 (1987).

Kunii, D. and O. Levenspiel, Circulating Fluidized Bed Reactors, *Chem. Eng. Sci.*, **52**, 2471-2482 (1997).

Kunii, D. and O. Levenspiel, Fluidization Engineering, 2nd ed., Butterworth-Heinemann, Massachusetts, (1991).

Kunii, D. and O. Levenspiel, Fluidization Engineering, Wiley, New York, (1969).

Kunii, D. and O. Levenspiel, The K-L Reactor Model for Circulating Fluidized Beds, *Chem. Eng. Sci.*, 55, 4563-4570 (2000).

Lainiotis, D.G., Optimal Adaptive Estimation: Structure and Parameter Adaptation, *IEEE Trans. Automat. Contr.*, **AC-16**, 160-170 (1971)

Lee, G.S. and S.D. Kim, Axial Mixing of Solids in Turbulent Fluidized Beds, *Chem. Eng. J.*, **44**, 1-9 (1990).

Lee, G.S. and S.D. Kim, Gas Mixing in Slugging and Turbulent Fluidized Beds, *Chem. Eng. Comm.* **86**, 91-111 (1989).

Li, T. and P. Wu, A Study on Axial Gas Mixing in a Fast Fluidized Bed, *in Circulating Fluidized Bed Technology III*, (eds. P. Basu, M. Horio and M. Hasatani), pp. 581-586 (1991).

Lim, K.S., J.X. Zhu and J.R. Grace, Hydrodynamics of Gas-Solid Fluidization, *Int. J. Multiphase Flow*, **21**, 141-193 (1995).

Loredo, T. J., From Laplace to Supernova SN 1987A: Bayesian Inference, in Maximum Entropy and Bayesian Methods (ed. P.F. Fougere), Kluwer Academic Publishers, Dordrecht, Netherlands, 81-142 (1990).

Magoon, D.H., K.A Met, A.R. Babcock and W.A. Van Beek, Equipment and Processes for Roasting Zinc Concentrates, Lead-Zinc '90 (eds. Mackey, T.S. and R.D. Prengaman), The Minerals, Metals and Materials Society, pp. 389-412 (1990).

Marmo, L, G. Rovero and G. Baldi, Modeling of Catalytic Gas-Solid Fluidized Bed Reactors, *Catalysis Today*, **52**, 235-247 (1999).

Massimilla, L., Behavior of Catalytic Beds of Fine Particles at High Gas Velocities, *A.I.Ch.E. Symp. Ser.* **69**(128), 11-12 (1973).

Masson E.A. and S.C. Saxena, Approximate Formula for the Conductivity of Gas Mixtures, *Phys. Fluids*, **1**, 361-369 (1958).

Matsen, J.M., Fluidized Beds, Chapter 10 in *Scale-up of Chemical Processes* (eds: Bisio, A. and Kabel, R. L.), 347-405 (1985).

McNab, W.W and B.P. Dooher, Uncertainty Analyses of Fuel Hydrocarbon Biodegradation Signatures in Ground Water by Probabilistic Modeling, *Ground Water*, **36**, 691-698 (1998).

Mleczko, L., T. Ostrowski and T. Wurzel, A Fluidized Bed Membrane Reactor for the Catalytic Partial Oxidation of Methane to Synthesis Gas, *Chem. Eng. Sci.*, **51**, 3187-3192 (1996).

Mori, S. and C.Y. Wen, Estimation of Bubble Diameter in Gaseous Fluidized Beds, *AIChE J.*, **21**, 109-115 (1975).

Morikawa, H., H.T. Bi, C.J. Lim and J.R. Grace, Entrainment from Pilot Scale Turbulent Fluidized Beds of FCC Particles, *in Fluidization X*, (eds. M. Kwauk, J. Li and W.C. Yang), pp. 181-188 (2001).

Murray-Smith, R. and T.A. Johanssen, eds., Multiple Model Approaches to Nonlinear Modeling and Control, Taylor and Frances, London (1997).

Natesan, K. and W.O. Philbrook, Oxidation Kinetic Studies of Zinc Sulfide in a Fluidized Bed Reactor, *Met. Trans.*, **1**, 1353-1361 (1970).

Nyberg, J., M.L. Metsarinta and A. Roine, Recent Process Developments in the Kokkola Zinc Roaster, in Lead-Zinc 2000 (eds. Dutrizac, J.E., J.A. Gonzales, D.M. Henke, S.E. James and A.H.J. Siegmund), TMS-The Metals and Materials Society, pp. 399-415 (2000).

Ouyang, S., S.G. Li and O.E. Potter, Circulating Fluidized Bed as a Chemical Reactor: Experimental Study, *AIChE J.*, **41**, 1534-1542 (1995).

Partridge, B.A. and P.N. Rowe, Chemical Reaction in a Bubbling Bed Fluidized Bed, *Trans. Instn. Chem. Engrs.* **44**, 335-348 (1966).

Patience, G.S., and J. Chaouki, Gas-Phase Hydrodynamics in the Riser of a CFB, *Chem. Eng. Sci.*, **48**, 3195-3205 (1993)

Puchyr, D. M.J., A.K. Mehrotra and L.A. Behie, Modeling a Circulating Fluidized Bed Riser Reactor with Gas-Solids Downflow at the Wall, *Can. J. Chem. Eng.*,**75**, 317-326 (1997).

Pugsley, T.S., G.S. Patience, F. Berruti and J. Chaouki, Modeling the Catalytic Oxidation of n-Butane to Maleic Anhydride Using a Circulating Fluidized Bed Reactor, *Ind. Eng. Chem. Res.*, **31**, 2652-2660 (1992).

Ramachandran, P.A. and L.K. Doraiswamy, Modeling of Non-Catalytic Gas-Solid Reactions, *AIChE J.* **28** 881-900 (1982).

Reid, R.C., J.M. Prausnitz and B.E. Poling, The Properties of Gases and Liquids, 4th ed., McGraw-Hill, New York (1987).

Rhodes, M., What is Turbulent Fluidization?, *Powder Tech.*, **88**, 3-14 (1996).

Richardson, J.F. and J. Szekely, Mass Transfer in a Fluidized Bed, *Trans. Instn. Chem. Engrs.*, **39**, 212-222 (1961).

Schoenfelder, H., Kruse, M. and J. Werther, Two-Dimensional Model for Circulating Fluidized Bed Reactors, *AIChE J.*, **42**, 1875-1888 (1996).

Schügerl, K., Experimental Comparison of Mixing Processes in Two- and Three Phase Fluidized Beds, in Proceedings of International Symposium on Fluidization (ed. A.H.H. Drinkenburg), University Press, Amsterdam, pp. 782-796 (1967).

Shiau, C.Y. and C.J. Lin, Analysis of Volume Change Effects in a Fluidized Bed Catalytic Reactor, *J. Chem. Tech. & Biotech.*, **56**, 295-303 (1993).

Sinclair, J., Hydrodynamic Modeling, Chap. 5, in Circulating Fluidized Beds (eds. J.R. Grace, A.A. Avidan and T.M. Knowlton), Chapman and Hall, London, pp. 149-180 (1997).

Sit, S.P. and J.R. Grace, Effect of Bubble Interaction on Interphase Mass Transfer in Gas Fluidized Beds, *Chem. Eng. Sci.*, **36**, 327-335 (1981).

Sotudeh-Gharebaagh, R., R. Legros, J. Chaouki and J. Paris, Simulation of CFB Reactors using ASPEN PLUS, *Fuel* **77**, 327-338 (1998).

Stiel, L.I. and G. Thodos, Thermal Conductivity of Non-polar Substances in the Dense Gaseous and Liquid Regions, *AIChE J.*, **10**, 26-30 (1964).

Sun, G.L., Influence of Particle Size Distribution on the Performance of Fluidized Bed Reactors, Ph.D. Dissertation, University of British Columbia, Vancouver, Canada (1991).

Tafreshi, Z.M., K. Opoku-Gyamfi. And A.A Adesina, A Two-Phase Model for Variable-Density Fluidized Bed Reactors with Generalized Nonlinear Kinetics. *Can. J. Chem. Eng.*, **78**, 815-826 (2000).

Thompson, M.L., H. Bi, and J.R. Grace, A Generalized Bubbling/Turbulent Fluidized Bed Reactor Model, *Chem. Eng. Sci.*, **54**, 2175-2185, (1999)

Thompson, M.L., Ph. D. Thesis, Combining Prior Models and Nonparametric Models of Chemical Processes, Massachusetts Institute of Technology, Cambridge, Mass. (1996).

Toomey, R.D. and H.F. Johnstone, Gaseous Fluidization of Solid Particles, *Chem. Eng. Prog.*, **48**, 220-226 (1952).

Van Deemter, J.J., Mixing and contacting in Gas-Solid Fluidized Beds, *Chem. Eng. Sci.*, **13**, 143-154 (1961).

Van Swaaij, W.P.M., The Design of Gas-Solids Fluid Beds and Related Reactors, *ACS Symp. Ser.* (eds. D. Luss and V.W. Weekman), **72**, 193-222 (1978).

Venderbosch, R.H., The Role of Clusters in Gas-Solids Reactions: an Experimental Study, Research Report, Twente University, Print Partners Ipskamp, Enschede, The Netherlands (1998).

Wainwright, M.S. and N.R. Foster, Catalysis, Kinetics and Reactor Design in Phthalic Anhydride Synthesis, *Catal. Rev.-Sci. Eng.*, **19**, 211-228 (1979).

Wei F. Y. Jin, Z. Yu and W. Chen, Lateral and Axial Mixing of the Dispersed Particles in CFB, *J. Chem. Eng. Japan*, **28**, 506-510 (1995).

Wen, C.Y., Flow Regimes and Flow Models for Fluidized Bed Reactors, *in Recent Advances in the Engineering Analysis of Chemically Reacting Systems*, (ed. L.K. Doraiswamy), Wiley, New Delhi, pp. 256-290 (1984).

Wen, C.Y. and Y.H. Yu, A generalized Method for Predicting the Minimum Fluidization Velocity, *AIChE J.*, **12**, 610-612 (1966).

Werther, J., and J. Wein, Expansion Behavior of Gas Fluidized Bed in the Turbulent Regime, *AIChE Symp. Ser.*, **90**(301), 31-44 (1994).

Westerman, D.W.B., The Catalytic Oxidation of Naphthalene on Vanadia Catalysts, Ph.D. Thesis, University of New South Wales, Sydney (1980).

Wilke, C.R., A Viscosity Equation for Gas Mixtures, *J. Chem. Phys.*, **18**, 517-519 (1950).

Won, N. and Kim, S.D., Gas Backmixing in Circulating Fluidized Bed, *Powder Tech.*, **99**, 10-78 (1998).

Wurzel, T. and L. Mleczko, Engineering Model of Catalytic Partial Oxidation of Methane to Synthesis Gas in a Fluidized Bed Reactor, *Chem. Eng. J.*, **69**, 127-133 (1998).

Yerushalmi, J. and A. Avidan, High Velocity Fluidization, in *Fluidization II* (eds. J.F. Davidson, R. Clift and D. Harrison), Academic Press, pp.225-291 (1985).

Yerushalmi, J. and N.T. Cankurt, Further Studies of the Regimes of Fluidization, *Powder Tech.*, **24**, 187-205 (1979).

Yerushalmi, J., D.H. Turner and A.M. Squires, The Fast Fluidized Bed, *Ind. & Eng. Chem. Proc. Des. & Dev.* **15**, 47-51 (1976).

Yoon, P. and G. Thodos, Viscosity of Non-polar Gaseous Mixtures at Normal Pressures, *AIChE J.*, **16**, 300-304 (1970).

Zhang, W., Y. Tung and F. Johnsson, Radial Voidage Profiles in Fast Fluidized Beds of Different Diameters, *Chem. Eng. Sci.*, **46**, 3045-3052 (1991).

Appendix A

Bed Properties Evaluation Scheme

The correlations, which are not listed in Table 2.3, but which were used in computing the hydrodynamic quantities in the bed within the model are summarized here.

Equivalent bubble diameter: As a result of bubble coalescence, the size of the bubbles increases with height in the bubbling regime. Clift (1986) compared several correlations for bubble size estimation and found that they all give comparable estimates. One of the widely used correlations is (Mori and Wen, 1975):

$$d_b(z) = d_{bM} - (d_{bM} - d_{bo})e^{-0.3z/D_t} \qquad (A1)$$

where the maximum bubble size d_{bM} is 1.87 times the initial bubble size formed at the grid, d_{bo}. That is:

$$d_{bM} = 1.87 d_{bo} \qquad \text{(size before slugging starts)} \qquad (A2)$$

$$d_{bo} = 79.13 \left[D_t^2 (U - U_{mf}) / N_{or} \right]^{0.4} \qquad (A3)$$

where N_{or} is the number of holes in the perforated plate distributor

Minimum fluidization velocity: Numerous correlations have been developed for the estimation of minimum fluidization velocities. Wen and Yu (1966) correlated many data in terms of the Archimedes and Reynolds number for minimum fluidization. A modified form of the well known Wen and Yu correlation due to Grace (1982) is:

$$U_{mf} = \frac{\mu}{\rho \bar{d}_p} \sqrt{(27.2)^2 + 0.0408 Ar} - 27.2 \qquad (A4)$$

Minimum bubbling velocity: The velocity at which bubbles first appear, minimum bubbling velocity, U_{mb}, has been found to depend on both particle and gas properties. A widely used correlation by Geldart and Abrahamsen (1978) is:

$$U_{mb} = 33 \bar{d}_p \left(\frac{\rho_g}{\mu_g} \right)^{0.1} \qquad (A4)$$

Note that for Groups B and D particles, *if* $U_{mb} < U_{mf}$, *then* $U_{mb} = U_{mf}$.

Average bubble rise velocity: A number of correlations have been developed for estimating the absolute bubble rise velocity. Clift and Grace (1985) reported a correlation that is widely used:

$$u_{br} = (U - U_{mf}) + f\sqrt{gd_b} \quad \begin{cases} f = 0.71 \rightarrow bubbling\,regime \\ f = 1.24 \rightarrow turbulent\,regime \end{cases} \tag{A5}$$

External mass transfer coefficient: The external mass transfer coefficient, k_c, is calculated from the correlation of Richardson and Szekely (1961), which was developed based on large data pool:

$$Sh = 0.375\,Re_p^{1.18} \qquad 0.1 < Re_p < 15 \tag{A6}$$

$$Sh = 2.01\,Re_p^{0.5} \qquad 15 < Re_p < 250 \tag{A7}$$

Note that the Sherwood number, Sh, has a value below 2 at low Re_p, which the authors attributed to gas mixing, most significant at low Re_p. They also did not detect any systematic dependence of the Schmidt number on the Sherwood number.

Core and annular voidage: The core and annular voidage can be determined from the widely used radial profile by Zhang et al (1991):

$$\varepsilon(r) = \bar{\varepsilon}^{[0.191 + \xi^{2.5} + 3\xi^{11}]} \quad \left\{ \xi = \frac{r}{R} \right. \tag{A8}$$

so that

$$\bar{\varepsilon}_C = \frac{2}{r_C^2} \int_0^{r_c} \varepsilon(r)r\,dr; \qquad \bar{\varepsilon}_a = \frac{2}{R^2 - r_C^2} \int_{r_c}^{R} \varepsilon(r)r\,dr \tag{A9}$$

Core radius: Many correlations have been proposed for calculating the core radius. The correlation by Bi et al. (1996) developed by regressing a large pool of solid flux measurements data is:

$$r_C = R - 0.5D_t\left(1 - \sqrt{1.34 - 1.3(1 - \bar{\varepsilon})^{0.2} + (1 - \bar{\varepsilon})^{1.4}}\right) \tag{A10}$$
$$0.80 \le \bar{\varepsilon} \le 0.9985$$

Appendix B

Thermophysical Properties Evaluation Scheme

1. The heat of reaction k can be written:

$$\Delta H_k = \Delta H_k^{ref} + \int_{T^{ref}}^{T} \Delta C_{Pg,k} dT \qquad \text{(B1)}$$

where

$$\Delta C_{Pg,k} = \sum_{i}^{N_c} v_{ik} C_{Pi} \qquad \text{(B2)}$$

2. The average specific heat capacity of the gas mixture is obtained from:

$$C_{Pg,mix} = \sum_{i}^{N_c} x_i C_{Pg,i} \qquad \text{(B3)}$$

The heat capacity is expressed as a polynomial function of temperature (Reid et al., 1987):

$$C_{Pi} = A + BT + CT^2 + DT^3 \qquad \text{(B4)}$$

The coefficients A, B, C, and D are constants to calculate the isobaric heat capacity of the ideal gas, with C_{Pg} in J/mol K and T in Kelvin.

3. The thermal conductivity of a gas mixture k_m is not usually a linear function of mole fraction. The equation of Mason and Saxena (1958), often used for low pressure gas mixtures, is (Reid et al., 1987):

$$k_{mix} = \sum_{i} \frac{x_i k_i}{\sum_{j} x_j A_{ij}} \qquad \text{(B5)}$$

$$A_{ij} = \frac{\left[1 + (\mu_i/\mu_j)^{1/2}(M_j/M_i)^{1/4}\right]^2}{\left[8(1 + (M_i/M_j)\right]^{1/2}} \qquad \text{(B6)}$$

with $A_{ii} = 1.0$. k_i and μ_i are the thermal conductivity and viscosity of pure component i.

The thermal conductivities of the pure gas components are determined from the Stiel and Thodos (1964) method (Reid et al., 1987):

$$k_i = \frac{\mu_i}{M_i'}\left[1.15(C_{Pg,i} - R) + 2.03R\right] \tag{B7}$$

k_i is in W/m K; μ_i in kg/m s; R and $C_{Pg,i}$ in J/mol K and M'_i in kg/mol.

4. The gas mixture viscosity, μ_{mix}, with compositional dependence for non-polar gas mixtures is obtained from the Wilke (1950) approximation (Reid et al., 1987):

$$\mu_{mix} = \sum_i \frac{x_i \mu_i}{\sum_j x_j \Phi_{ij}} \tag{B8}$$

$$\Phi_{ij} = A_{ij} \tag{B9}$$

The viscosity of the individual gas components are determined via the Yoon and Thodos (1970) method (Reid et al., 1987):

$$\mu_i \alpha_i = 10^{-7} \times \left[4.61 T_r^{0.618} - 2.04\exp(-0.449T_r) + 1.94\exp(-4.058T_r) + 0.1\right] \tag{B10}$$

$$\alpha_i = T_c^{1/6} M_i^{-1/2} P_c^{-2/3} \tag{B11}$$

The viscosity μ_i is in kg/m s; T_c (K) and P_c (atm) are the critical properties of the gas stream, T_r is the reduced temperature and M_i (kg/kmol) is the molecular weight.

5. The diffusivity of component i in the gas mixture $\mathcal{D}_{i,mix}$, is determined (Reid et al, 1987) from:

$$\mathcal{D}_{i,mix} = \frac{1}{\displaystyle\sum_{\substack{j=1 \\ j \neq i}}^{N_c} \frac{x_j}{\mathcal{D}_{ij}}} \tag{B12}$$

The binary diffusivity, $\mathcal{D}_{ij}$, is determined from the Fuller et al. (1966) method based on the atomic volume of gases, υ (Reid et al, 1987):

$$\mathcal{D}_{ij} = \frac{1.43 \times 10^{-7} T^{1.75}}{PM_{ij}^{1/2}\left[\left(\sum \upsilon\right)_i^{1/3} + \left(\sum \upsilon\right)_j^{1/3}\right]^{1/2}} \tag{B13}$$

$$M_{ij} = 2\left[\frac{1}{M_i} + \frac{1}{M_j}\right]^{-1} \tag{B14}$$

The diffusivity $\mathcal{D}_{ij}$ is in m^2/s; T in K, P in bar and M_i in kg/kmol.

The average molecular diffusivity of the gas mixture is obtained from:

$$\mathcal{D}_{mix} = \sum_i^{N_c} x_i \mathcal{D}_{i,mix} \tag{B15}$$

6. The effective thermal conductivity of bed solids is determined assuming that the effective solids diffusivity has the same numerical value as the thermal diffusivity (using the analogy between heat and mass transfer as suggested by Matsen, 1985):

$$k_e = E_z \times \rho_p(1 - \varepsilon)C_{Pp} \tag{B16}$$

where the effective axial dispersion coefficients of solids is given by:

- Bubbling/turbulent flow regime (Lee and Kim, 1990):

$$E_z = 1.058(U - U_{mf})D_t\left(\frac{gD_t}{U - U_{mf}}\right)^{0.653} Ar^{-0.368} \tag{B17}$$

- Fast fluidization flow regime (Wei et al., 1995):

$$E_z = 0.0139\frac{L_t\mu}{D_t\rho_g}(1 - \varepsilon)^{-0.67} \tag{B18}$$